SIMULATION AND STUDY OF THE CMS ENDCAP MUON ALIGNMENT SCHEME

A Thesis
Submitted to the Faculty

of

Purdue University

by

Robert H. Lee

In Partial Fulfillment of the
Requirements for the Degree

of

Doctor of Philosophy

May 2002

Dedicated to my wife, Angela

ACKNOWLEDGMENTS

I have been very fortunate to have both started and completed this journey with the guidance of Laszlo Gutay and David Eartly. They created the opportunity for me to succeed early on and continued to offer their assistance and guidance when it was needed most. Likewise, I owe Kaori Maeshima a tremendous debt of gratitude, as she has spent the past several years carefully monitoring my progress and providing me with the advice and daily counsel needed to complete this thesis. I would have been lost without her. I am lucky to count Laszlo, David, and Kaori as good friends.

I am also very fortunate that Hans Wenzel was kind enough to make a significant effort to help me understand the physics reconstruction software as well as provide me with the special computing resources required to run it quickly. His help was invaluable. I would also like to acknowledge the support of Fermilab and the Department of Energy for providing me with the resources to work in the USCMS Collaboration and complete my thesis.

My brother Ryan and my closest friends Ricardo, Denis, David, Todd, Kevin, Susan, Heather, Josh, Missy, Jess, Jeff, and the Hu family deserve thanks for their many years of friendship and for reminding me not to take things too seriously.

Finally, I am most grateful to Angela, who has made of all my endeavors much easier than they would have been without her, and to my parents, who gave me everything I needed to complete this work.

TABLE OF CONTENTS

LIST OF TABLES

Appendix Table

LIST OF FIGURES

Figure **Page**

Appendix Figure

ABSTRACT

Lee, Robert H. Ph.D., Purdue University, May, 2002. Simulation and Study of the CMS Endcap Muon Alignment Scheme. Major Professor: Dr. Laszlo Gutay.

The successful operation of the CMS Endcap Muon detector will entail meeting several significant technical challenges. Among these challenges will be the ability to accurately estimate the performance of the Endcap Muon detector and to anticipate or correct any potential problems during the design stage. This thesis presents the simulation and study of the Endcap Muon Alignment Scheme, a component of the Endcap Muon Detector designed to determine and track the location of Cathode Strip Chambers.

Information about the performance of the CMS Endcap Alignment System was gathered through an extensive testing of a prototype system and then used to create a simulation to predict the behavior of the system as designed. The results of these simulations indicate that the design of the EMU Alignment System is viable and can successfully reconstruct chamber locations along designated alignment lines throughout the CMS Endcap. A detailed error analysis and subsequent examination of the principle sources of uncertainty across multiple simulations show that the tolerances on components and their calibration are well understood and will ensure the successful reconstruction of CSC chamber positions within approximately 200μm in CMS RΦ and 500μm in CMS Z. In addition, physics studies of single muon events were performed with the general CMS Reconstruction Software (ORCA 5_3_1) to understand CSC misalignment effects on muon track reconstruction and predict how the Alignment System will impact the final determination of muon p_t and trigger rates in the Endcap Muon System.

1 INTRODUCTION

Modern high energy physics is driven by the enormous accelerators and detectors which allow physicists to probe interactions at very large energies. The Large Hadron Collider (LHC) at CERN is presently under construction and will ultimately offer a glimpse of physics at an energy level more than seven times of what is presently accessible. To observe interactions at the LHC, the Compact Muon Solenoid (CMS) detector is being constructed. It is hoped that data taken at CMS will contribute toward further understanding physics within the Standard Model [1.1] and/or discovering new physics beyond it.

The design and construction of CMS is technically complex and challenging. Each subsystem in the detector will require a substantial effort to develop hardware and software solutions for the challenges encountered. This thesis is focused on the development of only a small portion of this project, the Alignment Scheme of the CMS Endcap Muon (EMU) Subsystem. More specifically, this thesis examines the components which comprise the EMU Alignment System and makes an estimation of the System's performance and impact on CMS physics.

1.1 The Higgs Boson

The Standard Model has enjoyed much success in predicting the interactions of particles. Electroweak theory [1.2] in the Standard Model has shown that weak and electromagnetic interactions arise from a common SU(2) x U(1) symmetry, however the Standard Model does not account for why particles which mediate the weak force have mass while other force carriers are massless. Experimental evidence shows that while the photon may be massless, the $W^{\pm}$ and Z^0 mediators are massive. Moreover, the Standard

Model fails to predict any of the quark or lepton masses. An important part of completing the Standard Model will be to explain what hides the symmetry between weak and electromagnetic interactions and thus how particle masses may be generated.

The simplest prediction as to the origin of the mass within the Standard Model postulates that particles interact with a field (called the 'Higgs Field') to acquire mass. The degree to which these particles interact with this field would determine their mass. An important requirement of a theory utilizing such a field would be the preservation of the electroweak SU(2) x U(1) symmetry. Spontaneous symmetry breaking, in which the lowest energy states of the field have less symmetry than it Lagrangian, offers a way to give the $W^{\pm}$ and Z^0 bosons mass while keeping this symmetry invariant. The manner in which spontaneous symmetry breaking is employed with the concept of local gauge invariance in the generation of the Higgs field is called the Higgs Mechanism.

A direct consequence of the Higgs Mechanism and in keeping with the mediation of other field-particle interactions, a neutral Higgs boson is postulated. The experimental confirmation of such a particle would validate the presence of a Higgs field. As a consequence, a large effort has been made to find this particle with existing particle accelerators. To date, no experiments have confirmed the existence of the Higgs with a high degree of statistical certainty. Presumably, if a Standard Model Higgs particle exists at all, it is simply too heavy to produce enough of with existing accelerators. Other theories have also been proposed to extend the present Standard Model. Several of these theories postulate multiple Higgs particles (the Minimal Super Symmetric Model [1.3], for example) while others predict no Higgs particles at all (Technicolor [1.4]). In any case, what remains important is the Standard Model can in principle accommodate a Higgs particle which would indicate the presence of a mechanism to explain the aforementioned problems within the Standard Model.

LEP 2000 data indicates that the lower boundary of the Higgs mass is 114.1 GeV/c^2 at a 95% confidence level [1.5]. Though LEP 2000 announced several potential Higgs

candidates at the end of its final run near 115 GeV/c^2, the results were not conclusive. The Aleph and Delphi experiments at LEP initially reported five Higgs 4-jet candidate events at a mass of around 114 GeV against an expected background of 0.3 events. By the end of 2001, following a brief extension on LEP operation and an updated analysis of all available LEP data, the LEP L3 detector reported a Higgs candidate from a two jet and missing energy (neutrinos) event, the OPEL detector reported, with very low confidence, two 4 jet candidates, the Aleph detector maintained confidence in their initial results, while the Delphi detector lowered the significance on both of their initial 4 jet candidates with further recalibration of their detector. The lower bound on the Higgs mass was also revised to 114.1 GeV (at the 95% confidence level). [1.5]

Since the Higgs particle is expected to provide the mechanism for the generation of the quark and vector boson masses, the Higgs mass can be calculated directly from the top quark and W boson masses. However, the accuracy to which the Higgs mass can be determined from these parameters is very sensitive to the certainty with which these masses are known. Figure 1.1 shows the range of possible Higgs masses allowed if such a calculation is done with the present experimental measurements (and uncertainties) of the top and W masses in the context of the Standard Model.

The experimental evidence presented in Figure 1.1 indicates the most likely mass of the Higgs will be (at a 1σ confidence level) less than 500 GeV/c^2. The upper bound for the Higgs mass consistent with the agreement of all the experimental data in Figure 1.1 is 250 GeV/c^2.

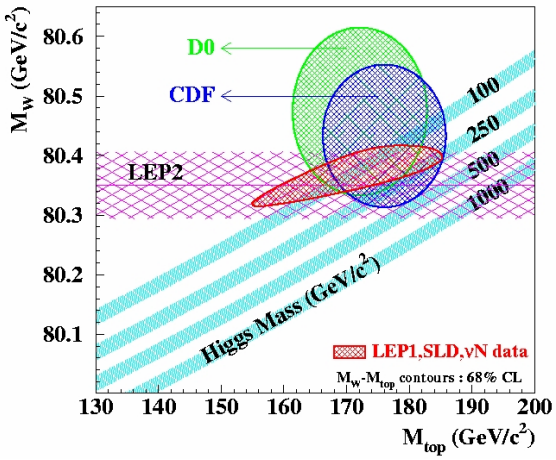

Figure 1.1: Range of possible Higgs masses calculated from experimental determinations of top quark mass and W boson mass in the context of the Standard Model. The shaded areas on the plot represent the measurement and associated errors that have been determined from direct top and W measurements at Fermilab CDF and D0 detectors, direct W measurements at LEP2000, and indirect measurements of top and W masses from LEP, SLC, and Fermilab neutrino experiments[1.6].

1.2 LHC and role of the CMS Detector

The CERN Large Hadron Collider (LHC) is being constructed to probe previously unobtainable energy regions and will be used in the search for the Higgs Boson. In addition to expanding the available range of energies to continue this search, the LHC is being designed to provide a high number of events to study. The LHC will principally operate at two luminosities (10^{33} $cm^{-2}sec^{-1}$ and 10^{34} $cm^{-2}sec^{-1}$) and is expected to collide protons with at a 14TeV center of mass energy.

The Compact Muon Solenoid (CMS) detector is a general purpose detector to be constructed at one of the LHC interaction points and will be used in the search for the Higgs boson, study of t- and b-quark decays, and the search for physics beyond the Standard Model. The fundamental design of this detector was premised on the implementation of a very good muon system motivated in part by the $H \rightarrow ZZ \rightarrow 2\mu^- 2\mu^+$ Higgs Boson decay channel. To facilitate the identification of particle type and charge of muons and other charged particles, the detector features a superconducting solenoid

capable of fields exceeding 4 Tesla. Aside from the muon system, all components of the detector are placed inside the solenoid. This arrangement is expected to be particularly advantageous in the search for $H \rightarrow \gamma\gamma$ decays. The endcaps of the detector consist of alternating layers of muon chambers and iron discs to return the large B field generated by the solenoid.

The principle components of the CMS detector include the Inner Tracker, Electromagnetic Calorimeter (ECAL), Hadronic Calorimeter (HCAL), and Muon System. Figure 1.2 shows the spatial arrangement of these components.

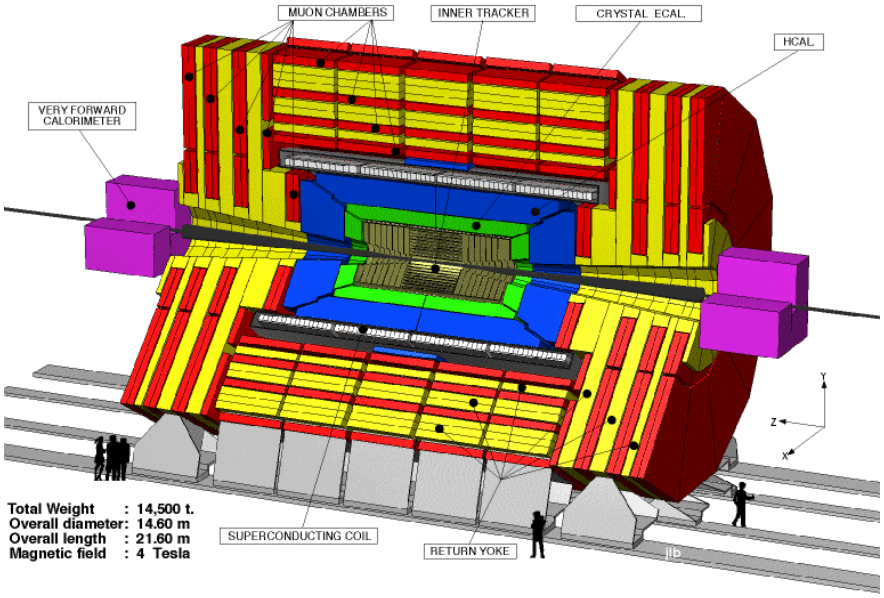

Figure 1.2: A 3D View of the Principle CMS Detector Subsystems [1.7].

1.2.1 Inner Tracking and Calorimetry in CMS

The Inner Tracker is being designed to measure the p_t of charged tracks in the region $|\eta| < 2.6$ (η regions of CMS are shown in Figure 6). The Inner Tracker will employ solid state and microstrip gas detectors for efficient b-tagging and lepton charge determination up to $p_t = 2$ TeV. The Electromagnetic Calorimeter lies immediately outside the Inner

Tracker, also covering $|\eta| < 2.6$, and utilizes lead tungstate crystals to measure EM energy. The ECAL is optimized to search for $H \rightarrow \gamma\gamma$ decays at high luminosity (10^{-34} $cm^{-2}sec^{-1}$) and will be able to make direct measurements of the photons direction in the $|\eta| < 1$ region. The Hadronic Calorimeter is constructed around the ECAL and will make complementary energy measurements of particles. To perform these tasks, this calorimeter must have good hermeticity, energy resolution, and segmentation as well as sufficient depth for the containment of hadron showers. The Hadronic Calorimeter consists of 18 identical wedges and is segmented in a manner that closely matches the arrangement of the barrel muon chambers and ECAL segmentation. The characteristic parameters describing the ECAL and HCAL are summarized in Table 1.1 and Table 1.2.

Table 1.1: Key parameters of the CMS Electromagnetic Calorimeter. Resolution is given as a function of incident photon energy while $\oplus$ denotes the terms add in quadrature [adapted from 1.3].

Resolution [MeV] (high Luminosity)	$5\%\sqrt{E} \oplus .5\%E \oplus 150$
Resolution [MeV] (low Luminosity)	$2\%\sqrt{E} \oplus .5\%E \oplus 150$
Segmentation in $\Delta\eta$ x $\Delta\phi$	.0145 x .0145
Depth in λ_R (radiation lengths)	25
Depth in λ_I (interaction lengths)	1.1

Table 1.2: Key parameters of the CMS Hadronic Calorimeter. Resolution is given as a function of incident single particle energy while $\oplus$ denotes the terms add in quadrature [adapted from 1.3].

Resolution [MeV]	$70\%\sqrt{E} \oplus 9.5\%E$
Segmentation in $\Delta\eta$ x $\Delta\phi$	.087 x .087
Depth in λ_I (interaction lengths)	25

1.2.2 Muon System

As previously discussed, the CMS detector is equipped with a Muon System that will provide excellent muon identification, momentum measurement, and triggering. Muon identification will be achieved with large area muon chambers placed behind a large absorber. At least 16 interaction lengths (λ_I) of material is present across $|\eta| < 2.4$. The

muon system is subdivided into two distinct subsystems: the Barrel Muon and Endcap Muon.

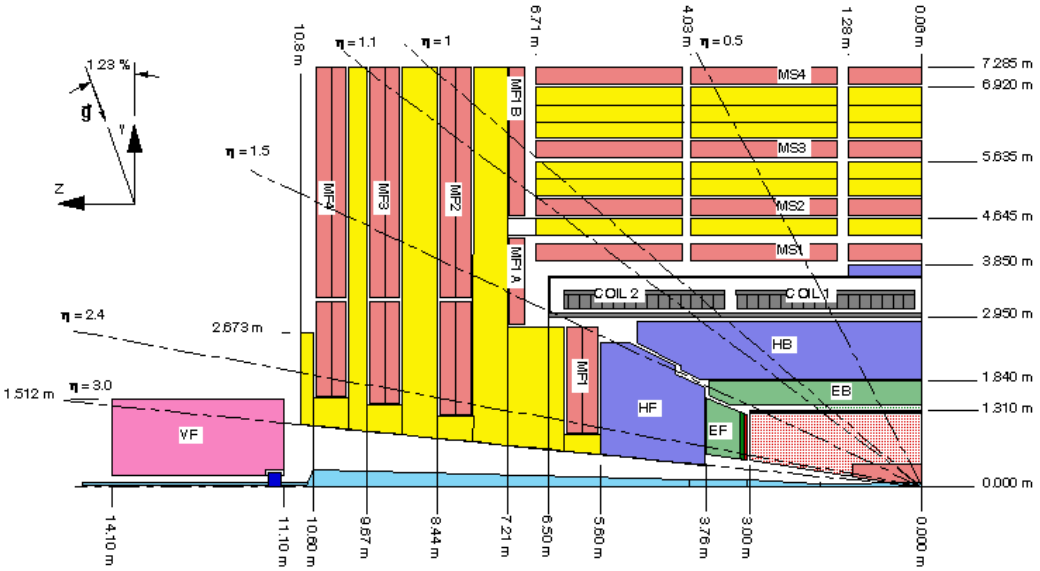

Figure 1.3: Cross Section of one quadrant of the CMS detector detailing placement Barrel Muon chambers (labeled MS1-4, in red) and the Endcap Muon chambers (labeled MF1-4, in red). [1.7]

The expected resolution of the CMS Muon system is summarized below, in Table 1.3. Resolutions in the Barrel and Endcap regions are comparable to each other.

Table 1.3: Desired Performance [Tracker + Muon] of CMS Muon System [1.8].

p_t	Expected Resolution
10 GeV	.5 – 1 GeV
100 GeV	1.5 – 5 GeV
1 TeV	50 – 200 GeV

1.2.2.1 Barrel Muon

The barrel muon system is comprised of two stations on the inside and outside of the iron return yoke (MS 1 and 4, Figure 6) and two stations located in slots within the iron (MS 2 and 3, Figure 6). The stations are segmented into five equal pieces parallel to the

beam pipe and comprised of 60 drift chambers on the interior of the detector and 70 drift chambers on the outer layer. Each drift chamber is comprised of twelve planes of drift tubes organized into four-plane 'Super Layers'. The planes comprising each Super Layer have parallel wires allowing each chamber to have two Super Layers to measure particle tracks in the ϕ plane and a third to monitor tracks along the Z plane. Moreover, each chamber plane in the Super Layers are staggered by half a drift cell length making it possible to determine the coordinate and orientation of impinging tracks without external timing by correlating the drift times in each plane. The maximum drift time for any drift cell in the chambers is 400ns, allowing the chambers to be used in first level triggering.

1.2.2.2 Endcap Muon

The Endcap Muon System is comprised of 4 discs of Cathode Strip Chambers (CSC) separated by the Return Field (RF) Iron discs (Figure 7, below). The RF iron acts as the principle mechanical support for the CSCs, absorber for incident particle showers, and a return for the large magnetic flux leaving the central solenoid. The CSCs on each disc are placed into two rings with 18 or 36 chambers in each ring. Chambers in the system form slight overlaps so that there is near 100% coverage for any incident muon track.

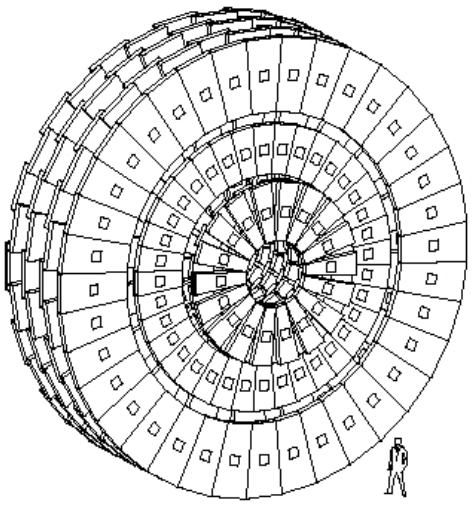

Figure 1.4: The orientation and spacing of the Endcap Muon CSC chambers. The RF iron, upon which the chambers are mounted, is not shown. [1.8]

The CSC chambers employed in the Endcap are multiwire proportional drift chambers with 50 μm intrinsic resolution and fast readout. Similar to the Barrel drift chambers, the CSCs are comprised of 6 planes, with each plane recording a two dimensional position of incident particles.

1.2.3 Expected Behavior of SM Higgs at the LHC

Production of the Higgs at the LHC is expected to be dominated by gluon-gluon fusion and WW (ZZ) fusion (Figure 1.5, below).

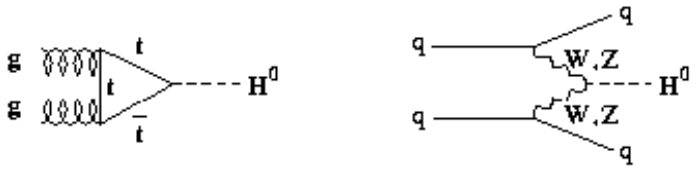

Figure 1.5: Feynman Diagrams for the two dominate production channels – gluon-gluon fusion (left) and WW (ZZ) fusion (right).

The production cross sections as a function of Higgs mass are shown in below in Figure 1.6. As the figure indicates, the production cross sections increase rapidly with the decrease in Higgs mass. Although other processes are expected to contribute to Higgs production in the LHC, the cross sections of these processes are significantly lower than WW (ZZ) fusion.

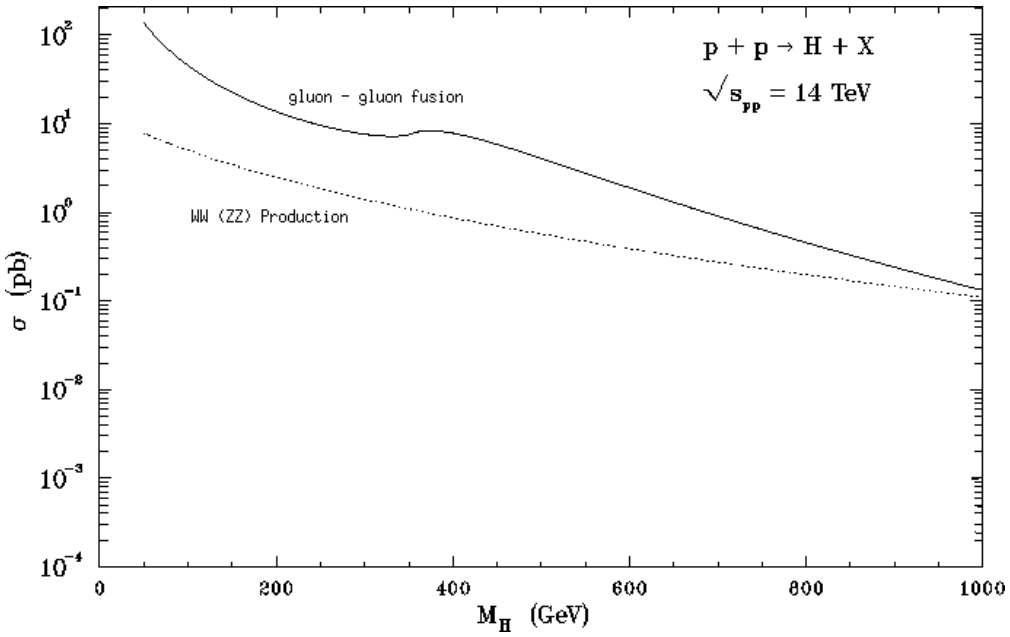

Figure 1.6: Cross Section of two dominate production channels as a Function of the Higgs Mass (m_H) [1.9].

Since the Higgs particle coupling is proportional to mass, branching ratios are expected to be dominated by dominated by heavier particles. For a Higgs mass less than 90 GeV, the H $\rightarrow$ b bbar branching ratio is extremely large, as the b quark is the heaviest possible particle accessible for a Higgs decay. As Figure 1.7 indicates, decays in to quarks or leptons less massive than the b quark will be very small (decay into gluons involves a quark loop).

For Higgs masses which lie between 90 and 600 GeV/c^2, decays into vector bosons become increasingly dominate. The H $\rightarrow \gamma\gamma$ decay emerges at approximately 90 GeV and, although extremely small, is potentially very important since the b bbar signal, as well as other quark and gluon decay signals, must be reconstructed from final decay products or intermediary particles and will involve large backgrounds (see Section 1.2.4.). Also of particular interest is the mass range 150 GeV/c^2 < m_H < 200 GeV/c^2 where the threshold of ZZ (though one Z must be below mass shell) and WW (where the WW may be on mass shell) production is met. This mass range corresponds to the dip in the ZZ branching ratio and slight elevation in the WW branching ratio on Figure 1.7. For

a $m_H \approx 2\ m_z$, the so called 'Golden Decay Channel' for $H \rightarrow ZZ \rightarrow 4$ leptons exists. The $H \rightarrow ZZ \rightarrow 4$ leptons ($\mu^{\pm}$ or $e^{\pm}$) decay, though infrequent ($Z \rightarrow \mu^{\pm}$ or $e^{\pm}$ branching ratio is only ≈ 3%), will likely prove to be a critical channel to monitor as the signal-to-background ratio is very favorable (See Section 1.2.4). The emergence of a ttbar decay channel becomes available for Higgs masses approaching $2m_t$.

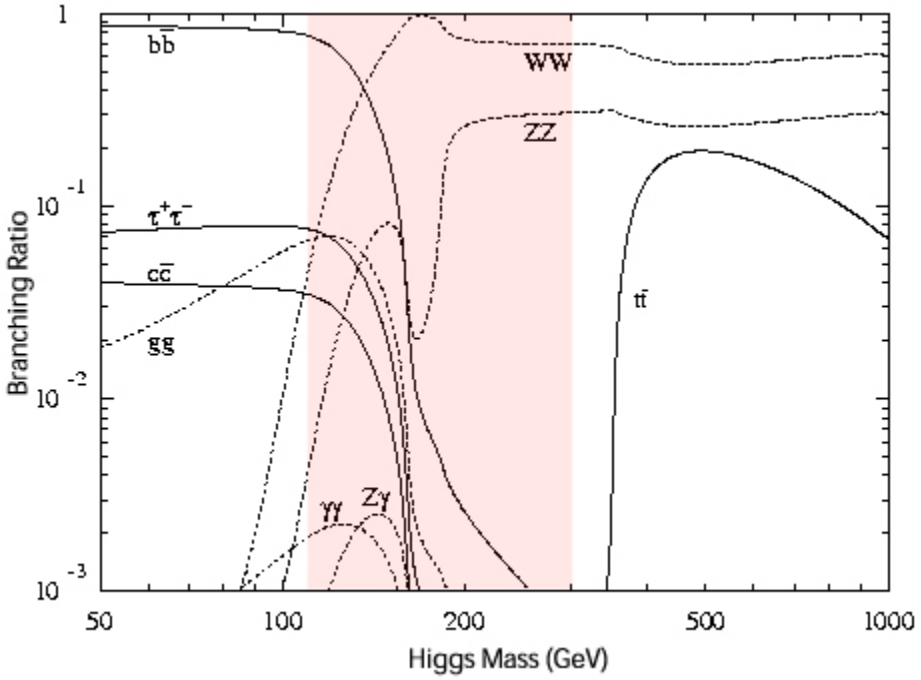

Figure 1.7: Plot of the expected dominate branching ratios for SM Higgs particle as a function of possible Higgs masses (m_H). The red band indicates the most likely mass region for m_H based on the experimental evidence from LEP2000 and Figure 1 (114.1 - 250 GeV/c^2) data [1.10].

As previously discussed, there are several indications that the mass of the Higgs will be light. However, for a heavier Higgs (>800 GeV/c^2), domination of $H \rightarrow ZZ$ and $H \rightarrow$ WW decays are still expected with a persistence of a somewhat smaller branching ratio for $H \rightarrow$ t tbar. The theoretical upper limit on the mass of the Higgs is expected to be on the order of 1 TeV, beyond which the Standard Model no longer provides an adequate explanation of observed phenomena (this is explained further in the following section).

1.2.4 Discovery Potential for Standard Model Higgs at CMS

The 'discovery' of a Higgs particle will occur after a sufficient number of Higgs decay channels are reconstructed over the remaining background (a Statistical Significance > 5, see Figure 1.8). The branching ratios of the various Higgs decays (Figure 1.7, red band) give some indication of likely discovery channels at CMS, but large backgrounds preclude the study of several of these channels. A short summary of the viability of each potential discovery channel is given in Section 1.2.4.1-5.

Simulation studies of the expected physics at the CMS detector [1.3,1.4,1.7] have indicated that the $H \rightarrow ZZ \rightarrow 4$ leptons and $H \rightarrow W+W- \rightarrow 2$ leptons 2 neutrinos channels offer potential Higgs discovery at the 5 σ level with 10^5 pb^{-1} of data (initial 3 year operation at $L_{LHC} \approx 10^{33}$ $cm^{-2}s^{-1}$ will give ~$10^4 pb^{-1}$/year). As Figure 1.8 indicates, the $H \rightarrow ZZ \rightarrow 4$ lepton and $H \rightarrow W+W- \rightarrow 2$ lepton 2 neutrino channels offer discovery potential across the full range of possible Higgs masses consistent with all available experimental data (see Figure 1.1).

Of the potential discovery channels, only the decays $H \rightarrow ZZ \rightarrow 4$ leptons and $H \rightarrow \gamma\gamma$ are likely to be determined by direct mass reconstruction. The $H \rightarrow W+W- \rightarrow 2$ lepton 2 neutrino channel must rely on the determination of missing E_t in the calorimeter rather than direct reconstruction of masses.

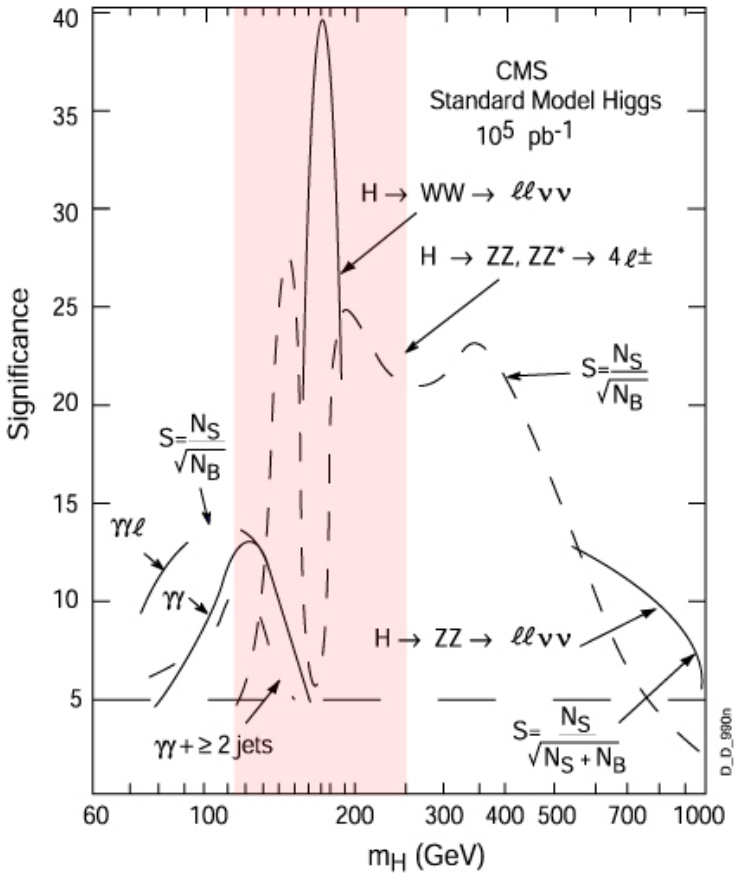

Figure 1.8: Estimated discovery potential for SM Higgs particle as a function of possible Higgs masses (m_H) with $5pb^{-1}$. The red band indicates the most likely mass region for m_H based on the experimental evidence from LEP2000 and Figure 1 (114.1 - 250 GeV/c2) data [1.7, adapted]. S > 5 indicates sufficient statistical certainty to claim discovery. The plots use the CTEQ2 and the EHLQ structure functions and were done in PYTHIA v5.7.

1.2.4.1 H → b bbar (Z, W± → b bbar)

The H → b bbar decay can in principle be determined by direct mass reconstruction; however very large background and the difficulty of reconstructing jet 4-vectors at the LHC has thus far precluded any Higgs discovery signatures in simulated analyses of this channel [1.12]. The same is true for the decay of any particle into q qbar immediately after the initial pp collision and is expected to preclude the study of other channels utilizing Z → b bbar and W± → b bbar decays. This effectively limits the study of H →

W+W- and H $\rightarrow$ ZZ to the H $\rightarrow$ W+W- $\rightarrow$ 2 lepton 2 neutrino and H $\rightarrow$ ZZ $\rightarrow$ 4 lepton channels as Z and W decays generally go to hadrons (branching ratio of ~70%).

1.2.4.2 H $\rightarrow \gamma\gamma$

The H $\rightarrow \gamma\gamma$ decay channel was once thought to provide the best chance for Higgs discovery in CMS. Despite the difficulties of discriminating potential signals in this channel in a pp collider (hadronization, large π^o production, etc.), a substantial financial and technical effort was made on the part of the CMS collaboration to optimize the performance of the Electromagnetic Calorimeter (ECAL) for H $\rightarrow \gamma\gamma$ decays across a Higgs mass range of 90 GeV to 150 GeV [1.7].

Prior to the measurement of the top quark mass in mid-1994, many physicists expected a 'light' top quark of < 160 GeV [1.13] (compared to the Particle Data Group Dec. 2001 accepted value of 174.3 ± 5.1 GeV). Consequently, many theoretical predictions of the SM Higgs upper mass bound during the initial ECAL design stage (~1992-1994) tended to be quite low – with claims of stringent mass limits of $m_H < 100$ GeV to less stringent predictions of < 200 GeV [1.14]. LEP searches had by this time set the lower Higgs mass bound at only > 63.5 GeV (at 95% CL).

Theoretical arguments providing an upper bounds on the Higgs mass typically characterize the Higgs model as an effective field theory which only remains valid up to some energy Λ (where $\Lambda > m_H$). In general, larger values of Λ imply smaller values of m_H; a $\Lambda \sim 10^{18}$ GeV (the Planck scale, at which new physics must enter) imply a value of $m_H < 200$ GeV [1.15].

Arguments placing further restrictions on this boundary, as well as arguments favoring a light Higgs (< 140 GeV), often cite the desire for a Higgs field vacuum expectation value that is fixed by the known strength of weak interactions, but a Λ value that is set well below the Planck scale. For example, with a m_H~115 GeV (the LEP limit), a value

of $\Lambda \sim 100$ TeV is implied [1.16]. This argument is made since the vacuum expectation value of the Higgs field depends upon Λ and hinges upon the demand that the stability of the vacuum may only be maintained if the coupling of the quartic self coupling term (the λ^2 term in the potential) does not become negative while running from the weak scale up to the scale Λ. If an additional condition is on the Higgs particle is made, that the self coupling term is small, the theory can be shown to restrict $m_H < 140$ GeV – precisely the range for which the CMS ECAL is optimized. The restriction is 'justified' by the desire to find a Higgs particle compatible with the previous two restrictions (low Λ, vacuum stability) and consistent within the framework of perturbation theory [1.17]. However, this last restriction also requires some fine tuning of parameters within the Standard Model that critics (and there are many [1.18][1.19][1.20][1.21]) point out is unnatural and has no analog elsewhere in the Standard Model theory. Moreover, several recent articles have also suggested that these restrictions do not necessarily confine m_H to < 130 GeV [1.22][1.23] and that a large value of Λ (~ Planck Scale) accommodates values of m_H which can only be found within a narrow range of 130 and 200 GeV [1.23].

Regardless of the theoretical arguments favoring the light Higgs for which the CMS ECAL is optimized, it is expected that the FNAL Tevatron will push the lower mass boundary of m_H to ~125 GeV [1.24] by 2006, the year operation of the LHC is anticipated to commence. As Figure 1.8 indicates, $S(H \rightarrow \gamma\gamma) \approx S(H \rightarrow ZZ \rightarrow 4 \text{ lepton})$ for a 125 GeV Higgs mass. This suggests that if the SM Higgs particle exists and has a mass > 125 GeV, discovery is much more likely to occur outside the $H \rightarrow \gamma\gamma$ channel.

1.2.4.3 $H \rightarrow W^+W^- \rightarrow$ 2 lepton 2 neutrino Events in CMS

A Standard Model Higgs particle with a mass > 125 GeV has a branching ratio favoring W+W- (Figure 1.7). The large WW branching ratio will make the monitoring of W± decays crucial to Higgs discovery. As Figure 1.8 indicates, the $H \rightarrow W^+W^-$ channel in which both W bosons decay into a lepton and neutrino offers the greatest discovery

potential for a Higgs mass of 155-180 GeV. Studies of channels utilizing decays of either W into a non lepton-neutrino pair are restricted by large backgrounds.

1.2.4.4 $H \rightarrow ZZ \rightarrow$ 4 lepton Events in CMS

The $H \rightarrow ZZ$ channel in which both Z bosons decay into four leptons covers the largest Higgs mass range for the most promising CMS discovery channels. $ZZ \rightarrow$ 4 lepton decay would also provide the cleanest and most unambiguous signal for Higgs discovery.

Studies of $H \rightarrow ZZ$ channels utilizing non-leptonic decays of either Z are restricted by large backgrounds (See Section 1.2.4.1).

1.3 Endcap Muon Position Monitoring System (EMPMS)

The manner in which the mounting of the CSC chambers on the YE Iron discs will be preformed should ensure local location accuracy for every chamber of at least 2mm using dowel pin holes machined into the discs. The dowel pin holes have been measured by photogrammetry during a trial assembly of each disc and determined to an accuracy of approximately 200-1000μm depending on the location of the hole. Although the chamber locations can be defined in this manner in the field free case and prior to installation, the location of the chambers will certainly change as the individual discs are installed into the final detector assembly and, more significantly, under the extremely high magnetic forces (> 10000 tones) generated by the solenoid.

The estimated positioning accuracy with which the individual YE Iron disc assemblies can be placed into the closed detector is estimated to be ±3mm prior to the activation of the solenoid. The deformation of the RF iron by magnetic forces once the solenoid is activated is expected to induce variations in the position and orientation of the CSCs by ≥ 5mm. Due to the non symmetric distribution of the iron support structures which hold the discs in place, these distortions will almost certainly be non-uniform.

CSC chambers in the Endcap are located on three or four point kinematics mounts that will move with local YE iron distortions and end up in different positions and/or orientations. The determination of CSC positions across the CMS RΦ coordinate is the most critical parameter to establish and track, as they will directly impact the determination of muon p_t.

The shifting of CSC chamber locations after installation and activation of the magnetic field is not unique to the Endcap Muon System. The Barrel Muon System will also require a mechanical alignment system. Additionally, both the Barrel and Endcap Alignment Systems must be referenced to the Central Tracker and Global CMS Coordinate System by a third mechanical alignment scheme, the Link Alignment System. The Link alignment system establishes a set of twelve laser lines that are accessible to both the Tracker and Muon alignment systems. These laser lines ("Primary Link lines") follow the phi segmentation of the Muon system and define twelve half planes in the CMS phi coordinate (six in each endcap, every 60 degrees). Two primary points on each MAB are used to reference a corresponding phi half plane. Due to the separation of the ME ±1/2 and ME±1/3 CSC rings along the CMS Z coordinate, the ME±1/2 CSC chambers will require an additional Link laser line (a "Secondary Link line", running parallel to the Primary line) provided by the addition of a small rhomboid prism in the Primary Link laser line.

1.3.1 The Need for an Endcap Muon Position Monitoring System

Since the final installation of the discs will place the CSC chambers on the interior of the detector, it will be impossible to make any accurate photogrametric survey of the chamber locations after final installation. However, the initial operation of the CMS detector will still require high definition of CSC chamber positions relative to the Central Tracker enable trigger on and define the tracks of incident particles. For this reason, it will be necessary to redefine and track the location and orientation of the CSCs with a

mechanical position monitoring ("alignment") system that is able to determine the location of CSCs with the solenoid magnetic field at its maximum.

1.3.1.1 Level 1 Trigger Requirements in the CMS Endcap

The number of muons from $H \rightarrow ZZ \rightarrow 4$ lepton events which can be expected to fall within the Muon Endcap System is largely dependent upon the mass of the Higgs particle. In general, higher pt muons can be expected to enter the Barrel region over the Endcap region. Thus it can be expected that muons from $H \rightarrow ZZ \rightarrow 4$ lepton events which arise from a high mass Higgs particle are likely to go toward the Endcap. A topology of $H \rightarrow ZZ \rightarrow 4$ muons events are shown in Figure 1.9. The histograms indicate that the number of muons from these events that can potentially be measured by CMS gradually increases as the Higgs mass approaches 500 GeV. This is do in part to the fact that the additional p_t imparted to the final state muons by virtue of arising (ultimately) from heavier Higgs particle pushes the particles toward lower regions in $|\eta|$. The net effect is to make the number of muons found in the Endcap System approximately equal to the number of muons found in the Barrel System.

The histograms in Figure 1.9 where generated with CMSIM 120 (PYTHIA v6.157b) Monte Carlo simulation of $H \rightarrow ZZ \rightarrow 4\ \mu$ by gluon-gluon fusion and WW (ZZ) Production at $\sqrt{s} = 14$TeV across all possible phi and eta ranges with initial and final state radiation included. Muons with p_t falling below the minimal CMS L1 Trigger Levels were rejected (20 GeV for single muons, 4 GeV for two muons). The binning of events was determined by the muon(s) $|\eta|$ location as it encounter the first layer of muon chambers (see Figure 1.3 for η division of the detector).

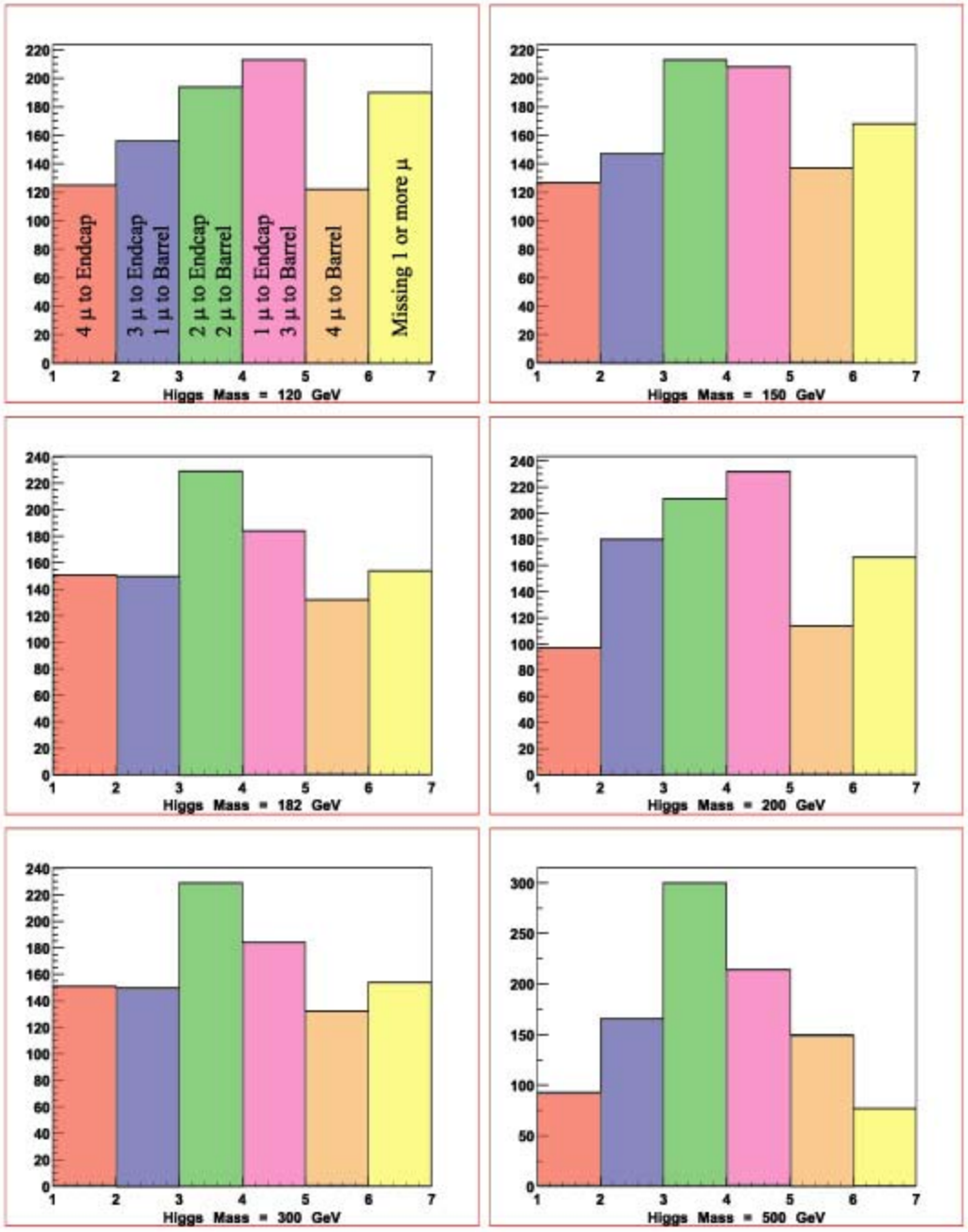

Figure 1.9: Distribution of muons in the CMS Barrel and Endcap Muon Systems from H $\rightarrow$ ZZ $\rightarrow$ 4μ events. Each histogram contains 1000 events generated with a Monte Carlo simulation and denote the location in the CMS Muon System where each muon is likely to be found: the Barrel Region, Endcap Region, or outside the active area of the detector.

In addition to H → ZZ → 4 lepton events in CMS, Z and W physics events will also of interest. Muon decays of these bosons (Z0 → 2μ, W± → μ + ν_μ) will require Level 1 triggering. For Z0 decays, only 1 muon is needed to trigger on the decay. A topology of Z0 and W± decay events likely to be found in the CMS detector generated via Monte Carlo simulation is shown below in Figure 1.10.

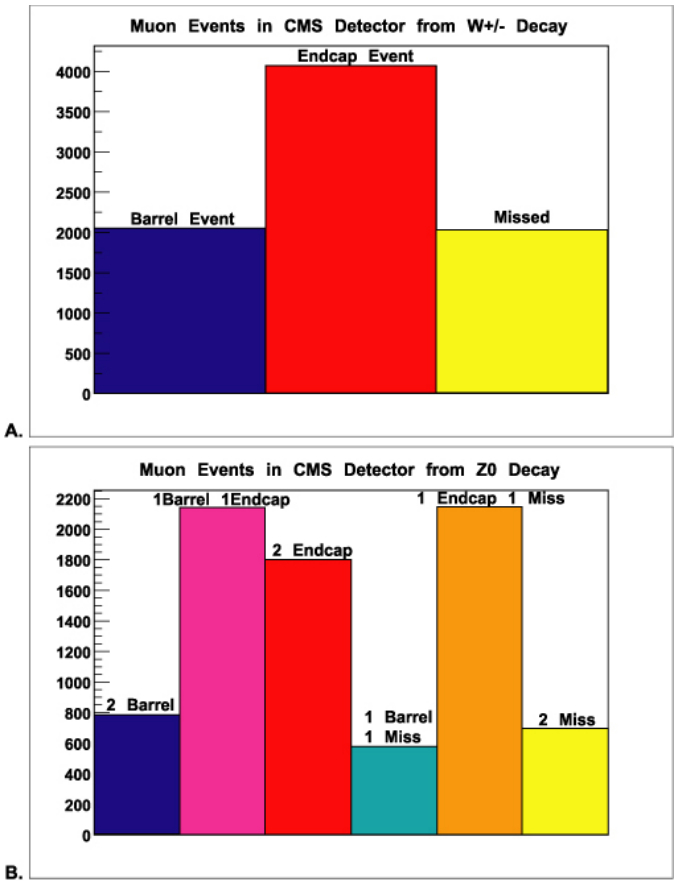

Figure 1.10: Distribution of muons in the CMS Barrel and Endcap Muon Systems for (A) W± → μ + ν_μ and (B) Z0 → 2μ. Figures (A) and (B) each contain 8200 events generated with a Monte Carlo simulation and denote the location in the CMS Muon System where each muon is likely to be found: the Barrel Region, Endcap Region, or outside the active area of the detector.

The histograms in Figure 1.10 where generated with CMSIM 120 (PYTHIA v6.157b) Monte Carlo simulation of W± → μ + ν_μ and Z0 → 2μ direct production at $\sqrt{s}$ = 14TeV across all possible phi and eta ranges with initial and final state radiation included.

Muons with p_t falling below the minimal CMS L1 Trigger Levels were rejected (20 GeV for single muons, 4 GeV for two muons). The binning of events was determined by the muon(s) eta location as it encounter the first layer of muon chambers (see Figure 1.3 for η division of detector). As the histograms indicate, far more Z0 and W± decays to muons will involve the Endcap region of the CMS detector. For the $W\pm \rightarrow \mu + \nu_\mu$ decays, it is evident that finding these events will require Level 1 triggering in the Endcap since there is only one muon to trigger on and roughly twice as many muons are likely to be found in the Endcap Muon System than in the Barrel Muon System. To trigger on Z0 decays, only one muon in the decay will be needed to initiate the trigger. The Figure 1.10B shows that the majority of $Z0 \rightarrow 2\mu$ events lay exclusively in the Endcap Muon System region and will require a Level 1 Endcap trigger to trigger on those events.

Trigger simulation studies indicate that the CMS Endcap trigger will "require phi precision ~ 1 mm (~0.1 CSC strip)" and, as typical Local Charge Track resolution (single chamber, average strip width) is 0.14*CSC strip width (≈1.3mm), the "CSC Track-Finder absolutely must include alignment corrections" [1.25]. If the positions of the CSC chambers are not defined within 1.3mm in Phi, a significant bias in the trigger will occur and impede the selection of $H \rightarrow ZZ \rightarrow 4$ lepton, $Z^0 \rightarrow 2\mu$, and $W\pm \rightarrow \mu + \nu_\mu$ events.

1.3.1.2 Endcap Track Reconstruction Requirements

The standalone resolution of the CSC chambers is ~150 μm [1.26], whereas multiple scattering effects for a 100 GeV muon (for which the muon system is optimized) are on the order of 200μm. Since multiple scattering precludes the definitive positioning of the particle immediately prior to its measurement, the relative positioning between any two chambers does not need to exceed 283μm (=√2 * 200μm). However, the determination of particle trajectories and momenta can be further constrained by attempting to match track segments in the CSC chambers to the CMS Tracking system. For optimal performance when matching muon tracks between the muon system and the rest of the CMS detector, the position of all CSC chambers should be (individually) determined

relative to the Tracker coordinate system. In this case, multiple scattering restricts the necessary positioning knowledge of CSC chambers approximately 200μm (a detailed estimate is made in Chapter 4). However, the resolution of the Inner Tracking System for the final determination of muon p_t is expected to dominate that of the Muon System, potentially minimizing the impact of CSC chamber misalignment for all but the highest p_t muons. These effects are addressed in detail in Chapter 5.

1.3.1.3 Design Requirements for the Endcap Alignment System

The design requirements of the Endcap Muon System indicate that the Endcap Alignment System must:

I. Establish the Initial Positions and Orientations of all Chambers and System Components
II. Track Chamber Positions (R,Φ, and Z)
III. Provide Phi Reference Planes in each Endcap Disc
IV. Transfer Tracker System Coordinate Information from Barrel Muon and LINK Alignment Systems

The accuracy with which chamber locations must be established and tracked is driven by the physics goals of the CMS experiment and operational requirements of the CMS trigger. The knowledge of chamber locations required for successful trigger operation is ~1-2mm relative to the tracker, however the accuracy required to make the requisite momentum measurements on 100 GeV muons (for which the Muon System is optimized) imposes much more stringent requirements in the CMS RΦ plane. As discussed previously (Section IIA), the multiple scattering of muons through the large amount of tracker material and iron present in the CMS detector imposes a limit of approximately 200 μm on the determination of any given muon track with the Standalone Muon System. Since the projected accuracy of the CSC chambers in all layers except ME ±1/1 is 150-200 μm, the most stringent requirement which might be imposed on the determination of

chamber locations of CSCs in CMS RΦ is approximately 200 μm. These requirements are examined in detail in Chapter 5.

1.3.2 Design of the Endcap Alignment System

What follows is a semi-technical description of the EMU Alignment Scheme. A more detailed discussion of system components and tolerances can be found in Appendix A and Chapter 3.

The approach taken to meet the design criteria has been to develop two dimensional transparent sensors for monitoring chambers along a laser line and to employ simple proximity sensors and calibrated rods for monitoring the spacing between discs and chambers.

The Digital CCD Optical Position Sensor (DCOPS) is composed of 4 single array CCDs arranged in a window frame and a control circuit fitted with an on board ADC and DSP chip. When the beam of a cross hair laser falls incident on the DCOPS, each CCD is then used to reconstruct the distribution of charge on its pixel array which corresponds to the distribution of photons in the corresponding leg of the laser. In this manner, the centroid of each leg of the crosshair laser can be determined relative to some point on the CCD window frame. If a crosshair laser falls incident on a string of DCOPS sensors, knowing the absolute spatial location of any two sensors (called reference sensors) in the line will allow for the determination of the incident laser line. Once the laser has been defined, the transverse locations of any remaining sensors placed in the laser line can be determined. Figure 1.11 shows how two known sensors can be used to determine the location of an unknown third. Since each DCOPS sensor utilizes four CCDs in a single measurement, there is a built in degree of redundancy as well as an intrinsic ability to resolve the angular orientations of unknown sensors.

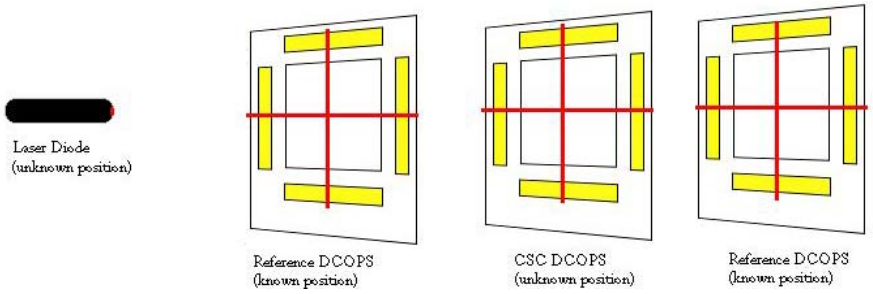

Figure 1.11: The Digital CCD Optical Position Sensor (DCOPS) concept. The position and orientation of the two Reference DCOPS are known and allow for the definition of the unknown laser line. Once the direction and orientation of the laser line is known, the position and orientation of the unknown DCOPS on the CSC can be determined in the directions perpendicular to the laser line.

A significant improvement to the DCOPS design was accomplished by attaching prisms to the face of the CCDs and then tilting the CCDs toward the center of the window. With this design, an additional degree of redundancy is incorporated into the system since the DCOPS sensors will now accommodate two independent measurements made from opposing crosshair lasers. A production model of this 'bi-directional' DCOPS sensor is shown in Figure 1.12.

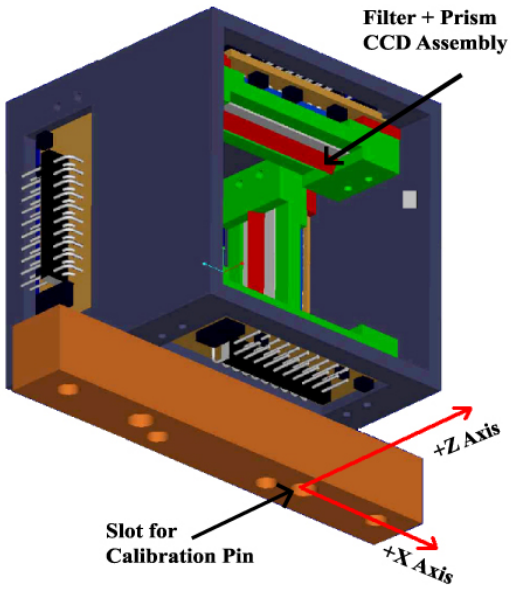

Figure 1.12: The Bi-Directional DCOPS Sensor. The face of the CCDs point toward the inside of the box and have red prisms attached. The crosshair laser line enters the box from the ±Z axis.

1.3.2.1 Straight Line Monitoring and CSC Tracking in ME ±234

To track the location and orientation of CSC chambers in a given layer, DCOPS sensors will be attached to each end of the CSC chambers to form Straight Line Monitoring (SLM) lines which transverse the diameter of each Endcap disc. The location of DCOPS sensors placed on the CSC chambers, and therefore the location of the CSC chambers, can be determined by knowing the exact location of two additional reference sensors, located off the CSC chambers at the endpoints of the SLM line. Figure 1.13 shows how three SLM lines will be used to define the location of CSC chambers on the ME ±2, ±3, and ±4 Endcap discs (reference sensors are not drawn in).

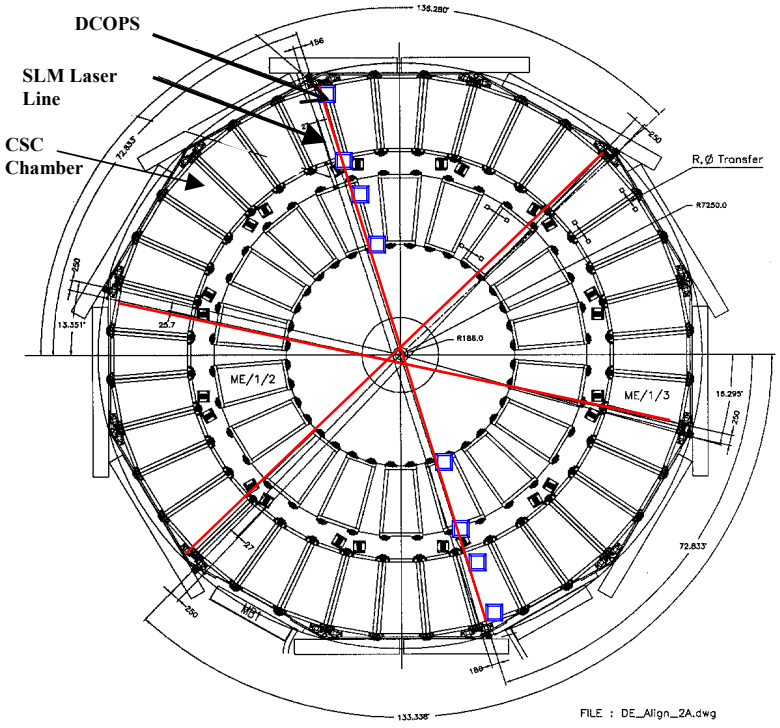

Figure 1.13: View of CSC chamber arrangement and location of Straight Line Monitor (SLM) laser lines used in tracking chamber positions. This view of the Endcap corresponds to a 'head on' view of Figure 1.14. DCOPS sensors are shown at each end of the CSC chambers (drawn on only one SLM line).

The location of the DCOPS SLM reference sensors must be inferred from a separate laser line running parallel to the beam pipe (Z-axis) of the CMS detector – the Axial Transfer Line, shown in Figure 1.14. The Transfer Laser Line is defined by two DCOPS sensors mounted on separate rigid mechanical structures called MABs (Module for the Alignment of the Barrel Muon) which are located on the outer parameter of the inner detector at the intersection of the Endcap Muon and Barrel Muon Systems.

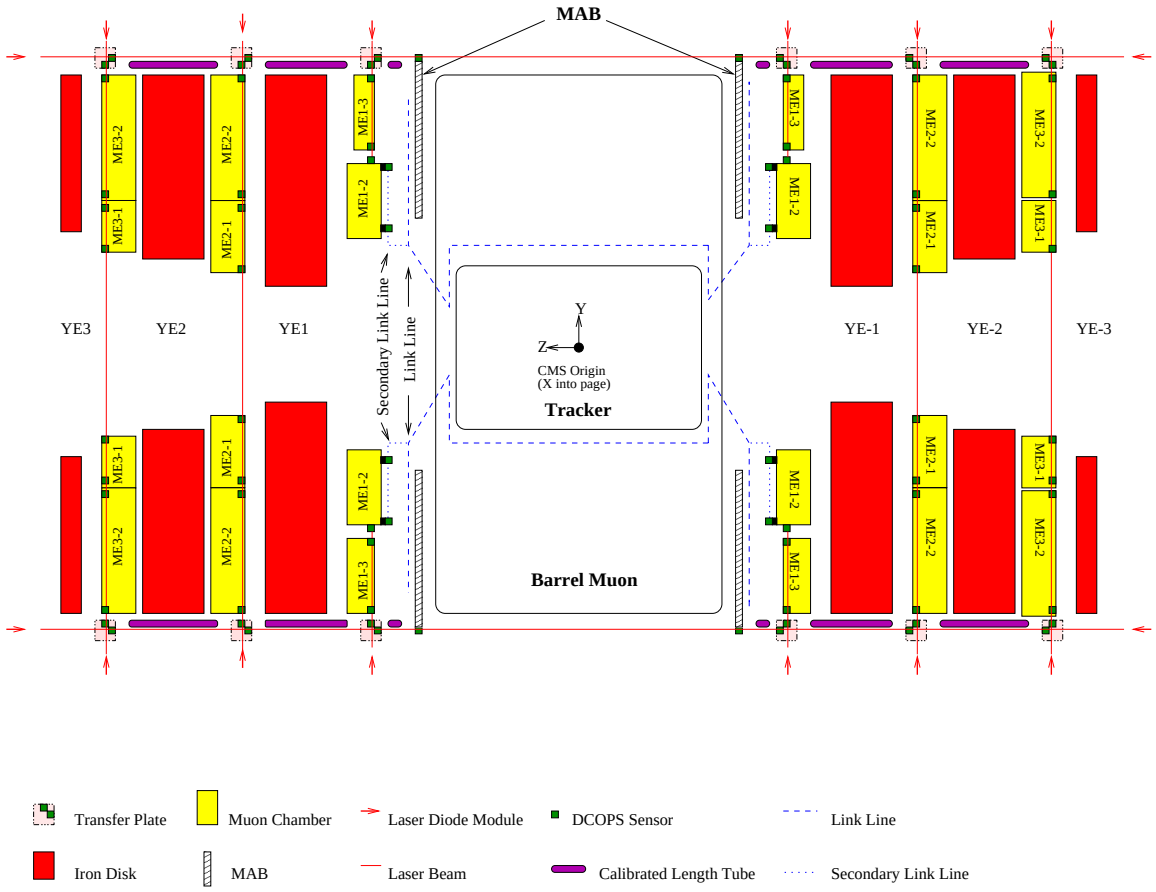

Figure 1.14: Diagram of Endcap Alignment System showing Transfer laser lines and Straight Line Monitor (SLM) laser lines used in tracking CSC positions.

Since the location of the MAB units are referenced to the Tracker coordinate system by the LINK system, the location of the DCOPS sensors mounted on the MABs are known. By using these DCOPS sensors as references on the Transfer Line, the location of other DCOPS sensors located along the Transfer laser line can be determined. The location of the reference DCOPS sensors in the SLM line are determined by a rigidly

connecting them to the DCOPS sensors located on the Transfer line with a special Transfer Plate (Figure 1.14, Figure A.8). Once the positions of the connecting Transfer line sensors are determined, the reference sensors on the SLM line become known and the remaining sensors in the SLM line can be determined. Since the DCOPS sensors only measure directions perpendicular to the laser lines, a host of proximity sensors and inclinometers are employed to determine the spacing between the DCOPS sensors and their angular orientations.

1.3.2.2 Straight Line Monitoring and CSC Tracking in ME ±1

As Figure 1.3 indicates, the additional iron on YE ±1 means that the arrangement of SLM lines used on ME ±2, ±3, and ±4 will not work in ME ±1 since there is a large separation between adjacent ME ±1 rings in Z. More importantly, the additional iron located behind the ME ±1/1 rings obstructs any line of sight measurements (as in ME ±2, ±3, and ±4) across the ME ±1 Endcap.

By using two LINK sensors and the Secondary Link Line generated by the LINK Alignment Group when evaluating the location and orientation of the MAB units, it is possible to define the location of ME 1/2 chambers (along the Secondary Link Line). An illustration of the ME±1 disc and CSC chambers is shown in Figure 1.15. Once the location of the ME ±1/2 chambers are known, the addition of a DCOPS sensor on the outer end of each ME ±1/2 chamber offers an inner reference point for a shortened crosshair SLM Line to define the location of DCOPS sensors mounted on the ME ±1/3. The outer endpoints of these shortened SLM lines are defined by the inclusion of Transfer Plates on the outer edge of the ME ±1 iron in a manner identical to the ME ±2, ±3, and ±4 SLM lines.

The displacement between the ME ±1/3 and ±1/2 chambers along the CMS Z axis is handled with an extension of the mounting bracket which secures the ME ±1/3 DCOPS sensors to the CSC chambers. Figure 1.16 illustrates the arrangement of the ME ±1/3 and

±1/2 chambers and the sensors along the SLM and Secondary Link lines. The outer reference sensor for the ME ±1/3 SLM lines are supplied with a transfer plate in exactly the same manner as in ME ±2, ±3, and ±4 SLM lines.

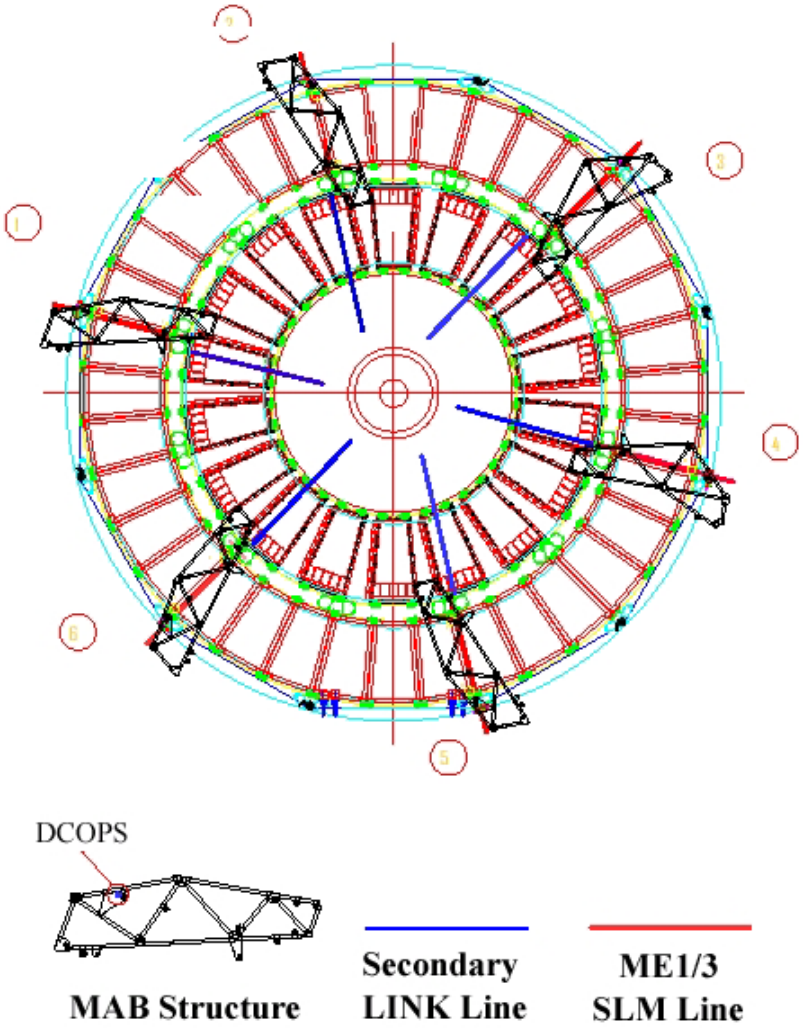

Figure 1.15: ME ±1 Chamber Arrangement and Placement of SLM and Secondary Link Laser Lines. Overlap of MAB Structures is shown, though they do not touch ME±1. ME 1/1 chambers are not shown. Note SLM lines do not cross the disc, but terminate at the edge of the ME±1/2 rings. [1.27]

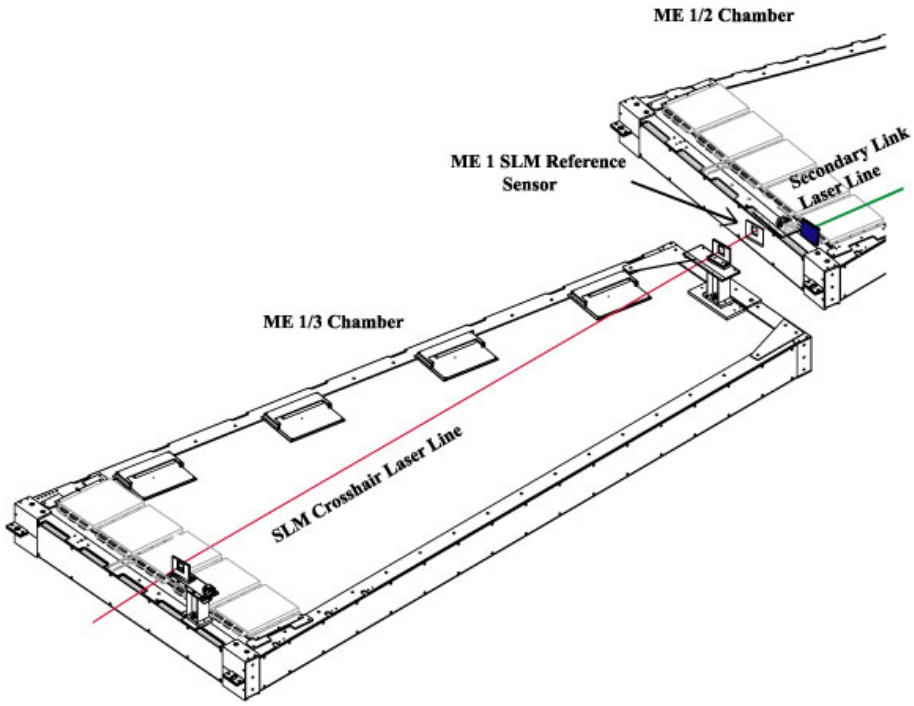

Figure 1.16: Detail of ME ±1 SLM and Secondary Link Laser Lines. The drawing shows a ME1/3 DCOPS Sensor SLM line (three sensors along the red laser line) and the ME1/2 CSCs Secondary Link Line (the green laser line intersecting a blue Link sensor). The DCOPS attached to the out edge of the ME1/2 Chamber serves as the final reference sensor in the ME 1/3 SLM line.

The scope of the EMU alignment system does not include the ME ±1/1 ring of CSC chambers (the innermost ring) and can rely on the alignment of the ME1/2 ring with the aid of a secondary laser line generated near the CMS Z axis from the LINK Alignment System. Since the Secondary Link Laser Line is cylindrical, the measurements of the ME ±1/2 chambers have a degree of freedom about the laser line which is not present in the other SLM lines. The initial design of the EMU Alignment scheme anticipated that a complementing set of measurements between the LINK sensors and the DCOPS sensor installed on the on outer the edge of these chambers would provide a sufficient constraint on rotations about the Secondary Link Line since the two laser lines are offset. It has been determined by a simulation of the system (see Chapter 3) that the inclusion of an inclinometer, similar to those on the transfer plates, will be required.

1.3.2.3 Locations of Off-SLM CSC Chambers

The EMU alignment scheme allows only for the direct determination of chambers along the SLM laser lines. CSC chambers located off of these SLM lines will have to be determined by some other means – likely by an extrapolation of the YE iron shape (as determined by the SLM lines) and a model (or measurements) of the magnetic field in the Endcap. It may also be possible to determine the location of off-SLM chambers by particle track reconstruction across the overlapping regions of chambers. In this case, chambers lying along the SLM lines (i.e. chambers with known positions and orientations) serve as reference chambers from which the location of neighboring chambers are found first. Remaining chambers could then be successively determined by using neighboring chamber locations (once found) as reference points for overlapping tracks. Neither of these methods (nor any other method) has been thoroughly investigated.

2 EMU ALIGNMENT SIMULATION AND RECONSTRUCTION

CMS Object Oriented Code for Optical Alignment (COCOA) is an Object Oriented software program designed to study optical components in the CMS Position Monitoring system by geometrical approximation. COCOA was designed by Pedro Arce for the study and use in the CMS Optical Position Monitor System, but was not created for use with the Endcap Alignment DCOPS sensors. The software was extensively adapted and debugged for use in the EMU alignment system.

2.1 COCOA Software Description and Fit Methodology

COCOA allows the user to reconstruct the position and angles of optical objects in a given system as well as propagate associated (RMS) errors. Calculations in COCOA are based on a non-linear least squares fit model and allow the user to provide estimations of errors on a model system as well as a set of actual measurements taken by the system. COCOA then reconstructs the system based on the errors provided by making variations in the positions of the modeled components corresponding to how well the errors are known. Errors can be defined as fixed, calibrated, or unknown. Components set to be fixed are not moved at all, those set to calibrated are free to be moved within the range of the error, and unknown quantities are completely free to be moved as the software sees fit. The final output of the software supplies the user with the optimal solutions for the input parameters such that the ideal measurements modeled by the program come as close as possible to the real measurements. The non-linear fitting method allows COCOA to fit a very large number of parameters in a fraction of the time required by conventional methods.

Although COCOA represents a somewhat sophisticated approach to the problem of reconstructing sensors in CMS, the challenges in the EMU alignment system which any software reconstruction package must address are significant. Although it may be relatively easy to estimate the location of individual sensor along a single laser line, the introduction of redundancy and geometrical loops makes an accurate estimation of spatial coordinates and rotations difficult. In the EMU alignment system, approximately 4000+ individual and compounded objects will be considered during a single reconstruction with the location of many of the components determined from redundant measurements. Moreover, COCOA is very flexible, offers arbitrary scalability, and the prospect of being immediately integrated with Link and Barrel Muon alignment reconstruction.

COCOA is designed to take the set of known components (ccds, lens, etc) and compose an idealized system with which it will generate a set of ideal measurements to compare against an actual set of measurements. In practice, the set of known components are said to compose a vector X while the real measurements associated with this vector constitute a set of equations $F(X)_{real}$. The errors associated with each real measurement are stored in a normalized matrix P. The difference between the ideal measurements and the real measurements are stored in a matrix D. COCOA is designed to continually update the idealized set of parameters (the matrix X) until they produce measurements which minimize the matrix D. The correction (or update) matrix dX is determined in the following manner:

$$dX = (A^t PA)^{-1}(A^t PD) \qquad \text{Equation 2.1}$$

The elements of matrix A (the design matrix) are determined from the partial derivatives of F(X) with respect to a particular component :

$$A_{ij} = \left(\frac{\partial F}{\partial X_j} \right)_i \qquad \text{Equation 2.2}$$

Once dX is determined, a new model $X_{new} = X + dX$ is created and the calculation is repeated. Successive iterations are performed until the correcting factor dX_k becomes very small. The final updated value of X contains the optimized location of the components in the ideal system and contains the 'best guess' as to where unknown components in the real system are located.

Propagation of uncertainties is handled by the determination of the variance-covariance matrix for the system based on X, F(X), and P. The variance-covariance matrix is dimensioned as (number of actual measurement values)x(number of components in the ideal model) and takes the standard form (with n as the normalization factor on P):

$$M = n^2\left(A^t P A\right)^{-1} \qquad \text{Equation 2.3}$$

The propagated errors of all components which compose the real system are given by the diagonal elements of M while the off-diagonal elements of this matrix are the correlations between the components.

The details of how COCOA optimizes the construction and manipulation of these matrices can be found in Reference [2.1].

2.2 Reconstruction of a Prototype EMU Alignment System Using COCOA

COCOA was employed to reconstruct and simulate measurements made during a June, August, and September 2000 series of tests simulating a subsection of the EMU Alignment scheme. In this section the results of these tests using a simple COCOA model with static reference sensors and fixed orientations will be discussed. The prototype alignment scheme and subsequent reconstruction of system parameters in COCOA offered the first proof of principle for the EMU Alignment System as well as provided important estimations of component performance.

2.2.1 Endcap Muon Position Monitoring System (EMPMS) Reconstruction at CERN ISR Test Hall

The primary goal of the CERN ISR tests is to reconstruct a full scale mock-up of a Cathode Strip Chamber (CSC) SLM (Straight Line Monitor) Line and connecting Transfer Line with DCOPS sensors and monitor the position of the sensor brackets to within 200μm of their expected positions.

The implementation of the EMPMS in the CMS detector will allow for the transfer of Tracker system coordinate information from the Barrel and LINK alignment system. This transfer is accomplished across the Module for the Alignment of the Barrel Muon (MAB) interface. Since the location of the MAB units are referenced to the Tracker coordinate system by the LINK system, the location of the DCOPS sensors mounted on the MABs is known. By using these DCOPS sensors as references, the location of other DCOPS sensors located along the Transfer laser line can be determined. DCOPS sensors along the SLM line must also be determined from the location of at least two known DCOPS sensors. The location of the reference DCOPS sensors in the SLM line are provided by rigidly connecting these DCOPS sensors to DCOPS sensors located in the Transfer line. Once the positions of the connecting Transfer line sensors are determined, the reference sensors on the SLM line become known and the remaining sensors in the SLM line can be determined. Of course, since the DCOPS sensors only measure directions perpendicular to the laser lines, a host of proximity sensors and inclinometers are employed to determine the spacing between the DCOPS sensors and their angular orientations.

A full scale model of this arrangement was implemented at the CERN ISR tunnel which included one Transfer line and SLM line. A sketch approximating the arrangement of the DCOPS sensors in the ISR tunnel is shown in Figure 2.1. In the figure, DCOPS et2 and et3 are located on the MABs and sensors et1 and es1 are rigidly

connected by a transfer link plate. Since only one of the MABs (et2) was constructed for the ISR tests, reference sensors et3 and es10 must be given by photogrammetry. Reference sensor et2 is specified by the location of the MAB while es1 is found by determining et1 and making a translation across the known geometry of the transfer plate. The angular orientation and spacing between the DCOPS sensors along their respective laser lines are given by photogrammetry.

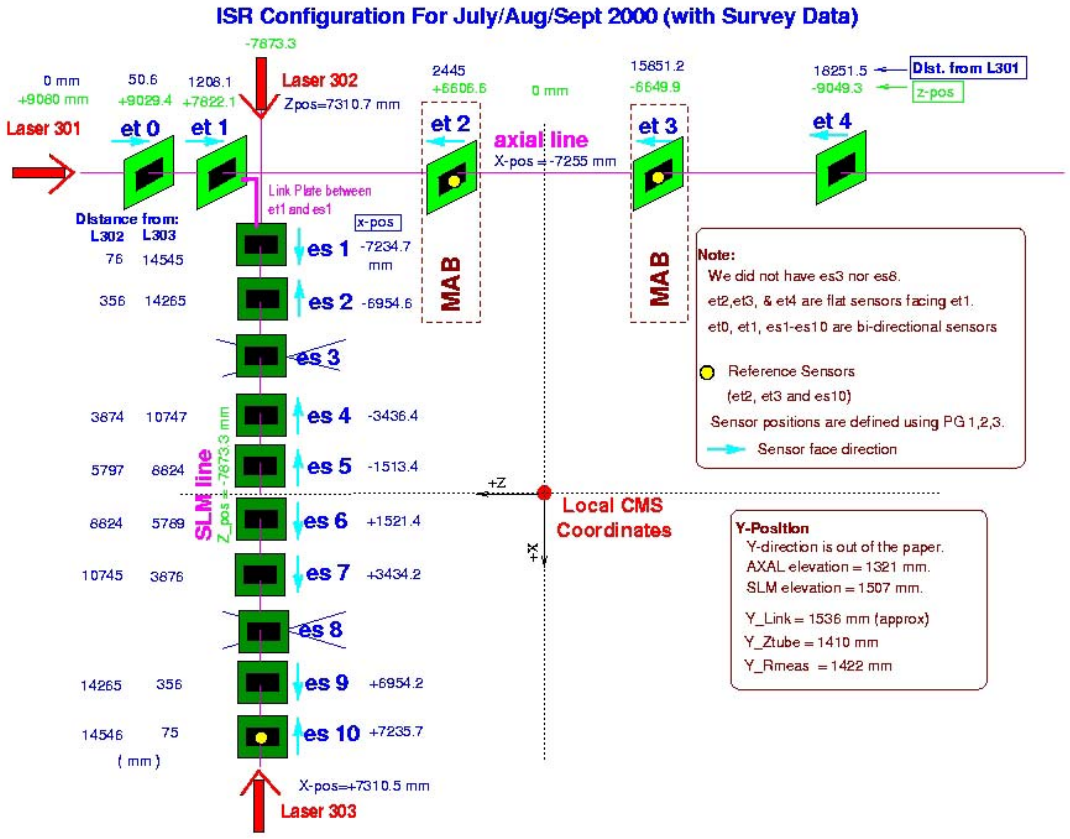

Figure 2.1: A Schematic Representation of the ISR Setup

For each of the sensors mounted in the ISR tunnel, the brackets on which the DCOPS sensors are mounted are defined by three photogrammetry targets. The photogrammetry targets have a relationship (as established by FNAL CMM measurements) to the dowel pins upon which the DCOPS sensors mount. The DCOPS sensors, in turn, have their CCD pixel arrays calibrated to the mounting points of the dowel pins (See Figure 2.2).

The calibration of the first pixel position in each sensor's CCD to the local dowel pin hole on the sensors circuit board was done by Northeastern University prior to the start of the ISR tests. The calibration was done in a manner so that only one measurement was given per CCD array in the direction of the pixel array. Transverse measurements were not considered (i.e. the offset of the pixel array from the axis of the dowel). Figure 2.2 (below) shows the parameters calibrated for a flat CCD sensor window. Calibration for bi-directional CCD windows are identical, however each bi-directional CCD also has an unmeasured component coming out of or into the page. Errors arising from the uncalibrated parameters in the dimensions perpendicular to the pixel array are thought to be negligible (esp. for bi-directional CCD offset along the beam axis).

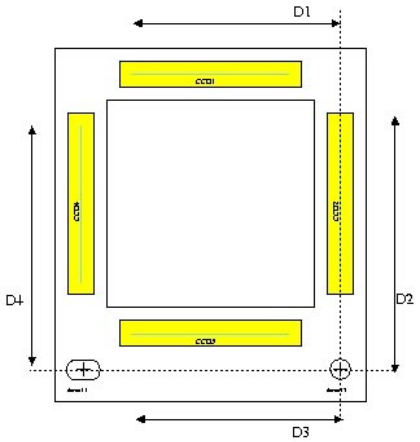

Figure 2.2: NEU DCOPS Calibration Parameters D1, D2, D3, and D4

By knowing these calibration parameters, the angular orientation of all the sensors, the distance between the sensors and the absolute position of two sensors in each line, all remaining spatial information of the sensors can be determined and monitored.

2.3 Implementation of COCOA for EMPMS ISR Testing

The DCOPS sensor configuration for EMPMS used in the ISR tests was implemented in COCOA version 1.4.0.

The software was essentially used to accomplish two tasks:

1. Determine the location of the reference dowel positions and orientations in the ISR hall for each DCOPS sensor bracket from available CERN Photogrammetry and FNAL CMM (Coordinate Measuring Machine) data.

2. Reconstruct the reference dowel positions for each of the DCOPS brackets in the laser line based on actual measurements taken by the sensors during the ISR test.

The EMPMS employed in the CMS Muon Endcap will not be able to rely on a photogrammetric survey of components in the system. Although the initial positions and orientations of the DCOPS sensors will be determined by photogrametery prior to installation of the Endcap into the Barrel, it is expected that the CSC chamber orientations (and hence the orientation of the DCOPS) will change significantly in the high magnetic fields generated by the solenoid. These shifts in sensor orientations will have to be determined by the EMPMS system. The present COCOA reconstruction model (Task #2) detailed in this note does not attempt to reconstruct potential shifts in the orientation of the DCOPS sensors. Rather these orientations are determined directly from the survey data (Task #1).

2.4 Determination of ISR Dowel Positions from Survey Information

To do a complete reconstruction of the optical sensors, the positions and orientations of at least two reference sensors in each laser line have to be known completely as well as the spacing of all the remaining sensors to be reconstructed. COCOA was used to determine the location and orientation of every sensor in the ISR test system (Task #1) from survey data. Deriving the location and orientation of all the dowel pins allows us to establish our two reference sensors for each line as well as to establish the separation and angular orientation of the remainder of the sensors. In addition, by specifying all dowel locations and orientations, we have created a set of reference dowel locations with which we can compare all future reconstructed measurements.

COCOA was employed to determine the location and orientation of the sensors by mapping the location of the three Photogrammetry targets on the bracket as seen by the CERN Survey Group in the ISR hall to the corresponding CMM measurements measuring the distance between those targets and the dowel pins. CERN Photogrammetry was done by determining the relative coordinates the specified targets within a local assembly area and then patching the assembly coordinates into the global ISR coordinates using reference socket targets. Initial uncertainties in CERN Photogrammetry (June 2000) in the ISR hall were quoted as < 90 μm within the global ISR coordinate system and < 30 μm for local assembly measurements. CMM Measurement uncertainties were quoted as < 12.7 μm. The analysis of the distances between individual photogrammetry targets in August 2000 indicated that the distances were preserved between CMM and CERN Photogrammetry measurements within understood errors. The estimates of uncertainties provided by the CERN Photogrammetry Group for the placement of the assemblies in the global ISR coordinate systems were later revised in December 2000 to incorporate the relative uncertainty and correlation of uncertainties within the survey grid. Final estimations of the uncertainty in SLM sensor placement within the global ISR grid were generally estimated as < 180 μm in Y and < 160 μm in Z.

The results from COCOA were checked independently on one sensor by the CERN survey group using an unknown commercial software package and to first order on all sensors by hand calculation. COCOA matched the CERN survey group measurements exactly and matched two independent hand calculations done by NEU and FNAL within 50 μm. Table 2.2 shows a comparison of each method for the determination of the dowel pin on sensor et3. The results from dowel et3 were typical of the other sensors, except for those assemblies around the transfer plate where CERN photogrammetry resolution was degraded to < 90 μm (local). The total (global) error in the dowel locations for sensors in this area is typically < 168 μm.

Table 2.1: Dowel Locations of DCOPS Sensor Brackets (CMS Coordinates) in ISR Hall.

Sensor	X CMS (mm)	Y CMS (mm)	Z CMS (mm)
et0	-7334.75	1370.08	9028.48
et1	-7256.93	1300.19[1]	7822.29
et2	-7327.37	1360.43	6606.56
et3	-7268.81	1288.83	-6649.45
et4	-7262.87	1291.97	-9049.56
es1	-7235.11	1485.99	7914.87
es2	-6954.62	1474.07	7903.23
es4	-3436.21	1475.80	7905.06
es5	-1512.8963	1476.70	7908.22
es6	1521.42	1478.33	7842.00
es7	3434.77	1477.26	7840.27
es9	6953.99	1476.56	7839.43
es10	7234.93	1545.31	7909.75

Table 2.2: Comparison of Dowel Locations in ISR Hall for Sensor et3

	X ISR (mm)	Y ISR (mm)	Z ISR (mm)	X, Y Error $(mm)^2$	Z Error $(mm)^2$
COCOA	-7268.81	1288.83	-6649.45	< 152	< 158
CERN Survey Group	-7268.81	1288.83	-6649.45	unk	unk
FNAL Hand Calc.	-7268.81	-1288.83	-6649.50	< 155	< 164
NEU Hand Calc.	-7268.81	-1288.83	-6649.50	unk	unk

One of the key advantages of using COCOA to derive the location of dowel pins in the ISR hall is the accurate determination of the angular orientation of the sensor. For example, in the Transfer Line all sensors are placed by COCOA in the ISR hall with their planar normals pointing along the ISR Z-axis and rotations always performed (in this order) about the X, Y, and Z ISR axes. Since the sensors are mounted on the dowels in a manner which matches the sensor face with that of the bracket and puts the normal of the sensor in line with the dowel pin, the orientation of the dowel pin is identical with that of

[1] Location of et1Y was broken by unrecorded adjustment on transfer plate. See Section 2.6.1 for a discussion of the et1 Y CMS location

the sensor. Table 2 shows the angular orientation for sensor et3 as determined by COCOA. Errors in a sensor's angular orientation are determined by the quadrature of local photogrammetry errors and global rotation of the photogrametry targets.

Table 2.3: Dowel Orientations for Sensor et3 as derived by COCOA

	X Angle (mrad)	Y Angle (mrad)	Z Angle (mrad)	Error X,Z (mrad)	Error Y (mrad)[3]
Sensor et3	-3.93	-6.51	.691	< 1.77	< 4.84

2.5 COCOA Reconstruction of ISR Test Setup

To reconstruct the Transfer and SLM lines within the framework of COCOA, the location of reference sensors et2, et3, and es10 were completely specified by the previously determined survey data. The remaining sensors had only their angular orientations and positions along the laser line specified. Variations of sensors et1 and es1 were bound together by a simulated transfer plate allowing es1 to become a reference sensor in the SLM line once the position of sensor et1 has been established by a complete reconstruction of the Transfer line. Laser sources were only specified by a single coordinate corresponding to the beginning of the laser line. No objects placed in the simulation were specified as 'fixed', but rather their positions and orientations were set within calibration limits or specified as unknown. COCOA was then set to recalculated and/or determine the location and orientations of all components based on a supplied set of measurements taken by the sensors. Our primary interest in the reconstruction was the determination of the unknown coordinates marking the sensor positions – those parallel to the X and Y ISR axes for sensors in the Transfer line and parallel to the Y and Z axes for sensors in the SLM line.

Several of the CCDs on the DCOPS sensors were not illuminated by the crosshair laser or suffered from poor fits due to highly unsymmetrical charge distributions and

[2] Errors about Y are slightly higher for reasons similar to those found in the position along Z in Table 2.1
[3] Errors about Y are slightly higher for reasons similar to those found in the position along Z in Table 2.1

poorly defined signals across the CCD pixel arrays. These CCDs were not included in the fitting algorithms employed by COCOA. Often, conditions in our system would change in a manner which allowed some CCDs to be included in our reconstruction while excluding others. A First Level Analysis Program was written to determine the centroid of the charge distribution in all the CCDs. The determination as to whether a CCD measurement was usable within the reconstruction was done through a careful examination of the FLAP data and study of FLAP fit sigma, how closely the FLAP fit matched the raw CCD distribution, and the actual value of the FLAP fitted mean. A more detailed discussion of the FLAP program and study of the raw CCD data can be found in a separate note.

Approximately 2100 measurement events (Transfer + SLM Line measurements) were processed utilizing this reconstruction method with 750 events being taken from a July/August run and 1350 events taken from a September run. In each test period, the number of events using Laser 302 was roughly equal to the number of events utilizing Laser 303. During the initial examination of the data, some anomalous events were removed from the dataset. These single events were typically separated by several hundred microns to more than a millimeter from the main body of data points. For the following analysis, approximately 10-30 events total were cut from both the original July and September data sets.

2.5.1 COCOA Reconstruction with References et2, et3, and es10

The results presented here summarize the reconstruction of Transfer and SLM Line sensors in the manner described previously. Sensors in both the Transfer and SLM laser lines were reconstructed and plotted as the deviation between their COCOA reconstructed location and surveyed location as a function of real UNIX time. These distributions were then projected into histograms and fit with an appropriate function to obtain a mean location for each test period.

2.5.1.1 July/August Results

A sample dataset of the COCOA reconstructed location of sensors with et2, et3, and es10 references in the July/August test period are shown in Figure 2.3 and Figure 2.4. The figures show a distribution of reconstructed sensor locations which is typical of this test period. [Note: The binning in these figures is much finer than the actual resolution of the distribution. This causes the nonphysical banding of data in the Figures.]

The distribution of sensor locations along the SLM line reconstructed from Laser 302 typically fell inside of a 150-180 μm range in Y and a 50-80 μm range in Z. The Laser 302 Y and Z distributions fell within the systematic errors of the reconstruction. Although the distribution of reconstructed values of the sensors' Y coordinates seems to indicate a slight upward drift in several sensors, scaling downward from approximately 100μm in es2-es5 to 50μm in es6 and es7, the systematic error associated with each event precludes any definitive correlations.

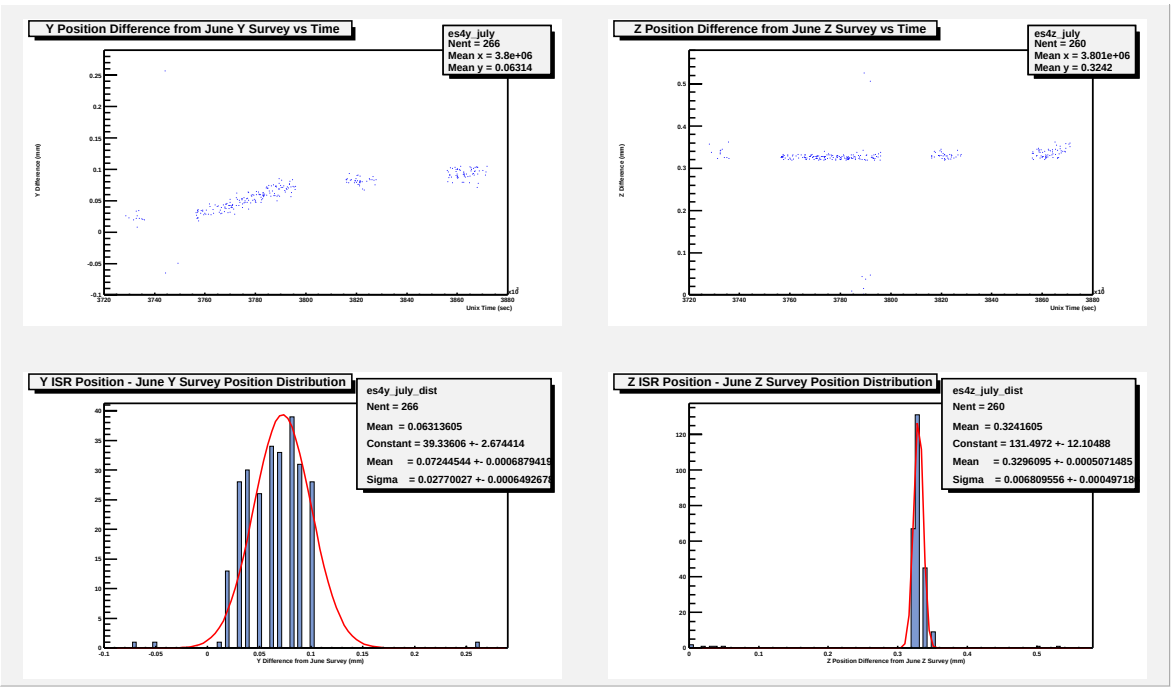

Figure 2.3: Typical Distribution of Reconstructed Positions for an SLM sensor in July/August for Laser 302 Using es10 as the Final Reference Sensor. (Bands are non-physical)

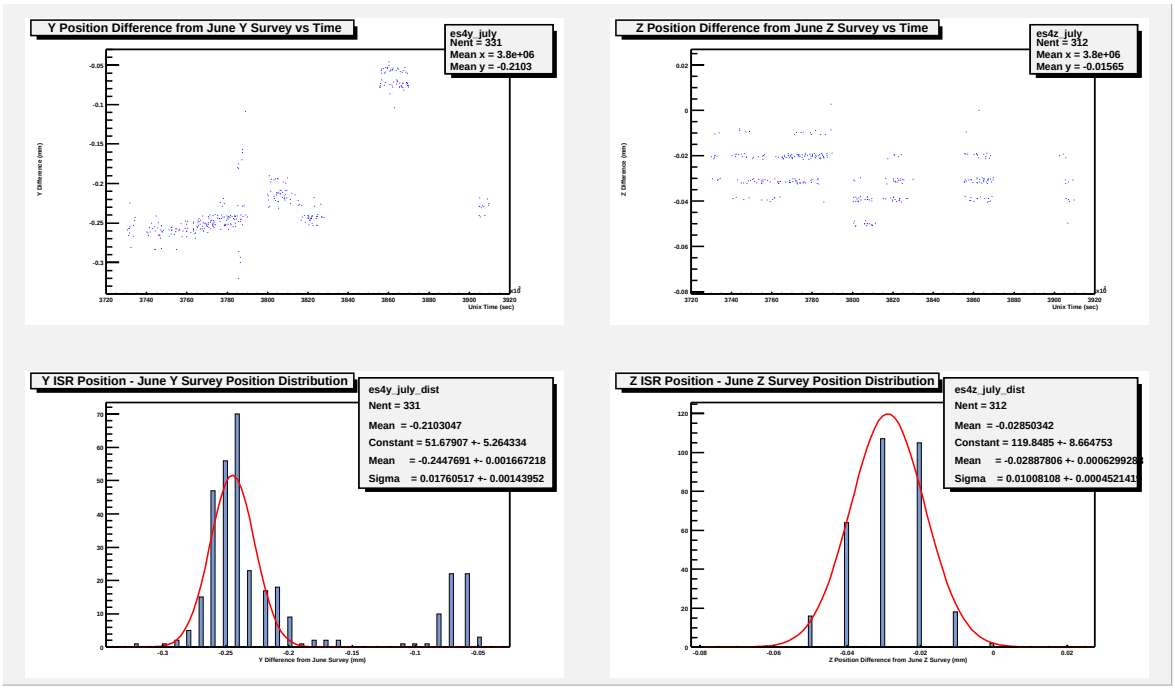

Figure 2.4: Typical Distribution of Reconstructed Positions for an SLM sensor in July/August for Laser 303 Using es10 as the Final Reference Sensor. (Bands are non-physical).

The characterization of the Laser 303 SLM data in this period is very similar to that of the Laser 302 data. All events contained in the distribution of reconstructed values with Laser 303 typically fall within the systematic errors associated with the reconstruction. The only exception occurs in a single cluster of events in the Y distributions near the end of the test period. This apparent 'jump' in the sensor Y-coordinate locations increases in magnitude with the distance of the sensor from the transfer plate. The Y coordinates of et1 or the transfer plate (es1) does not show any apparent shift in position which corresponds to the 'apparent' jump in these sensor positions. Aside from this extraneous cluster of events, reconstructed sensor locations typically well inside a 100μm range in Y and 20-40μm range in Z.

Transfer Line distributions typically fell inside a 60μm range for both the X and Y coordinate reconstructions with the exception of et4X, which has a range of 150 μm. The systematic errors exceeded the range of these distributions in all cases.

2.5.1.2 September Results

Figure 2.5 and Figure 2.6 show a distribution of reconstructed sensor locations which was typical of the September test period. The reconstruction of sensors in the SLM line using Laser 302 appears to be unstable for all the events in both Y and Z coordinates for the beginning of the test period. Rather than a tight distribution of points contained within the systematic error of the reconstruction, these initial events are not clustered about any particular value and scatter randomly across several hundred microns (>600 μm). This behavior terminates for all the sensors further into the test period with the values of the Y reconstruction falling into a 100μm range and Z reconstruction values into a 100-150μm range for sensors es2-6 and 150-200μm range for sensors es7 and es9. The end of the erratic behavior in these distributions coincides with the introduction of a new Laser 302 module. With the exception of the Z distributions of sensors es7 and es9, these distributions fall roughly within the range of values encompassed by the systematic error.

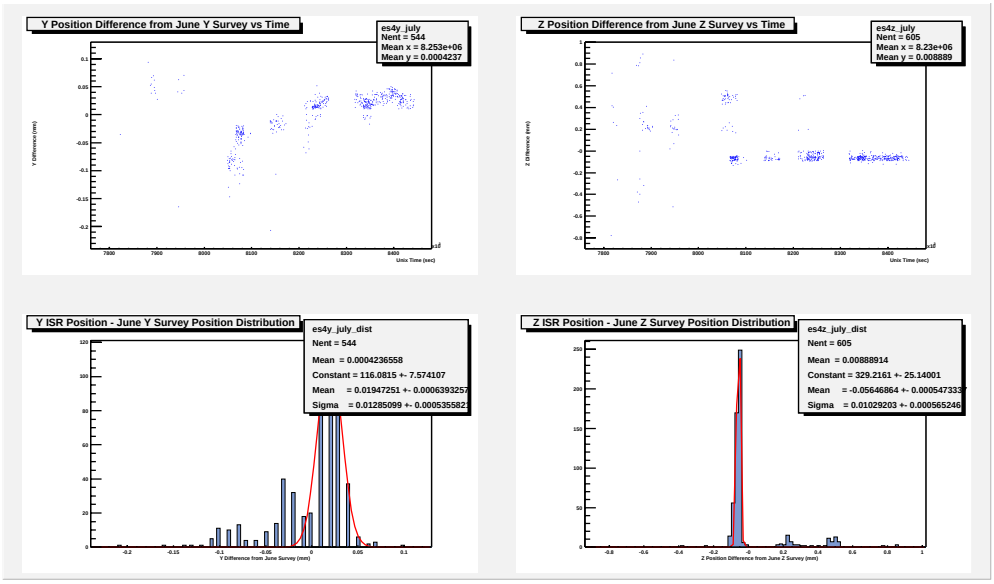

Figure 2.5: Typical Distribution of Reconstructed Positions for an SLM sensor in September for Laser 302 Using es10 as the Final Reference Sensor. (Bands are non-physical)

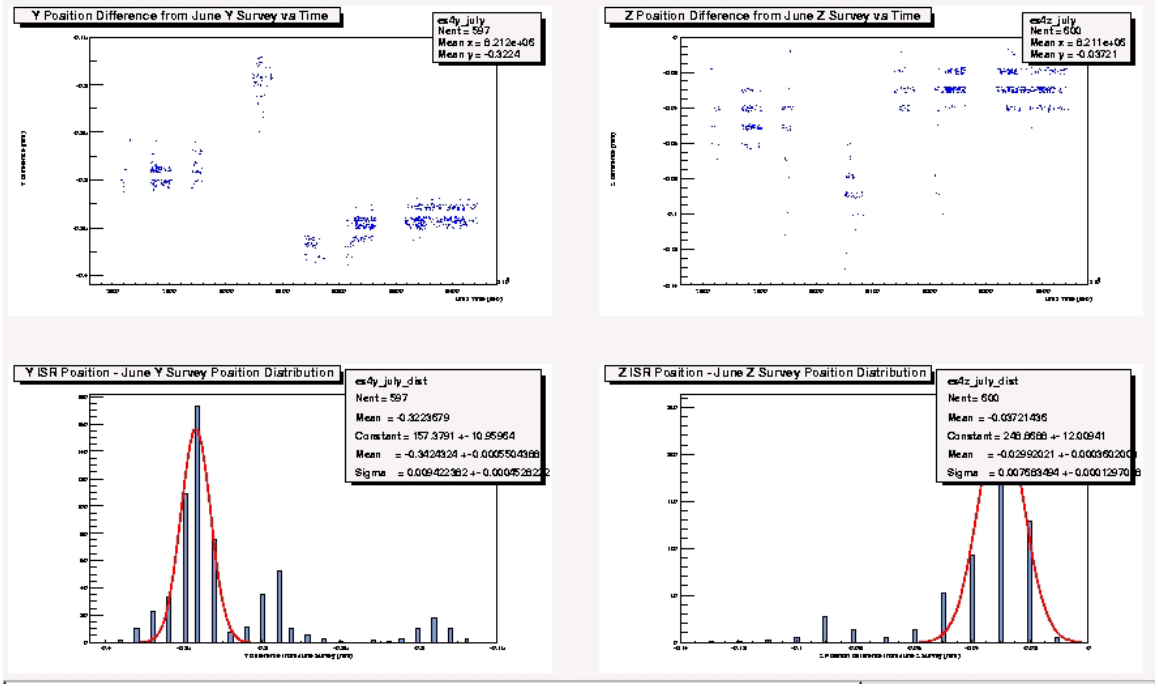

Figure 2.6**:** Typical Distribution of Reconstructed Positions for an SLM sensor in September for Laser 303 Using es10 as the Final Reference Sensor (Sensor es4). (Bands are non-physical)

Events reconstructed with Laser 303 do not show any of the erratic behavior associated with the Laser 302 events in the beginning of the test period. However, like the earlier reconstruction of the July Laser 303 events, the Y distributions of reconstructed events features a cluster of approximately 50 events which show an apparent jump in the positions of the SLM sensors. As before, the magnitude of this jump increases in magnitude with the distance from the transfer plate. Excluding this cluster of events, the distribution of reconstructed events in Y is confined within a 120μm region. Events in the distribution of Z coordinates also fall inside a 100μm range. Both of the main bodies of these distributions lie well within the systematic errors.

Reconstruction of events on the Transfer Line show distinct patterns in X and Y for all sensors except et4 Y. The sensors seem to track each other in both coordinates, though the entire distribution for both coordinates (across 150μm in X and Y) fall almost completely inside the systematic error. As in July, the et4 Y distribution of events is

slightly smeared over wider range (200μm) and slightly exceeds the systematic error on the sensor reconstruction. It is also entirely possible that miscalibration of the CCD-dowel relationship or survey errors could contribute substantially to this deviation.

2.5.1.3 Discussion of et2, et3, and es10 Reference Sensor Reconstruction

A summary of the results for all sensors from each test period are given in Table 2.4-6 and Figure 2.7-9. The reconstruction of SLM Y coordinates is consistent for both lasers during the two test periods. Furthermore, both lasers seem to track the locations of the SLM sensor Y locations in the same manner as the errors on the reconstructed positions overlap. A slight drift in the sensor Y locations can be seen in all four sets of reconstructed data. The fact that the same drift is evident for both lasers suggests that the placement of the es10 reference sensor or transfer plate may be different from the surveyed value.

Reconstruction of SLM sensor Z coordinates with Laser 302 is inconsistent between the July/August and September test periods. The Laser 302 September Z coordinate reconstruction matches almost exactly with the Z coordinate reconstructions done with Laser 303 for both test periods. An examination of the raw FLAP data from July indicates the Laser 302 peak in the es10 CCD which should track motions along the Z coordinates does not respond to small shifts in the orientation of the laser in the same manner as preceding sensors. Since es10 is a reference sensor, its inability to track Laser 302 in Z inhibits an accurate reconstruction of any SLM sensor Z coordinates. Impact on the Laser 302 July/August Y coordinate reconstruction from the inability to track the Z coordinate is presently being reviewed, though it is thought to be a second or third order effect. The effect does not appear in the September data as Laser 302 was replaced early in the test period. Sensor Z coordinate locations were found to be very close to their surveyed location, though es5 and es9 show somewhat higher deviations that the other sensors. No drift is evident in these distributions.

The reconstruction of sensors on the Transfer Line yields the expected results, with only the X position of et 4 being reconstructed well away from the surveyed location. Measurements on sensor et4 were restricted to two CCDs only with the peak on the CCD tracking the laser along the X axis suffering from a low signal to background ratio. As noted in the discussion of individual et4 events during the test period, the distribution of X coordinate reconstructions as a function of time was slightly more dispersed than those in the Y coordinate indicating some instability in the signal. The elevated location of the sensor et1 Y reconstruction can be seen to correspond exactly to the elevation of the es1 sensor Y location. The calibration of the Transfer Plate was broken during the photogrametry survey of the system in the ISR hall by moving the et1 sensor in Y, so this sensor was expected to significantly deviate from the surveyed location. Since the location of es1 was unchanged, a series of mechanical measurements between the et1 and es1 brackets was made to establish the new et1-es1 relationship and es1 expected location. These measurements have an estimate error of 500 μm. Deviations of this measurement from the actual separation of es1 and et1 are therefore expected to show the reconstructed Y coordinate location of et1 as being different from the calculated Y position of the sensor and the location of es1 as being askew since the et1-es1 relationship would be incorrectly specified. Section 2.6.4 details the problems with the calibration of the transfer plate.

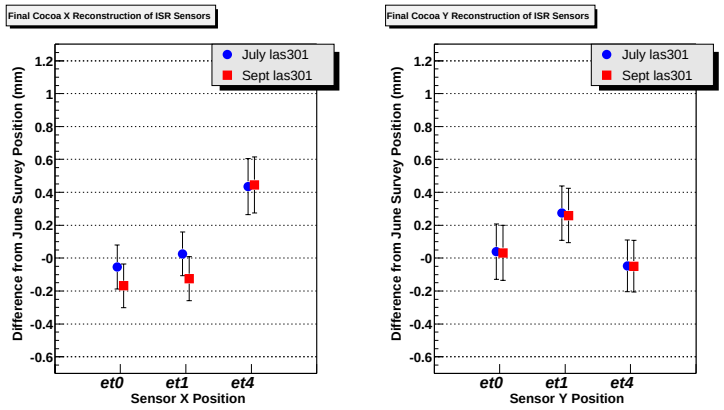

Figure 2.7: Transfer Line Results of COCOA Reconstruction for July/August and September Runs Using es10 as the Final Reference Sensor. Error bars indicate total uncertainty in sensor location as determined by COCOA.

Table 2.4: Deviation of COCOA Reconstruction of DCOPS Axial Dowel Pin Positions from Expected Survey Location with es10 Survey as Final Reference

Sensor	**July/Aug Laser 301**		**Statistical Error (July)**		**Sept[4] Laser 301**		**Statistical Error (Sept)**		**Systematic Error**	
	Xmean (μm)	**Ymean (μm)**	**Xerror (μm)**	**Yerror (μm)**	**Xmean (μm)**	**Ymean (μm)**	**Xerror (μm)**	**Yerror (μm)**	**Xerror (μm)**	**Yerror (μm)**
et0	-54	39	9	9	-168	32	8	21	133	168
et1	26	274	7	7	-125	259	15	13	133	165
et4	435	-47	28	10	445	-49	23	13	170	158

Table 2.5: Deviation of COCOA Reconstruction of DCOPS SLM Dowel Pin Positions from Expected Survey Location with Laser 302 and es10 Survey as Final Reference

Sensor	**July/Aug Laser 302**		**Statistical Error (July)**		**Sept[4] Laser 302**		**Statistical Error (Sept)**		**Systematic Error**	
	Ymean (μm)	**Zmean (μm)**	**Yerror (μm)**	**Zerror (μm)**	**Ymean (μm)**	**Zmean (μm)**	**Yerror (μm)**	**Zerror (μm)**	**Yerror (μm)**	**Zerror (μm)**
es1	276	13	7	fixed	258	13	15	fixed	165	53
es2	143	79	59	5	-25	-453	26	6	198	125
es4	72	330	28	7	20	-56	13	10	158	110
es5	136	569	22	11	74	245	13	17	158	107
es6	-328	494	12	9	-255	191	9	23	117	109
es7	-366	524	11	15	-281	322	11	26	110	116
es9	-383	638	9	35	-170	380	14	36	114	137

Table 2.6: Deviation of COCOA Reconstruction of DCOPS SLM Dowel Pin Positions from Expected Survey Location with Laser 303 and es10 Survey as Final Reference

Sensor	**July/Aug Laser 303**		**Statistical Error (July)**		**Sept[4] Laser 303**		**Statistical Error (Sept)**		**Systematic Error**	
	Ymean (μm)	**Zmean (μm)**	**Yerror (μm)**	**Zerror (μm)**	**Ymean (μm)**	**Zmean (μm)**	**Yerror (μm)**	**Zerror (μm)**	**Yerror (μm)**	**Zerror (μm)**
es1	276	13	7	fixed	263	13	12	fixed	165	53
es2	-262	0	12	8	-300	2	21	9	228	145
es4	-324	-30	9	8	-245	-27	18	10	188	122
es5	-211	214	15	8	-252	215	9	7	147	112
es6	-369	-15	8	8	-404	-8	5	7	120	104
es7	-446	-18	9	6	-457	-24	5	5	111	104
es9	-605	-271	7	7	-475	-247	4	4	117	117

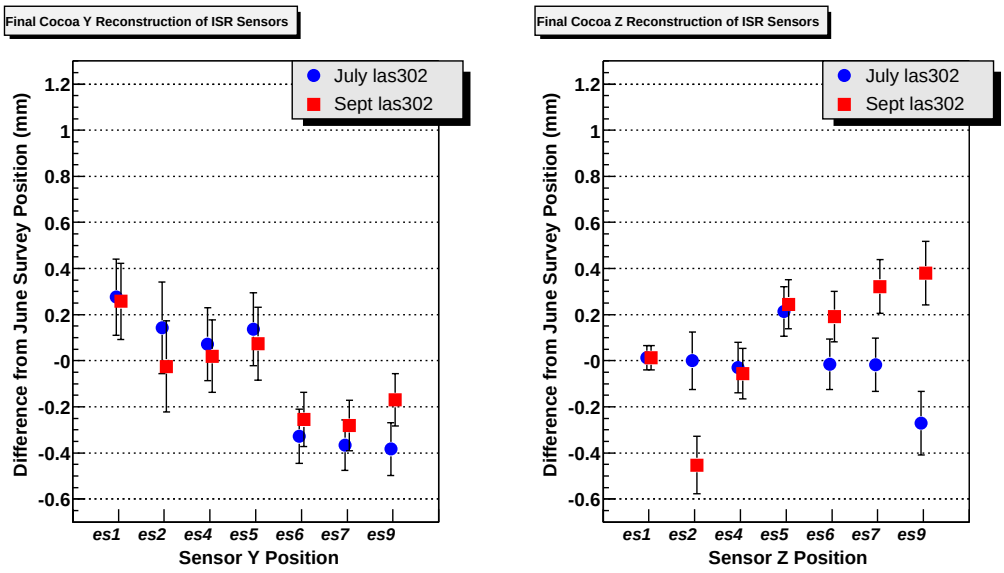

Figure 2.8**:** SLM Line (Laser 302) Results of COCOA Reconstruction for July/August and September Runs Using es10 as the Final Reference Sensor. Error bars indicate total uncertainty in sensor location as determined by COCOA.

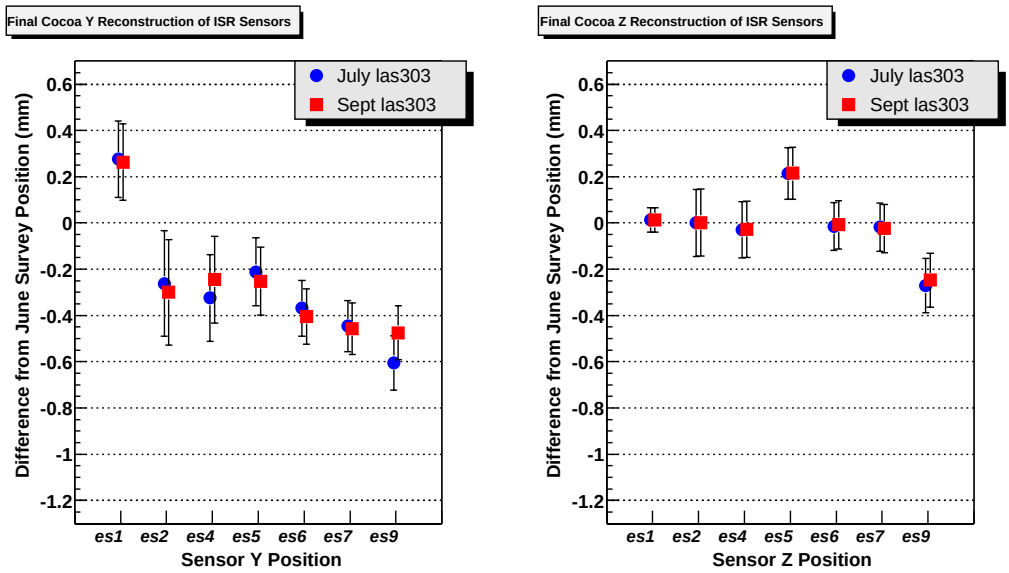

[4] Events fitted in Sept Data correspond to introduction of new laser diode in SLM line (525+ events). September events taken prior to the introduction of the new laser (100 events) where typically within 20-150μm of July positions.

Figure 2.9**:** SLM Line (Laser 303) Results of COCOA Reconstruction for July/August and September Runs Using es10 as the Final Reference Sensor. Error bars indicate total uncertainty in sensor location as determined by COCOA.

2.5.2 COCOA Reconstruction with References et2, et3, and es9

In an attempt to further study the principles and operation of the system, a second reconstruction with COCOA was done using the final reference sensor as es9 rather than es10. Since es9 is only 85mm ahead of es10 in the SLM line, it is the logical choice for the final reference sensor to check es10 reconstruction results. Reconstruction of sensors using es9 as the final reference was done using an incorrect rotation on es10, hence the reconstructed value of es10 do not match the value of es10 as it was used in 2.5.1 for the final reference sensor in the SLM line. The misorientation in es10 has been shown to have no significant influence on other SLM sensors in the laser line. A discussion of the problems encountered with the rotations of es10 is discussed in Section 2.6.1.

2.5.2.1 July/August Results

All the sensors were reconstructed with COCOA in the manner described previously. All of the reconstructed sensors in the ISR tunnel had their mean reconstructed positions in the tunnel plotted as a function of real UNIX time to examine the characteristic behavior of the system. Samples of characteristic plots for each SLM laser are given below in Figure 2.10 and Figure 2.11.

The distribution of reconstructed means along the CSC layer SLM typically fell within a 100-140 μm range in Y and a 40-80 μm range in Z for both lasers 302 and 303. Though both lasers appear to show a slight drift in the Y distributions, any apparent drift in the data cannot be resolved outside the systematic errors. All of the distributions appear to look very similar, with the exception of es10. As discussed in the review of the COCOA reconstruction of the SLM using es10 as a reference sensor (Section V.A.), the

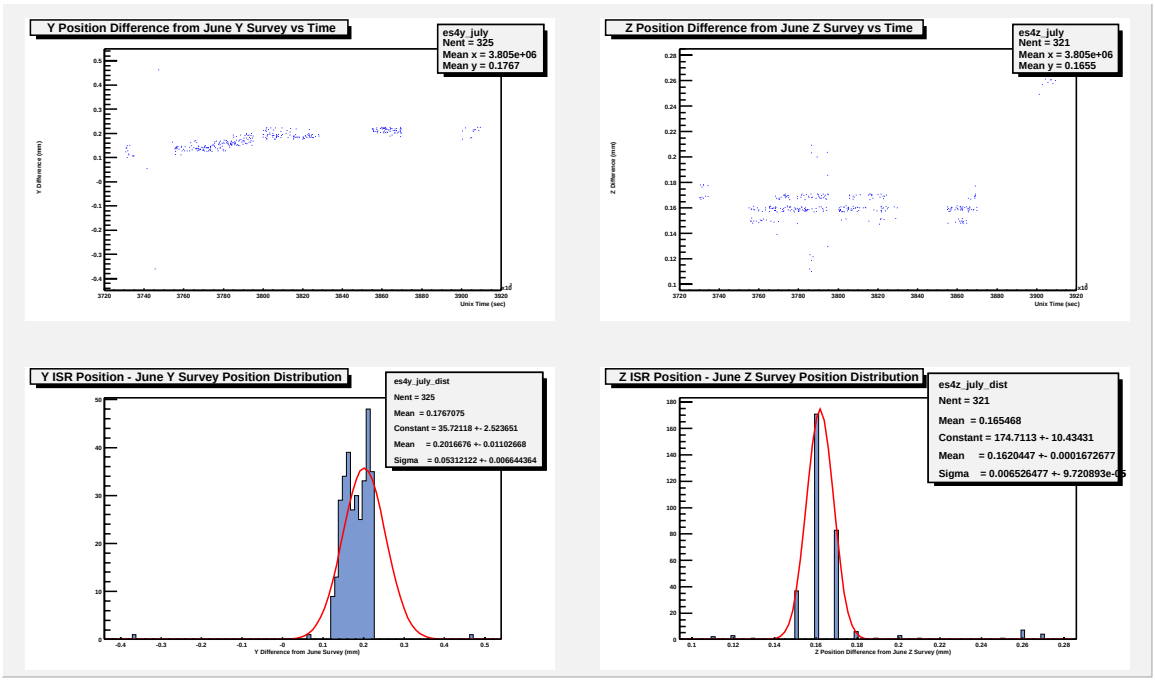

Figure 2.10**:** Typical Distribution of Reconstructed Positions for an SLM sensor in July for Laser 302 Using es9 as the Final Reference Sensor. (Bands are non-physical)

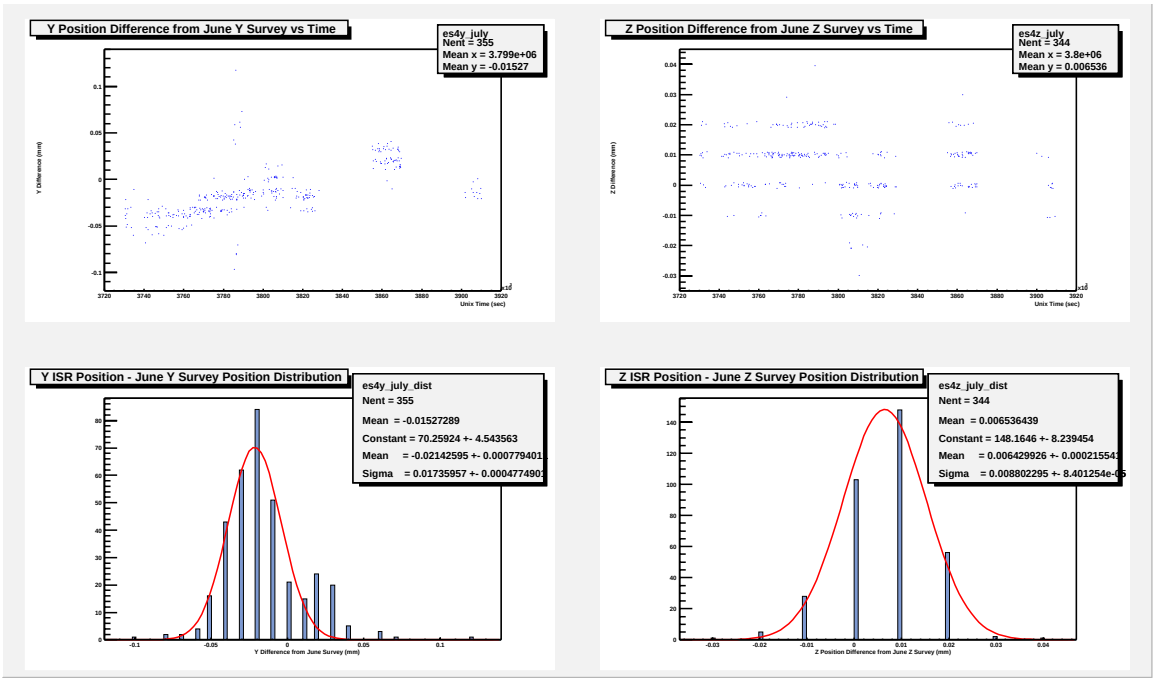

Figure 2.11: Typical Distribution of Reconstructed Positions for an SLM sensor in July for Laser 303 Using es9 as the Final Reference Sensor. (Bands are non-physical)

raw and fitted pixel distributions from FLAP were found to not track the distributions in the other SLM sensors, so this result in not unexpected.

The reconstruction of the Transfer line sensors yielded a distribution of the sensors' mean ISR positions that fell within the systematic error involved in the COCOA reconstruction. Though no correlations could be drawn out due to the systematic error, the resulting distributions (in X and Y) for sensors et0 and et1 looked fairly similar. The distribution of positions for sensor et4 seemed to mirror those of the other sensors in Y, but looked random in X. It should be noted that sensor et4 had only two CCDs (lower and far X ISR) illuminated by the laser and the preceding reference sensor, et3, did not have its upper CCD (which tracks X motions) illuminated, thus it was expected that et4's resolution would be degraded.

2.5.2.2 September Results

Sample plots from the September data set showing the position of a typical sensor are shown in Figure 2.12 and Figure 2.13. The distribution of COCOA reconstructed positions of the SLM sensors as a function of time all seem to be continuation of the previous July/August data until there is a large jump in the Laser 302 Y and Z and Laser 303 Y data. This apparent jump in sensor positions is most prevalent when the sensors were reconstructed with Laser 302, though a smaller apparent jump is observed along the Y axis when the reconstruction was done with Laser 303. The jump appears to coincide exactly with the replacement of Laser 302 and matches a jump in the raw and pixel distributions from FLAP. The amplitude of the jumps appears to gradually decrease in magnitude from es2 to es7 as the sensor distance from laser 302 increases. The Z positions of the SLM sensors do not appear to undergo any significant changes when reconstructed with Laser 303. Indeed, an examination of all sensors show significant changes between the July/August SLM sensor positions and September SLM sensor

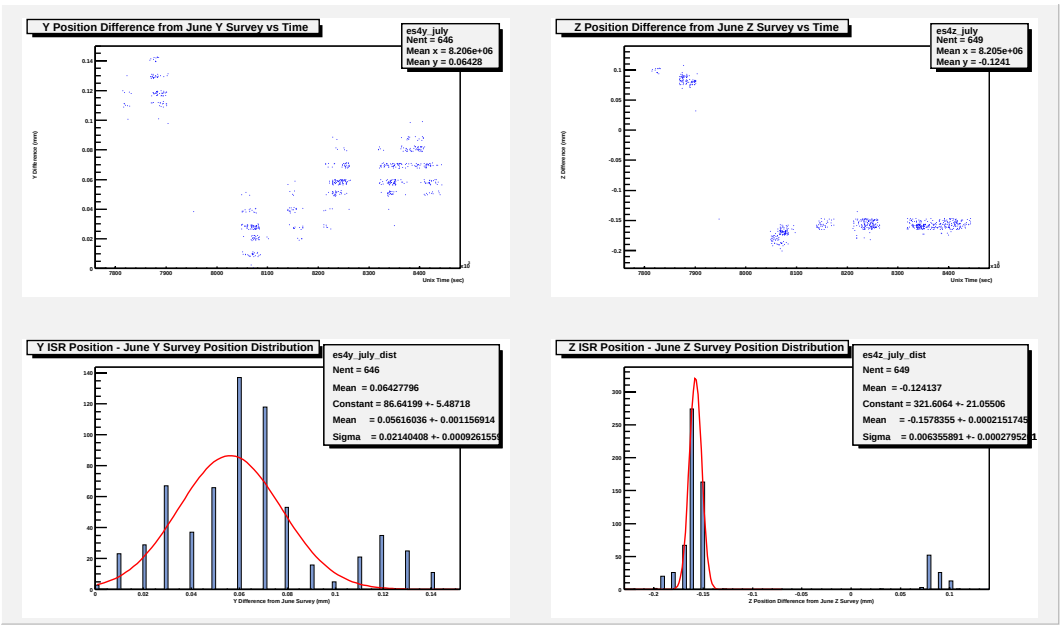

Figure 2.12 Typical Distribution of Reconstructed Positions for an SLM sensor in Sept for Laser 302 Using es9 as the Final Reference Sensor. (Bands are non-physical)

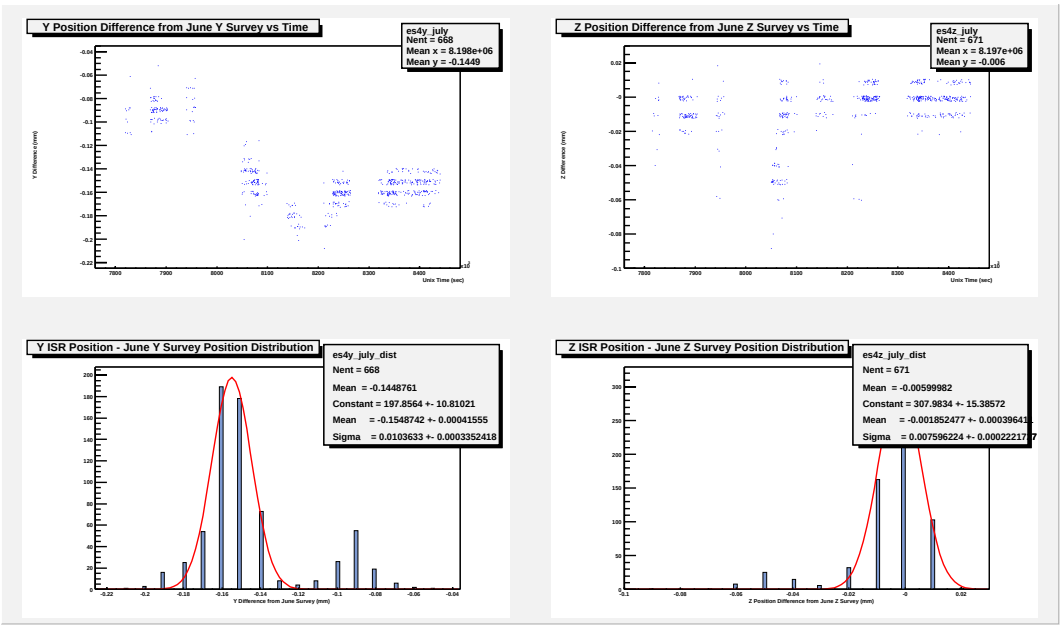

Figure 2.13**:** Typical Distribution of Reconstructed Positions for an SLM sensor in Sept for Laser 303 Using es9 as the Final Reference Sensor. (Bands are non-physical)

positions - except in the Z positions associated with Laser 303. Such shifts could potentially have been caused by disturbing the position or orientation of the transfer plate during the replacement of the laser; however it is not yet clear if this was the case. Raw FLAP data is presently being correlated with the September COCOA reconstruction to further study this phenomenon. Since the jump in apparent sensor positions was so significant and occurred early in the September test period, the time period prior to the jump (containing approximately 120 of 1300 events) was excluded from the analysis and the July/August test period was examined separately from the September test period.

An examination of the remaining September SLM data after the jump shows that the range of the entire distribution of mean positions for all sensors (and all lasers) typically fall within the systematic error of each sensor. The distributions appear to be much tighter than those in July as reflected by the smaller statistical errors associated with these events. The Transfer line sensor distributions (again they fall within the systematic error) appear very similar to those taken in July/August, though the September distributions are slightly more spread out. There is no apparent jump in the location of any Transfer line sensors.

2.5.2.3 Discussion of et2, et3, and es9 Reference Sensor Reconstruction

COCOA Reconstruction of the test setup using es9 as the final SLM reference show the Transfer Line, Laser 302 Z September, and all Laser 303 Z reconstructions remain essentially unchanged from the es10 reconstruction results. The drift in the Y coordinate reconstruction of the SLM sensors evident in Figure 4 for the es10 reconstruction is no longer visible. Rather, all of the sensor Y locations now lie roughly within 200 μm of their surveyed locations (es10 excluded). A slight shift in the sensor Y reconstructions is now observed between the July/August and September data and is more prevalent with the Laser 302 reconstruction. A summary of the results for all sensors from each test period are given in Table 2.7-2.9 and Figure 2.14-16. Placement of es10 in Figure 2.15 and Figure 2.16 is exaggerated by the misorientation of the es10 sensor. The corrected

Table 2.7: Deviation of COCOA Reconstruction of Axial DCOPS Dowel Pin Positions from Expected Survey Location with es9 Survey as Final Reference

Sensor	July/Aug Laser 301		Statistical Error (July)		Sept[5] Laser 301		Statistical Error (Sept)		Systematic Error	
	Xmean (μm)	Ymean (μm)	Xerror (μm)	Yerror (μm)	Xmean (μm)	Ymean (μm)	Xerror (μm)	Yerror (μm)	Xerror (μm)	Yerror (μm)
et0	54	39	9	9	-168	31	8	22	< 132	< 168
et1	25	-237*	7	7	-123	-257[6]	15	16	< 133	< 500
et4	435	-48	27	11	447	49	24	12	< 170	< 158

Table 2.8: Deviation of COCOA Reconstruction of SLM DCOPS Dowel Pin Positions from Expected Survey Location with Laser 302 and es9 Survey as Final Reference

Sensor	July/Aug Laser 302		Statistical Error (July)		Sept[5] Laser 302		Statistical Error (Sept)		Systematic Error	
	Ymean (μm)	Zmean (μm)	Yerror (μm)	Zerror (μm)	Ymean (μm)	Zmean (μm)	Yerror (μm)	Zerror (μm)	Yerror (μm)	Zerror (μm)
es1	276[6]	1	8	fixed	254	13	17	fixed	< 166	< 53
es2	205	67	44	6	-18	-471	17	12	< 211	< 125
es4	202	162	53	7	56	157	6	5	< 167	< 110
es5	282	312	27	11	124	101	13	5	< 146	< 107
es6	-80	106	22	18	-153	-42	10	6	< 121	< 109
es7	-68	58	21	17	-156	39	21	17	< 112	< 116
es10[7]	985	-932	8	46	771	-684	16	28	< 114	< 137

Table 2.9: Deviation of COCOA Reconstruction of SLM DCOPS Dowel Pin Positions from Expected Survey Location with Laser 303 and es9 Survey as Final Reference

Sensor	July/Aug Laser 303		Statistical Error (July)		Sept[5] Laser 303		Statistical Error (Sept)		Systematic Error	
	Ymean (μm)	Zmean (μm)	Yerror (μm)	Zerror (μm)	Ymean (μm)	Zmean (μm)	Yerror (μm)	Zerror (μm)	Yerror (μm)	Zerror (μm)
es1	276[6]	1	7	fixed	257	13	15	fixed	< 167	< 53
es2	-183	-40	38	8	-231	-41	22	15	< 147	< 146
es4	-21	6	17	9	198	-2	10	8	< 188	< 123
es5	58	291	11	8	-36	284	8	6	< 146	< 113
es6	19	129	11	9	-102	121	7	6	< 120	< 105
es7	17	177	10	17	-96	148	10	17	< 112	< 105
es10[7]	1211	-266	7	6	1082	-287	4	5	< 117	< 117

[5] Events fitted in Sept Data correspond to introduction of new laser diode in SLM line (525+ events). Events taken prior to the introduction of the new laser where typically within 20-150μm of July positions.
[6] Transfer plate Y definition was broken by at 1.71 mm ± .5 mm. This is survey position with estimated movement of transfer plate components. See Section IV.C for detailed description of problem.
[7] The orientation of Sensor es10 was found to be incorrect. Subsequent reconstruction of single events using the corrected orientation indicates the (Y,Z) location of es10 is closer to (182, -419) in July and (162, -439) in Sept

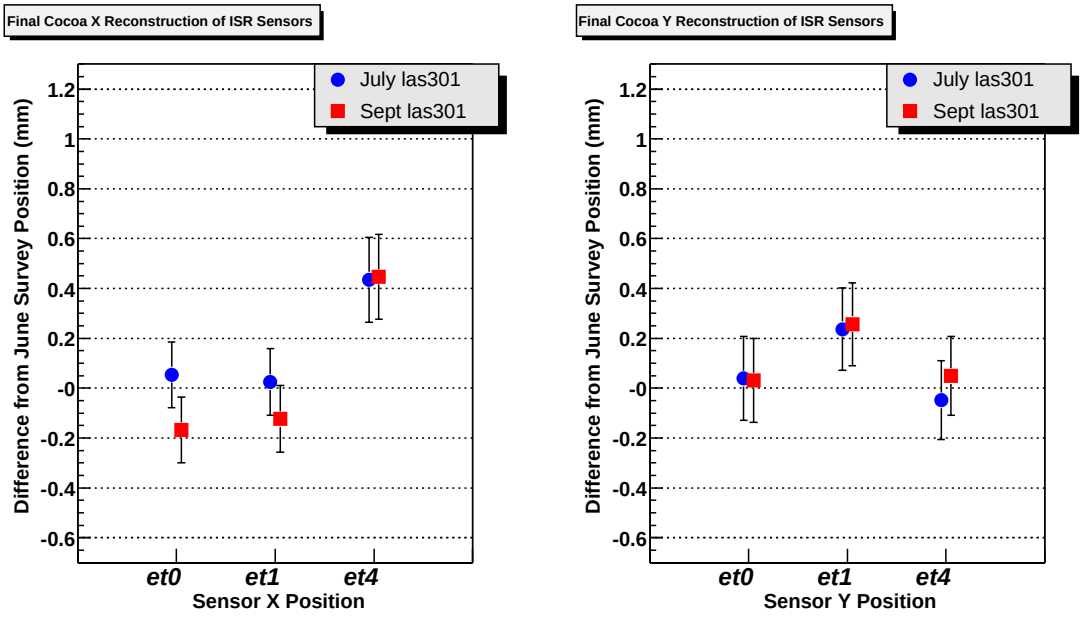

Figure 2.14**:** Transfer Line Results of COCOA Reconstruction for July/August and September Runs Using es9 as the Final Reference Sensor. Error bars indicate total uncertainty in sensor location determined by COCOA.

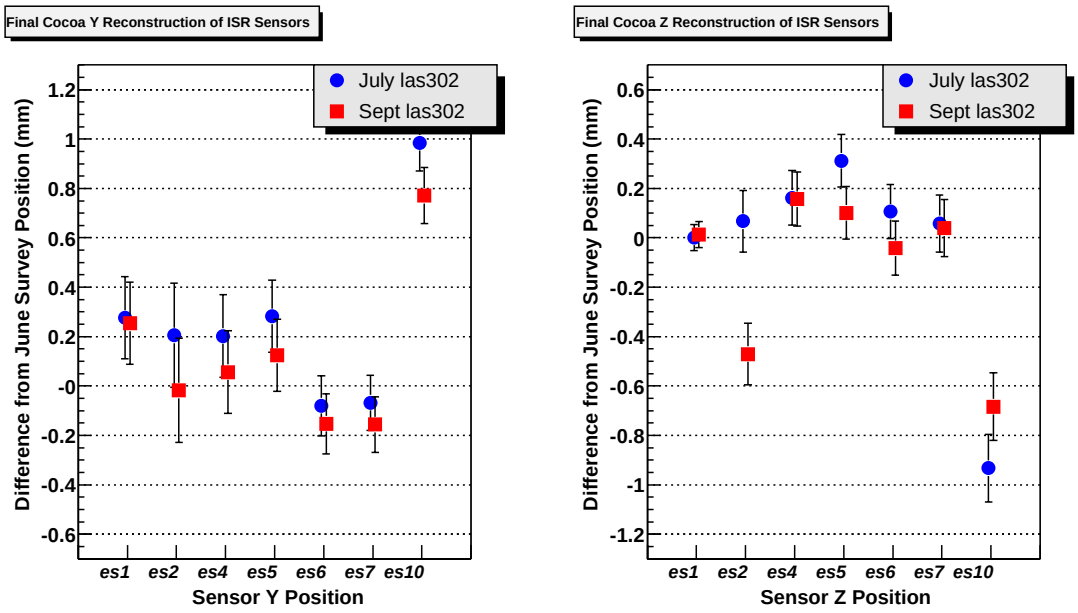

.

Figure 2.15**:** SLM Line (Laser 302) Results of COCOA Reconstruction for July/August and September Runs Using es9 as the Final Reference Sensor. Error bars indicate total COCOA uncertainty.

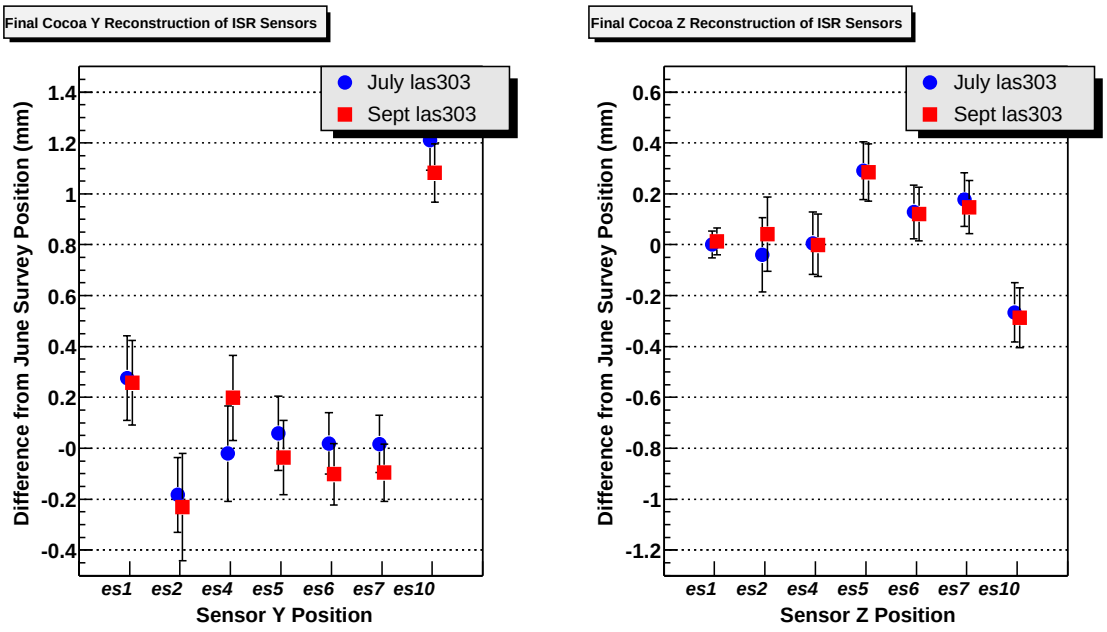

Figure 2.16**:** SLM Line (Laser 303) Results of COCOA Reconstruction for July/August and September Runs. Error bars indicate total uncertainty in sensor location as determined by COCOA.

orientation was used for the reconstruction of the SLM shown in Section 2.5.2. See Section 2.6 for a more detailed description of the problem.

As with the es10 reference sensor reconstruction, a comparison of Figure 2.15 and Figure 2.16 shows that the reconstructed Z coordinate positions of several of the sensors do not overlap. In particular, the reconstructed means of the Laser 302 es2, es5, and es10 Z coordinates in September show some disagreement with corresponding reconstructions using the other lasers. The discrepancy is, however, much less than with the es10 reconstruction since most error bars now overlap between the two lasers and test periods. Since sensor es10's operable CCDs monitoring changes along the Z axis were found not to track the CCDs in preceding sensors, the es10 result was expected.

2.5.2.4 Conclusions

Reconstruction of all DCOPS sensors within 200 μm of the June survey positions was achieved for most of the sensors in both reconstructions for both test periods if the errors in the CERN Photogrametry are considered. The elimination of the drift in the es10 reference sensor Y coordinate reconstruction by choosing es9 as the reference indicates the surveyed location of orientation of es10 is incorrect. The shifted location of es7's Y coordinate between the two reconstructions suggests the misplacement or impact of an incorrect orientation of es10 is on the order of 250-350 μm.

Figure 2.17 indicates that the reconstruction of sensors utilizing es9 as the final reference indicates that resolution of the entire ISR system (excluding es10) can be generalized as ~223μm for the July test period, ~150μm for the September test period, and ~187μm across both test periods. This again compares favorably to the uncertainty in the photogrammetric location of the dowel pins (σ_y =180 μm, σ_z =160μm) with which the reconstructed location of the dowel pins are compared.

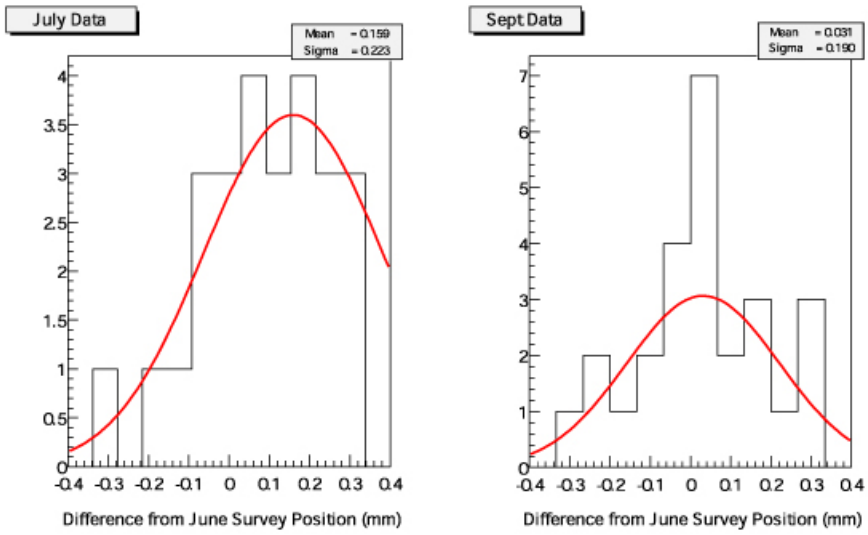

Figure 2.17**:** Summary of Reconstructed SLM and Transfer Sensor Locations for es9 Reference Reconstruction. Histograms represent the deviation of all reconstructed sensor locations from their initial photogrammetry survey location. Both Laser 302 and 303 reconstructions are included in the data. The averaged σ for both test periods is 187μm.

The most basic test as to whether or not the system works in a self consistent manner has been met: the apparent location and relative positioning of most sensors can be said to remain roughly within the projected error of the reconstruction independent of the choice of laser used along the SLM line. This test is much more critical than matching the reconstructed position of the sensor dowel pins to their surveyed location since survey errors can be large (>150 μm along SLM line, perhaps more in the case of the es10 Y coordinate). Some discrepancies between reconstructions based on the laser choice are expected since the sensors participating in the measurements may gain or lose CCDs or see completely different signal to background ratios. Perhaps more significantly, the active CCDs on the SLM reference sensors are switched with choice of lasers due to shadowing effects by preceding sensors. Thus, two sets of measurements utilizing each laser *with the same reference CCDs* on the endpoints are not available.

There is also ample evidence to suggest that the reconstructed positions of the sensors are independent of small variations in the orientation of the laser. An analysis of the individual CCDs used in the reconstruction shows several cases in which the angle of the laser seems to suddenly shift. Figure 2.18 shows the July distribution of raw centroid measurements in each CCD of sensor es4. Three distinct jumps in the location of the laser centroid can be clearly seen. The first jump in the distribution is approximately 30 pixels (30 pixel = 420μm). Figure 2.19 shows the reconstructed location of sensor es4 over the same period of time. There is no indication of any breaks or jumps in the distribution to suggest any sort of correlation with the jumps in CCD centroids in Figure 2.18 (σ_y = 10 μm, σ_z = 8 μm).

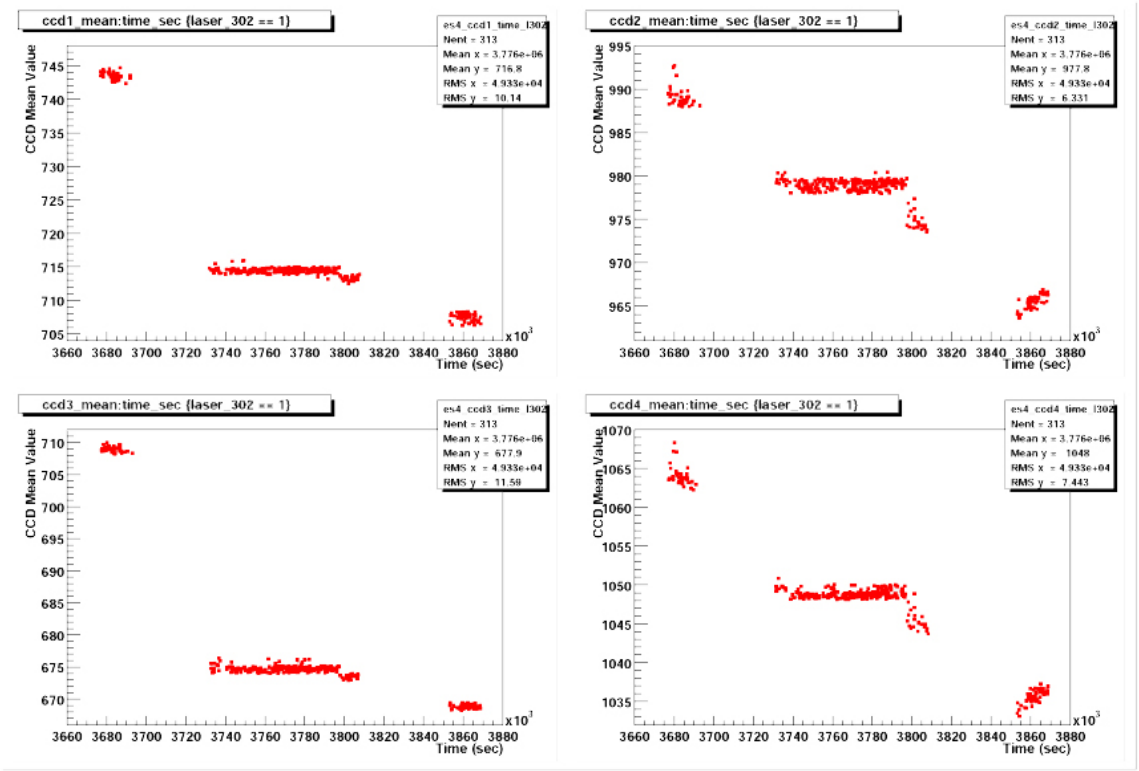

Figure 2.18: Distribution of raw CCD means in es4 during the July/August Run. Three distinct jumps in the pixel distributions can be seen.

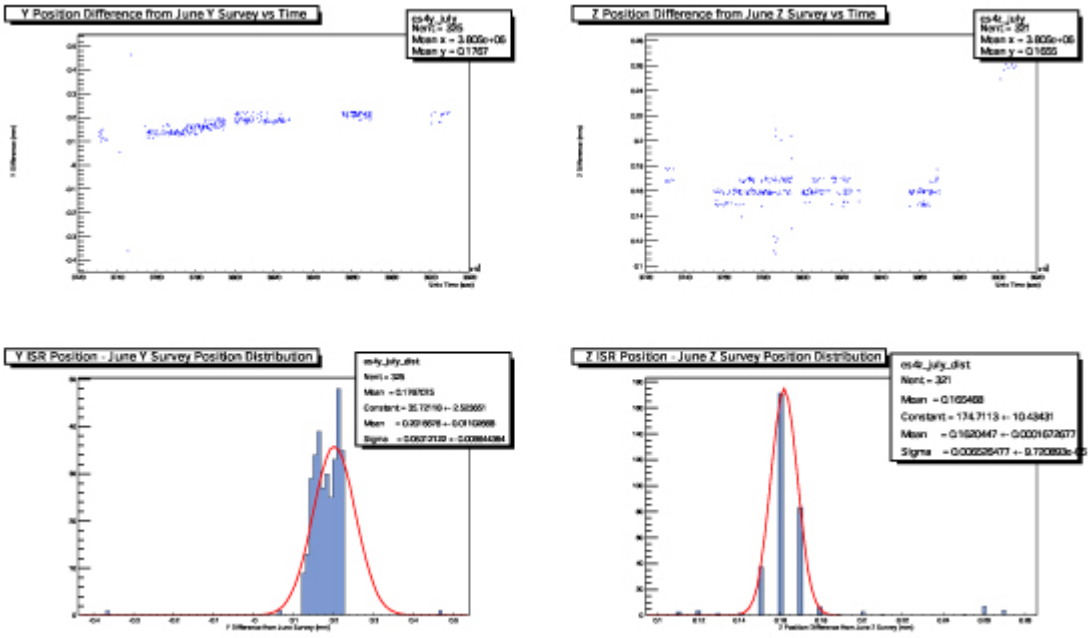

Figure 2.19: Distribution of COCOA Reconstructed location of es4 in the ISR hall during the July/August Run. No jumps in the data are evident. (Bands are non-physical)

As previously discussed, there does seem to be a clear correlation between the introduction of a replacement Laser 302 in September and the large jump in es9 reconstructed positions and the ending of the erratic behavior from those positions reconstructed with the es10 reference sensor. This effect is not entirely understood.

2.6 Limitations of the COCOA ISR Reconstruction

Not all sensors in the test hall could be reconstructed within the desired 200μm. Furthermore, the systematic errors were significant. Several factors which may have contributed to errors in the COCOA reconstruction are now addressed.

2.6.1 Determination of Angular Orientations

As discussed, the results presented were determined by fixing the angular orientation of the unknown sensors in COCOA to their surveyed orientation. This cannot be done in the final CMS system. Additional studies are underway to understand how well these angles can be determined from the COCOA reconstruction of actual CCD measurements and the impact on this has on the spatial resolution of the system.

COCOA determines the angular orientation of the dowel pins be finding the minimum error associated with the inverse of the matrix used to determine the best fit of the CMM data with the CERN survey data. In the case of es10, two local minima's to this fit occurred unusually close to each other. Although both minima's yielded slightly different dowel orientations (<1.5 degrees), they had identical dowel locations. Reconstructing with the larger of the two rotations introduced significant errors in the entire SLM line when es10 was used as the final SLM reference The larger rotation on es10 introduced errors in only the reconstructed location of es10 when es9 was used as the final SLM reference. Upon discovery of the second minima, the reconstruction of all events using the new (smaller rotation) orientation of es10 as the SLM reference was

performed. The location of es10 in the reconstruction using es9 as the final reference is the original (larger rotation) value.

2.6.2 Reference et2 MAB Motions

The absolute establishment of the positions of the reference sensors et2, et3, and es10 are the most critical parameters of the reconstruction. In the present COCOA simulation, the locations of et3 and es10 are given by photogrammetric measurements taken in June. These sensors were not moved or repositioned from their mounts until the end of the September tests. However, the et2 sensor was installed just prior to the July tests on a simulated MAB. Though a series of photogrammetry measurements were taken just prior to the beginning of the test periods, the MAB could have undergone small shifts in position and orientation. These small motions of the MAB (if any) were monitored by the LINK Alignment group. Test data from the EMU and LINK groups are presently being correlated to better understand possible motions. The ISR data can be reconstructed with a new COCOA simulation using a non-static MAB model if motions are supplied by the LINK group.

2.6.3 Calibration of DCOPS Sensors

In principle, the calibration of the sensors taken before the June ISR tests was to be compared to a recalibration of the sensors upon completion of the September tests. This measurement was to estimate both the stability of the sensors during the ISR tests as well as reconfirm the validity of the original calibration. However, serious problems with the original calibration and the recalibration were uncovered upon careful examination of the data, making any definitive estimation of the sensor calibration at the time of installation impossible. The sensors have since been recalibrated a third time and this data is being examined. However, the new set of calibrated data is being estimated as valid with a maximal uncertainty of 100 μm.

Instability in the mount points of the CCDs in each sensor is clearly insignificant in the flat CCD windows by construction. The bi-directional sensor windows may exhibit some instability, particularly after handling and installation of filter tapes on the window. Errors in the Reconstruction due to these instabilities have not yet been investigated.

It is expected that a better understanding of the calibration process will significantly drop the error associated with the calibrated parameters. A calibration of the parameters perpendicular to the pixel arrays is also planned.

2.6.4 Calibration of Transfer Plate

The transfer plate fixes the relationship of sensors et1 and es1 and allows for the reconstruction of the SLM line (which uses es1 and es10 as reference sensors). Since et1 is determined from the Transfer line reconstruction (using et2 and et3 as reference sensors), it is essential that relationship on the transfer plate is specified precisely - as errors in the definition of this relationship will be compounded with errors from the derived position of et1.

Unfortunately, after the CERN photogrammetry of the transfer plate components, the relationship between es1 and et1 was accidentally broken by someone making an unrecorded adjustment to plate. It is assumed that such adjustments were only made to the slide which mounts the et1 sensor. This difference appeared after the survey of the photogrammetry targets on these sensors was done. Based on the subsequent measurements with a micrometer, it is thought that the et1 sensor was lowered approximately 1.71 mm ± .5mm in Y CMS only. The transfer plate was secured in its final position and sent to FNAL for additional CMM measurements to determine the precise magnitude of the displacement.

The transfer plate was measured again at FNAL by CMM on February 6, 2001. It was determined at this time that the vertical (Y CMS) separation between the et1 and es1

reference dowel pins was 187.198 mm ± .030 mm. Since the adjustable slide on the transfer plate moves only the et1 sensor, the 'true location' of et1 can be inferred from the CERN Photogrammetry location of es1 and the CMM separation of the dowel pin to be 1298.792 mm ± .153 mm in Y CMS.

2.6.5 Additional Fit Parameters (Shadowing, Poor Centroids)

Not all sensors in the ISR tunnel were able acquire usable data from all four of their CCDs due to either a malfunction on the DCOPS board or the shadowing of the laser line by preceding sensor windows. As a result, COCOA reconstructed the laser lines using only two or three CCDs on these particular sensors. Fortunately, sensors with two unusable CCDs had at least one vertical and horizontal CCD operable allowing for a reconstruction of the dowel location in the requisite two dimensions. Reference sensors et2, et3, and es10 had three usable CCDs and reference sensor es1 had all four CCDs working. However, July Run 458 showed sensor et2 with only two operable CCDs. This introduced significant errors in the Reconstruction. For example, the et1 sensor reconstructed positions along the X axis showed very large deviations exceeding 200μm between successive events. This error was propagated across the transfer plate and introduced significant variations between events on the SLM line as well. By contrast, with the more typical readout of three CCDs on et2, reconstructed positions of et1 typically fell well within a range of 100 μm. Fit and reconstruction problems were also induced by very poor laser distributions in individual CCDs.

Since reference sensors et2, et3 and es10 each had a shadowed CCD, it seems plausible that successfully illuminating all four CCDs on these reference sensors would improve the accuracy and precision of the overall reconstruction. This issue is presently being studied with an idealized simulation model of the EMU system.

2.6.6 Redundancy of Second Measurements in SLM Line

Events reconstructed thus far have utilized SLM Laser 302 (with the beam running toward the es9 reference) or Laser 303 (with the beam running toward reference sensor es1) separately. Since data with either SLM laser is taken synchronously with the Transfer line, events reconstructed with Laser 302 have no direct correlation to those reconstructed with Laser 303. If SLM Laser 302 and 303 data could be taken very close in time, the tracking and resolution of the sensors within short time frames could be greatly improved by incorporating both sets of SLM data into a single reconstruction of the system. Simulations modeling the reconstruction of single events using both Laser 302 and 303 data as near simultaneous measurements are underway.

2.6.7 First Level Analysis of CCD Data

The processing of raw data from the DAQ included the determination of the mean pixel location of the charge distribution formed by the incident laser. This mean was later entered into COCOA as a starting point for a reconstructed measurement. A detailed study of the raw charge distribution in the CCDs and the determination of the mean value have been presented separately. The conclusion of this study is that the mean value of the charge distribution can be determined in the ISR within 1 pixel (<14 μm of rms error) under repeated, short term measurements. The studies examining medium and long term resolutions are thought to be limited by the stability of the laser diode. It should be emphasized that the spatial stability of the laser lines for time periods exceeding the integration time of the CCDs is not a requirement for a successful Reconstruction of the system. However, abnormalities in raw CCD data was not been correlated to the abnormalities in the reconstructed data.

Additional work has been done carefully refitting several of the raw CCD charge distributions ‘by hand’. The reconstructed position of the sensors was found to remain in essentially the same location as when reconstructed with the original FLAP automated

fits. We have concluded that the fitting of the centroids performed by FLAP is more than adequate for reconstruction of alignment positions within the required performance specifications.

3 SIMULATION OF THE FULL EMU ALIGNMENT SCHEME

The successful reconstruction of sensor locations in the prototype ISR system strongly suggests that the design of the EMU Alignment System is promising. However, the ISR prototype system does not provide sufficient enough grounds to make larger generalizations about the entire EMU Alignment scheme nor characterize the interactions between many of the components. A general simulation of the EMU alignment scheme is needed to evaluate the operational viability of the system as a whole, estimate the precision with which the system can reconstruct CSC chamber positions, and relate the contribution of uncertainties in the construction of individual components to the performance of the system as a whole. Simulations of an idealized EMU system were performed with COCOA v2.0.0. The simulations included all major system components and appropriate CSC chamber geometries.

3.1 Construction and Extraction of Simulation Parameters and Objects

To optimize the development of Endcap simulations in COCOA, it was decided to compose the simulated Endcap solely from objects arranged in a 'parent-child' relationship. This means that relatively simple collections of objects already defined in COCOA can be placed together to compose more complex objects. In this scheme, two DCOPS sensors can be arranged in a local coordinate system to define a CSC chamber (Figure A.5). Four CSC chambers, in turn, are arranged to form a SLM line, three SLM lines are arranged to form an Muon Endcap (ME) layer, and six ME layers are assembled to form the entire CMS Endcap Muon system. The modeling of components in this manner means that the location and orientation of all the individual components (dowel pins, chamber active reference centers, lasers, etc) does not need to be known in the general CMS coordinate system beforehand. Rather, the spatial relationships between

parent and child objects can be specified directly from CMS production drawings. This method works very well for six of the Muon Endcaps (ME±2, ±3, and ±4 Endcap), however the unique construction of the inner most Endcaps (ME ±1) requires a somewhat less symmetric approach, as SLM lines do not traverse the ME discs and a Secondary Laser Line must be introduced.

The extraction of the information necessary to define these relationships from CMS production drawings involves several steps and is not a simple exercise of comparing two points in a single drawing. For this reason, the exact manner in which parent-child objects were composed and assigned in the simulation is specified in Appendix A. Components included in the simulation include inclinometers, DCOPS sensors, LINK 2D transparent sensors, crosshair and beam lasers, and distance measuring devices. The objects created from these components include all the CSC chambers, transfer plates, and MABs used in the EMU alignment scheme.

The most important object in the simulation is the basic CSC chamber object. Though the details of CSC construction in the simulation are found in Appendix A, the approach taken to describe the basic ME chamber object is shown in Figure 3.1. Of principle importance is the manner in which the chamber 'center' is defined. Since tolerances between the separation of strip layers is not controlled in CSC chamber production, it has been decided to define a 'Reference Center' (or 'Active Centerpoint') for the chambers as the average strip position projected onto the upper strip plane. For a perfectly constructed CSC chamber (no uncertainties in construction), the centerline of the CSC chambers will fall along the Active Reference Center of the simulated chambers. Note: the 'Reference Center' and 'Active Centerpoint' will be simply referred to as the 'chamber center' for the remainder of this discussion.

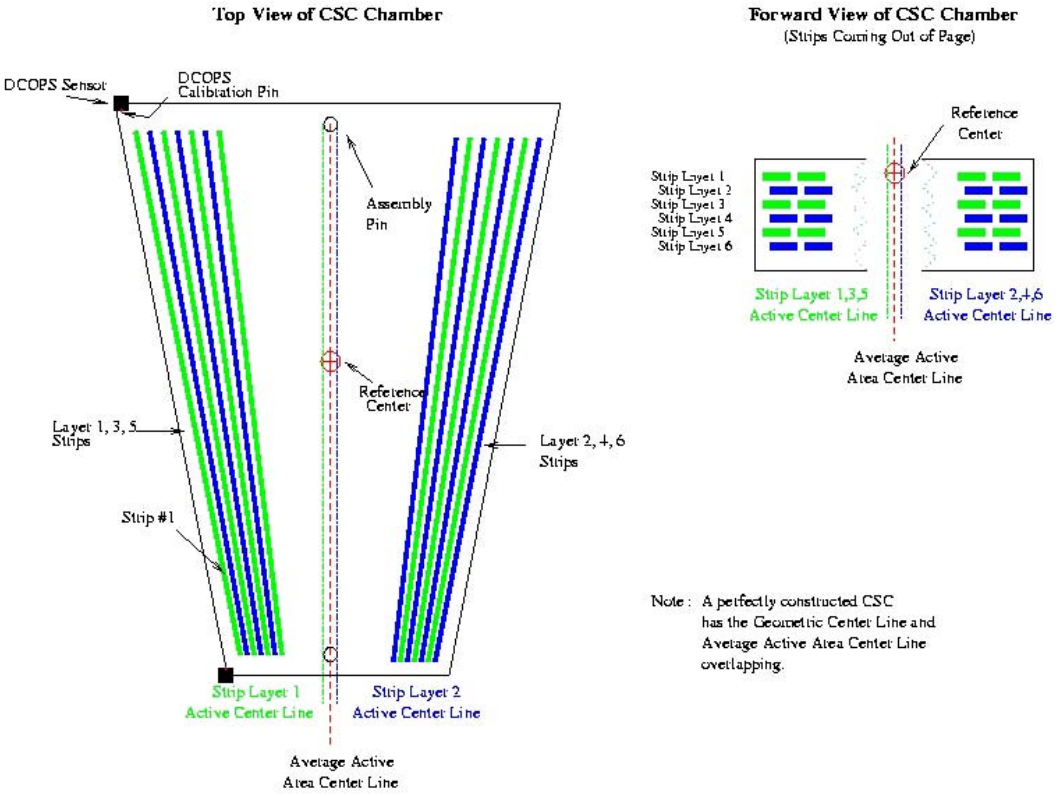

Figure 3.1: The Simulated CSC Chamber Geometry and Local Coordinate System in the Idealized COCOA Model. The 'Average Active Center' of the CSC chambers is taken as the Reference Center for COCOA EMU simulations.

3.2 Final Simulation Script Geometry Compared to Theoretical Placement

A complete model of the CMS EMU Alignment System constructed with the components detailed in Appendix A show layout and placement errors in the COCOA EMU simulation components of <5 μm along the Transfer Line (average deviation of .05 μm) and 10 μm along the SLM Line (average deviation of .81 μm). The discrepancies on SLM on the order of 10 μm occur only on the placement the inner ME ±2/1 DCOPS sensors relative to the ME ±2/1 CSC chamber centers. It has been decided that this error lies in the corresponding ME ±2/1 production drawings. The decision has been made to match components in the COCOA simulation to the final production drawings rather than

a perfect CMS geometry. It is expected that the tolerance on the construction of the components comprising the system will greatly exceed any of these small discrepancies in the production drawings.

A snapshot of a VRML model of the final simulation as generated by COCOA, showing only active components (lasers and all measurement devices), is shown in Figure 3.2.

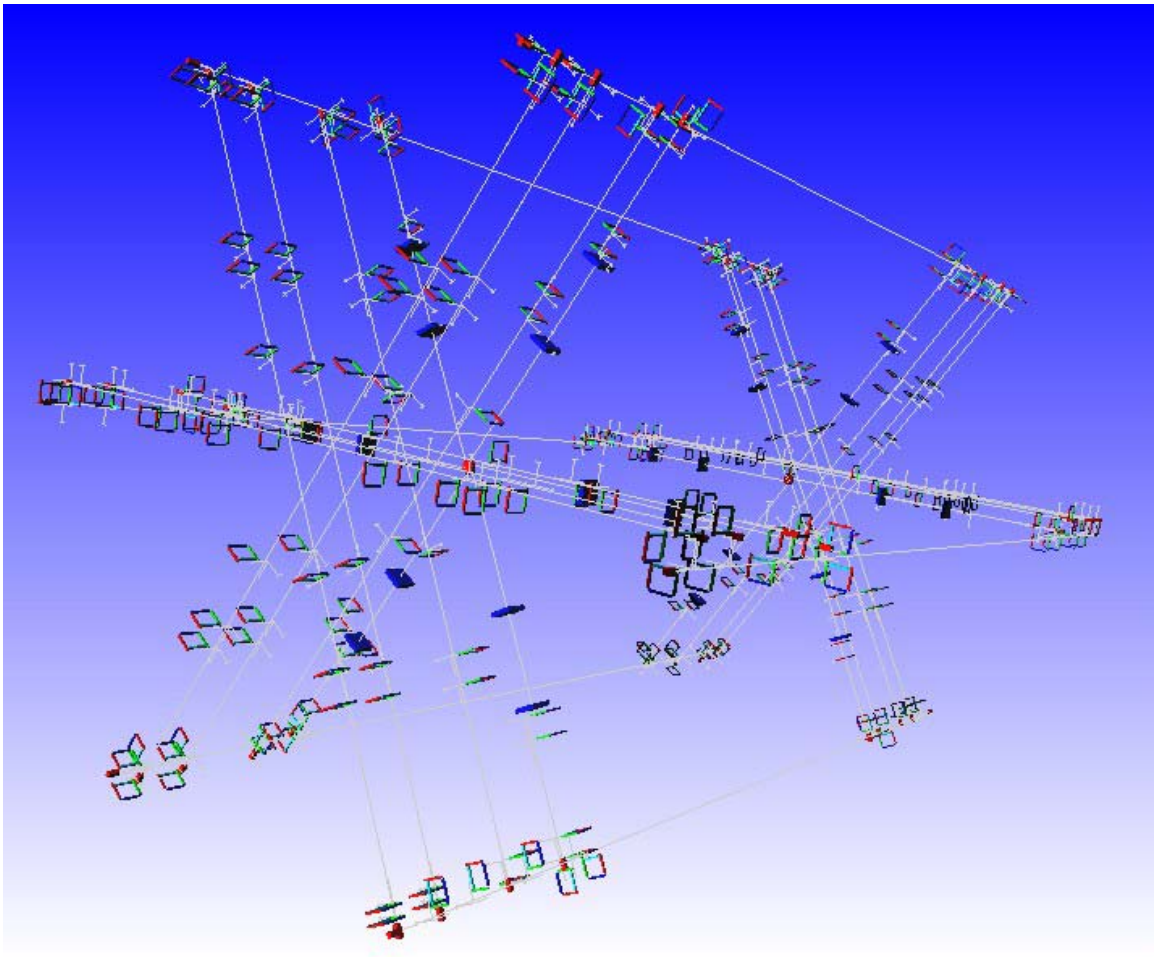

Figure 3.2: The Simulated EMU Alignment System. This is a COCOA generated VRML representation of the simulated geometry used for the idealized simulations of the EMU Alignment System.

3.3 Estimation of Uncertainties Used in EMU Simulations

The primary goal of the COCOA simulation of the EMU alignment scheme is to obtain an estimate of the uncertainties associated with the reconstruction of CSC chamber positions along the SLM laser lines and an understanding of the relationships and correlations between the various components of the alignment system. For simplicity, the most studies and simulations were done with the idealized EMU. The idealized EMU system contains all the EMU system components arranged in the manner detailed in Appendix A with uncertainties on the location and placement of the components set to the estimations detailed below. Since the system is ideal, it is assumed that all measurement devices are able to make a successful measurement and the full redundancy of the alignment scheme (multiple measurements of opposing lasers) is exploited. The effects of component failure (missing CCDs measurements from DCOPS, faulty laser modules, inadequate resolutions) should be examined separately.

3.3.1 Digital CCD Optical Position Sensor (DCOPS) Sensors

DCOPS sensors are viewed as a collection of four independent vectors, corresponding to the four CCD pixel arrays, referenced to a common calibration slot on the DCOPS hardware assembly (where the CSC calibration pin is to be inserted). Systematic uncertainties in the location of the origin of these vectors, i.e. the first active pixel position, are generally independent of the uncertainties associated with the pixel array orientation. Uncertainties in the location of any given pixel in a CCD to the calibration slot can be separated into uncertainties directly associated with the calibration of the first pixel position and those associated with the pixel array orientation and length.

3.3.1.1 Uncertainties in Direct Calibration of First Pixel Position

Calibration of first active pixel positions to the reference pins for large numbers of sensors is done on a specially designed test bench at Northeastern University (NEU).

The calibration bench is constructed of a laser diode assembly, a single directional DCOPS sensor that has been previously calibrated under a microscope, and a mount for the DCOPS sensor that is to be calibrated. In this arrangement, the calibrated DCOPS sensor acts as a mask to calibrate the uncalibrated DCOPS sensor. NEU indicates typical uncertainties in the first pixel location using this calibration technique will not exceed 40 μm [3.1].

3.3.1.2 Uncertainties in Pixel Array Orientation and Length

For simulation and reconstruction purposes, it is assumed that the four CCD vectors lie in the local DCOPS XY reference plane and run parallel to the X or Y axis. The error introduced by this assumption manifests itself as a correction to the Sony specified pixel-to-displacement conversion of 14μm per pixel along the array. The uncertainty in the determination of the position of the charge distribution will scale across the pixel array as the cosine of the angle by which the CCD array deviates from its optimal orientation.

The uncertainty introduced by the error in pixel array length and the misorientation of the pixel arrays can be estimated as the quadrature of the maximal error due to the misalignment of the pixel arrays within the CCD packages, the uncertainty in the length of the pixel array, and the maximal error due to misalignment of the CCD package within the DCOPS window frame.

3.3.1.3 Uncertainty of CCD Array and Packaging Positioning

Direct measurement of the pixel array length was performed on a representative sample of ILX-551 CCDs. In addition to the 2048 active pixels in each pixel array, one end of the array contains an additional 33 dummy pixels while the other end contains an additional 6 dummy pixels. The total length of the pixel strip is calculated to be 29.218 mm based on the Sony pixel specification of 14 x 14 μm^2 with no manufacturer quote on the uncertainty in pixel size.

Sony has provided estimates of uncertainties for the placement of the first pixel in the array in the CCD package, but does not offer any estimate as to the uncertainty in the pixel array length or orientation. These uncertainties where estimated as the maximal deviation from Sony specifications found in the small set of CCDs studied. Systematic errors embedded in the ILX551A CCD packages have been studied on a small sample of unmounted CCDs. Direct measurements of the pixel array lengths on these samples revealed a maximum discrepancy of (50 ± 10) μm with the Sony specification [3.1]. All measurements of the array lengths yielded a result which was always greater than the Sony specified value.

Uncertainty occurring in the final active pixel position as the result of a misalignment of the pixel array within the CCD package has been determined to be less than 4 μm based on a measured 15 mrad deviation of the array with the package edge (maximum misorientation found in the small sample of measured CCDs) [3.1].

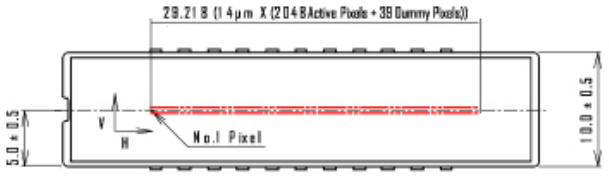

A. SONY ILX-551 CCD Manufacturing Specification

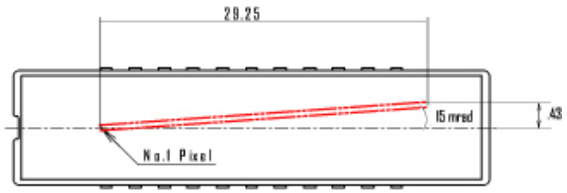

B. Measurement of Relavant CCD Parameters on Testbench

Figure 3.3: SONY ILX-551 CCD Specification and Direct Measurement (mm). The dimensional specifications and tolerances for the ILX-551 (A) quoted from Sony and the dimensions of a CCD taken from the small sample of studied ILX-551s (B) which exhibit the greatest deviation of the pixel array (in red) placement from the optimal location.

3.3.1.4 Uncertainty of CCD Package Orientation inside DCOPS Window Frame

Uncertainty occurring in the final active pixel position as the result of the misalignment of the CCD package, and thus the encased pixel array, scales as the cosine of misalignment. The present DCOPS window frame design incorporates a specially designed polycarbonate mount for the CCDs. Tolerances for the positioning of each end of the 53.71 mm long CCD mounts in the window frame is ±100 μm, contributing an error of less than 1 μm in the determination of the distance along the pixel array. Tolerances for the placement (orientation) of the CCDs within the polycarbonate mounts are estimated at >20 mrad, contributing a maximal uncertainty of less than 10 μm in the determination of the last active pixel in the array.

3.3.1.5 Final Estimation of Uncertainty in CCD Pixel - DCOPS Reference Pin Calibration

The final estimation of the uncertainty associated with the determination of the location of any given pixel in the DCOPS sensor relative to the CSC reference slot is taken to be the quadrature of all known errors in the determination of the first and last active pixel positions in the pixel array. In addition to the systematic errors associated with the placement of CCD arrays relative to the primary reference pin, the manner and stability in which the centroid of charge distributions are determined must be considered. It has been determined from the 2000 ISR Tests that centroids from successive measurements on the CCD are repeatable to ±14 μm. This uncertainty is characterized as the uncertainty associated with a particular measurement and considered separately in the COCOA simulation. The contributions and final estimate of the systematic uncertainty associated with the placement of pixels is given in Table 3.1.

Table 3.1: Contributions to Final Error in Determination of Pixel-to-CSC Reference Pin Calibration. Uncertainties due to misalignment and pixel array length are estimated as the worst case errors in the determination of the final active pixel position.

Uncertainty Origin	**Magnitude (μm)**
Direct Calibration of First Pixel (NEU Estimate)	40
Array Misalignment (inside package)	4
Array Length	50
Package Misalignment	10

3.3.2 CSC Active Center - DCOPS Reference Pin Calibration

As previously discussed, Cathode Strip Chambers are described in terms of their 'active center', which corresponds to the average of the individual panel active areas projected onto the plane of the first panel (See Appendix A for more detail on chamber definition). Determining the certainty with which this active center can be externally referenced is crucial to the successful simulation and reconstruction of the Endcap Muon System. Uncertainties in the determination of the relationship between CSC active cathode strips and DCOPS reference pins can be separated into uncertainties associated with individual panel definitions and manufacture, assembly of multiple panels to form the complete CSC chamber, the mounting assemblies which affix the DCOPS sensors to the surface of the assembled chamber, and deformations in the chamber after installation in CMS.

All estimations of uncertainties addressed here regarding CSC chamber and DCOPS mounting hardware tolerances are typically gathered from the specified tolerances placed on the fabrication of components. In most cases, particularly CSC panel definitions, adherence to these tolerances has been confirmed by direct measurement on an appropriate number of preproduction samples. However, there are many components which have not yet been produced on a large scale. Uncertainties for these components have been estimated from production drawings. A far more meaningful estimation of uncertainties for such components should be taken from the rms value of deviations found from a sufficient sample of the finished products.

In keeping with the convention established in Appendix A, the local chamber coordinate system is taken as right handed with the local Z axis running across the chamber centerline from the narrow end of the chamber to the wider end and the local Y axis running from the bottom layer to the top layer of cathode strips.

3.3.2.1 CSC Panel Definition

All cathode strip chambers are constructed of a polycarbonate honeycomb panels with 1.5 mm G-10 epoxy fiberglass skins coated with a 34 μm layer of copper. Individual panels are first drilled with two CSC Alignment Holes (where the CSC Alignment Pin will ultimately be inserted) along the centerline (See Figure 3.4). These two holes (±25 μm tolerance on the diameters) establish the reference system from which all other machining on the panel is established. A high precision router is then used to mill the cathode strips and associated artwork directly into the copper surface of the panel. Accuracy of the router has been confirmed by direct measurement. Errors in absolute strip position exhibit accumulative systematics over chamber width due to the manner in which they are milled. Quality control measurements on more than 300 panels have shown a σ(average active area) of 25 μm and rotational uncertainty of 7 μrad. However, measurements of the total active area across the widest end of these panels show a σ(width) of 40 μm whereas the same measurement across the narrow end of the panel reveals a σ(width) of 113 μm. Since the straightness strips have been measured as having a σ(rms) < 22 μm, the effect is likely due to the fact that the strips are milled into the panel in only one direction (from the wide end to narrow end).

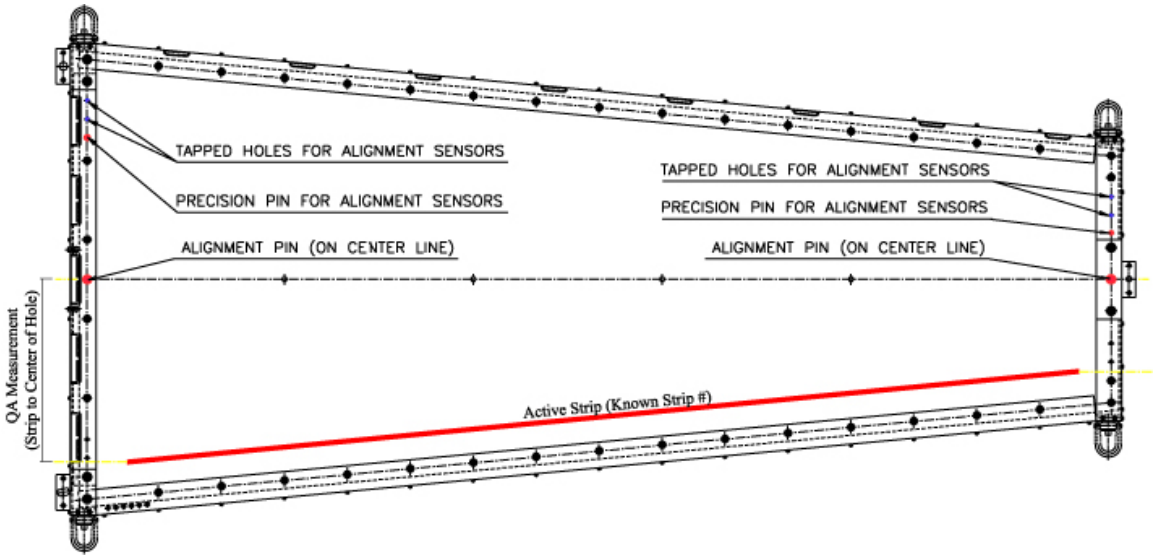

Figure 3.4**:** Placement of Pins, Holes, and Etchings on CSC Chamber [3.2].

Additionally, a series of ten slot cuts are placed on each panel for future calibration and quality control as well. The slot cuts are referenced directly to the center line defined by the two CSC Alignment Holes as well as a particular cathode strip number -- but not necessarily the first strip nor the same strip in all chambers. Each mark is referenced within ±25 μm to the center point of the CSC Alignment Holes and within ±25 μm to the particular strip being referenced (the "Reference Strip").

A series of secondary dowel pins and slots used to mount the DCOPS sensors to the chamber surface are also drilled at this time. On the wider end of the chamber, these holes position the precision pins and bolts used by the DCOPS mounting brackets to reference the CCDs directly to the cathode strips. On the narrow end, a series of holes for alignment pins are established which locate the plates for DCOPS mounting hardware to be glued to the panel surface. The locations of all holes are placed with a certainty of ±25 μm on the surface of each panel and have their diameters drilled to a certainty of ±25 μm.

3.3.2.2 Assembly of Final Chamber from Multiple Panels

Once all six panels are milled and prepared, they are layered to form the composite six layer CSC chamber. The precision with which each panel in the chamber is positioned with respect to neighboring panels can be estimated from the uncertainty with which the central CSC Alignment Holes are placed (±25 μm) and the tolerance placed on the diameter of the hole itself. Since the placement of all six layers are independent of each other, the maximal misalignment of any two given planes (two sets of holes, each with 25μm uncertainty in the diameter and relative location of their center points) is estimated to be ±50 μm. The uncertainty in the average center point across all six chamber planes is ±87 μm.

After the panels are stacked together, a frame is mounted to the edges of the chamber to add rigidity to the structure, protect connections, and form a Faraday shield around the electronics. Though the DCOPS mounting tower assemblies will mount on top of the frame structure, placement of the tower mounting hardware is completely determined by an alignment pin that sits in the previously drilled alignment holes. Since the CMS triggering requirements will accommodate relatively large uncertainties in the final determination of the chambers along the CMS Z coordinate, the placement of elements along the local Y axis of the chamber (CMS Z), including the frame, is not tightly controlled during manufacturing. The certainty with which the placement of the frame above the first strip plane will be known is estimated to be ±127 μm. The frame itself is estimated as being flat to ±25 μm whereas chamber flatness is estimated as no worse than ±200 μm across any 60 cm span. Tolerances on the panel thickness are asymmetric, +508 μm to -254 μm, and determined by the manner in which the panels are manufactured and cut.

3.3.2.3 Alignment Mounting Hardware

Mounting hardware to attach the DCOPS sensors to the chamber frames is similar across all chamber varieties. The mounting hardware consists of a series of spacers, shims, and mounting plates which secure the primary DCOPS mounting bar (where CCD-dowel calibration is done). CSC chambers in both inner and outer rings of ME ±2, ±3, and ±4 disks are placed into two layers. The chamber configuration for Trigger towers makes it necessary to mount hardware on the back layer for one outer CSC. Chambers on back layers will have mounting hardware called towers to give the attached DCOPS sensor an elevation in the SLM line which matches the front layer.

As previously noted, sensors affixed to the larger end of the chambers (+Z local end) are mounted directly to the chamber frame while sensors on the smaller end of the chamber (-Z local end) are attached to a special plate which is glued into position with the aid of a special pin and slot set during the fabrication of the chamber. The precision with which the inner plate can be glued to the surface of the chamber is determined from the tolerance with which the pin and slot are placed on the chamber surface (± 25 μm each) as well as the precision with which the receiving pin and slot are placed on the plate to be glued (± 25 μm each). Therefore, it is estimated that the DCOPS plates on the narrow end of the chamber can be glued in position within ±50 μm of the specified location - approximately the same tolerance with which they can be attached on the +Z local end to the chamber frame.

Although the heights of the towers on the back layers differ by 290 mm from the standard brackets, the plates and assemblies used are essentially the same. The mounting brackets are attached across two standoffs, each with an asymmetric tolerance of +.100 -0.000 mm. The standoffs locate a set of dowel pins on a stock Aluminum jig plate (± 125 μm thickness). The DCOPS mounting bar connects directly to this plate. Holes and pins used to secure the DCOPS are positioned and drilled to ±25μm, contributing an additional ±50 μm uncertainty in the referencing of the sensors to the strip positions.

The potential uncertainty in the orientation of the DCOPS sensors about the primary DCOPS dowel pin due to the uncertainty of the standoffs (separation of 88mm) is less than ±1μrad. Likewise, the uncertainties of the chamber frame positioning above the first panel on the chamber contribute an angular uncertainty about the same axis of less than ±1μrad as well. Rotational uncertainties about other axes are found to be only slightly larger, but can be safely neglected by COCOA as each CCD is one dimensional.

3.3.2.4 Deformation of Chambers and Chamber Components

One final consideration in defining the precision with which individual layers can be externally referenced is the deformation of the chambers when mounted in the detector. Since the CSC chambers are mounted vertically, the weight of the chambers creates a shearing effect across the six layers of the chamber. This effect is will be most prevalent when the shearing occurs perpendicular to the direction of the cathode strips. Thus, the effect is largest for chambers lying along the CMS X axis. The displacement of the individual layers due to the shearing force increases from the bottom layer (closest to the RF iron mounts) to the top layer. The maximal displacement of the uppermost layer has been directly measured as less than 25 μm.

3.3.2.5 Angular/Rotational Uncertainties

Components in COCOA are specified by their location and orientation making it necessary to estimate the rotational uncertainties with which the DCOPS sensors are placed on the chamber. Since the CCDs used in the DCOPS sensors are one dimensional pixel arrays, rotational uncertainties about the axis normal to the plane of the CCDs (DCOPS local Z axis) are the most important. Estimations of uncertainties about this axis, where it might be expected the slope and flatness of surfaces will contribute most, can also be estimated from the tolerance and separation on the mounting bracket standoffs, CSC panel/frame uncertainty (127μm), length (>>100cm), and flatness (±200

μm across 60 cm), and other tolerances placed on the components in the mounting bracket (Al plate, DCOPS window mounting bar - both ~25-50μm across ~90mm). The uncertainties about the DCOPS Z axis are summarized in Table 3.3.

Uncertainties about the DCOPS X and Y axis are determined from the uncertainties of the two precision pins or holes used to position components on the chamber and mounting brackets and the separation between them. In all cases, the uncertainties associated with the placement of pins and holes (~25-50μm) and the relatively large span of between them (~90mm) mean individual contributions to the rotational uncertainty in the orientation of the DCOPS sensors is on the order of 1 μrad. The uncertainties about the DCOPS X and Y axes are summarized in Table 3.2.

3.3.2.6 Final Estimation of DCOPS - CSC Active Center Uncertainties

The final uncertainty associated with the DCOPS reference pin - CSC active centers is determined from the quadrature of all estimated uncertainties in the plane of the strips (Table 3.3) and perpendicular to the plane of the strips (Table 3.2). The estimated rotational uncertainties about the DCOPS X, Y, and Z axes are summarized in Table 3.4 (DCOPS Z axis) and Table 3.5 (DCOPS X and Y axes). The rotational uncertainties have been estimated from the uncertainty and separation of the pins and/or holes which join components.

Table 3.2: Estimation of Error of DCOPS Positioning Above First Strip Layer (local Y axis). This table shows the uncertainties associated with the determination of the displacement between the DCOPS mounting plate and the first plane of cathode strips.

Uncertainty Origin	**Magnitude (μm)**
Panel Thickness (Maximal deviation)	508
Frame to Panel Placement	127
Mounting Bracket Chamber-Shim Standoff	100
Mounting Bracket Al. Plate	125
Final Estimation of Uncertainty in Y Plane of Chamber	**548 μm**

Table 3.3: Estimation of Error Transverse to CSC Chamber Centerline. This table shows the uncertainties associated with the determination of the displacement between the DCOPS alignment pin and the cathode strips transverse to the chamber centerline (local chamber X axis).

Uncertainty Origin	**Magnitude (μm)**
Central Alignment Pin - Notched Alignment Marks	25
Notched Alignment Mark - Numbered Reference Strip	25
Intrinsic Strip Positioning (from milling)	30
Averaged Centerline Across 6 Assembled Planes	87
Positioning of Primary DCOPS Alignment Pins/Holes	25
Diameter of Primary DCOPS Alignment Pins/Holes	25
Placement of Mounting Plate On Chamber	50
Placement of DCOPS Mounting Plate	50
Maximal Shearing Effect	25
Final Estimation of Uncertainty Along X Axis of Chamber	**129 μm**

Table 3.4: Estimation of Error of DCOPS Orientation About DCOPS CCD Plane Normal (local DCOPS Z axis). This table shows the uncertainties associated with the determination of the orientation between the DCOPS CCDs and the first plane of cathode strips. Most uncertainties were less than 1 μrad and have been rounded up.

Uncertainty Origin	**Magnitude (μrad)**
Upper Cathode Panel - Frame Relationship	1
Frame (or Fwd Glue Plate) - DCOPS Mounting Bracket Base	1
DCOPS Mounting Bracket Base - Mounting Bracket Shim Plate	1
Mounting Bracket Shim Plate - DCOPS Mount Bar	1
Straightness of DCOPS Mount Bar - DCOPS Window Frame	1
Total Uncertainty in DCOPS Orientation on Chamber	**2.2 μrad**

Table 3.5: Estimation of Error of DCOPS Orientation of DCOPS CCD Plane (local DCOPS X/Y axis). This table shows the uncertainties associated with the determination of the orientation between the DCOPS CCDs and the first plane of cathode strips. Most uncertainties were less than 1 μrad and have been rounded up.

Uncertainty Origin	**Magnitude (μrad)**
Upper Cathode Panel Pins/Holes	1
DCOPS Mounting Bracket Base	1
Mounting Bracket Shim Plate	1
DCOPS Mount Bar	1
Total Uncertainty in DCOPS Orientation on Chamber	**2 μrad**

3.3.3 Estimation of Other Simulation Parameters and Uncertainties

The complete simulation of the EMU alignment scheme includes several components in the Link Alignments system. Link components found in the COCOA EMU simulations include the MABs, Secondary Link lines, and the ME ±1/2 'ALMY' sensors. The uncertainties in the construction and/or performance of these components have been taken from a COCOA simulation of a quarter Link plane [3.3] and discussions [3.4] with the Link Alignment group. A summary of the uncertainties assigned to these components in the simulation is given in Table 3.6.

Table 3.6: Estimation of LINK System Uncertainties. This table shows the estimated uncertainties associated with components in the Link Alignment System included in the EMU Idealized COCOA Simulation

Uncertainty Origin	**Magnitude**
LINK Reconstructed MAB Position	135 μm
LINK Reconstructed MAB Orientation	10 μrad
DCOPS Location within MAB	50 μm
DCOPS Orientation within MAB	2 μrad
Definition of Secondary Link Line	10 μm, 2 μrad
ME ±1/2 ALMY Sensor Resolution	5 μm

3.4 Simulation Results (Idealized EMU System)

The primary goal of the COCOA simulation of the EMU alignment scheme is to obtain an estimate of the uncertainties associated with the reconstruction of CSC chamber positions along the SLM laser lines and an understanding of the relationships and correlations between the various components of the alignment system. For simplicity, most studies and simulations were done with the idealized EMU. The idealized EMU system contains all the EMU system components arranged in the manner detailed in Appendix A with uncertainties on the location and placement of the components set to the estimations previously discussed. Since the system is ideal, it is assumed that all measurement devices are able to make a successful measurement and the full redundancy of the alignment scheme (multiple measurements of opposing lasers) is exploited. The effects of component failure (missing CCDs measurements from DCOPS, faulty laser modules, inadequate resolutions) are examined separately.

The layout of CSC chambers, transfer plates, and SLM lines exhibit a high degree of symmetry between ME layers on YE Iron discs. The symmetry of most components is reflective between discs, which is to say chambers on ME+2 appear mirror symmetric to chambers on ME-2. This is not generally true for DCOPS sensors located on the transfer plates. The placement of DCOPS sensors into the transfer plate design for each ME disc was based on the ensuring that the pointing (i.e. the normal to the CCD plane) of the DCOPS sensors was consistent for all layers, the orientations of otherwise symmetric DCOPS sensors were rotated 180º about the local Y axis of the calibrated dowel pin. This effectively changes the distance between several of the transfer plate SLM DCOPS dowel pins and transfer plate Transfer Line DCOPS dowel pins. Additionally, the transfer plates located at Point 5 on the ME layers must be elongated to avoid possible conflict with the YE Iron supports. The extension of the distance between the calibrated dowel pins results in a leveraging of the uncertainties in the definition of the SLM laser and, ultimately, slight discrepancies in the spatial uncertainties between otherwise symmetric CSC chambers. This effect is seen across all eight ME discs. For this reason, simulation

results presented here will deal with the average of all SLM chamber uncertainties for a particular coordinate in a chamber ring, or the specification of a small range of chamber uncertainties for a set of objects or chambers in a single ME disc.

The software was also found to put an enormous drain on the available computer memory. The full EMU simulation of ME ±1, ±2, ±3 and ±4 Endcap Alignment System contained approximately 6200 separate objects to fit with at least 4700 non-zero correlations and was simply too large for the software to compute without exhausting its memory allocation. Though a memory leak was identified (but could not be traced) when running the code, the sheer number of parameters to compute requires a large amount of memory. Since each element in the matrix requires eight bytes of memory (double precision) and there are at least 9,000,000 elements in each matrix (≈ 6000 x 1500) for the full simulation, at least 72 MB of memory are required for each matrix constructed. As Section 2.1 indicates, at least seven unique matrices are required for a COCOA fit (> .5 GB). However since the fitting process requires an iterative update of matrices, the actual amount of memory required for a complete COCOA simulation of the EMU System can quickly exceed 1 GB of memory after several iterations. It was found that the largest simulation which could be successfully fit with the available computing resources (1 GB of memory) contained the ME ±2, ±3, and ±4 layer alignment systems.

3.4.1 Comparison of Large Simulations vs. Small Simulations

Using the full COCOA simulation model, several attempts were made to obtain a fit of the complete 8 ME disc system. These attempts failed with the computers reporting abnormal utilization and allocation of memory. Indeed, when the memory usage of the system was examined, it was found that a serious memory leak was present. The memory leak was not so serious as to preclude the fitting of smaller subsets of the full EMU simulation model. The largest simulation successfully fit consisted of the ME ±2, ±3, ±4 discs and transfer line system. Fifty-three smaller subsets of the ME ±2, ±3, ±4 discs and transfer line simulation were also completed and compared amongst themselves and the

larger 6 ME disc simulations. These subsets included all possible permutations of systems composed of at least two ME discs with full transfer line systems (i.e. all simulations had the same number of transfer plates in the system).

Comparisons made between systems within the 53 subsets of two ME disc systems showed very little variation (< 10%) between the certainties with which identical chambers could be reconstructed. Comparisons made between these two ME disc systems and the larger six ME disc system also yielded very little variation (< 5%) between the certainty with which identical chambers could be reconstructed. This seems to confirm that there is very little coupling of components across different ME discs.

3.4.2 Simulation of the Idealized System

The uncertainty in location for CSC chambers located along a particular SLM line may vary from the uncertainty of similar chambers located in other SLM lines. The discrepancies between chamber uncertainties in ME discs with a similar SLM arrangement of components is expected to be small (<10μm). For chambers in the same Endcap layer, this is primarily due to variations in the separation (i.e. lever arm) between transfer line and reference sensors placed on transfer plates located at the SLM endpoints. Chambers located on different ME discs are affected by the manner in which the SLM laser line crosses the chamber and/or the compounding of errors to inner ME chambers. Since SLM lines on ME ±1 discs are constructed in a very different manner from those on SLM ME ±2, ±3, and ±4 discs, more substantial variations are expected between chamber uncertainties when comparisons are made to ME ±1 chambers. The mean uncertainty with which chamber locations and orientations along the SLM lines can be reconstructed in the EMU alignment scheme is summarized in Table 3.7 and Table 3.8. The average deviations presented alongside the estimates represent the average deviation from the mean uncertainty determined for the all chambers located along a particular ME ring.

Table 3.7: Uncertainty in CSC locations along the SLM lines for the Idealized EMU System. The uncertainty estimates for chambers in ME ±1/2 layer have been done using two sets of resolutions for the inclinometers placed on the ME ±1/2 CSC chamber frames

CSC Chamber	**Mean Uncertainty in Chamber Locations**		**Average Deviation of Uncertainty**	
	CMS RΦ (μm)	**CMS Z (μm)**	**CMS RΦ (μm)**	**CMS Z (μm)**
ME±1/2 (no inclinometer)	515	717	17	9
ME±1/2 (σ inclinometer = short term ISR σ)	90	385	2	5
ME±1/2 (σ inclinometer = long term ISR σ)	187	415	2	1
ME±1/3	216	878	3	22
ME±2/1	205	467	10	12
ME±2/2	221	509	7	24
ME±3/1	230	491	14	15
ME±3/2	248	520	20	22
ME±4/1	241	525	14	17
ME±4/2	259	524	20	17

Table 3.8: Uncertainty in CSC Orientations About Axes Parallel to CMS Coordinate System and Through CSC Chamber Center Idealized EMU System. The uncertainty estimates for chambers in ME ±1/2 layer have been done using two sets of resolutions for the inclinometers placed on the ME ±1/2 CSC chamber frames.

CSC Chamber	**Mean Uncertainty in Chamber Orientation**		**Average Deviation of Uncertainty**	
	CMS RΦ (μrad)	**CMS Z (μrad)**	**CMS RΦ (μrad)**	**CMS Z (μrad)**
ME±1/2 (inclinometer short term ISR σ)	95	95	N/A	N/A
ME±1/2 (inclinometer long term ISR σ)	698	698	N/A	N/A
ME±1/3	138	1168	3	360
ME±2/1	113	812	0	252
ME±2/2	74	771	0	297
ME±3/1	834	888	244	261
ME±3/2	742	777	303	323
ME±4/1	725	909	383	241
ME±4/2	1105	839	126	315

In addition to variations in chamber reconstruction uncertainties between different SLM lines and ME discs, chamber reconstruction uncertainties within a particular SLM line may vary. This is expected since the spacing of DCOPS sensors is not the same for chambers on the inner and outer rings of the discs. Chambers of the same type and on the same SLM line are expected to have similar uncertainties.

The original ME ±1 alignment scheme did not incorporate inclinometers on ME ±1/2 chambers. It had been assumed that the ME ±1/3 SLM lines, having been offset from the Secondary Link laser lines, would provide sufficient angular definition about the local chamber Z axis for the ME ±1/2 chambers (sensors on these chambers cannot discern rotations about the laser lines). Simulations of the ME ±1 layer (results shown in Table 3.9 and Table 3.10without inclinometers revealed poor spatial and rotational resolution on all ME ±1 chambers and did not meet the estimated system performance. For this reason, inclinometers similar to those employed on the transfer plates were incorporated into the ME ±1/2 chamber frames. Simulations of the idealized system are performed with the resolution of these inclinometers set to be equivalent to the long term resolution of the inclinometers studied during the 2000 ISR tests.

Table 3.9: Uncertainty in ME ±1 CSC locations along the SLM lines for the Idealized EMU System without ME ±1/2 Inclinometers. The uncertainty estimates where prepared in an Idealized EMU ME±1 simulation.

CSC Chamber	**Mean Uncertainty in Chamber Locations**		**Average Deviation of Uncertainty**	
	CMS RΦ (μm)	**CMS Z (μm)**	**CMS RΦ (μm)**	**CMS Z (μm)**
ME±1/2 (no inclinometer)	515	717	17	9
ME±1/3 (no inclinometer)	291	965	5	111

Table 3.10: Uncertainty of ME ±1 CSC Orientations About Axes Parallel to CMS Coordinate System and Through CSC Chamber Center for Idealized EMU System without ME ±1/2 Inclinometers. The uncertainty estimates where prepared in an Idealized EMU ME±1 simulation.

CSC Chamber	**Mean Uncertainty in Chamber Orientation**		**Average Deviation of Uncertainty**	
	CMS RΦ (μrad)	**CMS Z (μrad)**	**CMS RΦ (μrad)**	**CMS Z (μrad)**
ME±1/2 (no inclinometer)	1517	1521	553	538
ME±1/3 (no inclinometer)	1331	1333	425	460

3.4.3 Relationships and Correlations Between EMU Components

Since COCOA calculations are based on variance-covariance matrix operations, the final matrix returned from the fitting process contains additional information concerning the relationship between reconstructed quantities in the simulated system. However, relationships between most components must be inferred by a series of simulations, with small variations in each simulation.

A large number of such simulations were conducted to explore the relationship between the largest sources of uncertainties within the EMU alignment scheme and several key components of the system. In general (details to follow), the uncertainties ascribed to system components in Section 3.3.2.6 were varied in a systematic manner to gauge their impact on the determination of CSC chamber positions. This information is particularly important during the design and pre-production stages of the EMU project, as the cost of manufacturing and materials is highly dependent upon the tolerances placed on the components and equipment being employed. It is also instrumental in validating the operational viability of the EMU alignment scheme. Since the EMU Alignment scheme will be staged with an initial deployment of ME ±1 and ME ±2 layer systems, the focus of these studies has been directed toward these ME layers.

3.4.3.1 Correlations Between 'Unknown' Quantities

The correlations between unknown entries in the simulation are given by the off-diagonal elements of the variance-covariance matrix returned by the COCOA fit. CSC chambers in the simulation typically showed hundreds of correlations with other components, however only a few correlations exceed .01 (1%). A typical sample of the most significant correlations between the five unknown chamber parameters (2 spatial, 3 rotational) and other unknown simulation parameters is shown in Table 3.11. The correlations given in Table 3.11 are representative of most CSC chambers in the simulation: the most significant correlations between unknown parameters were generally confined within SLM lines and connecting transfer lines.

Looking at a sample of the correlations between various transfer plates in Table 3.12, it is evident most correlations are less than 15%. The largest correlations exist between transfer plates located along the same Transfer laser line (see Appendix A, Section 5.2.6, for labeling scheme). The coupling of individual Transfer Laser Lines across SLM lines (i.e. opposing Transfer Lines) was expected to be weak since the transfer line MAB reference points are relatively well known and the six indirect interactions between the three pairs of opposing Transfer Laser Lines are connected only by initially undefined SLM laser lines. Since correlations between transfer plates are weak, and correlations between transfer plates and chamber along the same SLM lines are always less than 1, correlations between CSC chambers which do not fall along the same SLM laser lines are weak (< 5%).

Table 3.11: Sample Correlations between Reconstructed Entries for CSC Chamber ME–22_15 (SLM-23). The correlation between entries shown in the table is taken directly from the off-diagonal matrix elements of the variance-covariance matrix used in the COCOA fit. This sample (it is not complete) of entries represents the largest correlations found for this chamber and was prepared from an ME ±1 and ME ±2 simulation. Entries are taken to be in the local coordinate system of the objects they describe (Appendix A).

ME-22_15 Parameter	**Dependent Object**	**Correlation**
Centre_Y	slm-23/me-22_32_angles_Z	0.143
Centre_Y	slm-23/me-21_8_centre_Y	0.136
Centre_Y	transfer1_angles_X	0.081
Centre_Y	slm-23/me-21_8_centre_Y	0.059
Centre_Z	slm-23/me-22_15_angles_X	0.769
Centre_Z	transfer1_angles_Z	0.326
Centre_Z	slm-23/me-21_8_angles_X	0.326
Centre_Z	slm-23/me-22_32_angles_Y	0.294
Centre_Z	slm-23/me-22_15_angles_Z	0.273
Centre_Z	transfer-1_angles_X	0.017
Angles_X	transfer-1_angles_X	0.457
Angles_X	slm-23/me-22_32_angles_Y	0.279
Angles_X	transfer1_angles_Z	0.265
Angles_X	slm-23/me-21_8_angles_X	0.265
Angles_X	slm-23/me-22_15_angles_Z	0.187
Angles_Y	transfer-1_centre_Y	0.651
Angles_Y	transfer1_angles_Z	0.183
Angles_Y	transfer1_angles_X	0.183
Angles_Y	transfer-1_angles_Y	0.040
Angles_Z	slm-23/me-21_8_centre_Y	0.618
Angles_Z	slm-23/me-22_32_angles_Y	0.177
Angles_Z	slm-23/me-21_8_angles_X	0.111
Angles_Z	transfer1_angles_Z	0.111
Angles_Z	transfer-1_angles_X	0.017

Table 3.12: Sample Correlations between Reconstructed Entries for Transfer Plate. The correlation between entries shown in the table is taken directly from the off-diagonal matrix elements of the variance-covariance matrix used in the COCOA fit. This sample (it is not complete) of entries represents the several non-zero correlations found between transfer plates in an ME ±2, ±3, ±4 simulation. Transfer plates labeling has all objects designated as 'transfer_plateAB', where two plates with the same value of 'B' lay on the same Transfer laser line (see Appendix A, Section 5.2.6)

Object 1	**Object 2**	**Correlation**
transfer_plate21_centre_X	transfer_plate24_centre_Z	0.03
transfer_plate-21_centre_X	transfer_plate-31_centre_X	0.10
transfer_plate-21_centre_Z	transfer_plate-31_centre_Z	0.10
transfer_plate24_centre_Z	transfer_plate26_centre_Y	0.02
transfer_plate24_centre_Z	transfer_plate34_centre_Z	0.14
transfer_plate24_centre_Z	transfer_plate36_centre_Z	0.03
transfer_plate22_centre_Z	transfer_plate32_centre_Z	0.14
transfer_plate26_centre_Y	transfer_plate36_centre_Z	0.09
transfer_plate34_centre_Z	transfer_plate36_centre_Z	0.08
transfer_plate-32_centre_X	transfer_plate-42_centre_X	0.02
transfer_plate44_centre_X	transfer_plate-31_centre_Z	0.01
transfer_plate44_centre_X	transfer_plate-21_centre_Z	0.01

3.4.3.2 Correlations Between 'Known' and 'Unknown' Quantities

Correlations between the uncertainties in the construction of components within the simulation and the certainty with which chambers can be reconstructed provides valuable information for the design of these components being studied. The goal of exploring the relationships between the design of EMU components and the performance of the system is to maximize system performance while minimizing costs. Particular attention was paid to chambers in the ME ±1 and ±2 layers, as muons traversing these layers experience a much greater magnetic field, and thus a larger sagita, than in the ME ±3 and ±4 layers.

In general, these studies examined the dependence of chamber spatial CMS RPhi uncertainties versus the resolution or tolerances of a particular component. Simulations were done with two opposing ME layers (i.e. ME ±1 or ±2), a full Transfer Line system,

inclusion of inclinometers on ME ±1/2 (resolutions set at long term ISR values), and in a manner otherwise consistent with the simulations used to produce Table 3.7 and Table 3.8 unless specified.

3.4.3.3 LINK Interface to EMU Alignment System

The interface of the EMU alignment scheme to the Link alignment scheme provides Tracker coordinate information to the MABs and Secondary Link lines. The certainty with which MAB and Secondary Link lines are defined directly impacts the precision with which chambers centers can be reconstructed. Uncertainties in the Link interface fall into three categories: uncertainties in the construction of the MABs, uncertainty in the definition of the Secondary Link lines, and uncertainties in the rhomboid prism which split the Primary and Secondary Link Lines. Uncertainties in the rhomboid prism can also be regarded as any other potential uncertainty which propagate to both the MABs and Secondary Link lines.

The estimated uncertainty in MABs position and orientation is given in Section 3.3.3. This estimated includes allowances for distortions in the MAB as well as the placement of a DCOPS sensors within the structure. Figure 3.5 shows how the uncertainty in reconstructed CMS RPhi chamber positions in ME ±1 and ±2 varies as a function of the uncertainty on the MABs.

Since ME ±1 chambers are reconstructed in part by the Secondary Link line, the dependence on Transfer Laser lines (and thus the MABs) is relatively weak. This is particularly true for the ME ±1/2 chambers, where there is no dependence on the MABs for spatial reconstruction in CMS RPhi. The short lever arm between the ME ±1 (outer) Transfer Plates and placement of the ME ±1/3 SLM reference sensor on the ME ±1/2 chamber frame dampens the interaction between the MABs and ME ±1/3 chamber reconstruction as well.

ME ±2 chambers (as well as ME ±3 and ME ±4 chambers) must be reconstructed solely from the MABs. As a result, a strong coupling between the uncertainties on the MABs and reconstructed chamber locations is seen.

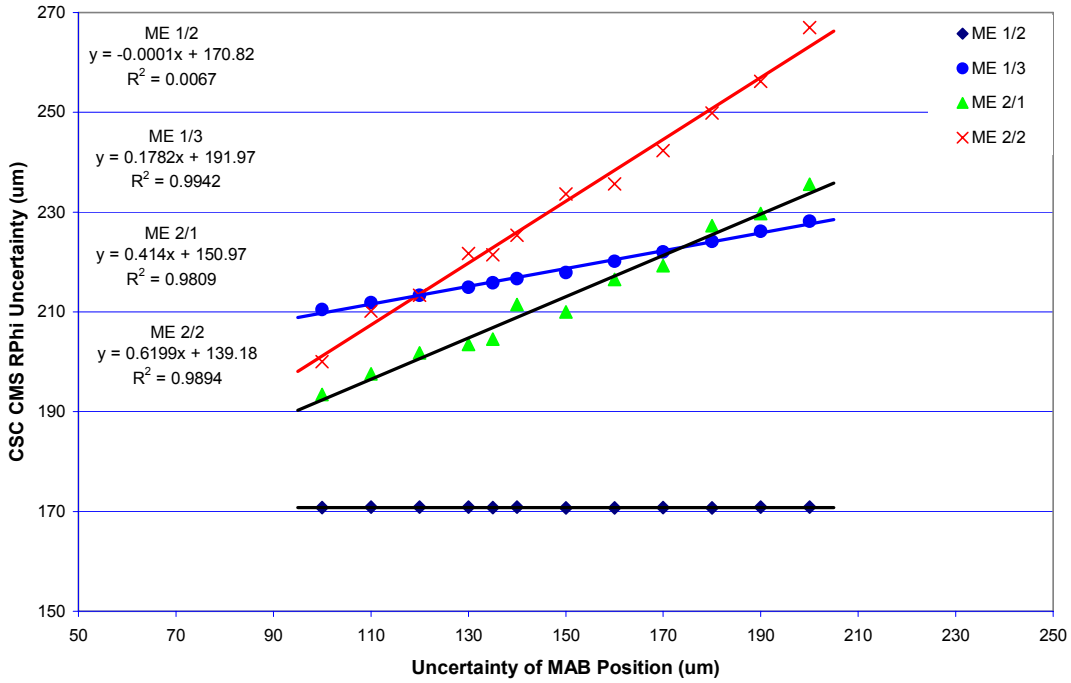

Figure 3.5: Reconstructed CSC RPhi Chamber Uncertainty vs. Tolerance on MAB Position. The plot shows the average uncertainty in reconstructed chamber locations as a function of the uncertainty estimate on the determination of the placement of the MABs within CMS.

The correlation between ME ±1 chambers and the Secondary Link lines is likely to be strong for ME ±1/2 chambers, but weaker for ME ±1/3 chambers, as the ME ±1/3 chambers reconstruction relies strongly on MABs. Figure 3.6 shows the uncertainty of reconstructed RPhi chamber location in ME ±1 as a function of Secondary Link line definition. As expected ME ±1/3 chambers show very little change as the Secondary Link line resolution is varied. Surprisingly, the coupling of the Secondary Link line resolution and the ME ±1/2 chambers is non-linear. This is most likely due to either the dominance of other errors in the reconstruction of ME ±1/2 chambers when the

Secondary Link line is well defined, or an indication that ME ±1 SLM reconstruction is more complicated than previously thought.

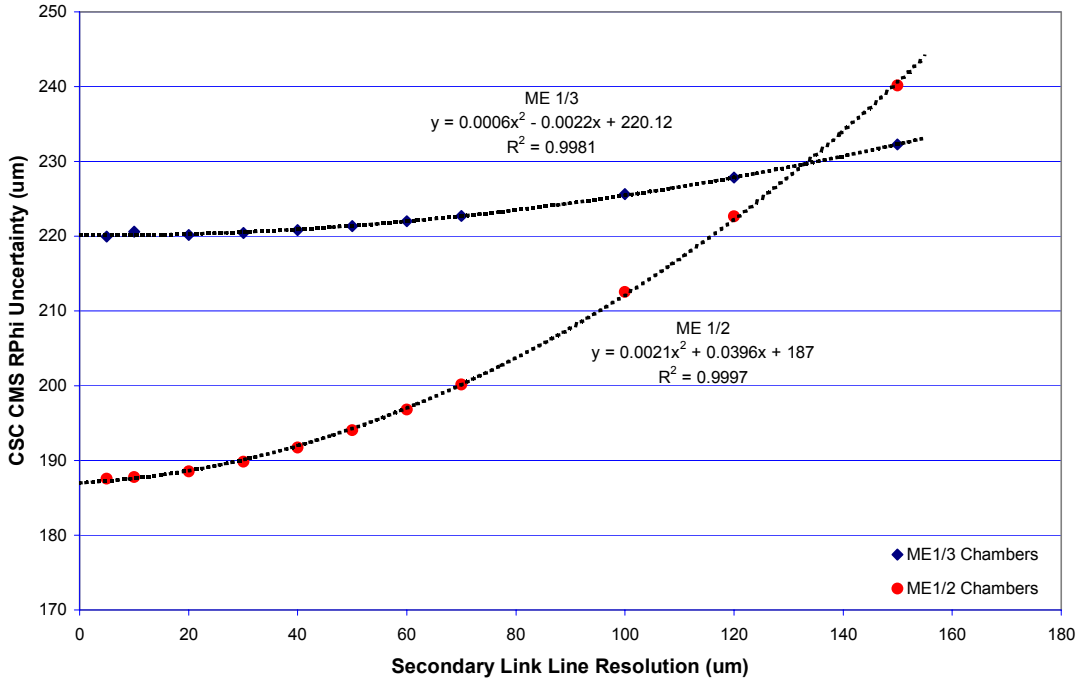

Figure 3.6: Reconstructed CSC RPhi Chamber Uncertainty vs. Secondary Link Line Resolution. The plot shows the average uncertainty in reconstructed chamber locations as a function of the uncertainty estimate on the placement of the Secondary Link Line.

3.4.3.4 DCOPS-Reference Center Tolerance

Figure 3.7 shows how the uncertainty in the CMS RPhi position of the CSC chambers vary with the uncertainty in the chamber construction (along the chamber's local X axis). For all chambers, this relationship is linear. The slope indicates the correlation between uncertainties in chamber construction and reconstructed chamber RPhi positions is roughly 1:3, except on the ME ±1/2 chambers where it is closer to 1:4. The significantly higher correlation on the ME ±1/2 chambers is due the much lower uncertainties associated with the definition of the Secondary Link lines and resolution of the ME ±1/2

LINK CMOS sensors. Correlations decrease slightly for chambers located in ME layers further away from the MABs as the net uncertainty is generally larger (See Figure 3.5).

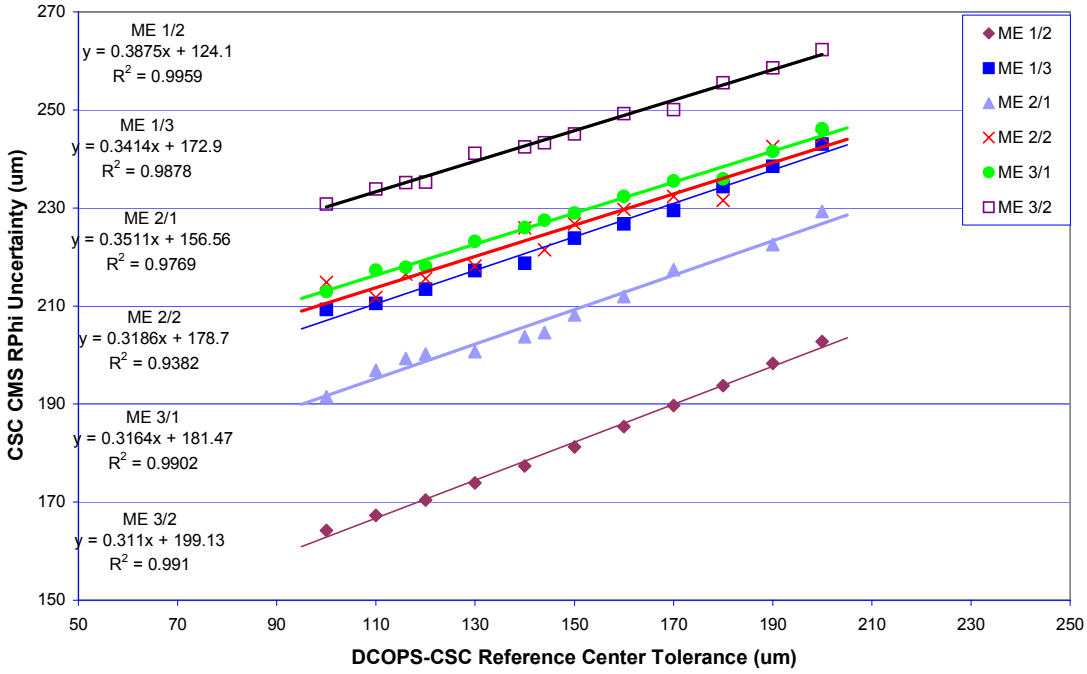

Figure 3.7: Reconstructed CSC RPhi Chamber Uncertainty vs. DCOPS-CSC Reference Center Tolerance. The plot shows the average uncertainty in reconstructed chamber locations as a function of the uncertainty estimate on the relative placement of the primary DCOPS calibration pin with the chamber reference centerpoint.

3.4.3.5 DCOPS Pixel Resolution

DCOPS sensors make measurements by fitting the charge distribution across the CCD pixel arrays. Each pixel in the array is approximately 14 μm wide. The resolution of the DCOPS sensors is in large part determined by the quality of the fit and the shape of the distribution to be fit. Typical short term fluctuations in the fitted centroids during the 2001 ISR tests suggested that the short term resolution of the DCOPS sensors in the ISR tunnel to be on the order of 1 pixel, however it is certainly possible that the conditions in the CMS detector will decrease the stability of these measurements. Figure 3.8 shows the uncertainty in the reconstructed chamber RPhi locations as a function of DCOPS pixel

resolution. As the figure indicates, an uncertainty of up to three pixels in the location of the centroids still provides a resolution of better than 250 μm on the reconstruction (in CMS RPhi) of chamber centers. The independence of ME ±1/2 chambers in Figure 3.8 is expected since the measurement devices are not DCOPS sensors (thus no CCD pixel resolutions to degrade). The uncertainties in ME ±1/2 chamber locations are plotted to illustrate the independence of these chambers to degraded measurements in ME ±1/3 chambers positions.

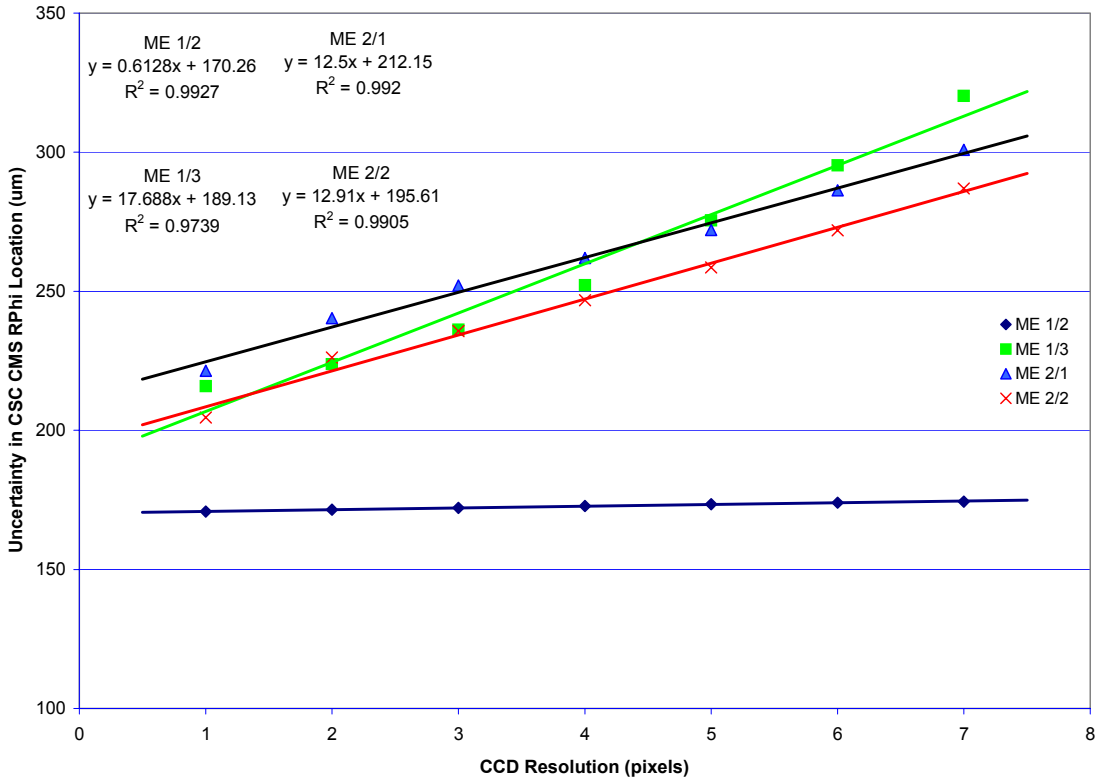

Figure 3.8: Reconstructed CSC RPhi Chamber Uncertainty vs. DCOPS Pixel Resolution. The plot shows the average uncertainty in reconstructed chamber locations as a function of DCOPS pixel resolution. One pixel is 14 μm wide. ME ±1/2 chamber sensors are not DCOPS sensors and have not been varied.

3.4.3.6 ME ±1/2 Inclinometer Resolution

Although it was quickly established that the inclusion of inclinometers were required on ME ±1/2 chamber frames, it was unclear if the use of the same inclinometers on the transfer plates would provide sufficient resolution (as well as a sufficient margin of safety) to successfully reconstruct chamber locations. A series of simulations was performed to investigate the dependence of ME±1 chamber reconstruction on inclinometer resolution. Figure 3.9 shows the dependence of the uncertainty in the determination of reconstructed CMS RPhi ME ±1chamber positions as a function of ME ±1/2 inclinometer resolution. The uncertainty in the ME ±1/2 chamber RPhi location is seen to approximately double in a linear as the fashion inclinometer resolution is varied from its nominal short term resolution to the long term resolution. ME ±1/3 RPhi chamber resolution remains roughly independent of the inclinometer resolution, though, as Table 3.7-Table 3.10 indicate, there are other chamber parameters which depend upon the resolution of the inclinometers.

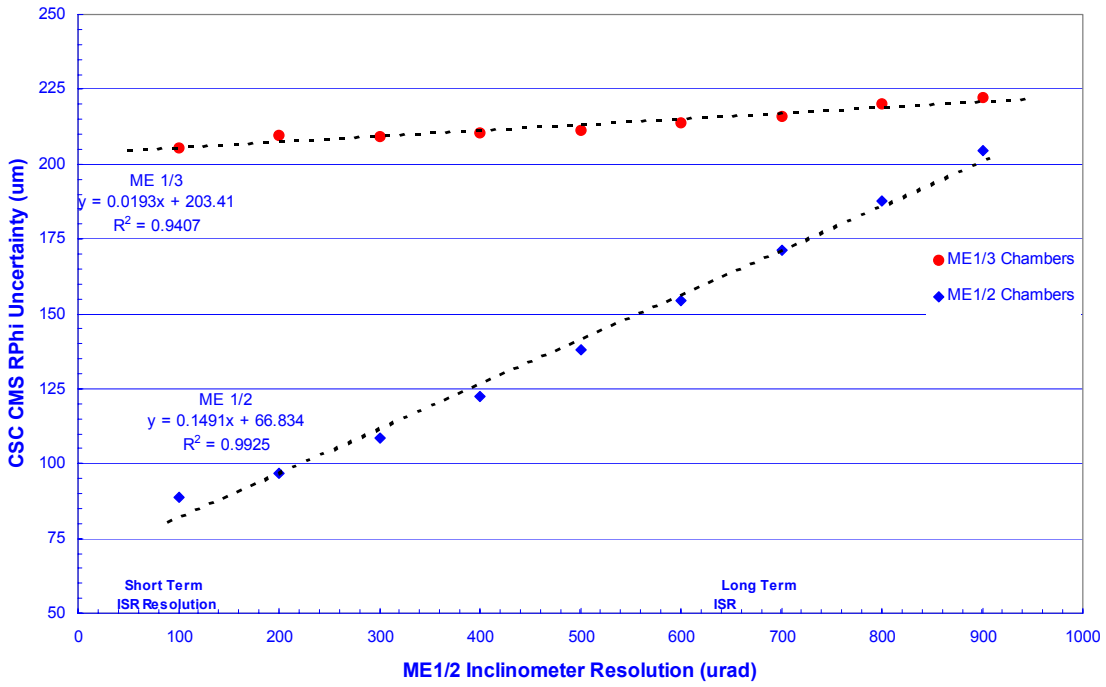

Figure 3.9 ME±1 CSC Chamber Resolution vs ME±1/2 Inclinometer Resolution.

The determination of the ISR inclinometer resolutions used in the simulation is based upon the results of the extended, uncorrelated, and uncorrected measurements over the approximately three months of testing during the 2000 ISR Tests. It is likely that further work with these inclinometers will increase the precision of these measurements.

3.5 Conclusions

The results garnered from COCOA simulations of the Idealized EMU System indicate that the design of the EMU Alignment scheme is viable and can reconstruct chamber locations along SLM lines with an uncertainty of ≈200μm in CMS RΦ and ≈500μm in CMS Z. A detailed error analysis and subsequent examination of key sources of uncertainties across several simulations show that the tolerances on component construction and DCOPS calibration are well understood and meet the necessary requirements to ensure the successful reconstruction of chamber positions.

Although the simulation assumes the entire system operates perfectly (unlikely for any complex system), in many cases the estimations of uncertainties and tolerances in components modeled in the simulation have been very conservative (symmetrizing asymmetric tolerances, assuming little or no additional calibration on CSC chambers, taking long term uncorrelated resolutions of ISR sensors). It is also likely that several sets of measurements could be simultaneously fit in the COCOA simulation to compensate for failed or damaged components. More importantly, the additional knowledge about components in the system acquired over the next 3-5 years prior to the commissioning of the CMS detector is likely to further constrain the fits made by COCOA and further minimize the uncertainties associated with the reconstruction of SLM sensors and CSC chambers.

4 PHYSICS PERFORMANCE OF THE CMS ENDCAP MUON DETECTOR

The quality of muon track reconstruction in the CMS Endcap Muon System is dependent upon a multitude factors. The final determination of track parameters will be made with measurements affected by both physical and mechanical uncertainties. Though many of these uncertainties have been previously examined to some degree, the recent implementation of the CMS Object Oriented Reconstruction and Analysis (ORCA) software analysis tools offer the opportunity to reexamine these uncertainties in greater detail with updated, more realistic geometry. With modifications to ORCA version 5.3.1, a detailed simulation study has been conducted on the Endcap Muon System to evaluate the impact of CSC chamber misalignment by direct manipulation of the simulation geometry. A brief outline of the relevant physical and mechanical considerations which must be considered when reconstructing muon momenta in the Endcap is provided as well as a summarization of previous simulation results. Results from a simulation study examining the intrinsic performance of the Endcap System in ORCA are discussed.

4.1 Overview of Measurement of Momenta in the CMS Endcap

In general, the measurement of momenta in a uniform magnetic field for a charged particle is done by measuring the bending of the particle trajectory (sagita) in the plane transverse to the magnetic field. From the sagita measurement the transverse momenta for the incident particle can be determined:

$$s[m] \approx \frac{d^2}{8}\frac{1}{R[m]} = \frac{d^2}{8}\left(\frac{.3B[T]}{p_t[GeV/c]}\right)$$ Equation 4.1

Where s = sagita
$1/R$ = radius of curvature of muon path
d = distance the muon has transverse in the magnetic field
B = magnetic field perpendicular to trajectory
p_t = transverse momenta of charged particle

In the CMS Endcap Muon System, such measurements are complicated by large magnetic field gradients and copious amounts of shielding between each point of measurement. Furthermore, the magnetic field in the Endcap region is a non-uniform fringe field. This field causes incident muons to bend along not just one radius of curvature, but two or more. The resulting muon trajectories and large magnetic gradients mean that muon tracks in the Endcap will have varying radii (Figure 4.1) and must by fit in a considerably more complicated fashion than Equation 4.1 suggests.

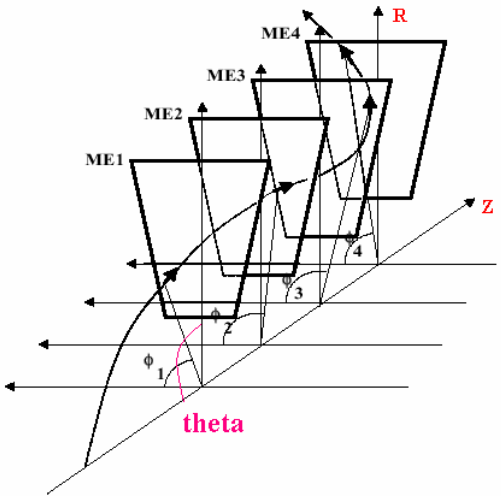

Figure 4.1: Trajectory of a Muon Traversing the CMS Endcap Region [4.1].

4.1.1 Overview of Muon Track Formation

As muons enter the volume of the CSC chambers, electrons from the gas mixture filling the chambers are ejected and form hits on the six cathode strip and anode wire planes. Collections of hits across the cathode and anode planes are grouped into Cathode Local Charge Tracks (CLCT) and Anode Local Charge Tracks (ALCT). The group of hits which form the CLCT and ALCT are then compared against a predefined set of hit patterns. Patterns can be matched for hits across as few as three anode and cathode planes and have 99% efficiency when matched across four or more planes. If the hits contained by the CLCT are found to match one of the predefined hits patterns, the CLCT is validated and combined with information in the ALCT to form a Track Segment. Two or more track segments may then be used to create a Track candidate and define a localized sagita value. Sagita values are then compared against tabulated values of $\int B \cdot dl$ for the position of the hit pattern, from which values of p_t can be immediately estimated.

Once localized cathode LCT hit patterns have been resolved and p_t estimations of Track candidates have been made, the next step is to collect the hit patterns and estimate the original muon track parameters. This requires a filter to separate false hit patterns (from bremsstrahlung, high energy electrons, etc.) from true muon hit patterns as well as reconstruct the track parameters. The Kalman Filter [4.2] accomplishes both of these tasks. The Kalman Filter is an iterative fitting process that estimates track parameters at each measurement point while recursively updating previous estimates along the way. New track segments (at measurement points for which the Kalman Filter has not yet arrived) are incorporated into the fit only if their positions fall within the extrapolation of previous measurements.

Once the fitting process has completed, a smoothing algorithm is applied to improve convergence and remove background hits. The Kalman Filter also applies a vertex constraint as well as matching against track segments found in the Tracker. The final fit provides three different estimations of the track parameters which are based on: only the

Muon System, the Muon System + a vertex constraint, and on the Muon System + Inner Tracker System.

4.1.2 Characterization of Momentum Resolution

The Kalman Filter is at heart a least squares fit optimization which assumes the errors included in the fit are Gaussian. The uncertainties induced by large angle multiple scattering and catastrophic energy losses will tend to produce decidedly non-Gaussian distributions in muon p_t. For this reason, the error estimations returned from the final Kalman Filter correlation matrix typically understate the uncertainties in the final track parameters.

A more realistic estimation of track parameters can be deduced from distributions of the residuals from generated data. The residual for p_t^{-1} is defined as:

$$\frac{\Delta p_t}{p_t} = \frac{p_t^{-1}{}_{Reconstructed} - p_t^{-1}{}_{Generated}}{p_t^{-1}{}_{Generated}} \qquad \text{Equation 4.2}$$

The standard deviation of the residual distribution provides the better estimation of track uncertainties for tracks with low to moderate p_t (< 200 GeV), even with the presence of non-Gaussian tails. For high p_t tracks, the residual distribution becomes highly asymmetric, but can be approximated as a distribution similar to the low to moderate p_t tracks on a 'pancake-like' background. For the ORCA simulations discuss in Chapters 4.3-4.4 and Chapter 5, these distributions were fit with a Gaussian curve across their central peaks, but the percentage of tracks found outside three sigma of the fit are also examined as an additional estimate on the quality of the track reconstruction being performed and, when variations in a measurement are taken, the dispersion of the residual distribution.

4.2 Limiting Factors For Measurement of Momenta in the CMS Endcap

The determination of muon momenta in the Endcap System is impeded by several factors. The most important of which include:

- Physical processes such as Multiple Coulomb Scattering and Energy Loss which alter particle trajectory prior to measurement
- The inclusion of false CSC hits in the track fit
- Intrinsic resolution and efficiency of the CSC chambers
- Uncertainty in the magnetic field maps (i.e. $\int B \cdot dl$)
- Misalignment of the CSC chambers

Each of these factors are discussed in the context of the ORCA studies presented at the end of this chapter to characterize the accuracy with which muon p_t can be reconstructed.

4.2.1 Physical Constraints Affecting Momenta Measurement

There are several physical processes which limit the resolution achievable for the measurement of momenta in the Muon System. The dominate processes which must be considered include Multiple Coulomb Scattering and Energy Loss (dE/dx). No single process dominates across the entire momenta range of the incident muons. Rather, the prominence of each process depends upon the momenta of the incident muon being measured.

4.2.1.1 Multiple Coulomb Scattering

As a charged particle passes through matter, it encounters the electric fields of nearby atomic nuclei, which exert forces that can make small modifications to the particles trajectory. The effect of a large number of such interactions on a particle can introduce a

significant deviation in a particular particle's path and exit angle as it emerges from the material and significantly affect the measurement of muon momenta.

The degree to which multiple scattering affects the determination of a muon's path through the muon system depends upon the material encountered as well as the initial momentum of the muon. In general, higher momentum particles experience smaller angular deflections than low momentum particles. Since multiple scattering is an entirely random process, the average scattering angle (deviation from entry angle) will be zero. However, muon chambers must track muons one at a time, so multiple scattering imposes a fundamental limit on the ability of the muon system to track a particular incident muon. For small angles, as is the case in most high energy particle detectors, the scattering distribution is approximately Gaussian and typical deviations (θ_{rms} in a plane) can be estimated as :

$$\theta_{rms} = \frac{13.6\text{MeV}}{\beta cp} z \sqrt{\frac{x}{X_0}} \left[1 + .038 \ln\left(\frac{x}{X_0} \right) \right] \qquad \text{Equation 4.3 [4.3]}$$

where θ_{rms} = rms of Gaussian scattering distribution
X_0 = radiation length of material being traverse
x = thickness of material being traversed
z = charge number of incident particle

The material which presents the highest probability for large scattering angles in the CMS Endcap are the RF iron disks where the ratio x/X_0(Fe) varies from 15 to 90. A precise determination of multiple scattering effects in the CMS Muon System must account for all material present in the muons path. In CMS, the amount of material which must be traversed is dependent upon both the ϕ and η coordinates of the path through the detector. The determination of θ_{rms} across paths which contain multiple layers of materials must be done by specifying a new value of X_0 for the composite of the material (adding successive values of θ_{rms} in quadrature does not work since the distribution is only approximated as being Gaussian). Moreover, Equation 4.3 holds only in the limit where $(x/X_0) < 100$.

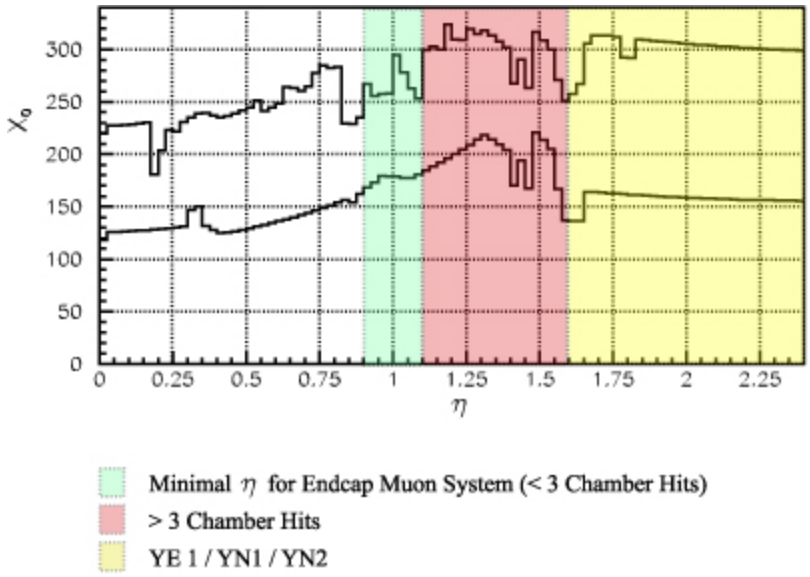

Figure 4.2: GEANT Based Determination of Xo In the CMS Muon System (at $\phi = 10°$). The two curves indicate the total radiation length (Xo) of material in front of the first (lower curve) and last (higher curve) muon chambers. The highlighted regions of the plot indicate η regions which contain Endcap Muon Chambers. The red and green areas denote regions which do not contain the additional YN1 and YN2 iron. All incident particles falling in the red and yellow regions lie solely in the Endcap Muon System (> 3 chamber hits). [4.6]

In addition to the direct impact of multiple scattering on the determination of particle momenta, the collisions of incident particles with material can occasionally provide the recoil electrons with enough energy to exit their bound state within the atom and manifest themselves as extra hits in neighboring drift chambers. The freed recoil electrons (called 'δ electrons') typically have low momenta and exit the material at large angles. The impact on the reconstruction of particle tracks is addresses in the context of chamber hit efficiencies (Section 4.2.3.2).

4.2.1.2 Energy Loss

Energy losses will be encountered by particles traversing the CMS detector. This will result in degraded momenta at each point of measurement. The principle sources of

energy loss in CMS are due to Ionization and Radiative Processes. Expressions for energy loss are given in terms of *dE/dx*, which is regarded as stopping power of the material being traversed.

4.2.1.2.1 Ionization

In addition to multiple scattering effects, Coulomb interactions with atomic electrons in the various detector materials will cause incident muons to lose energy, resulting in an additional small decrease in the particle's momentum. The net energy loss for a muon traveling through a specified material along a known path is, like multiple scattering, dependent upon its initial momentum and the statistical nature of the interaction.

The mean loss of energy loss per unit distance traversed (dE/dx) is estimated by the Bethe-Bloch equation:

$$-\frac{dE}{dx} = K\frac{Z}{A}\frac{1}{\beta^2}\left[\frac{1}{2}\ln\left(\left(\frac{2\gamma^2\beta m_e c^2\beta^2}{I}\right)^2\left(\frac{1}{1+2\gamma m_e/M+(m_e/M)^2}\right)\right)-\beta^2\right]$$

Equation 4.4 [4.3]

where $\frac{dE}{dx}$ = mean loss of energy loss per unit distance traversed
I = mean excitation energy of the material (eV)
β = velocity of incident particle (in units of c)
A = atomic mass of the material
Z = charge number of material
M = mass of incident particle
K = .0307 MeV g^{-1} cm^2

For muons in the CMS Endcap (p_t > 10 GeV), this function characterizes only a slight increase in the stopping power of the material with increased muon momenta (rising as a slow logarithm roughly .4 MeV $g^{-1}cm^2$ from p = 10GeV to p = 100 GeV).

4.2.1.2.2 Radiative Processes

Charged particles accelerated in the Coulomb fields of atoms in a material will emit photons ("Bremsstrahlung radiation" when the photon is real, "pair production" when the photon is virtual and gives rise to a e^+e^- pair.). The mean free path for emitting this radiation is simply X_o, the radiation length of the material being traversed. More specifically, X_o is defined by the mean distance with which an electron loses all but 1/e of its energy by bremsstrahlung. In this case, the fractional energy loss is given (almost by differentiation of this definition) by Equation 4.5:

$$\frac{dE}{dx} = \frac{\rho E}{X_o} \qquad \text{Equation 4.5}$$

where ρ = density of material

The 'critical energy' for a muon traversing the YE Iron disks occurs above 321 GeV, where radiative effects become larger than ionization effects [4.3].

4.2.1.2.3 Net Average Energy Loss

The average net energy loss for muons traversing iron is shown in Figure 4.3. In general, a muon with $p_t \approx 100$ GeV in the CMS Endcap has a total momenta between 150 and 500 GeV – approximately where radiative effects begin to induce important deviations from the nearly constant effect of ionization.

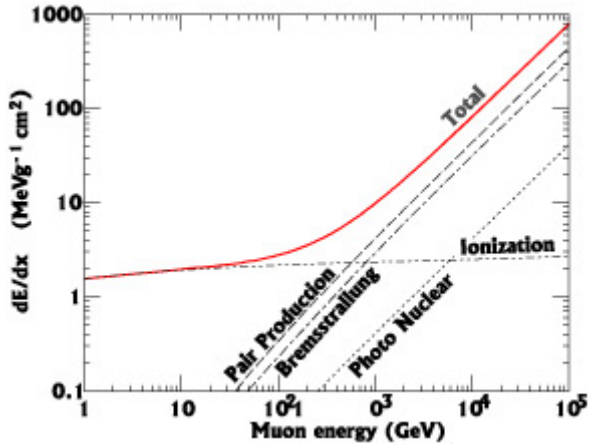

Figure 4.3: Energy Loss for a Muon Traversing a per unit Volume of Iron. The total energy loss is shown in red. [4.6, adapted].

4.2.1.3 Detector Design Constraints Affecting Momenta Measurement

There are several factors inherent in the design of Muon System components which limit the precision with which muon momenta can be determined. These factors, which include the intrinsic resolution of the CSC chambers, the uncertainty in chamber locations, the performance of on and off chamber electronics/software, and the certainty with which local magnetic fields can be estimated, are determined in part by the availability of appropriate funding and technology. Additionally, the factors limiting system performance maybe amplified or attenuated depending upon the momenta of the incident muons to be measured or the severity of the physical processes indicated in Section 4.2.1. For this reason, a significant simulation effort to optimize and understand the performance of the Muon System was undertaken.

4.2.2 Intrinsic CSC Resolution

The intrinsic resolution of CSC chambers has been used as the principle benchmark to gauge the performance and impact of all other sources of uncertainty. The design of the CSC chambers ensures a nominal level of performance at an acceptable cost. The requirements placed on the CSC design consist of the following [4.4]:

- High reliability and low maintenance
- 150 μm offline spatial resolution in CMS Φ
- < 2mm spatial resolution in CMS Φ at the L1 Trigger level
- >92% bunch crossing identification (per chamber) at 25ns per bunch
- No aging after 10 years of full LHC luminosity

The mechanical construction of the chambers has already been addressed in Chapter 3, Sect 3.3.2. As Figure 4.4 indicates, each chamber consists of seven copper skinned panels stacked to create six gaps. The gaps are strewn with anode wires while the panels are etched to form cathode strips. Anode wires (diameter = 50μm) are spaced at 3.12 mm, while cathode strips are milled to form widths which are constant across the CMS Φ plane - $\Delta\Phi$ = 4.6 mrad for ME ±234/1 and $\Delta\Phi$2.3 mrad for ME ±234/2 (which corresponds to approximately 16mm from the wide end of the chamber to 7mm on the narrow end). The gap between each cathode strip is a constant .5mm. It important to note that ME ±1 chamber dimensions vary slightly from the other chambers due to their slightly smaller dimension and placement in CMS.

Electronics on the CSC chambers are designed to reconstruct the trajectories of muons through the six cathode planes into Local Charge Track (LCT) segments. Both anode and cathode LCT segments are constructed. Cathode electronics feature a front end amplifier with a 100ns pulse shaping time which is branched into two pathways [4.4]. The first pathway leads to a comparator chip which defines the position of incident muon hits for the Level 1 Trigger to within one-half a strip width (± quarter-strip width). It is here where LCT patterns are formed. The second pathway leads to a series of switched capacitor arrays and chips which sample and stores the analog waveforms every 50ns. Once the Level 1 Trigger conditions have been met (Section 4.2.3), 8 to 16 consecutive of these samples are digitized by local ADCs and passed along to the DAQ network where they are kept for later analysis. The design of the anode electronics is similar to that of the cathode electronics, though the anode electronics are optimized to provide more accurate timing data than in the cathode. Anode electronics contain amplifiers with a 30ns pulse shaping time, though they are considerably coarser than corresponding

cathode pulse shapes. For this reason, anode LCTs are expected to be used to provide only 'hit/no hit' information, though wire group information can be incorporated into offline DAQ analysis.

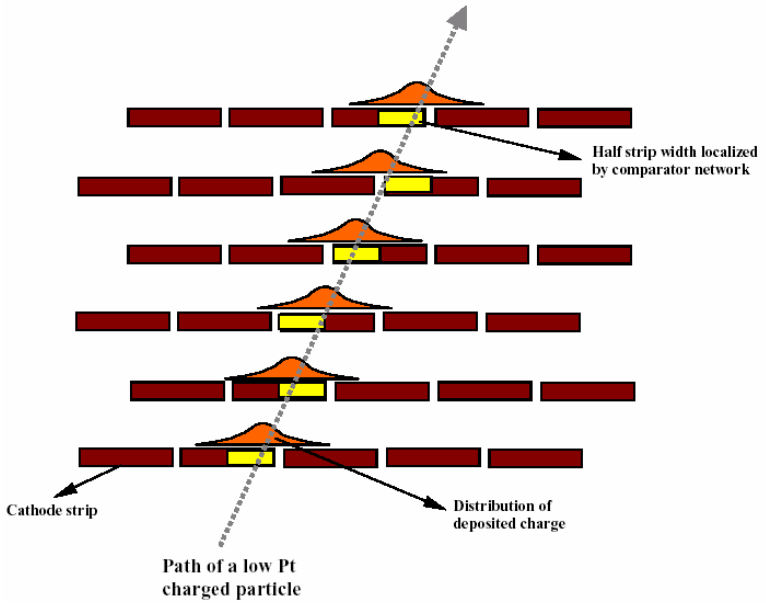

Figure 4.4: Sample Particle Trajectory and Emergence of the Resulting Cathode LCT Pattern [4.5]. Cathode strip patterns can be immediately identified to within one-half a strip width for processing into Level 1 Trigger algorithms.

4.2.3 Level 1 Triggering

Once anode and cathode LCTs have been constructed and verified as consisting of only valid hit patterns, additional on-chamber electronics are used to associate anode and cathode LCTs as well as tag patterns with the appropriate bunch crossing time. The best two patterns from each chamber are then sent for additional consideration in the Level 1 Trigger. The two most promising cathode LCTs are then compared against LCTs from eight other chambers in the same triggering sector (60° slices of each Endcap Disk). The three best track segment candidates are then culled from each triggering sector and passed along to be compared against similarly formed track segment candidates in the Barrel Muon System. Of all track candidates selected across the entire Muon System, the four best candidates are then sent to the Level 1 Global Muon Trigger. The most recent

simulation results have shown that muon $1/p_t$ values can be reconstructed directly from LCT information to within 30% when LCT information is taken from two ME stations and within 20% when taken from three ME stations for all values of η ($p_t < 100$ GeV only, as high pt tracks are limited by strip widths) [4.5].

4.2.3.1 Offline Spatial Resolution

The expected design performance of the CSC chambers is 150μm in offline reconstruction in CMS RΦ. Test beam data taken from two full scale CSC prototype chambers in 1999 at the CERN Gamma Irradiation Facility (GIF) indicates that this goal is obtainable. The GIF facility provides a fairly constant source of ~200 GeV muons paired with a high γ background. The tests [4.4] evaluated the residuals of hits in a single plane from a fit of hits in the remaining five planes. The results indicate that single plane resolutions vary substantially with strip width and the trajectory of the incident particle (Figure 4.5). Muons which impact the center of the strips show the worse resolution (~250-400 μm), though those which cross between two strips show marked improvement (~150 μm). Since the six cathodes are offset by one-half of a strip width, there will likely be several strips available with the favorable resolution. Monte Carlo simulations suggest that the final spatial resolution of the chambers will be close to 80-85 μm [4.4]. Although the Monte Carlo simulations do not include δ electrons and assume tight calibrations, they do indicate that final spatial resolution of the CSC chambers should meet or exceed 150μm. It is critical to note that high background and the limited calibration planned for production CSC chambers is likely to push the 'intrinsic' six layer resolution closer toward the 150μm target.

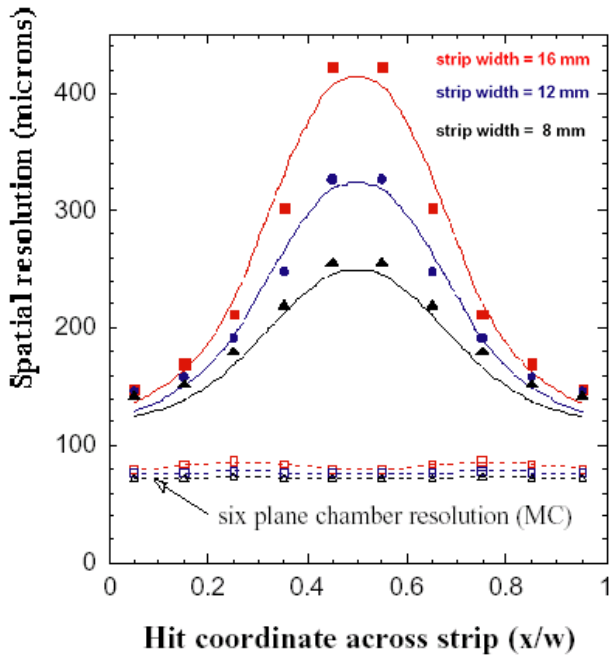

Figure 4.5: Spatial Resolution as a Function of Strip Width (2000 Test Beam Data, ~200 GeV muons). Single CSC plane resolution varies as a function of strip width. The 0 and 1 points on the x axis correspond to a particle trajectory which crosses exactly between the strips. The single plane resolutions are extrapolated to six plane resolutions by Monte Carlo. The improvement is dramatic as the six cathode plane arrangement includes overlapping strips [4.4].

4.2.3.2 Hit and Track Formation Efficiency

CSC chamber 'Hit Efficiency' refers to the chambers' ability to (locally) trigger on discriminate incident muons above the expected background. Although there is a large amount of shielding between the interaction point and Endcap chambers, high background is still expected (so called 'minimum bias' events). Additionally, the emission of muon induced secondary particles can create additional hits in a chamber plane, complicating the formation of LCT and track segments within the chamber. It is also possible for muon secondary particles (δ-electrons) to generate fake muon hits (defined as ≥ 3 individual layers recording hits) in the chamber.

Test beam data taken at the CERN SPS indicates that fake muon hits may be generated approximately at a 3% level for 100 GeV muons and 10% level for 300 GeV muons [4.4]. These same tests, conducted on prototype chambers, indicate that approximate 92% of tracks can be successfully reconstructed within the chambers nominal resolution.

The reconstruction of muon tracks is typically done across three or more CSC chambers (in the standalone muon system case). The most important factor that governs the efficiency and rate of the Level-1 CSC Trigger is the resolution of p_t, which is directly affected by individual CSC chamber hit efficiency, as false or missed hits may alter the quality and quantity of information available for reconstruction. A poor resolution means that some signal muons will fluctuate below the trigger threshold (loss of efficiency). Direct simulation of the CSC Track finder in ORCA 4_5_3 [4.6] (which includes minimum bias and neutron background, but excludes pile-up events) indicates the single muon track finding efficiency will be 92.5% for low p_t muons in the Endcap. Efficiencies for higher p_t muons are somewhat lower, as high p_t muons tend to induce larger amounts of bremsstrahlung and δ electrons. For a sample of 100 GeV muons, the track formation efficiency decreases to 88%. A 300 GeV single muon samples yielded a track formation efficiency of 82%.

4.2.4 The Magnetic Field

The central feature of the CMS detector is the large (4T) solenoid which, when completed, will be the world's largest, most powerful solenoid magnet. As the momentum measurement of charged particles in CMS is based on the bending of their trajectories, both a large magnetic field and a good understanding of the field are necessary.

Extensive modeling of the magnetic fields in CMS has been done. These models indicate that the central region of the detector will be very uniform, principally due to the

large number of windings and favorable ratio of solenoid length to radius. The large return field of the solenoid will mean that the field immediately outside the forward ends of the solenoid (the Endcap Muon System) will saturate the surrounding iron and, since the forward geometry is relatively complex, result in a very non-uniform field. Saturation of the iron in the Barrel Muon System is expected to be much less severe than in the Endcap, so field should remain relatively uniform in this region. A quarter plane map of this field is shown in Figure 4.6.

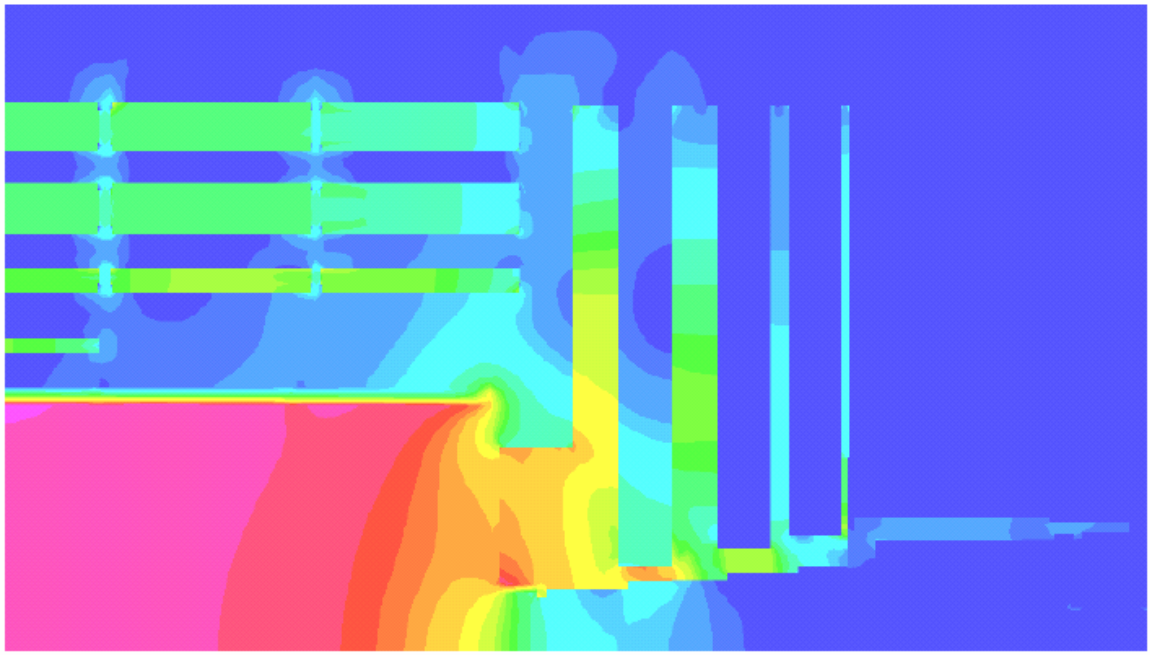

Figure 4.6**:** Quarter Plane Magnetic Field Map of the CMS Detector. The pink shaded region corresponds to field strength of approximately 4T, yellow to 3T, green to 2T, aqua to .9T, and blue < .75T.

Although extensive models of these fields exist, direct measurements of the fields must be taken during the experiment. Small imperfections in the casting of the iron, variations in the permeability of the return yokes, misalignment of magnet components during installation, and slight asymmetries in the detector design can all induce relatively large deviations from expected fields. As Equation 4.1 notes, measurement of a transverse moment (p_t) in these fields is proportional to the ratio of B_z and the sagita (s)

of the particles trajectory. The uncertainty in the measurement of p_t can thus be approximated as:

$$\sigma_{p_t}^2 = \sigma_s^2 + \sigma_{B_z}^2 + \sigma_{Physical\,\mathrm{Pr}ocesses}^2 \qquad \text{Equation 4.4}$$

Though muons in the Endcap region are not determined by the measurement of a single sagita as Equation 4.1 suggests, the term in Equation 4.4 can nevertheless be understood as the uncertainty in the direct measurement of track parameters (intrinsic resolution of the chambers, fitting algorithm selected, misalignment, etc). The third term in Equation 4.4 ($\sigma_{Physical\,\mathrm{Pr}ocesses}^2$) accounts for any additional uncertainty induced by physical processes (multiple scattering and energy loss) during and immediately prior these measurements. In general, the uncertainty with which the magnetic field must be determined within the volume of the detector should not exceed these uncertainties. Since the initial simulations of the CMS detector assumed a perfect knowledge of the magnetic field, but include estimations of the intrinsic chamber resolution and physical processes, the estimated (worst case) resolutions of magnetic field measurements can be summarized as follows:

Central Tracking Region	$\sigma_{B_z}^2 < 4\%$
Barrel Muon Region ($\eta < 1$)	$\sigma_{B_z}^2 < 10\%$
Endcap Muon Region ($\eta > 1$)	$\sigma_{B_z}^2 < 15\%$

At present, these estimations are several times larger than the expected performance of even the simplest magnetic probes to be employed throughout the detector [4.8]. Present plans call for the placement of moveable Hall probes in the Central Field regions (accuracy of <10 Gauss) and Hall generator devices (current loop devices) in the Endcap/Barrel Muon areas (accuracy of $\sim$ 1-2%).

4.3 Simulated Performance of the Endcap Muon System Using CMSIM

Simulation studies of the CMS Endcap Muon System have generally utilized CMSIM [4.9], a Fortran GEANT 3 based detector simulation. Results of simulation studies of the Muon System using the CMSIM program can be found in the Muon Technical Design Review [4.6]. CMSIM software development was moved to a 'maintenance only' status in February 1999, when development was focused on ORCA, a new C++ reconstruction and simulation tool for use in CMS. ORCA software is presently (February 2002) in an advanced developemental state, though it is not readily accessible to casual users.

4.3.1 CMSIM Description

Before ORCA was developed, the CMSIM program was used to do the general study and design of the CMS detector. CMSIM allows users to propagate generated particles, produce simulated detector responses ("hits and digis"), and reconstruct particle trajectories based on the simulated responses. The reconstruction methods employed by CMSIM are dependent upon the simulation being conducted; which is to say that CMSIM cannot be used to reconstruct raw data taken from the real CMS experiment.

An extremely brief snapshot of the developments in CMSIM with relevance to the understanding of Muon simulation results is given below:

- CMSIM v100-118 (Mar 1995 - July 2000) used two dimensional magnetic field maps and two dimensional fitting for reconstruction. The Endcap region has large, three dimensional field gradients which were regarded is having been poorly described by this model.

- CMSIM v112 (Nov 1997) introduced a tentative algorithm for the Kalman Filter. The implementation under went several revisions prior to CMSIM 118 (July 2000).

- CMSIM 118 (February 2000) significant updates in CSC and Endcap geometry included, though the changes assume (incorrectly) that Endcap ME discs were mirror symmetry.

- CMSIM 120 (Nov 2000) significant updates in Endcap, Silicon Tracker, and Calorimeter geometry introduced. Prior models of Endcap geometry were incorrect in assuming too much symmetry in the placement of CSC chambers.

- CMSIM (all versions) did not properly implement the correct number of CSC wire groups (Section 4.2.2) nor enforced constant $\Delta\Phi$(CMS) CSC strip widths. This has been corrected in present releases of ORCA.

Several CMSIM studies found that the global Muon System + Tracker fit produced unusually low efficiencies for Endcap eta regions below |1.8| (all ME ±1/23 and ME ±234/2 chambers). The problem was determined to be a result of the underlying reconstruction package in CMSIM 114 and most likely impacts all studies done prior to 2000. [4.10].

4.3.2 Summary of CMSIM Results

Initial Muon System simulations (CMSIM v100-114) included in the 1997 Muon TDR [4.6] provided the estimates of muon track momenta resolution found in Figure 4.7. As the figure indicates, all muon momenta resolutions in the endcap remain relatively constant up to $|\eta|=1.5$, whereupon the resolution begins to degrade as tracks no longer traverse the entire radius of the Inner Tracker.

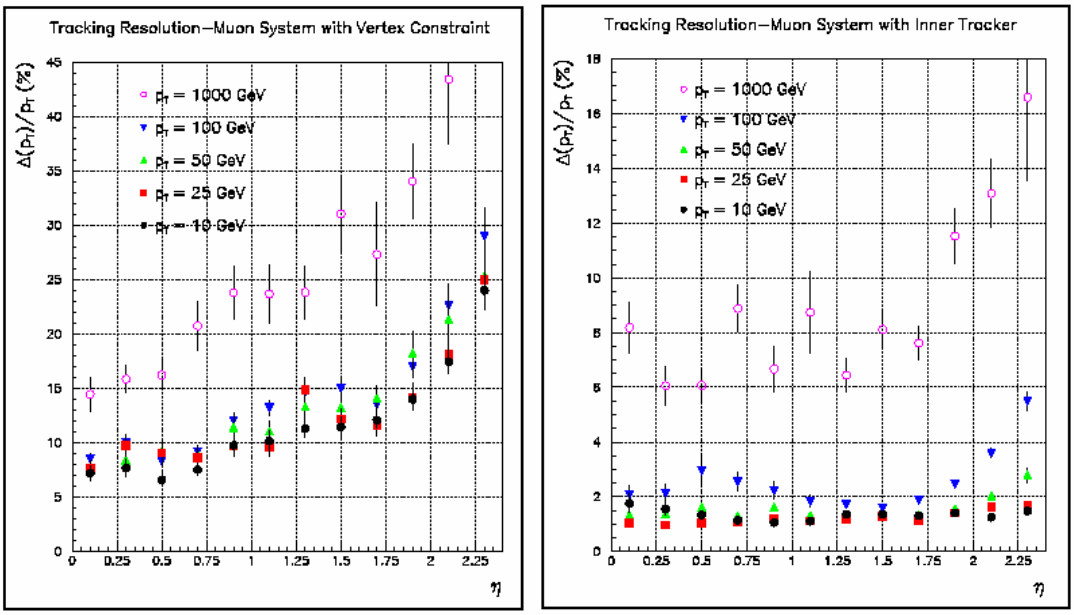

Figure 4.7: CMSIM Simulated Muon System Performance As a Function of η. The plot on the left details the simulated performance of the Muon System as characterized by the Standalone Muon + Vertex Constraint Fit. The plot on the right details the simulated performance as characterized by the Muon + Tracker Fit. [4.6]

The initial studies on the required resolution of the alignment system were done during the initial CMS design stage as well (1990-1994). These studies [4.11][4.12] simulated misalignment by random displacements of each CSC chamber. It was assumed chambers had intrinsic resolutions of 100μm (or 75μm) and 100% Track Finding efficiencies. The study asserts that the determination of muon transverse momenta does not degrade significantly so long as the alignment system resolution does not exceed the intrinsic chamber resolution. However, the misalignment of chambers greater than the intrinsic resolution of the CSC chambers used in the simulation was not examined.

A more recent, and more realistic, study of misalignment and muon reconstruction resolution in the Endcap was completed in March 1999 utilizing CMSIM 114 [4.10]. This study assumed an intrinsic (six layer) CSC resolution of 150μm and incorporated updated CMSIM geometry. For the study, samples of single muon were sent through the detector simulation at three values of η (1.6, 2.0, 2.4) and the entire phi region. A

simulation was first performed with perfect alignment to record the detector hits and then followed by a second simulation to reconstruct the muons (Muon + Tracker only), but with the detector response of each event in the first simulation randomized about the original response values to simulate the misalignment of ME Station positions.

The study found p_t resolutions to be dependent upon both the type of misalignment induced on chamber positions and generated muon p_t. The type of misalignment which induced the greatest effect in the reconstruction of muon p_t was the randomization of independent ME station positions in the RΦ plane. Randomizing the rotations of ME stations about the CMS Z axis did not induce an effect of quite the same magnitude, particularly for muons with $p_t \leq 100$ GeV, since the initial vectors created by the LCT and CLCT hit patterns which seed the reconstruction algorithm still point toward the interaction point. In general, higher momentum particles ($p_t > 500$ GeV) were much more sensitive to misalignments resulting in significantly degraded p_t resolutions.

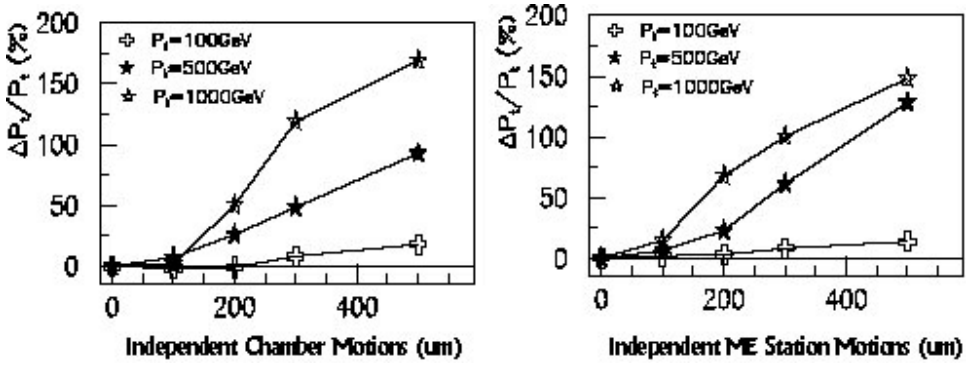

Figure 4.8: Reconstructed p_t Resolutions as a Function of Random CSC Chamber and ME Station Misalignment.

The residual distributions were found to be not entirely Gaussian and were observed in some cases to have many entries outside of the central distribution. The authors of the study introduced a '3σ Exclusion' defined by the percentage of particles outside of the three sigma limit imposed by the Gaussian fit of the original (perfect alignment) muon sample. The 3σ Exclusion estimate was found to degrade in a manner similar to the p_t resolutions.

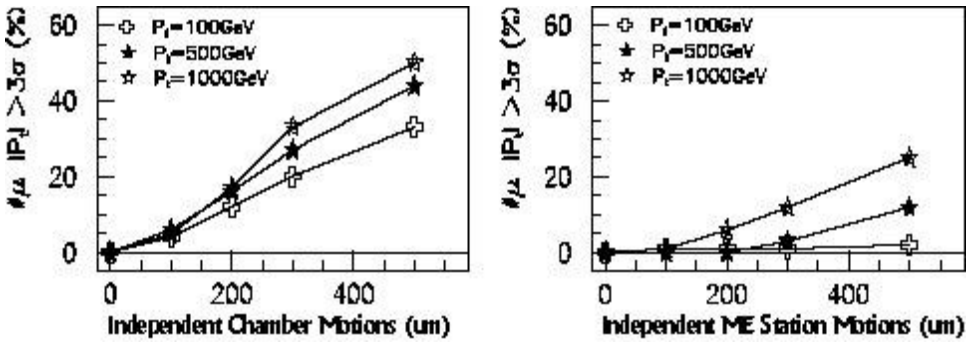

Figure 4.9: The '3σ Exclusion' Estimate as a Function of Random CSC Chamber and ME Station Misalignment

Using the criteria that misalignment effects should not be allowed to degrade p_t resolution by more than 20% or the quality of the p_t fit (as defined by the number of hits straying more than three sigma from the fitted distribution) by more than 10%, the study concluded that misalignments of approximately 200μm were acceptable for muon $p_t \approx 100$ GeV, but that misalignments should be limited to approximately 150μm for higher momenta particles (p_t > 500-1000 GeV). These simulations also found CSC motions along the CMS R and Z directions of up to 1mm did not induce significant degradation of muon p_t resolution.

4.4 Simulated Muon System Performance with ORCA

ORCA (Object-oriented Reconstruction for CMS Analysis) [4.13] was created as a framework for the general reconstruction of CMS physics events from both simulation and the real data from the experiment. When the project is completed, it will allow users to reconstruct simulated and real data in almost exactly the same manner. ORCA is not designed to generate particles or characterize their propagation through the detector. CMSIM/GEANT 3 is still used to model the detector geometry (including magnetic field maps) and to determine the path of simulated particles through the detector. ORCA does, however, offer package components which are capable of simulating the detailed detector response ('hits and digis') of particles traversing the detector volume.

ORCA is still in a stage of rapid development. The reconstruction of events is done in custom built programs written and compiled by the user with the aid of the classes and methods available in the ORCA software package. As a result, the primary users of ORCA have been those most closely associated with its development and coding (i.e. very few 'casual users'). A brief snapshot of the developments in ORCA with relevance to the understanding of Muon simulation results is given below:

- ORCA 3 (July 2000) muon reconstruction becomes available on whole detector (with validated results)
- ORCA 4_5_0 (Feb 2001) significant tracker improves in algorithms and performance. Calorimetry has performance improvements.
- ORCA 5_1_0 (Sept 2001) the first implementation of persistent Tracker tracks and persistent global trigger decisions. Very significant upgrade of underlying ORCA packages making much of ORCA 5 incompatible with ORCA 4.

In general, the classes and methods presently implemented within the ORCA software package allow users to reconstruct muon tracks in the CMS detector across three levels of detail: initial track determination, the Standalone Muon System operation, and the Muon System working in conjunction with the Inner Tracker. The three levels are summarized, in their hierarchical order, below:

- L1MuonReconstruction (L1)

LCT patterns are formed across the CSC anode / cathode planes. Potential muon track segments are sorted and send to the Level 1 trigger, where the initial determination of muon tracks are made.

- L2MuonReconstruction (L2)

Pt is redefined using the muon reconstruction with the L1MuonReconstruction seed. Pt is then redefined once again by applying a vertex constraint resolution for even better

pt resolution. Selections may then be made on fit parameters (χ^2, vertex constraint, etc.) for non-prompt muon rejection. Isolation cuts using calorimeter information are also applied at this time. The seeding of the L1MuonReconstruction values is sufficiently coarse enough that the L2MuonReconstruction may be considered as generally independent of the L1 Reconstruction.

- L3MuonReconstruction (L3)

The L2MuonReconstruction muon track is refit with the inclusion of Tracker information.

Since both L2 and L3 reconstruction methods are seeded with information from previous fits (ultimately from the L1 hardware level), it should be noted that the present implementation of ORCA does not yet contain a true offline reconstruction method.

4.4.1 Endcap Studies in ORCA

As indicated in Section 4.3, the release of ORCA v5 provides users with a significantly more powerful tool to study muon reconstruction in the Endcap region than with previous software. Modifications and updates to the Endcap geometry, individual CSC chambers, Trigger, and Reconstruction algorithms employed in this release will make it worthwhile to reevaluate several aspects of the expected physics performance for the Endcap Muon System prior to confining studies to effects which deal solely with the misalignment of CSC chambers.

An implementation of ORCA_5_3_1 was used to examine the effect of single muon reconstruction in the Endcaps. All simulations were performed using PYTHIA 6.1.0 [4.12] as the Monte Carlo generator, CMSIM 120 as the detector simulation, and ORCA_5_3_1 for the recording of simulated detector hits and digitization ('hits and digis'). Simulation settings where done in accordance with the standard and default settings suggested for the CMS experiment [4.13] unless specifically noted.

The evaluation of detector simulations which explore the effect of misalignment on the reconstruction of particle momenta in the Endcap were performed with a modified release of ORCA_5_3_1, which accommodates direct access to chamber geometry during the initialization and construction of the Endcap Muon simulation.

Studies were typically conducted with single muon samples of 2000 events with fixed values of p_t directed to restricted and unrestricted regions of eta and phi. All events were then reconstructed with ORCA_5_3_1 L2 and L3 Reconstructors and analyzed in the same manner.

4.4.1.1 Intrinsic Detector Response (Perfect Alignment)

Figure 4.10 and Figure 4.11 show the typical Muon System performance, in terms of the p_t^{-1} residual distributions, of the Level 2 and Level 3 Reconstruction as a function of eta for several values of p_t. The plots were constructed from single muon samples at fixed values of eta and unrestricted values of phi. Error bars on the plot indicate the quality of the fit used to determine the value of σ plotted.

The standalone muon system with the vertex constraint imposed (L2 reconstruction) can be seen to remain relatively constant in performance between $1.3 \leq |\eta| \leq 1.7$. Beyond $|\eta| = 1.7$, the resolution begins to degrade or, in the case of muons with $p_t \approx 1$ GeV, the residual becomes considerably less well defined (i.e. larger error bars). Both the residual p_t^{-1} distribution and p_t^{-1} distribution becomes very difficult to fit for large values of p_t at high eta. This effect is likely due to the decreased radius of curvature in the RPhi bending plane for the increasing total muon momentum of these particles (p_{total} increases with eta for fixed p_t) and the lower magnetic field strengths in the high eta regions. The slight increase in the residual at $|\eta| = 1.1$ is due in part to the complicated nature of this region in the detector. Values of $|\eta|$ less than 1.3 lie in a region which overlaps both the Barrel and Endcap Muon Systems. For this region, triggering and reconstruction

algorithms are considerably more complex and typically induce slightly more uncertainty in measurement values.

The addition of Tracker information to the Muon System fit (L3 Reconstruction, Figure 4.11) significantly improves the p_t resolutions with the exception of very high p_t muons in high eta regions. In the Tracker, particles which do not traverse the entire radius of the solenoid undergo less bending in the magnetic field and show an increase in their corresponding p_t residuals. This effect is particularly prominent in the p_t = 1000 GeV muon sample in regions of $|\eta| > 1.5$.

The track finding efficiency (# muons found/ # muons generated) of the L2 and L3 reconstruction methods are shown in Figure 4.12 and Figure 4.13 The efficiency of the L3 Reconstruction shows a significant drop for the region of $|\eta| = 1.1$, which corresponds to the overlap region of the Muon Barrel and Endcap Systems. As noted previously, fitting and matching track segments in this region is substantially more difficult.

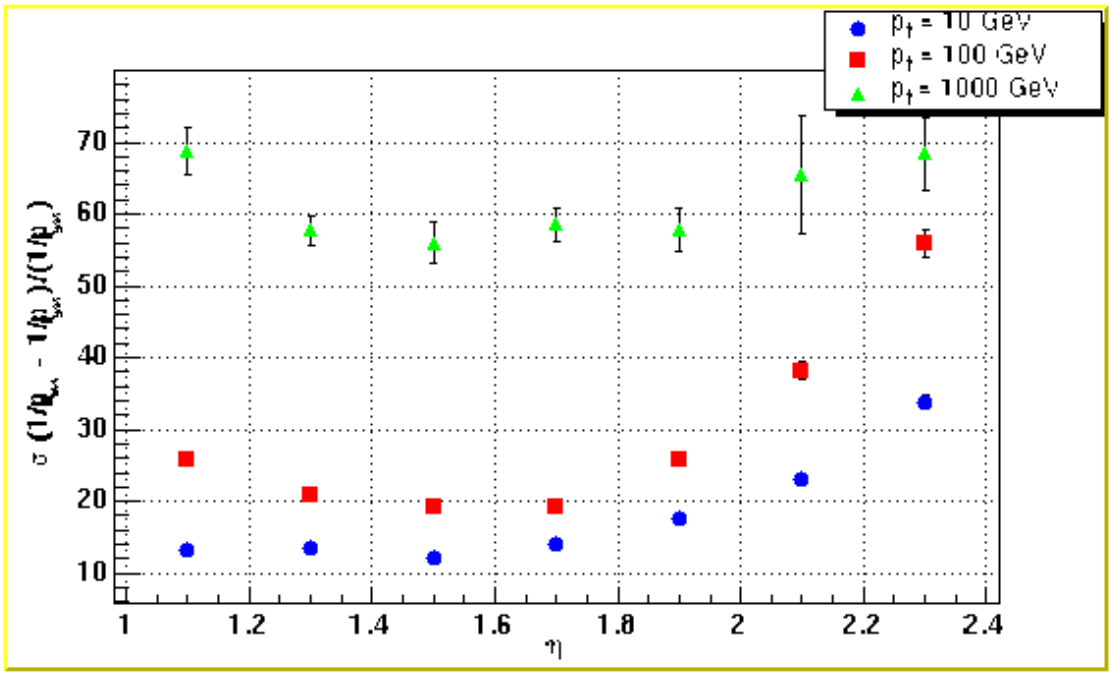

Figure 4.10: The Muon System Standalone + Vertex Constraint p_t Resolution as a Function of η.

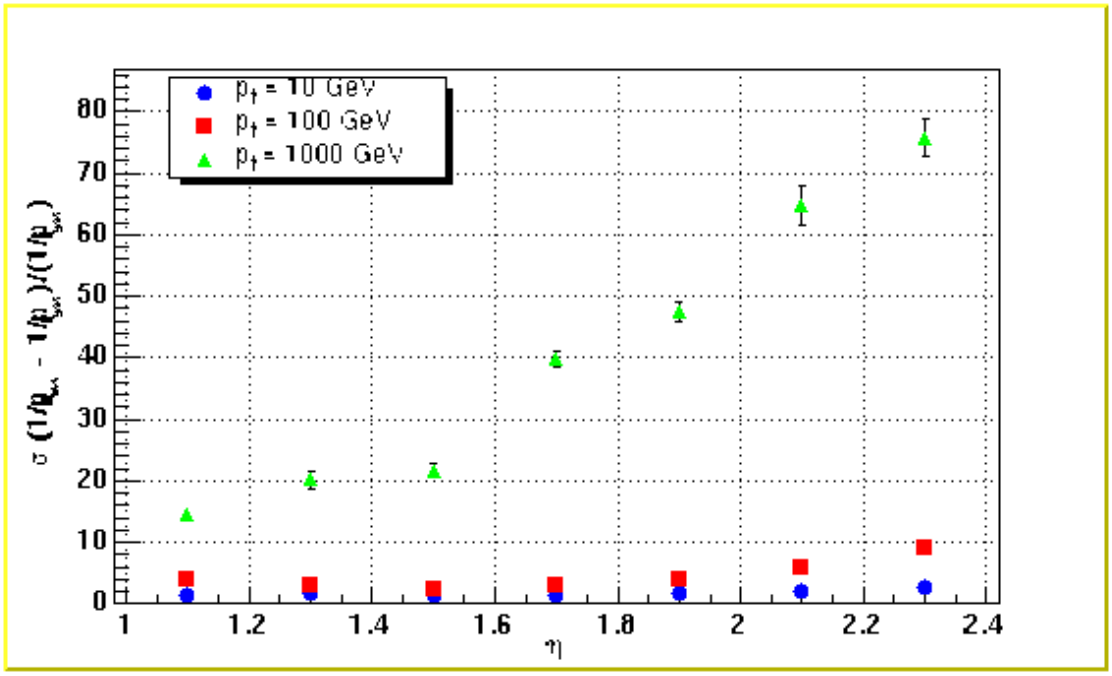

Figure 4.11: The Muon System + Inner Tracker p_t Resolution as a Function of η.

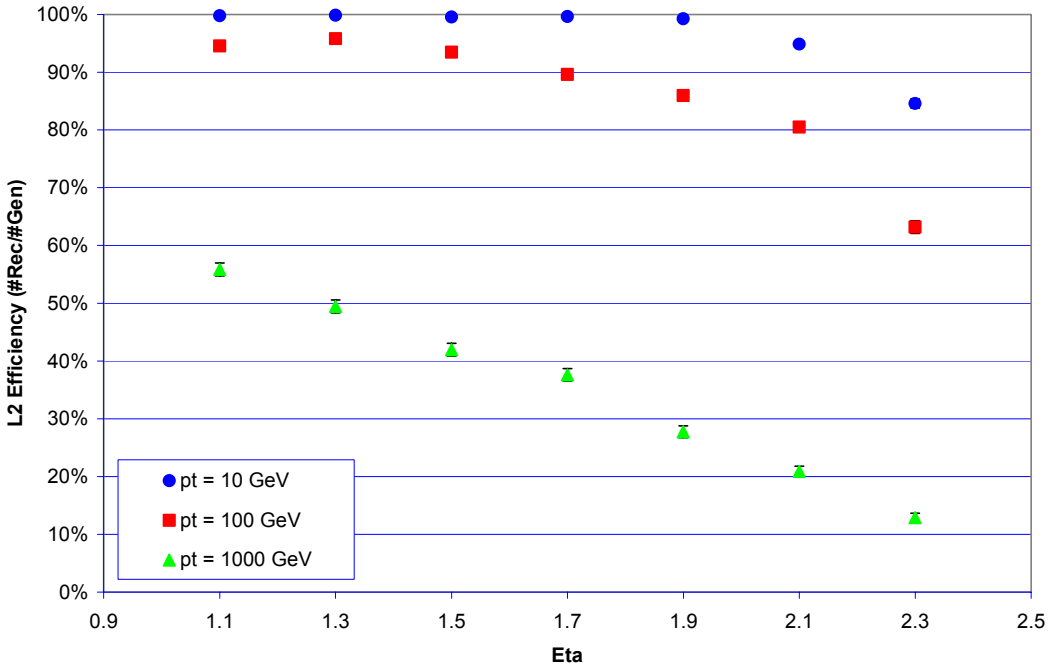

Figure 4.12: Muon Standalone + Vertex Constraint (ORCA L2) Efficiency as a Function of η. The error bars are estimated from the binomial distribution.

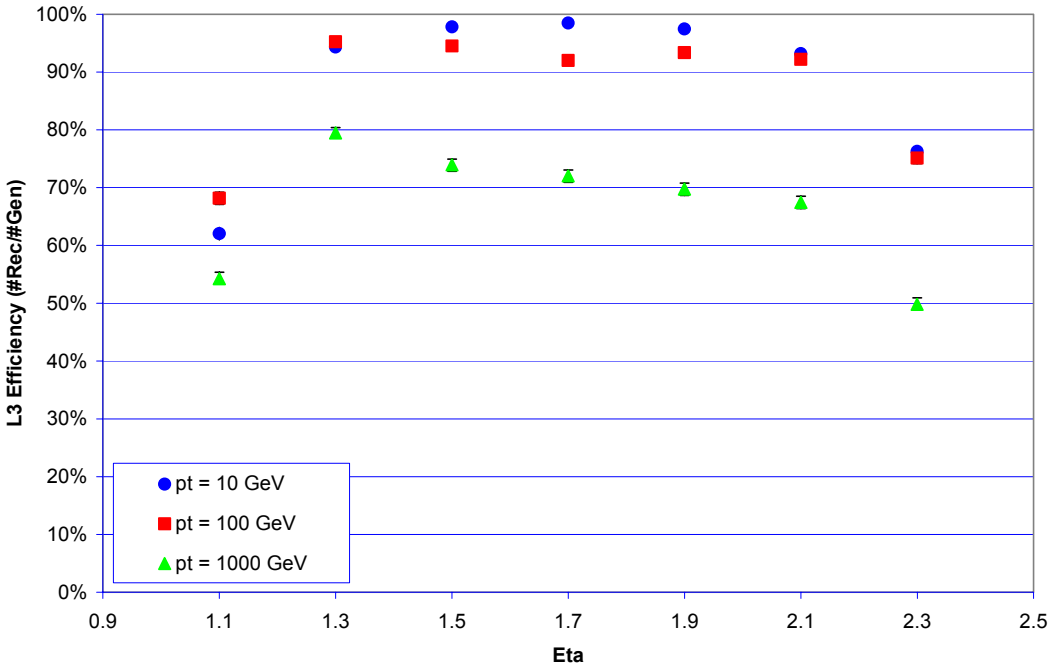

Figure 4.13: Muon System + Inner Tracker (ORCA L3) Efficiency as a Function of η. The error bars are estimated from the binomial distribution

4.4.1.2 Effect of Multiple Scattering

Using CMSIM, the effects of multiple scattering in the Endcap chambers was used to provide a upper estimate on the precision with which CSC chamber positions might be determined.

Figure 4.14 and Figure 4.15 show the reconstructed values of p_t^{-1} of single muons for two locations in eta at fixed values of phi for the case with and without multiple scattering effects. Multiple scattering effects for the reconstruction of muon p_t in the Standalone Muon System are more significant than for the complete Muon + Tracker fit. This is due to the dominance of Tracker resolutions described in Section 4.4.1.1 and the relatively small amount of material to be traversed within the central tracking chamber.

The asymmetry of the resulting distributions in the Muon Standalone histograms can also be attributed to directly to multiple scattering. As Section 4.2.1.1 notes, the asymmetry should be higher for particles which enter the scattering material at higher angles (i.e. not perpendicular to the surface), thus it might be expected that low $|\eta|$ regions in the Endcap should illustrate a higher degree of asymmetry. However, the inclusion of the additional iron behind ME ±1/1 significantly increases the effects of multiple scattering for regions of $|\eta| \geq 1.7$, as the ratio of material to be traversed to the radiation length of the material increases by a factor of 3 when $|\eta|$ exceeds 1.7.

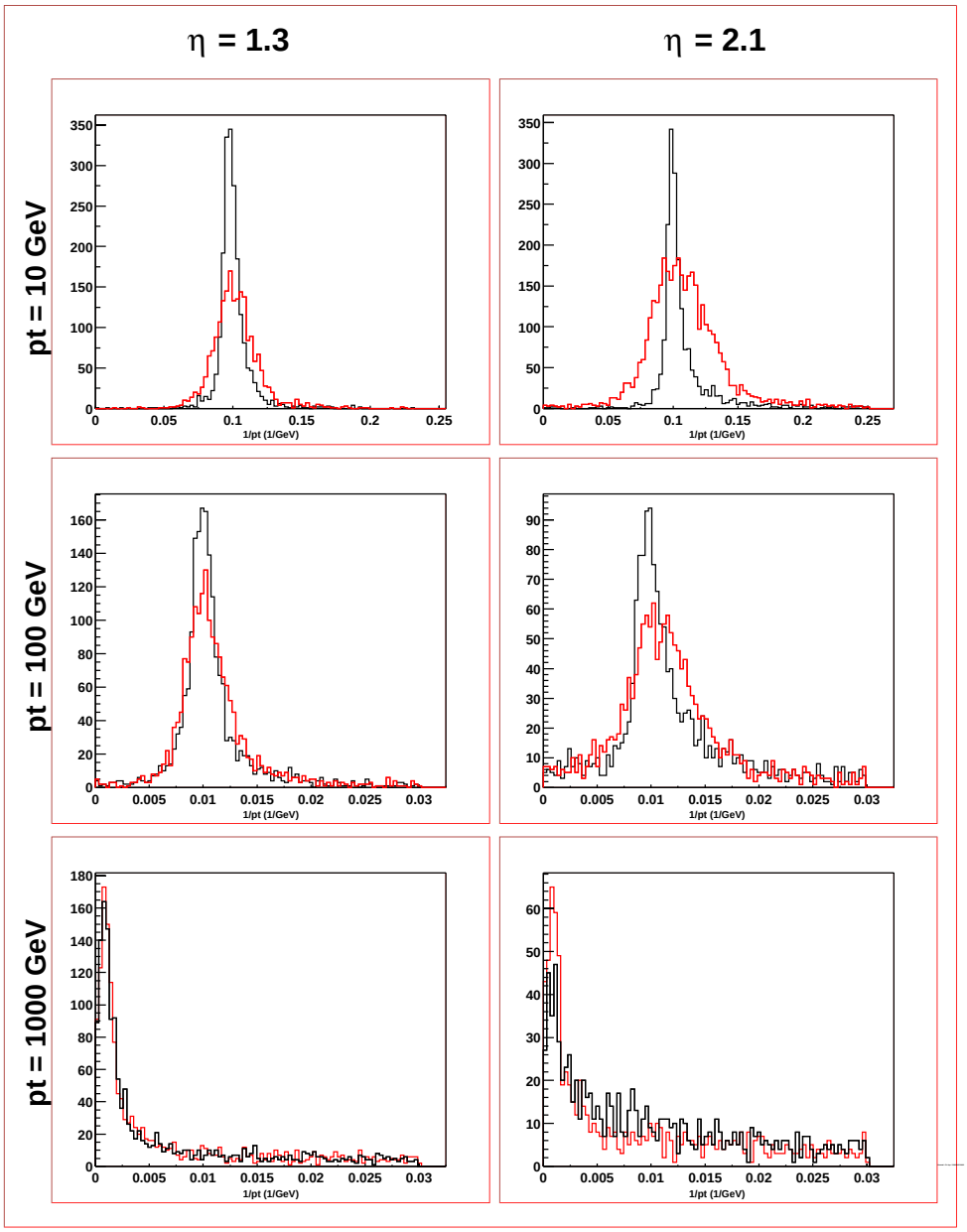

Figure 4.14: Effect of Multiple Scattering on the p_t^{-1} Distributions in the Muon System Standalone + Vertex Constraint Fit (ORCA L2). The reconstructed distribution with multiple scattering is shown in (red).

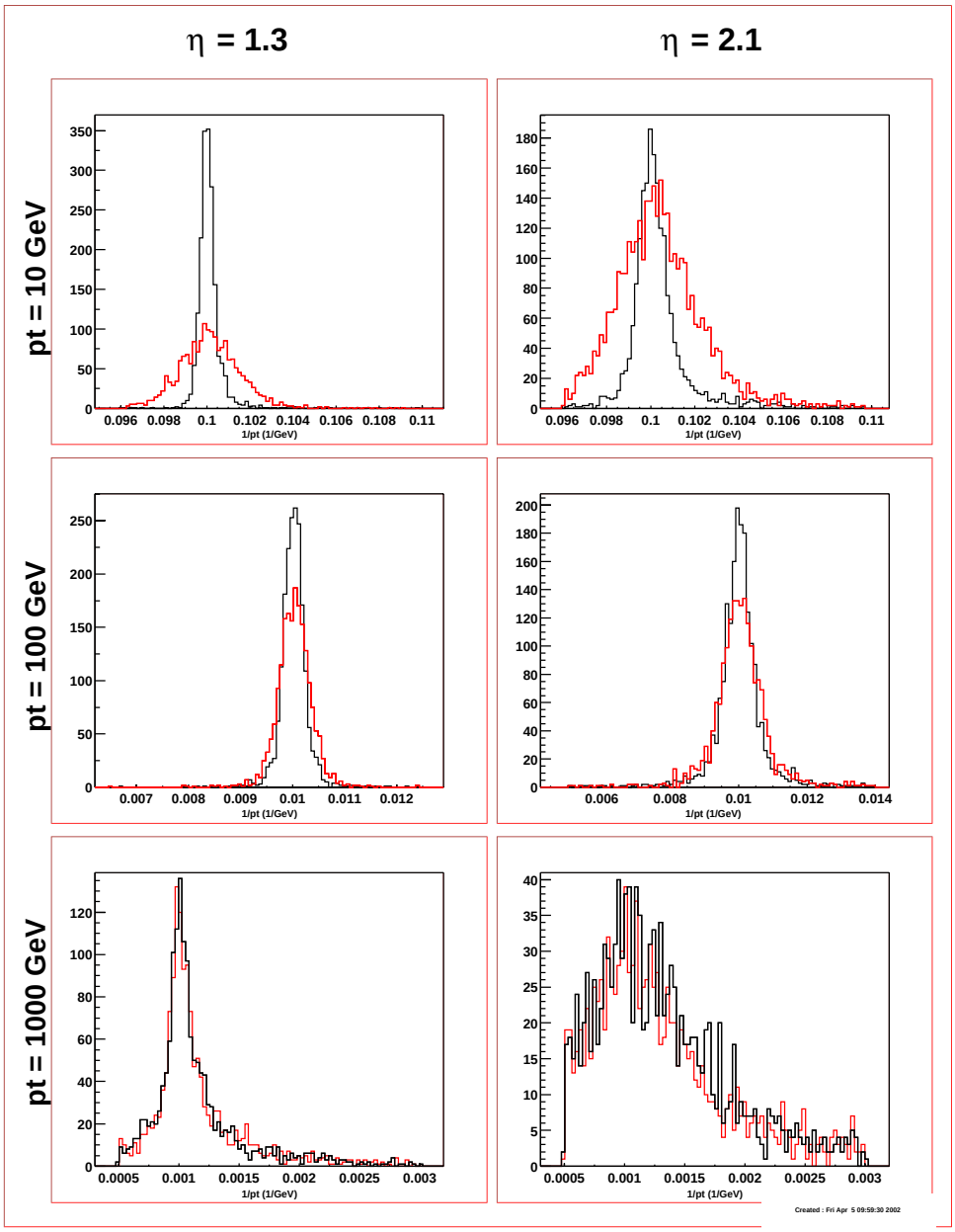

Figure 4.15: Effect of Multiple Scattering on the p_t^{-1} Distributions in the Muon System + Inner Tracker Fit (ORCA L3). The reconstructed distribution with multiple scattering is shown in (red).

Using the 3σ Efficiency estimate (Section 4.3.2) to compare the fitted p_t^{-1} residual distribution of muons with and without multiple scattering effects present, the muons reconstructed at the L2 level show comparatively less dispersion than muons reconstructed at the L3 level (Figure 4.16). This can be attributed to the comparatively coarse nature of the L2 reconstruction, where small deviations in a particles trajectory are less likely to be discerned. The increase in the number of muons outside of three sigma in the L3 residual distributions also correlates with the decrease in L3 resolution with higher.

The effect of multiple scattering on the final reconstruction of muons for all |η| is shown in Figure 4.17 and Figure 4.18. For muons with p_t = 100GeV, multiple scattering can be seen to effect the Standalone Muon System resolution on the 5-10% level, while the inclusion of the Tracker into the reconstruction minimizes the effect to 1-2%.

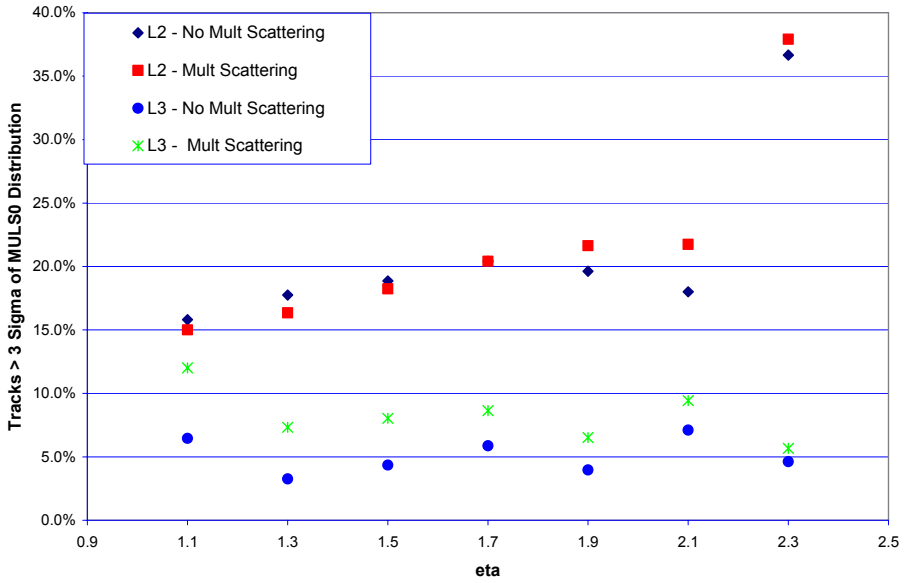

Figure 4.16: 3σ Efficiency Estimation of the ORCA L2 and L3 Residual Distributions as a Function of |η|.

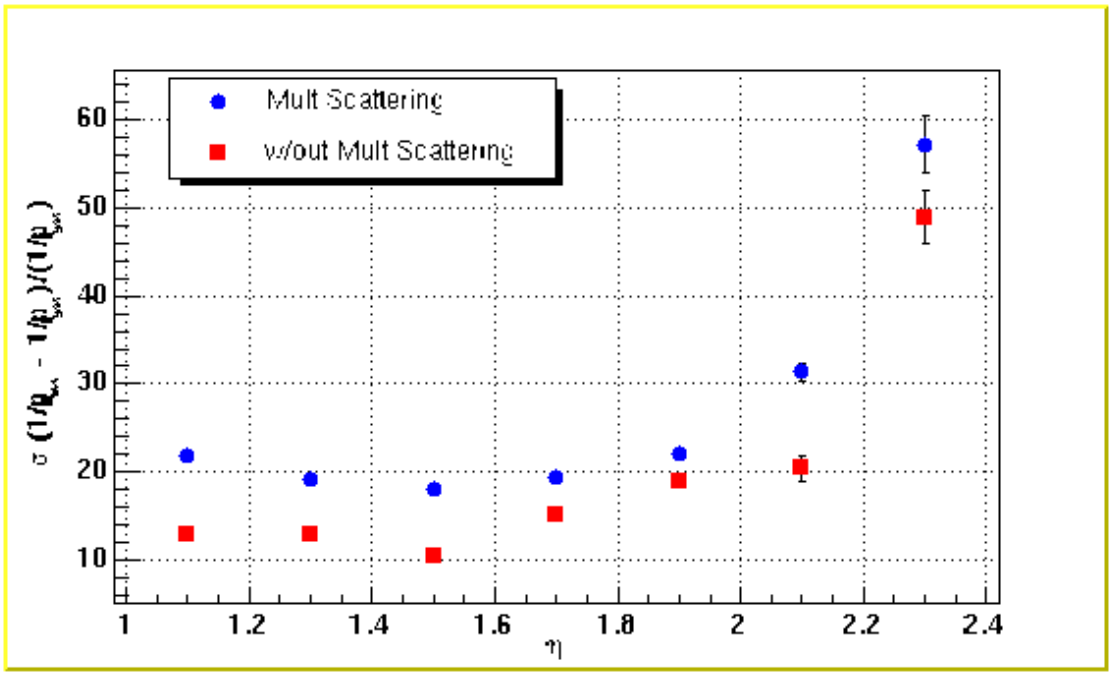

Figure 4.17: Effect of Multiple Scattering on a p_t = 100 GeV Muon Reconstructed with the Muon System Standalone + Vertex Constraint Fit (ORCA L2) as a Function of |η|.

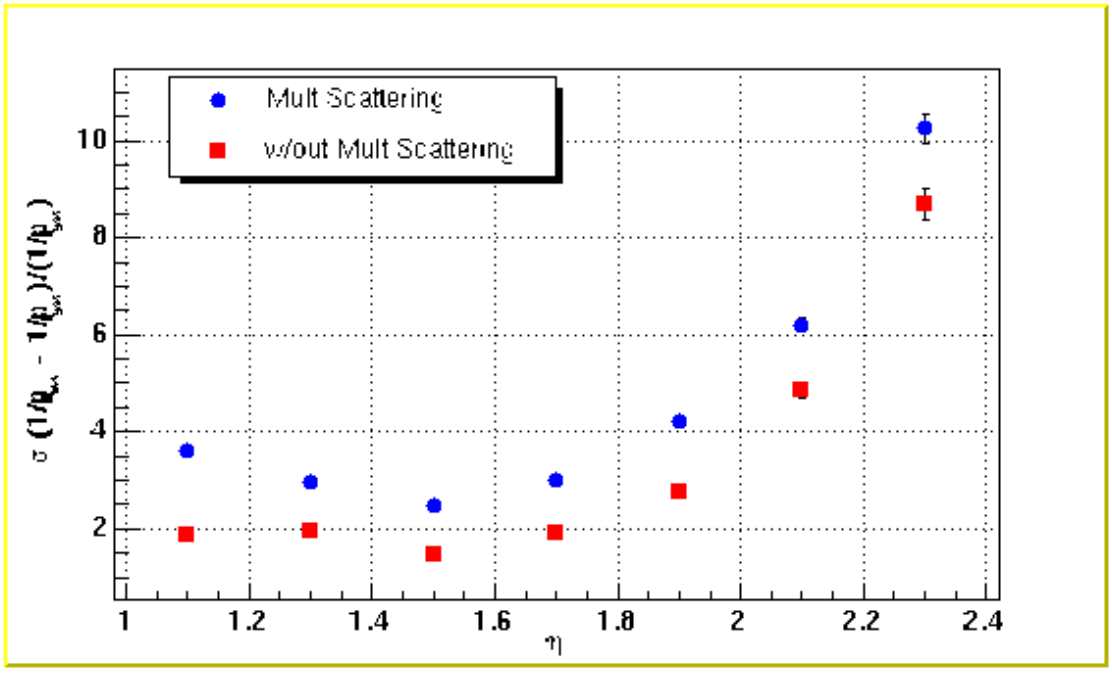

Figure 4.18: Effect of Multiple Scattering on a p_t = 100 GeV Muon Reconstructed with the Muon System +Inner Tracker Fit (ORCA L3) as a Function of |η|.

5 EFFECT OF CSC CHAMBER MISALIGNMENT

CSC chambers are expected to be surveyed after installation on the YE iron disks, but prior to the final positioning of the disks themselves. Although photogrammetric surveys similar to those used during the 2000 ISR Tests can yield resolutions of approximately 250μm when multiple views of the same object being surveyed are available, it is expected that the reduced number of viewpoints available for the survey of the CSC chambers during installation will effectively limit the resolution of some chambers positions to approximately ±1mm [5.1]. After positioning the iron disks, these uncertainties are likely to increase beyond 1mm. Once the disks are positioned in the detector, further survey will be impossible. As the magnetic field is applied in the solenoid, the iron disks are expected to move by as much as ±3mm in the CMS XY plane. Distortions in the disks themselves are expected to further shift the location of the CSC chambers. It is important to note that aside from the EMU Alignment System there are no plans to survey or otherwise determine the initial location of the ME disks once the magnetic field is activated.

A modified version of ORCA v5_3_1 was used to study of the impact of CSC chamber misalignment on p_t resolution and single muon trigger rates by supplying a random or constant shift to the location of the CSC chambers in the CMS RPhi plane prior to the reconstruction of simulated events. The Barrel Muon Drift Chambers were never misaligned. They are assumed to remain in their nominal location for all the simulations. This is likely to affect only the study results obtained for the narrow Endcap-Barrel overlap region at $|\eta| = 1.1$.

Studies of the Muon System with perfect alignment indicate that the resolution of the CMS Inner Tracker will dominate the final (ORCA L3) p_t reconstruction across all but

the highest p_t ranges (≈ 1 TeV). As a comparison of Figure 4.10 and 4.11 indicates, the ORCA L2 Reconstruction resolution may remain comparatively coarse without significantly affecting L3 Reconstruction results. The effect of slight CSC chamber misalignments on the final determination of low to moderate muon p_t should therefore be minimal when the Inner Tracker is used. Very high pt muon tracks ($p_t \approx 1000$ GeV), however, can be expected to show a greater sensitivity to misalignment in the L3 Reconstruction as the sagita measured in the Inner Tracker for these tracks will be much smaller than for similar tracks with lower p_t. The determination of muon p_t in the Muon Standalone System is also important for the Level 1 Global Muon Trigger, as the uncertainty of the p_t determination by the Standalone Muon System will affect the trigger rate.

5.1 Effect of Random CSC Misalignment on Muon p_t Reconstruction

Applying a random shift to the location of CSC chambers is intended to mimic the uncertainty associated with the placement of individual chambers on a ME disk (either before or after the application of the magnetic field). The application of random shifts was done in a manner which assures that the total distribution of all displacements applied to every individual chamber in the CMS RΦ plane matches a Gaussian distribution with a specified value of σ = 200, 500, 1000, and 2000μm. The direction of the random displacements in the CMS RΦ plane was chosen randomly from a flat distribution in Φ.

5.1.1 Effect of Random CSC Misalignment on L3 Reconstruction

The L3 Muon Reconstruction in ORCA incorporates the Inner Tracker into the final determination of muon pt. Figure 5.1 and Figure 5.2 shows the influence of the random misalignment of CSC chambers on the L3 reconstruction for low to moderate ranges of pt. Figure 5.5 presents a sample of the p_t^{-1} residual distributions for three values of generated p_t at $|\eta| = 1.9$. The dominance of the Inner Tracker in the determination of L3

resolutions reduces the sensitivity of the reconstructed L3 p_t^{-1} resolutions to random CSC misalignment for low p_t muons. Shifts in the p_t^{-1} resolutions for generated muons between 10-100 GeV are evident, though the net effect of these shifts, even for random misalignments up to 2mm, generally reduces the net resolution of the final L3 resolutions by $\leq$ 1%. The sensitivity of the L3 p_t^{-1} resolutions to random misalignment are summarized in Table 5.1 as the relative change in p_t^{-1} resolution (σ) as defined by Equation 5.1:

$$\text{Relative Change in } p_t^{-1} \text{ Resolution} = \frac{\sigma_{misalignment} - \sigma_{perfectalignment}}{\sigma_{perfectalignment}} \times 100\% \qquad \text{Equation 5.1}$$

Table 5.1 indicates that the sensitivity of low p_t muons (< 100 GeV) to random chamber misalignment is minimal for all magnitudes of misalignment up to 2mm, where the effect reaches up to the 10% level. For muons with p_t = 100GeV, the loss of resolution for 1mm of misalignment is equivalent to 2mm of misalignment at lower p_t (20-50 GeV). For p_t = 100 GeV muons, the relative shift in resolutions reaches the 20-30% level at 2mm of misalignment. The impact of misalignment is larger in regions of high $|\eta|$, where it was previously noted to have a larger uncertainty in reconstructed p_t compared to lower regions of $|\eta|$.

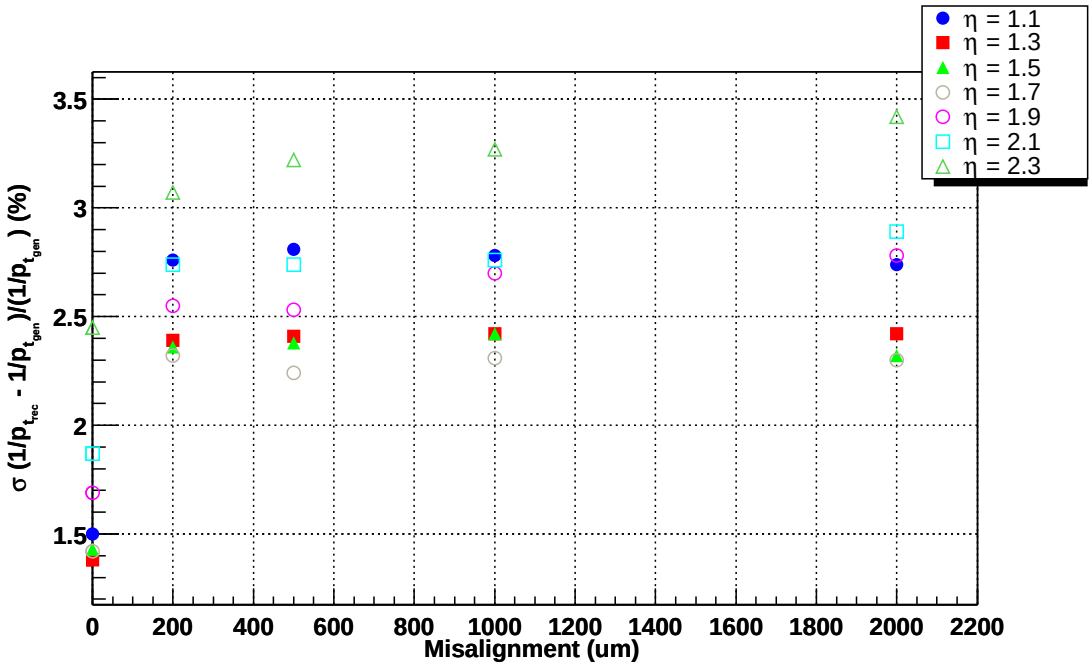

Figure 5.1: Muon System + Inner Tracker (ORCA L3) Resolution for the Reconstruction of p_t = 10 GeV Muons vs. Random CSC Misalignment.

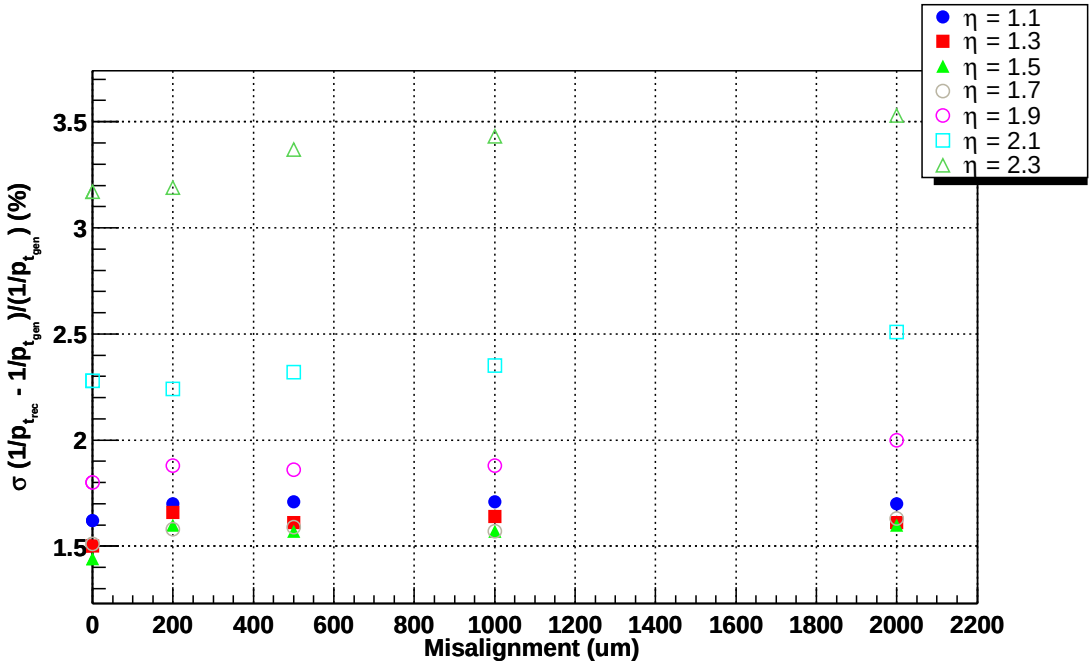

Figure 5.2: Muon System + Inner Tracker (ORCA L3) Resolution for the Reconstruction of p_t = 20 GeV Muons vs. Random CSC Misalignment.

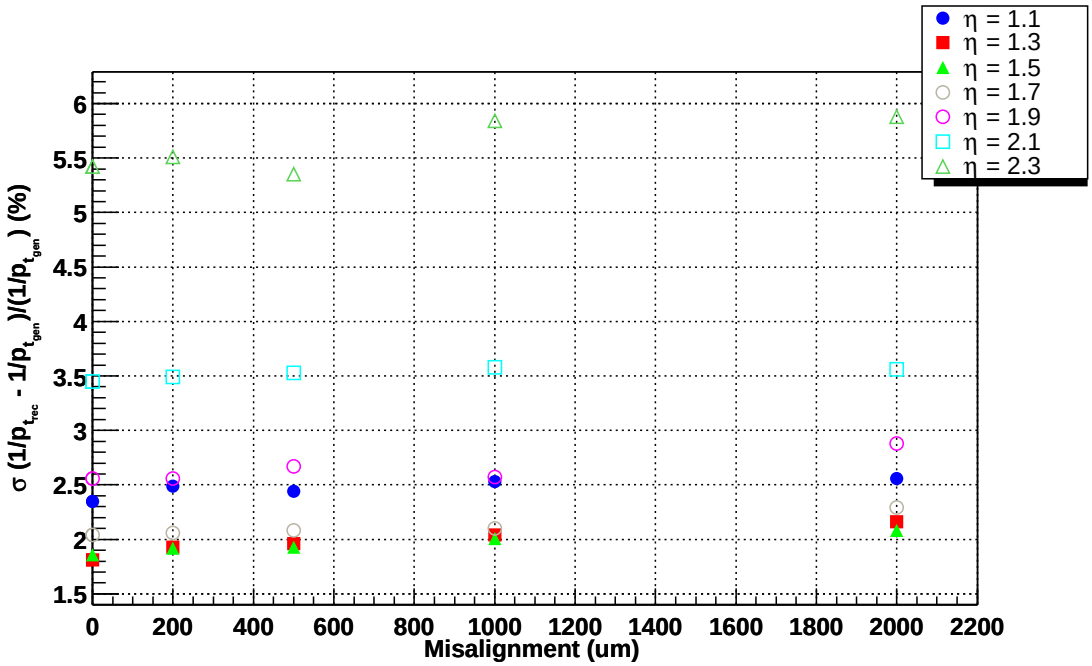

Figure 5.3: Muon System + Inner Tracker (ORCA L3) Resolution for the Reconstruction of P_t = 50 GeV Muons vs. Random CSC Misalignment.

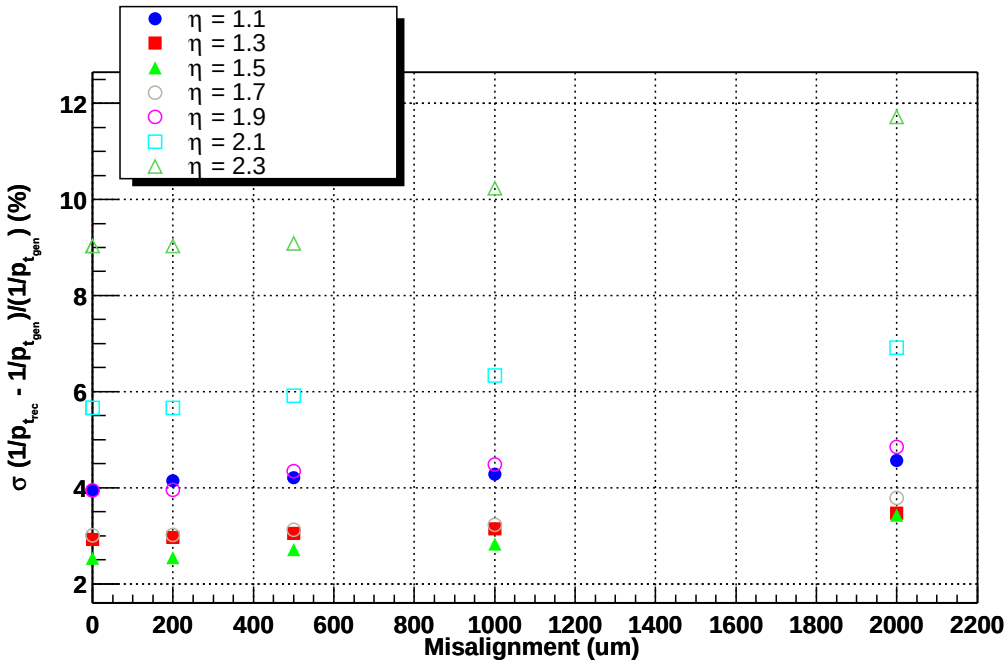

Figure 5.4: Muon System + Inner Tracker (ORCA L3) Resolution for the Reconstruction of P_t = 100 GeV Muons vs. Random CSC Misalignment.

Table 5.1: Relative shift in L3 Muon System + Inner Tracker p_t^{-1} resolutions from perfect alignment with random CSC misalignment. The relative shift in the resolution is defined by Equation 5.1.

L3		CSC Misalignment			
		200um	500um	1mm	2mm
pt=20 GeV	eta = 1.1	5%	6%	6%	5%
	eta = 1.3	11%	7%	9%	7%
	eta = 1.5	11%	9%	9%	11%
	eta = 1.7	5%	5%	4%	8%
	eta = 1.9	4%	3%	4%	11%
	eta = 2.1	0%	2%	3%	10%
	eta = 2.3	1%	6%	8%	11%
pt=50 GeV					
	eta = 1.1	6%	4%	8%	9%
	eta = 1.3	7%	8%	13%	19%
	eta = 1.5	3%	4%	8%	12%
	eta = 1.7	1%	2%	3%	12%
	eta = 1.9	0%	4%	0%	13%
	eta = 2.1	1%	2%	4%	3%
	eta = 2.3	2%	0%	8%	8%
pt=100 GeV					
	eta = 1.1	5%	7%	8%	16%
	eta = 1.3	2%	4%	8%	19%
	eta = 1.5	0%	7%	12%	36%
	eta = 1.7	0%	4%	7%	26%
	eta = 1.9	0%	10%	13%	23%
	eta = 2.1	0%	4%	12%	22%
	eta = 2.3	0%	0%	12%	28%
pt=1000 GeV					
	eta = 1.1	4%	18%	69%	110%
	eta = 1.3	28%	40%	61%	92%
	eta = 1.5	5%	3%	23%	50%
	eta = 1.7	21%	35%	77%	50%
	eta = 1.9	21%	26%	56%	53%
	eta = 2.1	18%	26%	63%	105%
	eta = 2.3	7%	69%	57%	65%

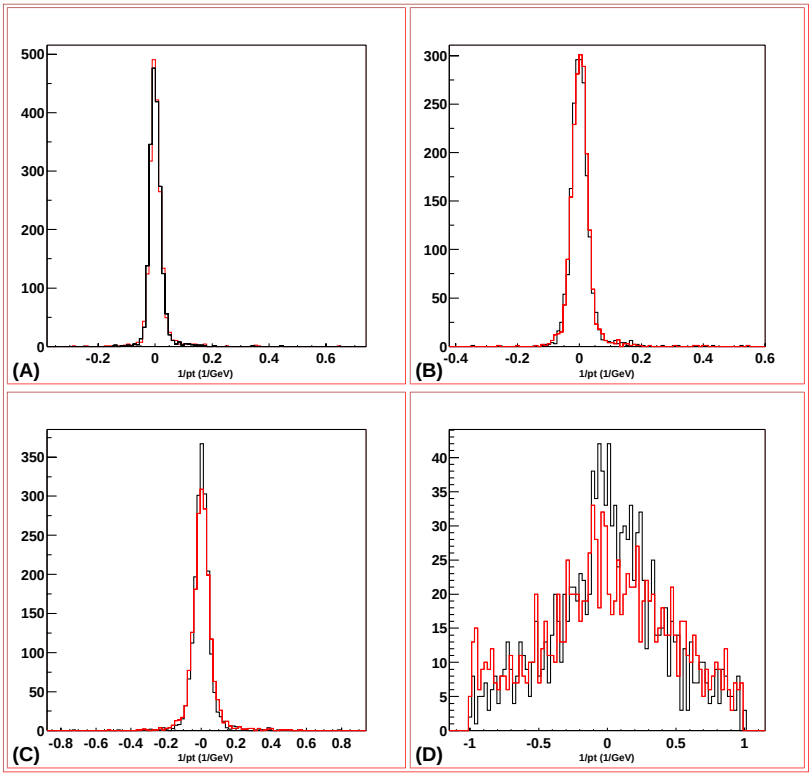

Figure 5.5: Sample p_t^{-1} Muon System + Inner Tracker (ORCA L3) Residual Distributions Before (in black) and After (in Red) ±1mm Random CSC Misalignment at $|\eta| = 1.9$ for p_t = (A) 20 GeV, (B) 50 GeV, (C) 100 GeV, and (D) 1000 GeV.

The L3 reconstruction of high p_t muons ($p_t \approx 1000$ GeV) will rely more on the Muon System than lower p_t, as large momenta will produce small sagitas which will be difficult to resolve in the Inner Tracker. Figure 5.6 shows the variation in L3 p_t^{-1} resolution as a function of random CSC misalignments for $p_t = 1000$ GeV muons. The effect is much larger than for lower p_t muons, as even moderate misalignments introduce net shifts exceeding 10% of the resolution without misalignment. The sensitivity of the L3 p_t^{-1} resolutions are summarized in Table 5.1 as the relative change in p_t^{-1} resolution with chamber misalignment again defined by Equation 5.1. Table 5.1 indicates that the resolutions in several regions of eta degrade by 20-30% for only 200μm of random misalignment. Misalignments beyond 200um further degrade p_t resolution past the 50% level. Sensitivity to random chamber misalignment is even observed at $|\eta| = 1.1$, where

the particle trajectory allows several points of measurement by the Barrel Muon drift chambers which have not been misaligned. The residual values are also seen to exceed 100% for the regions of $|\eta| \geq 2.1$ with random CSC displacements of 2mm.

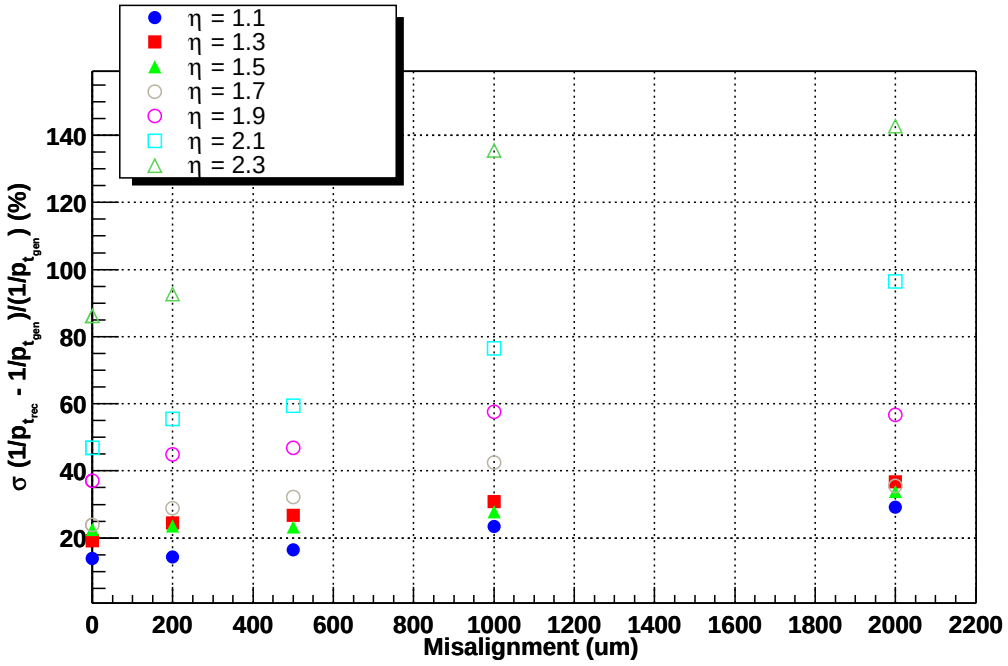

Figure 5.6: Muon System + Inner Tracker (ORCA L3) Resolution for the Reconstruction of P_t = 1000 GeV Muons vs. Random CSC Misalignment.

The effect of misalignment on the quality of L3 residual distributions is shown in Table 5.2 as the 3σ Efficiency estimation defined in Section 4.3.2. The increase in entries outside the three sigma limit of the original distribution is directly attributable to the dispersion of events near the central distribution. It should be noted that even the L3 residual distributions from perfect CSC alignment show a much higher number of entries beyond three standard deviations than is expected from a perfect Gaussian distribution, where 1.3% of entries are expected outside of the three σ limit. As Table 5.2 and Figure 5.5 indicate, the L3 residual distributions typically remain well behaved for $p_t \leq 100$ GeV with random CSC misalignments up to and including 2mm. For 2mm of random CSC misalignment, the fraction of entries beyond three standard deviations of the original

distribution for muons with p_t = 100 GeV almost doubles, though this increase occurs after 1mm of random misalignment has been introduced. Table 5.2 and Figure 5.5 also indicate that the L3 residual distributions for muons with p_t =1000 GeV are comparatively less well formed than similar distributions at lower p_t.

Table 5.2: Percentage of Entries Beyond Three Standard Deviations of the Initial Muon System + Inner Tracker (ORCA L3) p_t^{-1} Residual Distributions for Various Degrees of Misalignments.

L3		CSC Misalignment				
		None	200um	500um	1mm	2mm
pt=20 GeV	eta = 1.1	8%	7%	7%	7%	7%
	eta = 1.3	6%	5%	6%	5%	6%
	eta = 1.5	3%	3%	3%	3%	3%
	eta = 1.7	3%	3%	3%	3%	3%
	eta = 1.9	3%	4%	4%	5%	7%
	eta = 2.1	4%	5%	5%	4%	6%
	eta = 2.3	6%	7%	6%	7%	8%
pt=50 GeV	eta = 1.1	9%	8%	8%	7%	8%
	eta = 1.3	4%	4%	4%	4%	5%
	eta = 1.5	2%	2%	2%	2%	4%
	eta = 1.7	4%	4%	5%	5%	6%
	eta = 1.9	3%	3%	3%	4%	5%
	eta = 2.1	5%	5%	5%	6%	7%
	eta = 2.3	7%	12%	13%	13%	16%
pt=100 GeV	eta = 1.1	8%	7%	7%	8%	8%
	eta = 1.3	3%	3%	3%	4%	5%
	eta = 1.5	3%	2%	4%	4%	7%
	eta = 1.7	6%	5%	6%	7%	11%
	eta = 1.9	4%	5%	5%	7%	7%
	eta = 2.1	6%	6%	7%	8%	11%
	eta = 2.3	7%	6%	7%	8%	12%
pt=1000 GeV	eta = 1.1	18%	18%	21%	23%	34%
	eta = 1.3	18%	24%	17%	16%	18%
	eta = 1.5	10%	12%	11%	11%	21%
	eta = 1.7	16%	8%	9%	8%	22%
	eta = 1.9	8%	7%	8%	10%	11%
	eta = 2.1	15%	12%	11%	11%	17%
	eta = 2.3	20%	25%	24%	24%	22%

5.1.2 Effect of Random CSC Misalignment L2 Reconstruction

As outlined in the ORCA simulations detailing the intrinsic performance of the ORCA L2 Muon Reconstruction, the resolutions obtained for the reconstruction of muon p_t depend strongly on the particular value of $|\eta|$ being examined. The effect of misalignment for p_t=10, 20, 50, and 100 GeV tracks on ORCA L2 Muon Reconstruction p_t resolutions are summarized as a function of $|\eta|$ in Figure 5.7 - Figure 5.10. A sample of the resulting p_t^{-1} residual distributions before and after ±1mm of random CSC misalignment for p_t=20, 50, 100, and 1000 GeV are shown in Figure 5.11. The effect of even slight CSC misalignment ($\geq$ 200 μm) on muons with p_t=1000 GeV was significant enough to prevent a successful fit to a Gaussian distribution for most values of eta. Table 5.3 summarizes the sensitivity of the Muon Standalone + Vertex (L2) p_t^{-1} resolutions to the random CSC misalignments introduced as defined.

In general, the sensitivity of the reconstructed p_t^{-1} resolutions can be seen to increase for regions of high $|\eta|$ and high muon p_t. The one exception to this trend appears at $|\eta|$ = 1.5, where neighboring regions of $|\eta|$ show less sensitivity to random misalignments. It is not clear why p_t resolutions should exhibit an increased sensitivity to misalignment in this region, though it lies in an area where muon trajectories just miss measurement by ME 1/1 and exit the central detector at the end of the solenoid. Conversely, p_t resolutions at $|\eta|$ = 1.1 typically lag the large shifts which the random misalignments induced at high values of $|\eta|$. This occurs because the Barrel Muon drift chambers have not been misaligned and muons in this region traverse the Barrel-Endcap overlap region where measurement by Barrel Drift chambers is possible.

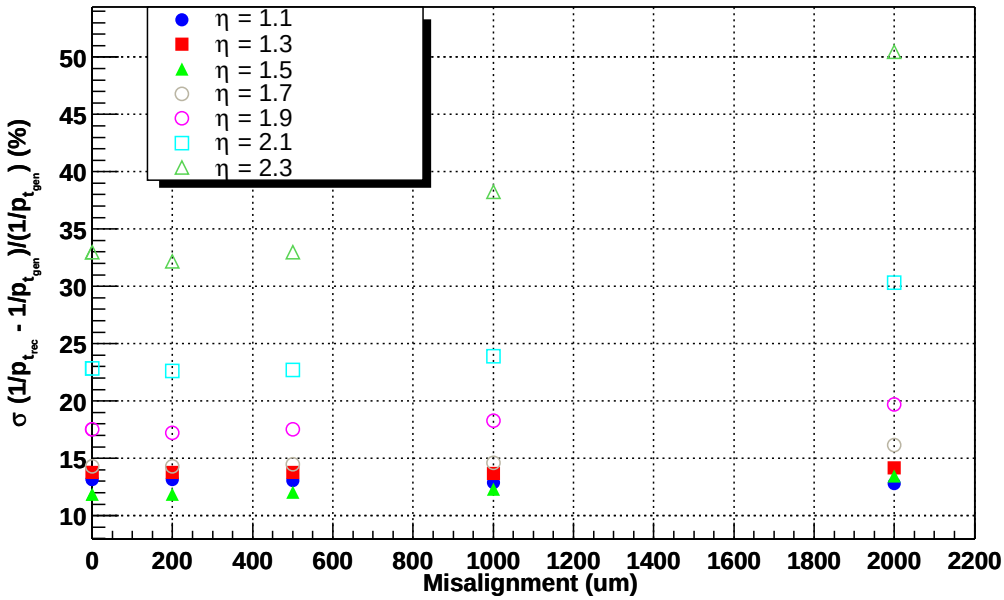

Figure 5.7: Standalone Muon System + Vertex Constraint (ORCA L2) Resolution for the Reconstruction of P_t = 10 GeV Muons vs. Random CSC Misalignment

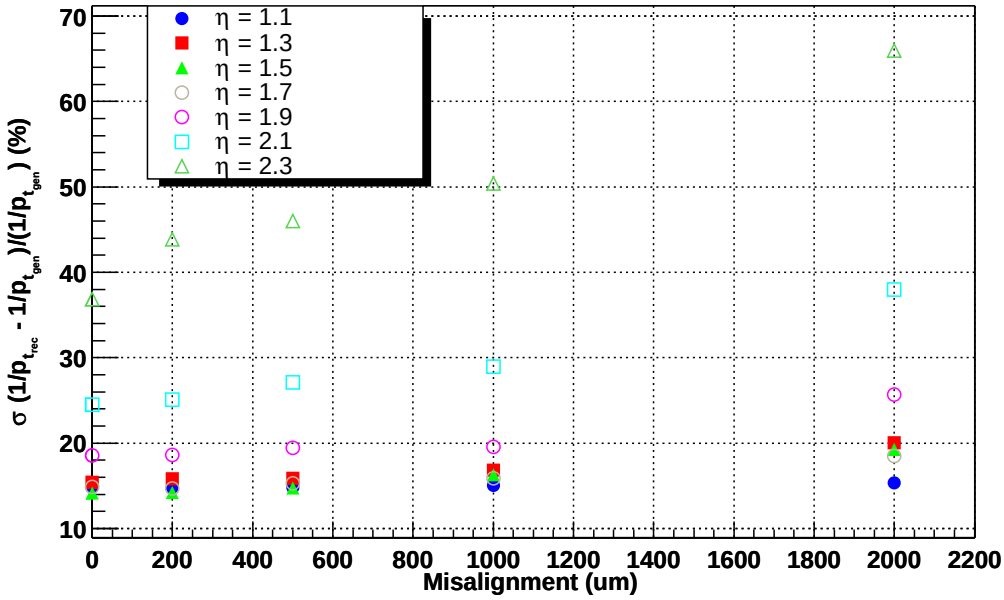

Figure 5.8: Standalone Muon System + Vertex Constraint (ORCA L2) Resolution for the Reconstruction of P_t = 20 GeV Muons vs. Random CSC Misalignment.

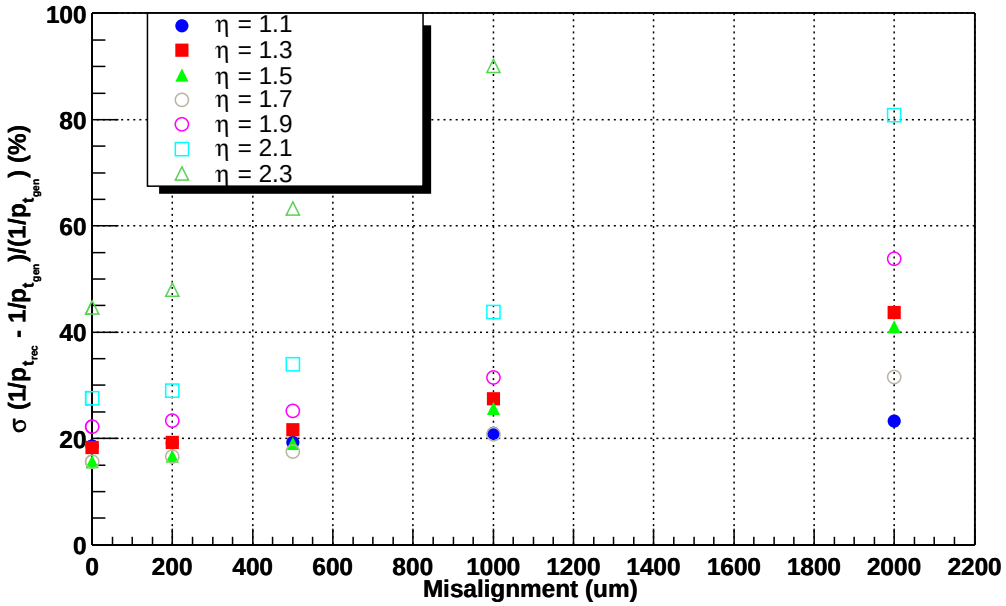

Figure 5.9: Standalone Muon System + Vertex Constraint (ORCA L2) Resolution for the Reconstruction of P_t = 50 GeV Muons.

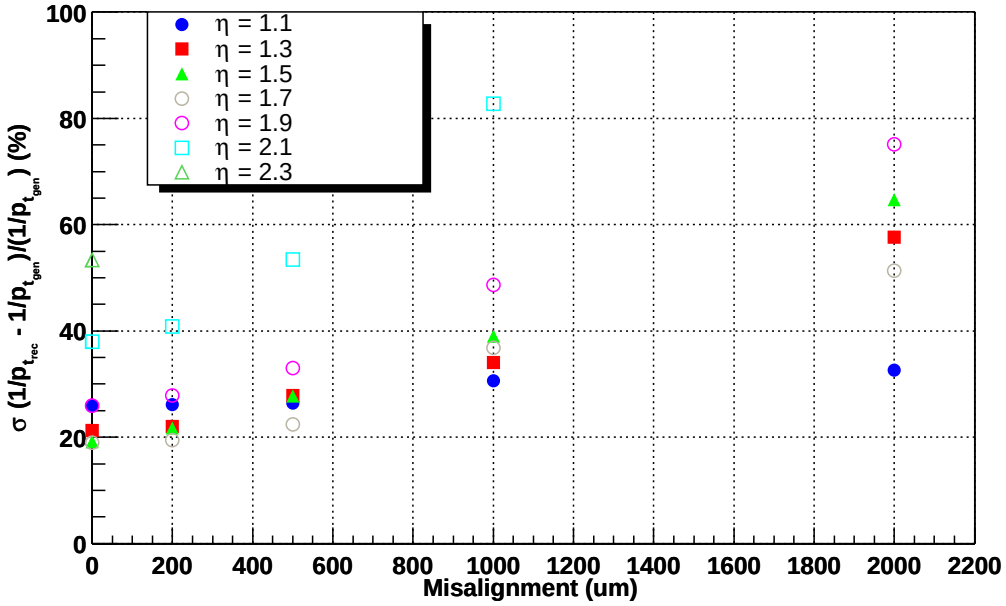

Figure 5.10: Standalone Muon System + Vertex Constraint (ORCA L2) Resolution for the Reconstruction of P_t = 100 GeV Muons.

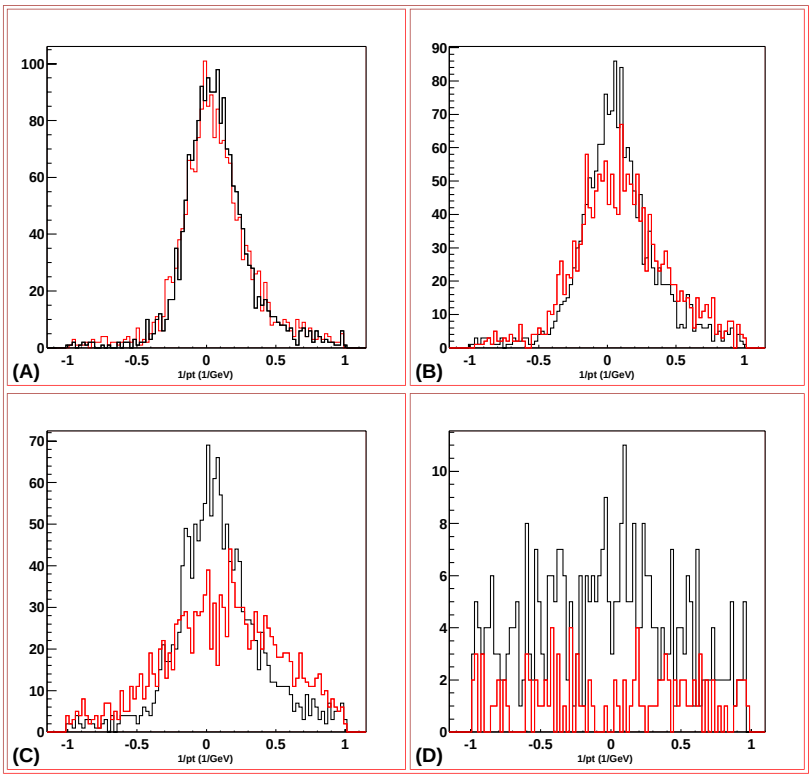

Figure 5.11: Sample p_t^{-1} Standalone Muon System + Vertex Constraint (ORCA L2) Residual Distributions Before (in black) and After (in Red) ±1mm Random CSC Misalignment at $|\eta|$ = 1.9 for p_t = (A) 20 GeV, (B) 50 GeV, (C) 100 GeV, and (D) 1000 GeV.

As larger misalignments were introduced, several of the residual distributions at high $|\eta|$ and/or high p_t became very difficult to fit with a Gaussian distribution. These distributions at times had p_t resolutions which exceeded 100% and showed a significant dispersion when compared to the distributions obtained with the nominal placement of CSC chambers. The dispersion in the L2 p_t^{-1} residual distributions was estimated by the percentage of entries in the distribution which exceeded three standard deviations of the original (perfect alignment) distribution. The effect of misalignment on the dispersion of p_t measurements is shown in Table 5.4. The dispersion of entries in the distribution does not necessarily indicate that the quality of the applied fit to estimate the resolution of the measurement is degrading, but that the overall distribution is expanding. Of particular importance is the size of the tails (very high and very low p_t measurements). These tails may allow background muons which should be rejected by the Level 1 Trigger to be

erroneously assigned a higher p_t value which exceeds the trigger threshold. Conversely, the high p_t tracks that will be of principle interest with a low p_t assignment could be immediately rejected by the L1 Muon Trigger. The rejection of these events is not described by the resolutions presented in Table 5.3 and Figure 5.6 - Figure 5.10, as the fits used to make these estimates are constrained around the central distributions. The fraction of entries in the residual distributions can be seen to remain relatively constant up to random CSC misalignments of 1mm for $p_t \leq 100$ GeV. At 2mm of misalignment, the number of entries begins to increase and is an indication that the entire distribution, primarily the tail, is dispersing.

Table 5.3: Relative shift in ORCA L2 Standalone Muon System + Vertex Constraint p_t^{-1} resolutions from perfect alignment with random CSC misalignment. The relative shift in the resolution is defined by Equation 5.1.

L2		200um	500um	1mm	2mm
pt=10 GeV	eta = 1.1	0%	0%	0%	0%
	eta = 1.3	0%	0%	0%	3%
	eta = 1.5	0%	1%	4%	14%
	eta = 1.7	0%	1%	2%	13%
	eta = 1.9	0%	0%	4%	12%
	eta = 2.1	0%	0%	5%	33%
	eta = 2.3	0%	0%	16%	53%
pt=20 GeV					
	eta = 1.1	0%	0%	1%	3%
	eta = 1.3	3%	3%	9%	30%
	eta = 1.5	1%	4%	15%	36%
	eta = 1.7	0%	3%	7%	25%
	eta = 1.9	0%	5%	5%	38%
	eta = 2.1	2%	11%	18%	55%
	eta = 2.3	19%	19%	37%	79%
pt=50 GeV					
	eta = 1.1	3%	3%	13%	25%
	eta = 1.3	6%	18%	50%	139%
	eta = 1.5	7%	22%	65%	163%
	eta = 1.7	6%	12%	33%	102%
	eta = 1.9	5%	13%	41%	142%
	eta = 2.1	5%	23%	59%	193%
	eta = 2.3	7%	42%	102%	308%
pt=100 GeV					
	eta = 1.1	1%	2%	18%	26%
	eta = 1.3	3%	31%	60%	171%
	eta = 1.5	13%	44%	103%	237%
	eta = 1.7	2%	18%	94%	170%
	eta = 1.9	7%	27%	88%	190%
	eta = 2.1	8%	41%	118%	442%
	eta = 2.3	27%	130%	242%	621%

Table 5.4: Percentage of Entries Beyond Three Standard Deviations of the Initial Muon System + Inner Tracker (ORCA L2) p_t^{-1} Residual Distributions for Various Degrees of Misalignments.

L2		CSC Misalignment				
		None	200um	500um	1mm	2mm
pt=10 GeV	eta = 1.1	5%	5%	5%	5%	5%
	eta = 1.3	4%	4%	4%	4%	4%
	eta = 1.5	5%	5%	5%	5%	5%
	eta = 1.7	7%	7%	7%	8%	12%
	eta = 1.9	6%	5%	6%	6%	9%
	eta = 2.1	7%	7%	7%	8%	10%
	eta = 2.3	16%	17%	17%	18%	22%
pt=20 GeV						
	eta = 1.1	6%	6%	6%	6%	6%
	eta = 1.3	6%	6%	6%	6%	7%
	eta = 1.5	7%	7%	8%	9%	11%
	eta = 1.7	10%	10%	9%	10%	13%
	eta = 1.9	10%	10%	10%	12%	17%
	eta = 2.1	11%	11%	11%	12%	21%
	eta = 2.3	15%	15%	15%	16%	18%
pt=50 GeV						
	eta = 1.1	11%	11%	11%	11%	13%
	eta = 1.3	10%	11%	11%	16%	28%
	eta = 1.5	12%	13%	13%	18%	30%
	eta = 1.7	15%	15%	15%	17%	24%
	eta = 1.9	19%	19%	21%	22%	34%
	eta = 2.1	20%	20%	22%	25%	45%
	eta = 2.3	23%	24%	26%	31%	53%
pt=100 GeV						
	eta = 1.1	14%	14%	14%	16%	17%
	eta = 1.3	16%	16%	18%	24%	37%
	eta = 1.5	20%	19%	22%	29%	43%
	eta = 1.7	25%	24%	24%	30%	38%
	eta = 1.9	27%	27%	28%	35%	49%
	eta = 2.1	28%	29%	29%	36%	52%
	eta = 2.3	34%	34%	40%	42%	64%

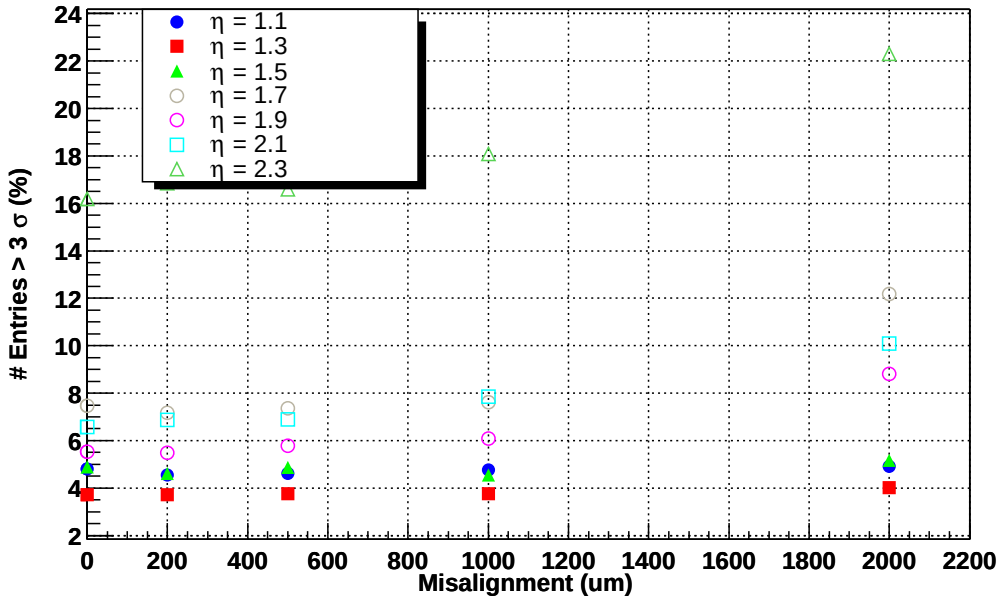

Figure 5.12: Percentage of Entries in the Muon Standalone + Vertex Constraint (ORCA L2) p_t^{-1} Residual Distributions which Exceed Three Standard Deviations of the Original (Perfect Alignment) Residual Distribution as a Function of Random CSC Misalignment for p_t=10 GeV.

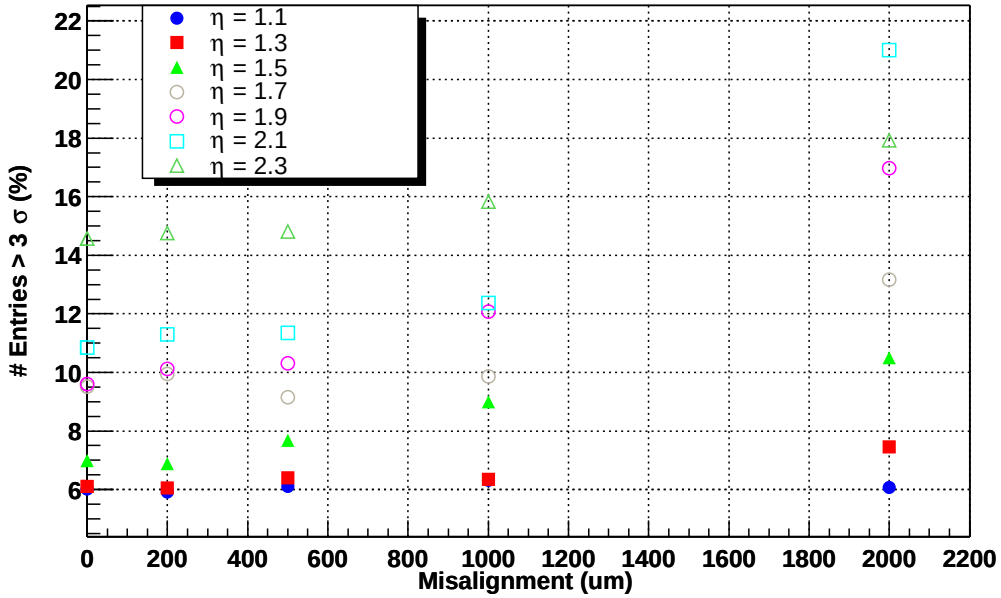

Figure 5.13: Percentage of Entries in the Muon Standalone + Vertex Constraint (ORCA L2) p_t^{-1} Residual Distributions which Exceed Three Standard Deviations of the Original (Perfect Alignment) Residual Distribution as a Function of Random CSC Misalignment for p_t=20 GeV.

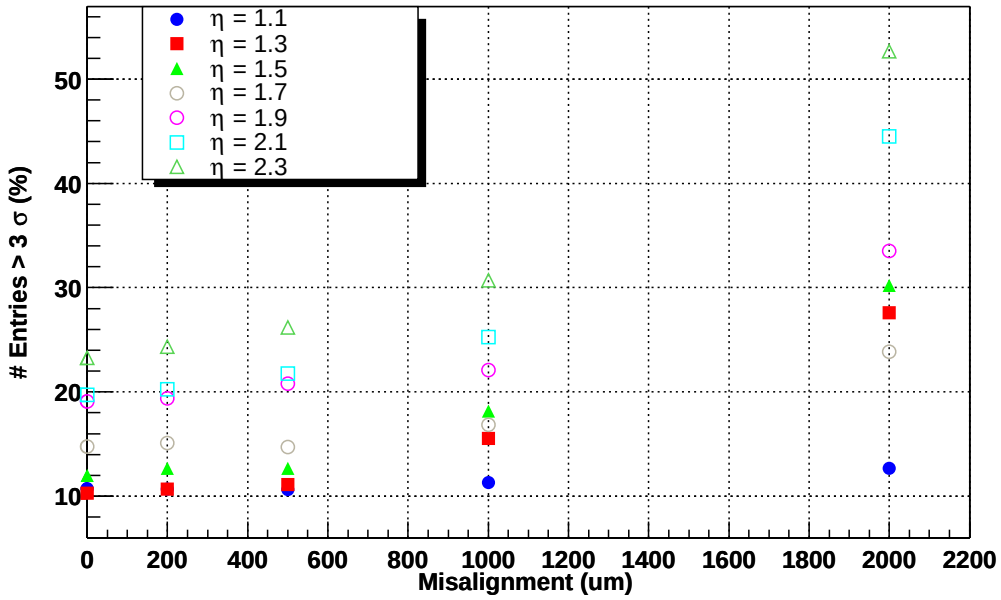

Figure 5.14: Percentage of Entries in the Muon Standalone + Vertex Constraint (ORCA L2) p_t^{-1} Residual Distributions which Exceed Three Standard Deviations of the Original (Perfect Alignment) Residual Distribution as a Function of Random CSC Misalignment for p_t=50 GeV.

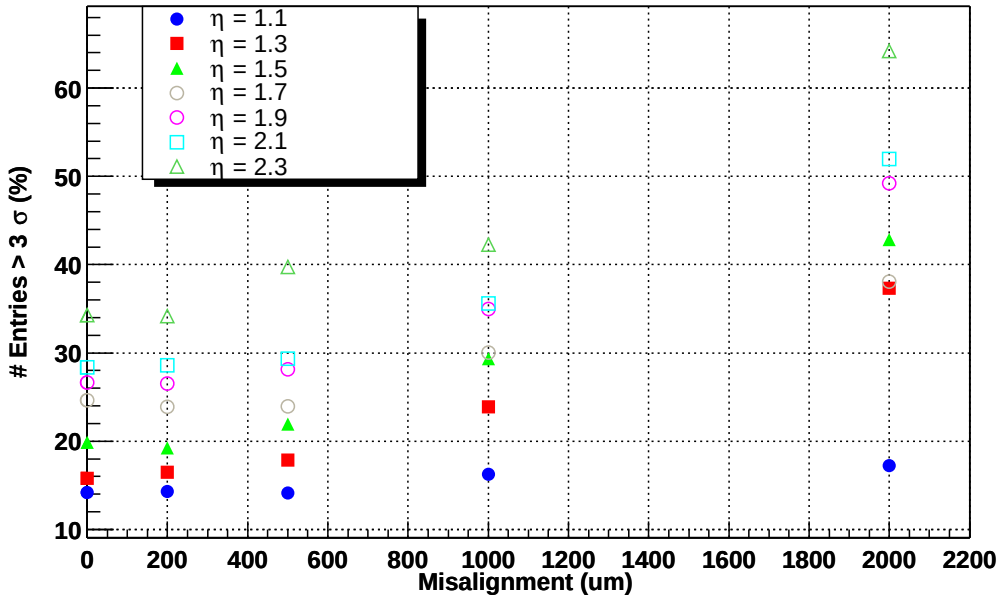

Figure 5.15: Percentage of Entries in the Muon Standalone + Vertex Constraint (ORCA L2) p_t^{-1} Residual Distributions which Exceed Three Standard Deviations of the Original (Perfect Alignment) Residual Distribution as a Function of Random CSC Misalignment for p_t=100 GeV.

5.2 Effect of ME Station Misalignment on Muon p_t Reconstruction

Muon Endcap station misalignment was examined in ORCA by applying a constant shift to all chambers in a particular ME disk. There are presently no plans (aside from the EMU Alignment System) to provide additional survey measurements to determine the location of the ME disks once the magnetic field is activated. The combination of all possible ME disk motions is quite large, so only one possible subset of the motions are considered for this study. It is presumed that the worst case scenario for the misalignment of ME disks will shift neighboring YE Iron disks in opposite directions. Since ME ±2 and ME ±3 CSC chambers are mounted on the same YE iron disk (see Figure 1.5), a constant shift of 1, 2, and 3mm along the CMS +X axis for ME ±1 and ±4 and the CMS –X axis for ME ±2 and ±3 have been chosen for this study.

5.2.1 Effect of ME Disk Misalignment (Constant Shift) on L3 Reconstruction

The Muon System + Inner Tracker resolution for the reconstruction of single muon tracks is shown in Figure 5.16-Figure 5.19 as a function of ME Station displacement. The plots indicate that the decrease in p_t^{-1} resolution for low p_t muons is generally no worse than what was observed under random misalignments. Muons with p_t = 100 GeV behave in a similar manner for ME disk misalignment of 1mm, but the high $|\eta|$ regions quickly degrade beyond that. Muons with p_t = 1000 GeV showed a substantial drop in p_t^{-1} resolution across all $|\eta|$ for entire range of ME station motions simulated.

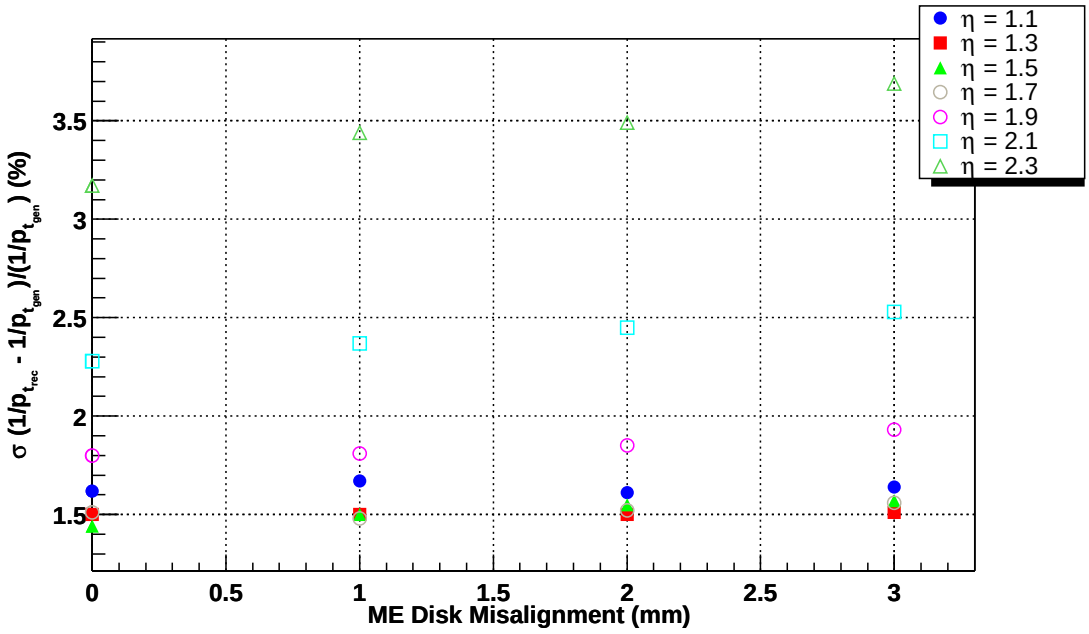

Figure 5.16: Muon System + Inner Tracker (ORCA L3) Reconstruction Resolution for p_t = 20 GeV Muons as a Function of ME Station Misalignment.

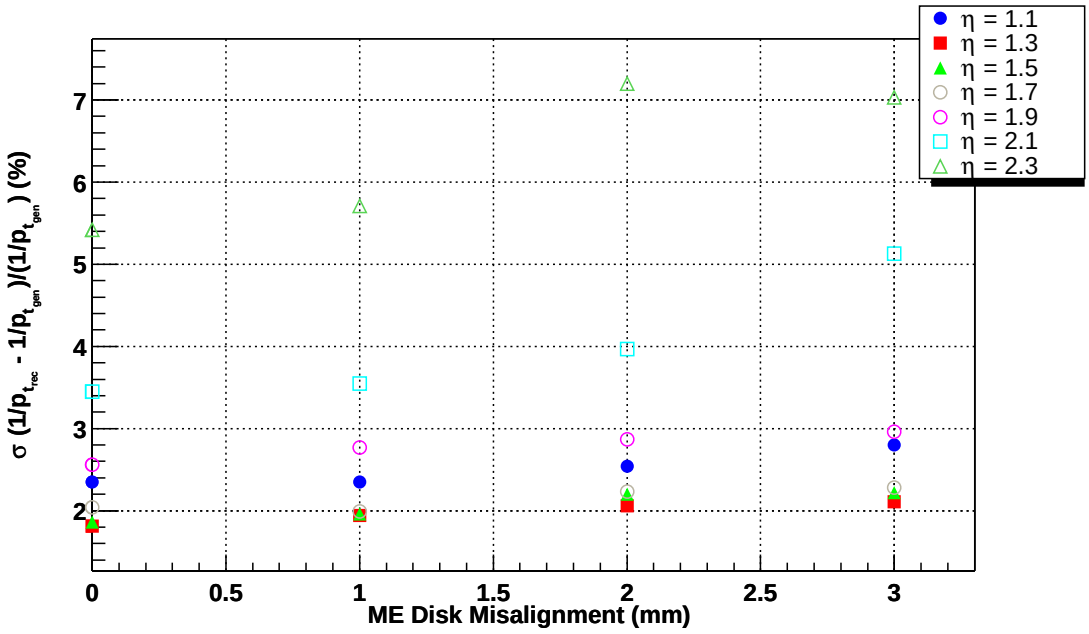

Figure 5.17: Muon System + Inner Tracker (ORCA L3) Reconstruction Resolution for p_t = 50 GeV Muons as a Function of ME Station Misalignment.

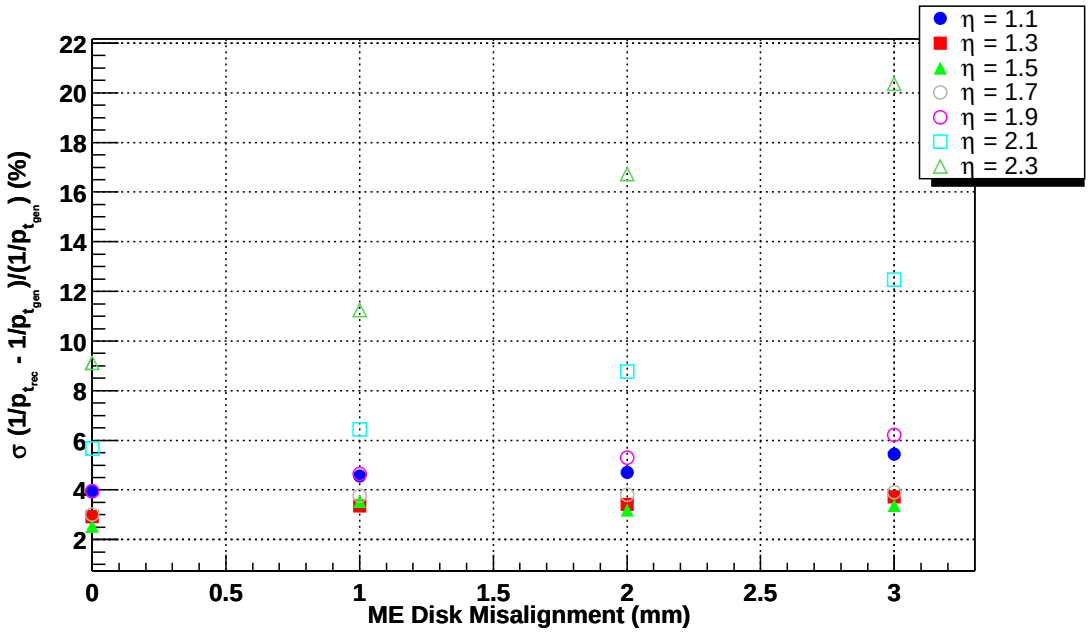

Figure 5.18: Muon System + Inner Tracker (ORCA L3) Reconstruction Resolution for p_t = 100 GeV Muons as a Function of ME Station Misalignment.

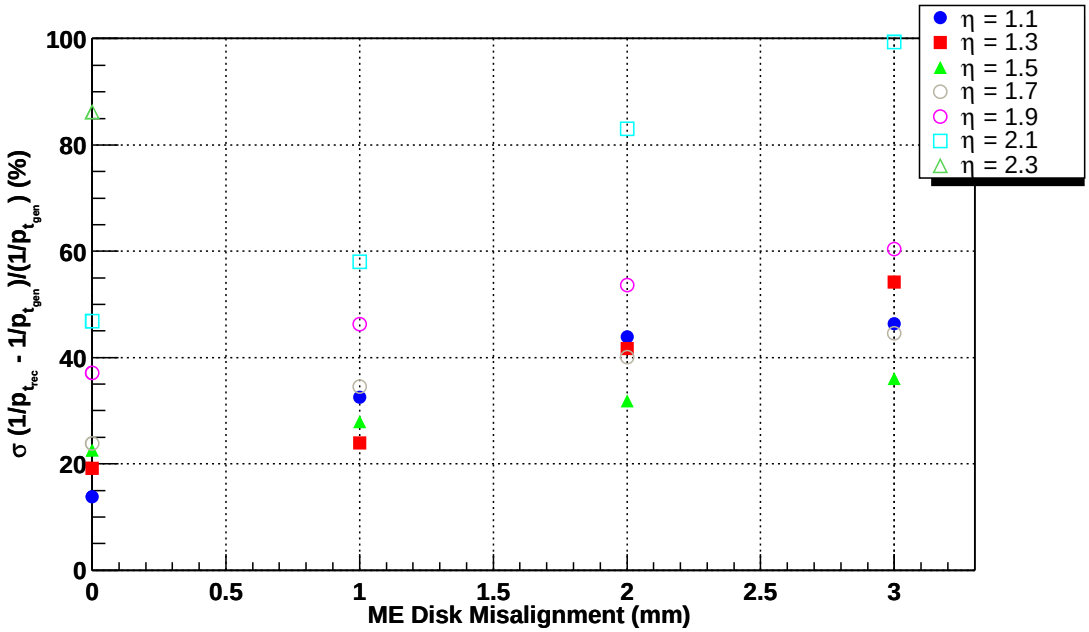

Figure 5.19: Muon System + Inner Tracker (ORCA L3) Reconstruction Resolution for p_t = 1000 GeV Muons as a Function of ME Station Misalignment.

5.2.2 Effect of ME Disk Misalignment (Constant Shift) on L2 Reconstruction

The net effect of displacing ME stations across the same axis is to systematically offset the relative placement of cathode strip positions between chambers in opposing stations. For displacements of ME stations along the CMS X axis, this means that the relative strip positions between chambers located near the CMS X axis will shift primarily along the CMS R coordinate, while relative strip positions located between chambers along the CMS Y axis will shift primarily along the CMS RΦ coordinate. Since the muon p_t is primarily determined from the difference in the azimuthal angle of the particle between the points of measurement at each ME station, chambers which are shifted primarily along the CMS R coordinate are expected to show very little sensitivity to the net displacement, as the motion is directed primarily along the length of the CSC. CSC chambers located near the CMS Y axis are expected to have a heightened sensitivity to ME station displacements along the CMS X axis, as these displacements will dramatically increase the separation between the strips in the CMS Φ coordinate. A sample of the muons reconstructed with the Muon Standalone + Vertex Constraint (ORCA L2) fit is shown in Figure 5.20 for a new shift of 1mm along the CMS X axis as a function of the location of the muon in CMS Φ. The sinusoidal pattern evident in the distributions is caused by the relative insensitivity of the reconstruction to shifts along the length of the CSC strips. The amplitude of the patterns increases as the shift (i.e. misalignment) between ME Stations increases. The effect is not seen in the ORCA L3 reconstruction due to the dominate resolution of the Inner Tracker.

A summary of the Muon Standalone + Vertex Constraint p_t^{-1} resolution is shown as a function of ME Station misalignment in Figure 5.20-Figure 5.24. With the application of Equation 5.1, the relative decrease in resolution is given for ME Station misalignment in Table 5.5. The resolutions presented in the figures and table are averaged over all values of phi. These plots show that the systematic shifting of the YE iron disks along the CMS X axis in the manner previously described leads to a substantial drop in L2 p_t^{-1} resolution.

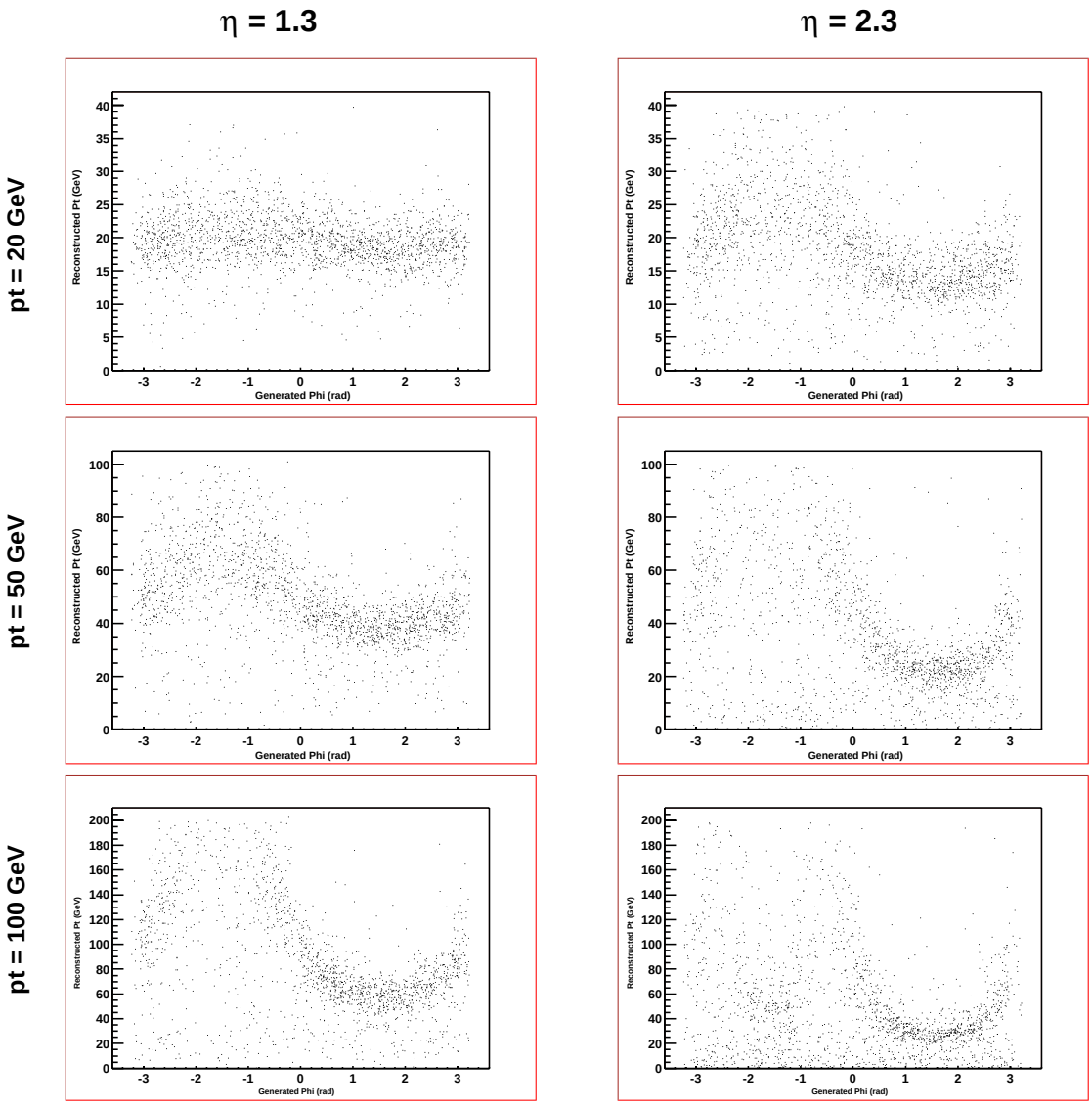

Figure 5.20: Standalone Muon System + Vertex Constraint (ORCA L2) Reconstruction of Muon p_t at $|\eta|$ = 1.3 and 2.1 for 1mm ME Station Misalignment.

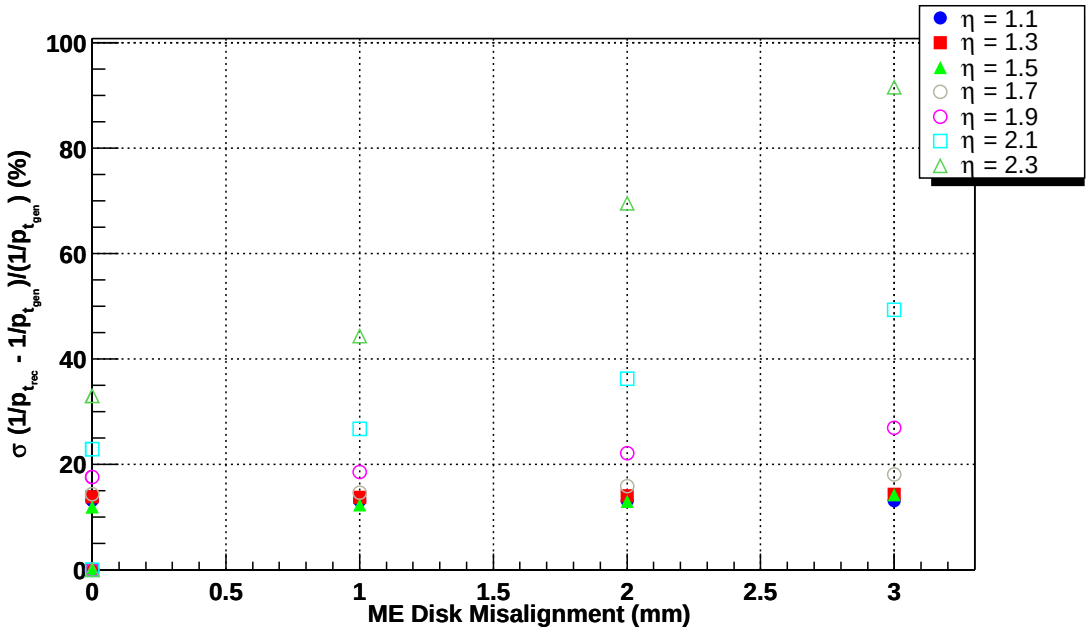

Figure 5.21: Standalone Muon System + Vertex Constraint (ORCA L2) Reconstruction Resolution for p_t=10 GeV Muons as a Function of ME Station Misalignment.

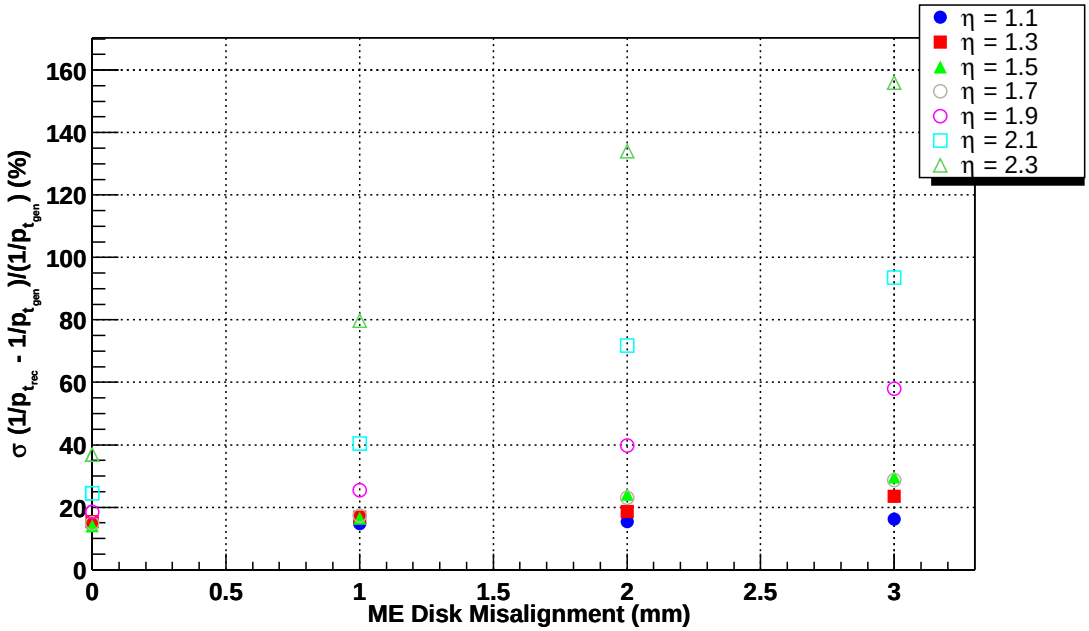

Figure 5.22: Standalone Muon System + Vertex Constraint (ORCA L2) Reconstruction Resolution for p_t = 20 GeV Muons as a Function of ME Station Misalignment.

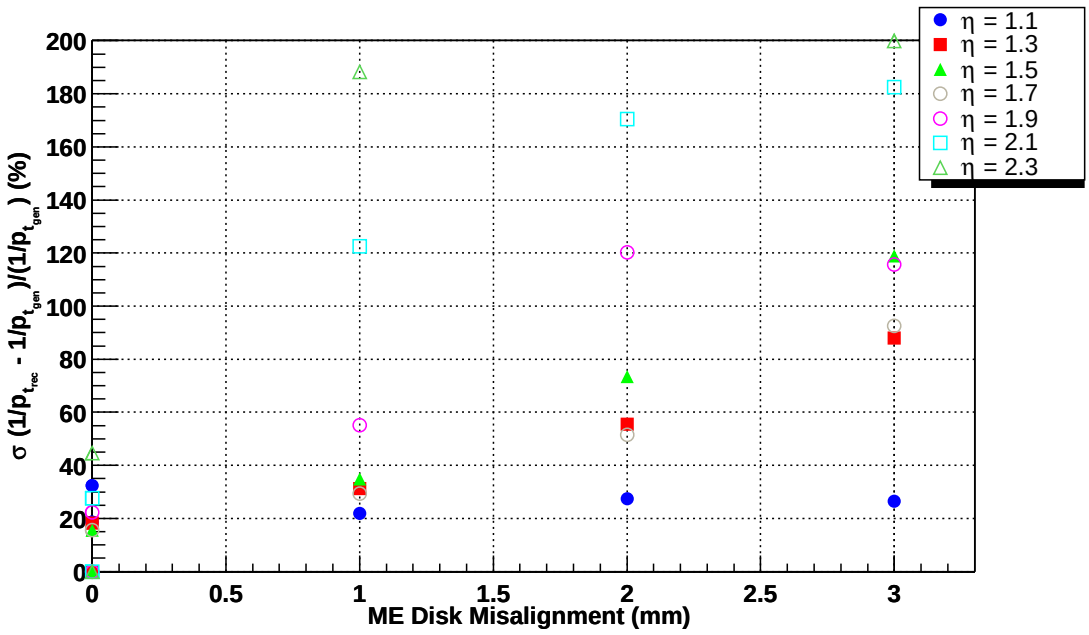

Figure 5.23: Standalone Muon System + Vertex Constraint (ORCA L2) Reconstruction Resolution for p_t = 50 GeV Muons as a Function of ME Station Misalignment.

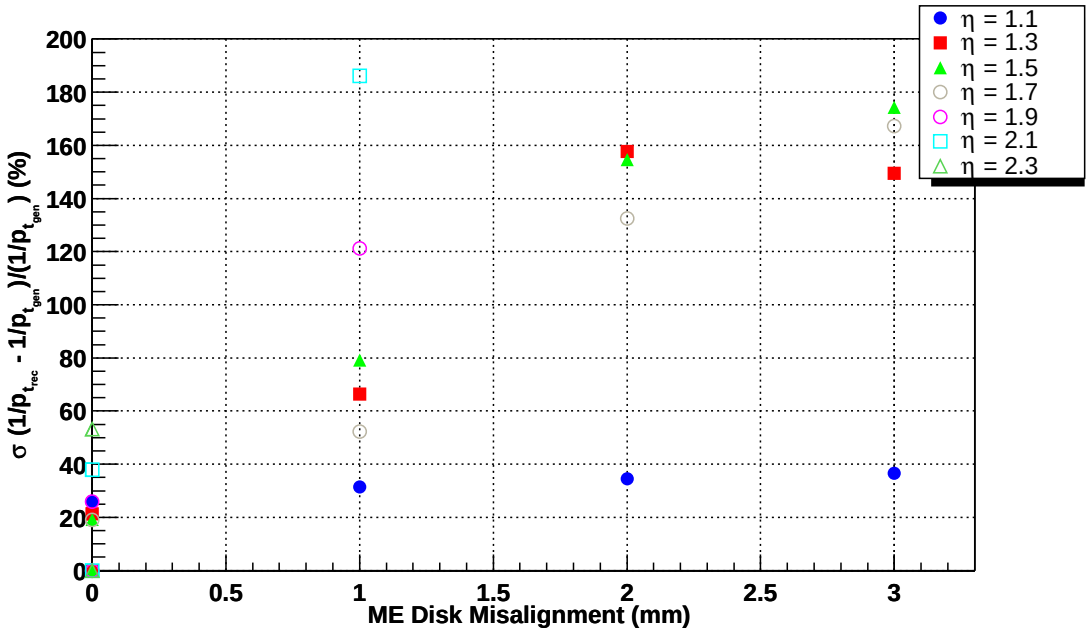

Figure 5.24: Standalone Muon System + Vertex Constraint (ORCA L2) Reconstruction Resolution for p_t = 100 GeV Muons as a Function of ME Station Misalignment.

Table 5.5: Relative Shift in Standalone Muon System + Vertex Constraint Fit (ORCA L2) p_t^{-1} resolutions from perfect alignment for ME Station Motions. The relative shift in the resolution is defined by Equation 5.1.

L2	ME Station Misalignment			
		1mm	2mm	3mm
pt=10 GeV	eta = 1.1	-1%	-1%	-1%
	eta = 1.3	0%	2%	4%
	eta = 1.5	3%	9%	20%
	eta = 1.7	2%	11%	26%
	eta = 1.9	6%	26%	54%
	eta = 2.1	17%	59%	116%
	eta = 2.3	35%	111%	178%
pt=20 GeV				
	eta = 1.1	-1%	3%	9%
	eta = 1.3	9%	21%	53%
	eta = 1.5	16%	56%	94%
	eta = 1.7	16%	54%	93%
	eta = 1.9	37%	115%	213%
	eta = 2.1	65%	193%	282%
	eta = 2.3	116%	264%	323%
pt=50 GeV				
	eta = 1.1	18%	47%	74%
	eta = 1.3	71%	204%	382%
	eta = 1.5	124%	370%	662%
	eta = 1.7	88%	228%	491%
	eta = 1.9	148%	441%	420%
	eta = 2.1	344%	518%	561%
	eta = 2.3	321%	381%	-547%
pt=100 GeV				
	eta = 1.1	22%	33%	41%
	eta = 1.3	212%	641%	602%
	eta = 1.5	313%	705%	808%
	eta = 1.7	175%	596%	779%
	eta = 1.9	368%	694%	708%
	eta = 2.1	391%	1235%	No Fit
	eta = 2.3	707%	277%	No Fit

As Figure 5.21 - Figure 5.24 indicate, the shifting of ME Stations in opposite directions by even ±1mm will significantly degrade p_t resolution for all but the lowest p_t muons. For muons with $p_t \geq 100$ GeV, the resolutions extracted from the residual distributions quickly exceed 100%. Muon tracks at $|\eta| = 1.1$ see very little loss in resolution since the Barrel Muon Drift Chambers are not misaligned.

5.3 Effect of Misalignment on the L1 Endcap Muon Trigger

A Level 1 Muon Trigger is required in the Endcap System to restrict the large rate of background muons from overwhelming the data acquisition (DAQ) system. The inclusive Level 1 Muon Trigger will discriminate between events based solely whether or not the reconstructed p_t of the highest p_t muon track found matches or exceeds a preset trigger threshold level. The precise value of the trigger threshold depends upon the total muon trigger rate and the rate allowed for DAQ. The manner in which the Muon System determines the p_t to be compared against the threshold is identical to the L2 ORCA reconstruction method.

The total rate of data (background + signal events) allowed by the CMS global DAQ for the Endcap Muon System is budgeted at 3 kHz. A trigger selection must be set to reduce the expected total rate of muons for the corresponding beam luminosity to this rate. It is also desirable to set the trigger threshold as low as possible to prevent the unnecessary exclusion of interesting physics events. A 3 kHz integrated muon trigger rate in the Endcap is expected to impose inclusive muons p_t cuts of 4.5, 10, and 25 GeV for operating luminosities of 10^{32}, 10^{33}, and 10^{34} $cm^{-2}s^{-1}$. A PYTHIA simulation of the expected muon rates in the Endcap as a function of muons p_t is shown in Figure 5.25 for a beam luminosity of 10^{-34} $cm^{-2}s^{-1}$. The total rate of muon events in the Endcap is expect to be approximately 100 kHz per unit of η at high luminosity (10^{34} $cm^{-2}s^{-1}$).

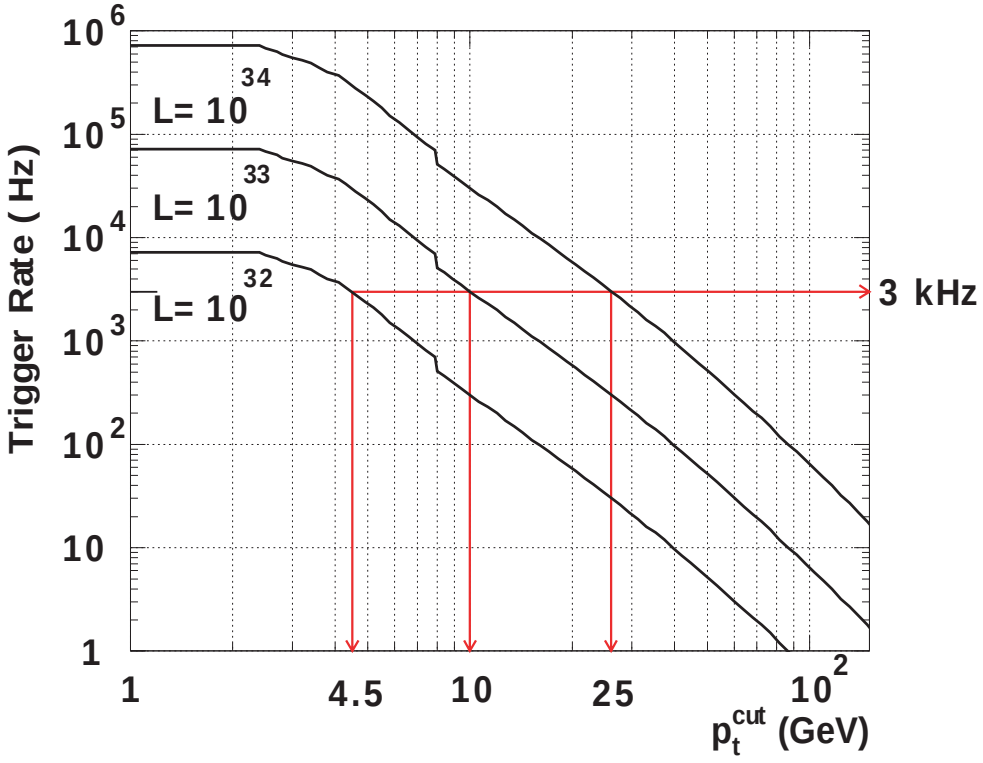

Figure 5.25: Expected Level 1 Muon Trigger Rates in the Endcap for the Three Principle Operating Luminosities at the LHC. Arrows have been added to indicate the 3kHz trigger rate budgeted for the Muon Endcap and the resulting p_t cuts which must be made. The cuts assume perfect alignment of the CSC chambers and CSC chamber resolutions determined by CMSIM [5.2].

The falloff of the Trigger Rates shown in Figure 5.25 is logarithmic and indicates that even a slight shift to a lower p_t threshold will lead to a large increase in the total muon background encountered by the CSC chambers. Likewise, any uncertainty in the initial assignment of muon p_t for muons just below or at this threshold will substantially increase the total muon background for the chambers.

A complete study of the trigger rates and trigger threshold in the Endcap should ultimately be made with additional ORCA simulations of minimum bias events and special trigger simulation software. Such studies will require large amounts of computing time and data storage and go beyond the scope of this study. However, a simple estimation of the effect is discussed.

To estimate the impact of CSC resolution on the selection of the trigger threshold, the averaged resolution of each set of CSC chambers used in the determination of p_t to be applied against the threshold is shown in Table 5.6 and Table 5.7 for nominal and distorted CSC alignment. The resolutions are estimates obtained by the ORCA simulations performed in Chapters 4 and 5. The averages were done in a manner to characterize each set of CSC chambers likely to be used to determine muon p_t for the range of muon momenta near the proposed trigger threshold. The averages represent a global Endcap Muon System average taken from the resolutions of all events reconstructed in the range $1.3 \leq |\eta| \leq 2.3$ as well as two segmented averages representing the combination of ME ±1/2 + ME ±234/2 CSC chambers found in the interval $1.3 \leq |\eta| \leq 1.7$ and the ME ±1/1 + ME ±234/1 CSC chambers found in the interval $1.7 \leq |\eta| \leq 2.3$. Chambers in the ME ±1/3 layer ($|\eta| = 1.1$) were not considered in any of the averages, as tracks found in this region overlap with the Barrel Drift Chambers, which were never misaligned in the studies.

The 'Endcap Average' CSC resolutions in Table 5.6 and Table 5.7 are comparable to previous work with CMSIM which characterized the Endcap Muon Trigger Rate as a function of CSC resolution, where the performance of the Standalone Muon System was described as having an average resolution across the entire Endcap. The results of these studies are shown in Figure 5.26 with the p_t threshold which must be imposed to meet the budgeted 3kHz Trigger Rate overlaid [5.3]. Figure 5.26 shows that degrading the average CSC chamber single muon p_t resolution from 30% to 40% will force the inclusive muon trigger p_t threshold from 22 GeV to 105 GeV in order to maintain the 3 kHz Trigger Rate. Restricting the single muon p_t resolution to less than 30% implies that the location of individual CSC chambers must be known within ±1mm and that ME Station motions must be monitored to better than ±1mm .

Table 5.6: Averaged Standalone Muon System + Vertex Constraint (ORCA L2) Single Muon p_t Resolution for Random CSC Misalignment for Low p_t Muons. The measurement ranges are grouped and averaged in a manner to approximate measurements made with ME 1/1 + ME234/2 ($1.3 \leq |\eta| \leq 1.7$) and ME 1/1 + ME234/2 ($1.7 \leq |\eta| \leq 2.3$) for the range in momentum likely to be important in determining Trigger Performance.

Single Muon pt	Measurement Range	Random CSC Misalignment				
		0um	200um	500um	1mm	2mm
pt = 10 GeV	$1.3 < \eta < 1.7$	12.8%	12.8%	12.9%	13.0%	13.8%
	$1.7 < \eta < 2.3$	21.9%	21.6%	21.9%	23.8%	29.2%
pt = 20 GeV	$1.3 < \eta < 1.7$	14.8%	15.0%	15.3%	16.6%	19.7%
	$1.7 < \eta < 2.3$	23.7%	25.6%	27.0%	28.7%	37.0%
pt = 50 GeV	$1.3 < \eta < 1.7$	16.9%	18.0%	20.3%	26.6%	42.3%
	$1.7 < \eta < 2.3$	27.6%	29.2%	35.0%	46.6%	87.2%
CSC Average	$1.3 < \eta < 1.7$	14.9%	15.3%	16.2%	18.7%	25.3%
	$1.7 < \eta < 2.3$	24.4%	25.5%	28.0%	33.0%	51.1%
Endcap Average	$1.3 < \eta < 2.3$	21.2%	22.1%	24.0%	28.2%	42.5%

Table 5.7: Averaged Standalone Muon System + Vertex Constraint (ORCA L2) Single Muon p_t Resolution for ME Station Misalignment for Low p_t Muons. The measurement ranges are grouped and averaged in a manner to approximate measurements made with ME 1/1 + ME234/2 ($1.3 \leq |\eta| \leq 1.7$) and ME 1/1 + ME234/2 ($1.7 \leq |\eta| \leq 2.3$) for the range in momentum likely to be important in determining Trigger Performance.

Single Muon pt	Measurement Range	ME Station Misalignment			
		0um	1mm	2mm	3mm
pt = 10 GeV	$1.3 < \eta < 1.7$	12.8%	13.0%	13.5%	14.3%
	$1.7 < \eta < 2.3$	21.9%	26.1%	35.9%	46.5%
pt = 20 GeV	$1.3 < \eta < 1.7$	14.8%	15.8%	17.0%	19.9%
	$1.7 < \eta < 2.3$	23.7%	24.9%	39.7%	52.5%
pt = 50 GeV	$1.3 < \eta < 1.7$	16.9%	33.1%	64.5%	103.5%
	$1.7 < \eta < 2.3$	27.6%	98.8%	139.4%	147.7%
CSC Average	$1.3 < \eta < 1.7$	14.9%	20.6%	31.7%	45.9%
	$1.7 < \eta < 2.3$	24.4%	49.9%	71.7%	82.2%
Endcap Average	$1.3 < \eta < 2.3$	21.2%	37.7%	75.2%	103.8%

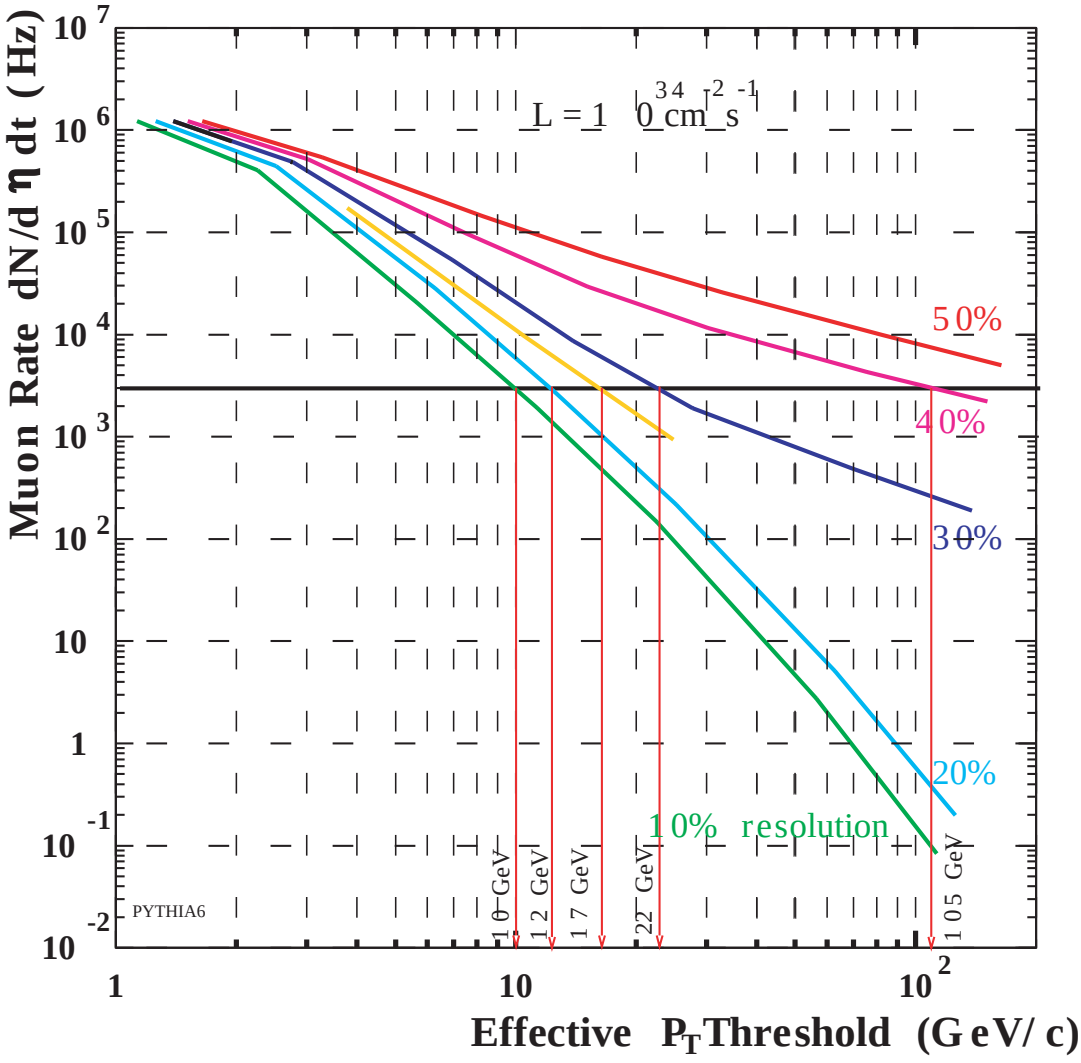

Figure 5.26: Inclusive Endcap Muon Trigger Rates For CSC Chambers with Various Resolutions as a Function of Threshold p_t. The red arrows indicate the intersection of each curve with the budgeted 3kHz Trigger Rate in the Endcap and is labeled with the required p_t threshold required to meet it [5.3].

5.4 Impact of Elevated Single Muon p_t Trigger Thresholds on $H \rightarrow ZZ \rightarrow 2\mu^+\mu^-$ Events

The effect of elevating single muon p_t thresholds in the Endcap according to the manner in which p_t resolution is degraded by misalignment has been evaluated for $H \rightarrow ZZ \rightarrow 2\ \mu^+\mu^-$ events in the Endcap. A sample of 1000 $H \rightarrow ZZ \rightarrow 2\mu^+\mu^-$ events in which all four muons fall in the range $1.1 \leq |\eta| \leq 2.4$ was generated with PYTHIA 6.1.5.2 for six possible Higgs masses (m_H = 120, 150, 182, 200, 300, and 500 GeV). Figure 5.27 shows the single highest p_t muon of the four muons available to the Level 1 Endcap Muon Trigger for each of Higgs masses generated.

The fraction of these events which were triggered on by the inclusive single muon trigger was then examined for the five p_t thresholds determined by the budgeted trigger rate in the Endcap and the p_t resolution of the CSC chambers after random misalignment. Figure 5.28 shows the fraction of $H \rightarrow ZZ \rightarrow 2\mu^+\mu^-$ Endcap events missed by the inclusive single muon trigger. As this Figure indicates, $H \rightarrow ZZ \rightarrow 2\mu^+\mu^-$ Endcap events from lower mass Higgs particles suffer from a larger number of missed events, though even a majority of events generated with a Higgs mass of 300 GeV are missed when the p_t threshold is elevated beyond 100 GeV.

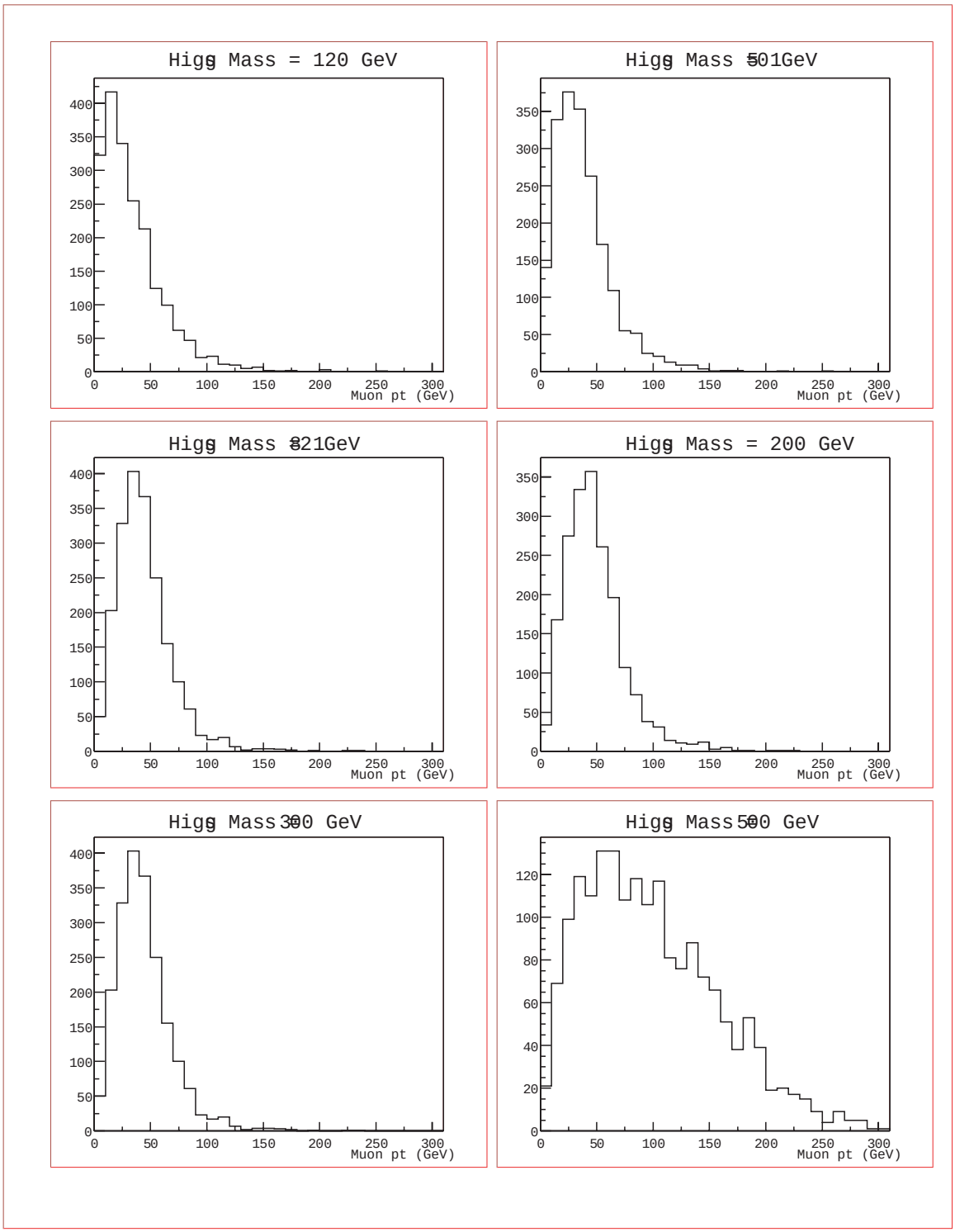

Figure 5.27: Histogram of the Highest p_t Muons From 1000 H→ ZZ →$2\mu^+\mu^-$ Events with All Four Muons Falling in the Range $1.1 \leq |\eta| \leq 2.4$ For 6 Different Higgs Masses Generated With PYTHIA 6.1.5.2.

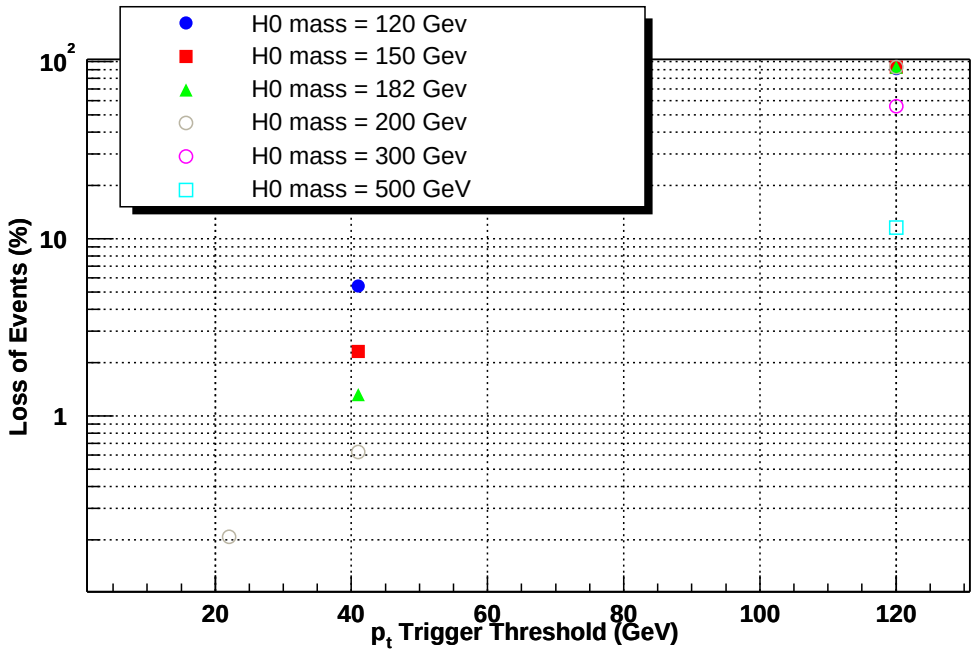

Figure 5.28: Efficiency of Inclusive Muon p_t Trigger For H→ ZZ →2$\mu^+\mu^-$ Events in the Endcap for the 5 p_t Thresholds Illustrated in Figure 5.26.

5.5 Summary and Discussion of Results

The physics simulations conducted in ORCA suggest that the knowledge of CSC chamber locations in the CMS RΦ plane within ±1mm is adequate for the p_t reconstruction and inclusive trigger of single muon events in the Endcap Muon System. The uncertainty in CSC chamber locations along the EMU Alignment System SLM lines in CMS RΦ has been estimated as ≤ 200-250μm on ME ±234 and < 150μm for ME ±1/2 CSC chambers. The alignment of ME ±1/1 chambers along LINK laser lines is estimated as ≈150 μm. The simulations suggest that the estimations of off-SLM CSC chambers must be made on the order of ±1 mm to accommodate the desired Level 1 Inclusive Single Muon Trigger Rate of 3kHz. Regardless of the uncertainties in off-SLM chamber positions, 200-250μm definition of ME Station positions along the CMS X/Y axes by the EMU Alignment System has been shown to restrict potentially serious gross uncertainties in ME Station positioning (i.e. shifts in the YE Iron Disks) which, in the extreme case, could seriously impede the determination of muon p_t and trigger selection.

The ORCA simulation studies did not consider the effects of minimum bias or pile-up events in p_t reconstruction nor the impact of misalignment on the reconstruction of di-muon topologies. Additional studies on the impact of misalignment on Global Muon Trigger Rates using ORCA are recommended, as CSC chamber misalignments had the largest impact on the Standalone Muon System performance, which uses a reconstruction method similar to that employed by the CMS Level 1 Triggering Scheme.

LIST OF REFERENCES

LIST OF REFERENCES

[1.1] S.L. Glashow, Nucl. Phys. 22, 588. 1961.
D. Griffiths. *Introduction to High Energy Physics*, John Wiley & Sons, 1987;

[1.2] S. Wienberg. Phys. Rev. Lett. 19, 1264. 1965

[1.3] S. Coleman and J. Mandula, Phys. Rev 159, 1251. 1967.
L. Hall et al., Phys. Rev. D27, 2359. 1983

[1.4] S. Weimberg, Phys. Rev. D19, 1277. 1979.
L. Susskind, Phys. Rev. D20, 2619. 1979

[1.5] ALEPH, DELPHI, L3, and OPAL Collaborations. Search for the Standard Model Higgs Boson at LEP, CERN-EP/2001-055, 11 July, 2001.

[1.6] M. Dittmar, Perspectives of SM Higgs Measurement at the LHC. PRAMANA J. Phys., Vol 55, Nos 1 & 2, July & August 2000.

[1.7] CMS Collaboration. The Compact Muon Solenoid Technical Proposal, CERN/LHCC 9438, LHCC/P1 1994

[1.8] CMS collaboration. The Muon Project Technical Design Report, CERN/LHCC 97-32, 1997

[1.9] Z. Kunst. The Standard Model Higgs at LHC: Branching Ratios and Cross Sections. Proceedings of the Large Hadron Collider Workshop, Vol II, CERN 90-10, Oct 1990.

[1.10] HDECAY: a Program for Higgs Boson Decays in the Standard Model and its Supersymmetric Extension, A. Djouadi, J. Kalinowski, and M. Spira, hep-ph/9704448, April, 1997, adapted

[1.11] R. Kinnunen, D. Denegri. Expected SM/SUSY Higgs Observability in CMS. CMS Note 1997/057. April 17, 1997.

[1.12] M. Dittmar, Perspectives of SM Higgs Measurement at the LHC. PRAMANA J. Phys., Vol 55, Nos 1 & 2, July & August 2000.

[1.13] S. Matsumoto, Constraints on the electroweak universal parameters and the top and Higgs masses from LEP/SLC data, hep-ph/9411388 vol 1, Nov 1994

[1.14] Qiros, M., Bounds on the Higgs mass in the standard model and minimal supersymmetric standard mode, HEPPH-9411403, November 1994

[1.15] Gunion, Strange, Willenbrock. Weak Coupled Higgs Bosons, hep-ph/9703391

[1.16] G. Altarelli. The Standard Electroweak Theory and Beyond, hep-ph/0011078 v1 6 Nov 2000

[1.17] Fabio Siringo. Light Higgs bosons from a strongly interacting Higgs sector, hep-ph/0105018 v1 2 May 2001

[1.18] Gunion, Strange, Willenbrock. Weak Coupled Higgs Bosons, hep-ph/9703391

[1.19] Greg W. Anderson and Diego Castaño. Measures of Fine Tuning, Physics Letters B347: 300-308 (1995)

[1.20] John Ellis and Douglas Ross. A light Higgs Boson would invite Supersymmmetry, Phys.Lett. B506 (2001) 331-336

[1.21] Chankowski, Ellis, et al. Haggling over the fine-tuning price, Nucl.Phys. B544 (1999) 39-63

[1.22] Fabio Siringo. Light Higgs bosons from a strongly interacting Higgs sector, hep-ph/0105018 v1 2 May 2001

[1.23] G. Altarelli. The Standard Electroweak Theory and Beyond, hep-ph/0011078 v1 6 Nov 2000

[1.24] M. Carena, J. S. Conway, H. E. Haber, J. D. Hobbs, et al, Report of the Higgs Working Group of the Tevatron Run 2 SUSY/Higgs Workshop Fermilab-Conf-00/279-T

[1.25] D. Acosta, T. McDonald. Study of the Optimum Momentum Resolution in the CMS Muon System. CMS Note 2001/033, July 24, 2000.

[1.26] D. Acosta et al., Nucl. Instrum. and Meth. A453 (2000)182-187.

[1.27] Drawing by F. Feyzi, unpublished, modified

[2.1] Brunel, L., Simulation and Reconstruction Software for Opto-Geometrical Systems. CMS Note 1998/079, Nov 10, 1998.

[3.1] COPS Sensor Board Calibration, J. Moromisato et al, Oct 2000, unpublished.

[3.2] CMS Collaboration, Adapted from un-credited FNAL production drawing, Aug 2001.

[3.3] Link Alignment Group, “Simulation and Performance”, Muon Alignment EDR / Muon EDR-3 Documentation, Nov 2000.

[3.4] Private communication with Pedro Arce, IFC Santander, Nov 2000.

[4.1] D. Acosta, T. McDonald, Study of the Optimum Momentum Resolution in the CMS Muon System. CMS Note 2001/033, July 24, 2000

[4.2] Y. Fisyak, W. Ko, J. Rowe. Kalman Filter Approach for Track Finding and Fitting in the CMS Muon and Inner Tracker Systems. CMS TN-1994/297

[4.3] D.E. Groom et al, Review of Particle Physics (PDG). The European Physical Journal C15 (2000), pg 183

[4.4] D. Acosta, G. Apollinari, et al., Large CMS Cathode Strip Chambers: Design and Performance., Nuclear Instruments and Methods in Physics Research, A 453 (2000) 182-187

[4.5] S.M. Wang, D. Acosta, Simulation Studies on the Transverse Momentum Resolution of the CSC Track-Finder, April 5, 2000, CMS IN 2000/026

[4.6] CMS collaboration. The Muon Project Technical Design Report, CERN/LHCC 97-32, 1997

[4.7] D. Acosta et al., Simulated Performance of the CSC Track-Finder, CMS NOTE 2001/033, 21 June 2001

[4.8] R.P. Smith, Mapping the Magnetic Field of the CMS Detector, 3 March 1998, CMS IN 2001/014

[4.9] CMSIM Users Guide, http://cmsdoc.cern.ch/cmsim/cmsim.html

[4.10] E.Calvo et al., Influence of alignment errors on the CMS Endcap single muon Pt measurement, CMS IN 1999/047, March 1, 1999

[4.11] V. Karimaki, G. Wrochna, Alignment Error and Muon Resolution, CMS TN/94-199, 16 Nov 1994

[4.12] V. Karimaki, Study of the Muon Momentum Resolution in the Forward Region, CMS TN/93-124, Sept 1993

[4.13] ORCA CMS OO Reconstruction, http://cmsdoc.cern.ch/orca/

[4.14] T. Sjostrand et al., PYTHIA v6.1, hep-ph/0010017

[4.15] CMS Collaboration, CMS Production Website, http://cmsdoc.cern.ch/cms/production/www/html/general/index.html

[5.1] Private conversation with Sergei Lusin, David Eartly, April 2002.

[5.2] G. Bruno, Workshop CMS Italia SW & CP, 23 Nov 2001.

[5.3] Figure adapted from plot supplied by D. Acosta, April 2002.

[A.1] Drawing by F. Feyzi, unpublished, modified

[A.2] CMS Collaboration. The Compact Muon Solenoid Technical Proposal, CERN/LHCC 9438, LHCC/P1 1994

[A.3] Adaptation of drawing by R. Terry, NEU

[A.4] Drawing by F. Feyzi, unpublished, modified

[A.5] Drawing by F. Feyzi, unpublished, modified

APPENDIX

APPENDIX

Construction Of The Idealized COCOA Simulation Model

The choice in labeling conventions used to specify objects and parameters throughout this document is generally consistent with commonly accepted naming conventions within CMS. However, as COCOA is a geometrical simulation, the complexity of the fitting routines and modeling of complex geometries require that multiple local coordinate systems be devised for many of the components used in the simulation. Additionally, the EMU Alignment consists of several unique objects and structures that are not found elsewhere in the CMS detector. This appendix describes the labeling scheme used throughout this document as well as the construction of the Idealized EMU simulation within COCOA. It offers a very detailed examination of all components in the system as well as the precise placement of the objects in the simulation.

A.1 Definition of Chamber Labeling Scheme in CMS

As discussed previously, the Endcap Muon System is comprised of 4 Muon Endcap (ME) discs of Cathode Strip Chambers (CSCs) separated by the YE(±η) Return Field (RF) Iron disks. The RF iron acts as the principle mechanical support for the CSCs, absorber for incident particle showers, and a return for the large magnetic flux leaving the central solenoid. The CSCs on each of the ME ±2, ±3, and ±4 disks are placed into an inner ring of 18 20-degree and outer ring of 36 10-degree chambers. The ME ±1 rings 1,2, and 3 are composed of 36 10 degree chambers.

The location of a particular CSC in CMS is specified by a three digit number denoting the ME disc, whether it is in the inner or outer ring of chambers, and the chamber position on the ring. By convention, the ME discs are label in order of their placement from the interaction point, with the nearest disc in the +η Endcap designated as ME +1 and the nearest disc to the interaction point in the -η Endcap designated as ME -1. The two rings of chambers comprising a ME ±2, ±3, or ±4 disc are labeled 1 for the inner ring and 2 for the outer ring. The final number specifying the ring position of a particular chamber is determined by simply counting the number of chambers from the X(global CMS) = 0 axis as viewed from the interaction point. Counting is done in a clockwise fashion for rings in the +η Endcap and in a counter-clockwise fashion for the -η Endcap. The chamber intersecting the X (global CMS) = 0 axis is counted as the first chamber in the ring. References to specific CSCs in CMS might look like this: ME +2/2/1, ME -1/1/17, or ME 4/2/30. Figure A.1 illustrates how this labeling scheme is employed for a particular ME disc.

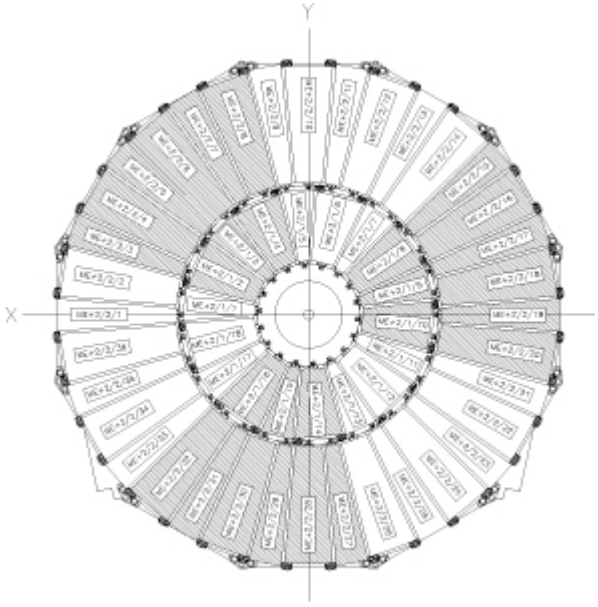

Figure A.1: Typical ME Layout. Drawing of ME2, as viewed from interaction point, with proper labeling of CSC chambers. [A.1]

A.1.1 Local Definition of Cathode Strip and Anode Wire Planes

The naming and numbering convention used to describe the location of cathode strips and anode wires and has been described in CMS Internal Note 2000/004. This convention has been adopted for the present simulation/reconstruction scheme.

The Cathode Strip Chambers are composed of seven trapezoidal honeycombed panels separated by small gaps. All panels except the middle panel are milled with cathode strips running the length of the panel on their inner faces while the gaps between the panels are spanned by anode wires which transverse the panel width (See Figure A.2, below).

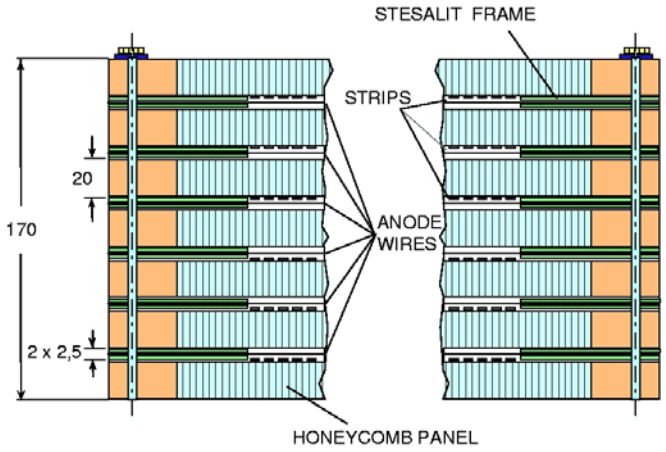

Figure A.2: Cross Section of Six Layer Cathode Strip Chamber. Dimensions in mm. [A.2]

The design of the CSC chambers calls for all cathode strip readout electronics to be mounted on the outside surface of one of the chamber faces. For a single chamber, the labeling scheme designates the chamber face on which these electronics are mounted as the top layer and the nearest cathode strip plane to this face as the first strip plane. Individual strips in the planes are number are numbered from left to right (1 to *n*) when the top of the chamber is viewed from the smaller to larger end of the trapezoid. Anode wire planes are designated in a manner identical to that of the cathode strip planes, while

the numbering of individual anode wires in a plane increases as from the smaller to larger end of the trapezoid (1 to n). Figure A.3 illustrates the labeling scheme.

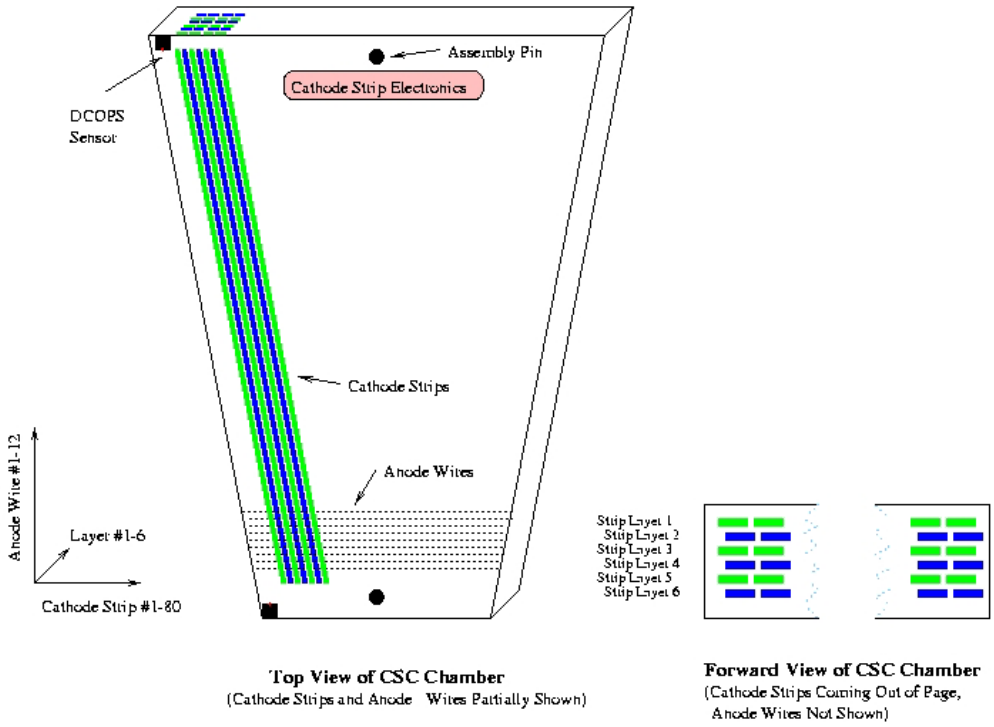

Figure A.3: Single Cathode Strip Chamber Labeling Scheme

A.1.2 Global Orientation of Cathode Strip and Anode Wire Planes

Chambers placed in the +η Endcap are mounted on the YE iron planes such that the first plane of cathode strips is nearest the interaction point for ME1 and ME2 chambers and furthest from the interaction point for ME3 and ME4 chambers. This arrangement means the numbering of cathode strips in the +ηEndcap increases with ϕ for ME1 and ME 2 while decreasing with ϕ for ME3 and ME4. In the -η Endcap, the positioning of the first plane of cathode strips for all chambers is identical to the +η Endcap. However, since the chambers are positioned on the opposite side of the interaction point, the

numbering of cathode strips in the -ηEndcap decreases with ϕ in ME-1 and ME-2 while increasing with ϕ for ME-3 and ME-4.

A.2 Development of COCOA Simulation and Definition of Simulated Objects

To optimize the development of Endcap simulations in COCOA, it was decided to compose the simulated Endcap solely from objects arranged in a 'parent-child' relationship. This means that relatively simple collections of objects already defined in COCOA can be placed together to compose more complex objects. In this scheme, two DCOPS sensors can be arranged in a local coordinate system to define a CSC chamber (Figure A.3). Four CSC chambers, in turn, are arranged to form a SLM line, three SLM lines are arranged to form an Muon Endcap (ME) layer, and six ME layers are assembled to form the entire CMS Endcap Muon system. The modeling of components in this manner means that the location and orientation of all the individual components (dowel pins, chamber active reference centers, lasers, etc) does not need to be known in the general CMS coordinate system beforehand. Rather, the spatial relationships between parent and child objects can be specified directly from CMS production drawings.

This method works very well for six of the Muon Endcaps (ME±2, ±3, and ±4 Endcaps), however the unique construction of the inner most Endcaps (ME ±1) requires a somewhat less symmetric approach, as SLM lines do not traverse the ME discs and a Secondary Laser Line must be introduced. For this reason, the modeling of the ME±1 Endcaps will be addressed separately.

The extraction of the information necessary to define these relationships from CMS production drawings involved several steps and was not a simple exercise of comparing two points in a single drawing. For this reason, the assignment of errors in the simulated system will be addressed separately.

A.2.1 Digital CCD Optical Position Sensor (DCOPS) Sensors

The Digital CCD Optical Position Sensor (DCOPS) is composed of 4 single array CCDs arranged in an open frame and connected to a control circuit fitted with an on board ADC and DSP chip. As the beam of a cross hair laser falls incident on the DCOPS, the intersection of each leg of the laser and CCD results in the accumulation of charge across the CCD pixel array. The mean of the charge distribution on the array can be extracted with a simple fit. By knowing the size of the each pixel comprising the array, the distance between the first pixel in the array and the center of the intersecting crosshair leg (taken to be the mean of the charge distribution) is determined. The first active pixel in each CCD array is referenced to the slot base of the DCOPS mounting structure on a specially designed calibration bench. This calibration then references the CSC strips to the laser lines.

The referencing of all CCDs to a common reference point on the sensor allows for the location and orientation of the entire crosshair laser to be inferred. Alternately, if the location and orientation of the incident crosshair is already known, the charge distributions along the pixel arrays can be used to track the position of the reference point and orientation of the sensor. By monitoring two such reference points and sensor orientations on each CSC chamber, the orientation and position (transverse to the incident laser) of the chambers can be deduced.

By convention, the local coordinate system of all DCOP sensors originates at the common reference point to which the CCD pixel arrays are calibrated. The axes of the local system are orientated such that the +X axis runs away from the sensor aperture and the +Y axis runs parallel to the sensor vertical (Figure A.4). The DCOPS sensor must be carefully calibrated prior to use as a measurement device. Table A.1 shows a sample of what is required for the calibration of a typical DCOPS sensor.

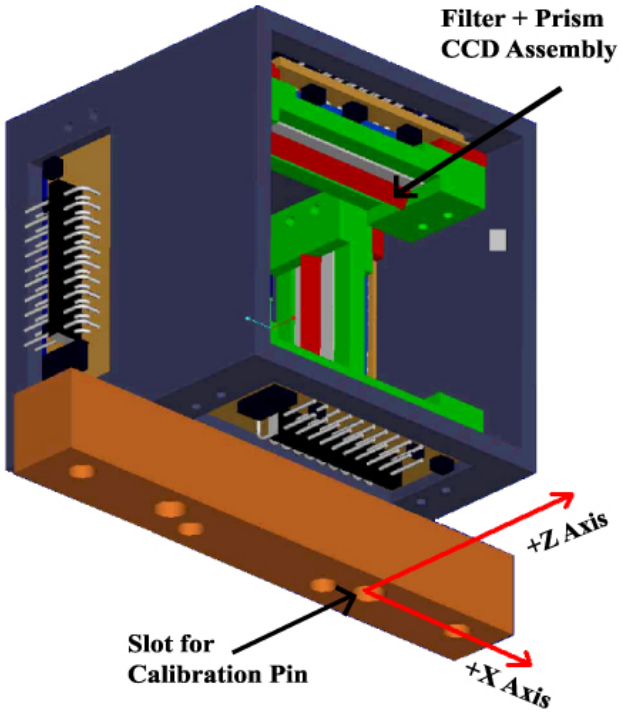

Figure A.4: 3-D View of a DCOPS Sensor. The local right handed coordinate system of the DCOPS is shown in red (Y axis runs vertically). Calibration of the sensor is done by referencing of the first active pixel in this local system. [A.3]

The initial simulation of DCOPS sensors in COCOA is based on production drawings in which the midpoint of the active pixel arrays in the CCDs are placed along the middle of the box frame.

Table A.1: Location of First Active Pixel of CCDs of a Typical DCOPS Sensor in the Local DCOPS Coordinate System as Defined by Figure A.4. Values followed by an asterisk (*) denote a dimension which will requires very precise calibration.

Component	**Placement in DCOPS Reference Frame**		
	X (mm)	**Y (mm)**	**Direction of CCD Vector**
CCD 1 (Upper)	-36.829*	65.75	+X
CCD 2 (Right)	-8.171	57.579*	-Y
CCD 3 (Lower)	-36.829*	20.75	+X
CCD 4 (Left)	-45	57.579*	-Y

The CCD vector is determined to run as the direction of the increase in pixel address across each linear array. This means the CCD vectors are orientated in the DCOPS window frame to point toward the local +X and -Y DCOPS axes.

A.2.2 CSC Chambers

The Cathode Strip Chambers (CSC) in COCOA are defined solely in terms of the relative position and orientation of DCOPS primary calibration pin to the active center of the chamber (with the exception of ME ±1/2 CSCs, discussed later). Although determining the location and orientation of the cathode strip planes is the ultimate goal of the reconstruction and simulation, there is no need to reference the location of the strips in the fitting routine since the relationship between the active center of the chamber and the first strip position does not participate in any direct measurement. Once COCOA has been employed to determine the position and orientation of the chamber in CMS, the first strip position can be immediately specified from prior calibration.

DCOPS sensors are referenced to the cathode strips by a series of carefully constructed mounting plates and dowel pins. The definition of CSCs in COCOA must contain at least two vectors to describe the location of two DCOPS dowel pins. These vectors have been initially determined from production CSC drawings and are locally referenced to the 'Reference Center' of the chambers. The Reference Center of the CSCs is defined to lie on the plane of the first layer of strips and transversely positioned as the average center point of all the individual layers. Because successive layers of strips are offset by half the strip width, the average center point will not lie on the active center of the first strip layer. Figure A.5 shows a diagram of a typical CSC chamber and the relationship between the cathode strip to the geometrical and Reference center points. If the CSCs are perfectly constructed, the Reference Point will lie on along the geometrical center of each chamber and panel.

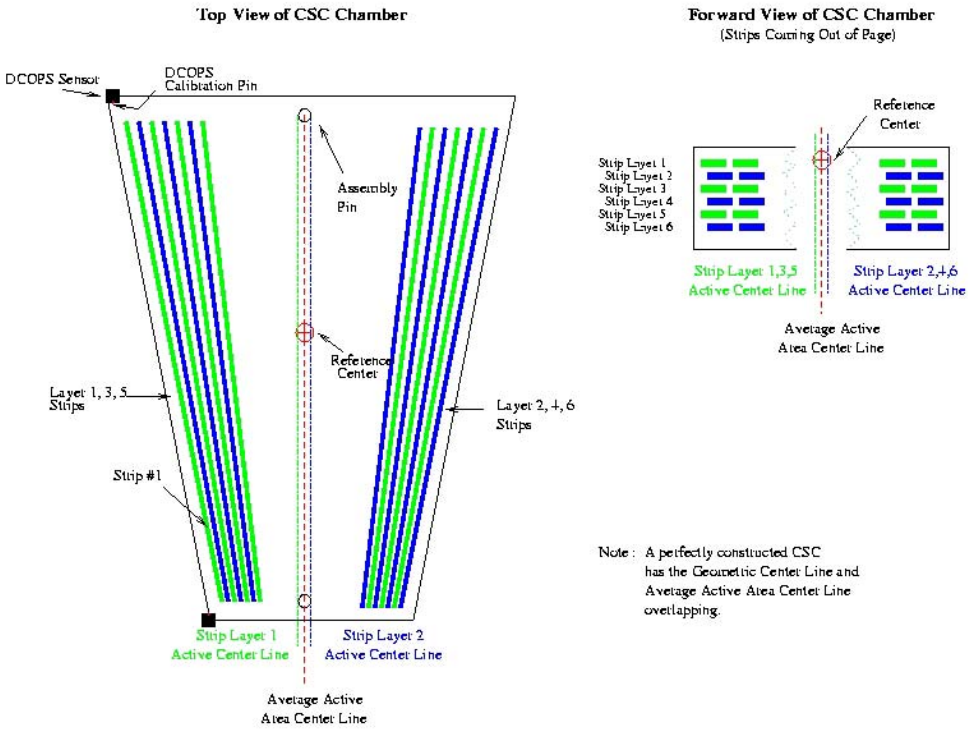

Figure A.5: Strip Layout and Reference Center Definition (definition of active center)

The active center of a CSC forms the origin of a local right handed chamber coordinate system. In this system (shown in Figure A.3 and Figure A.5), when the chamber viewed from the top, the local Z axis increases with the increase in anode wire number and the local X axis increases with the decrease in cathode strip number. The position of the primary calibration dowel pin and orientations of the CSC mounted DCOPS in this system are given below in Table A.2. The positioning of the DCOPS on the CSC chambers will fall on the left or right of the CSC geometrical center line (shown in Figure A.5), depending on the location of the chamber in CMS. Since these positions are symmetric about the chamber centerline, and the DCOPS are to be defined solely by the relative location and rotation of the primary calibration pins, it becomes necessary to place some DCOPS on the chambers with additional 180° rotations. This has the consequence of destroying any generalization of DCOPS orientations in the CMS, but it will maintain the symmetry of the CSC chambers and simplify the installation of

alignment hardware by forcing the primary DCOPS alignment pin to always be positioned toward the chamber center.

Table A.2: DCOPS Primary Dowel References and Sensor Orientations for "Left Handed" CSCs. "Right Handed" CSCs differ by rotations of 180 degrees and have inverse X values. Dimensions are given with respect to the CSC Reference Center in local chamber coordinates. Coordinates have been extracted from CMS CSC production drawings (FNAL). ME ±1/2 chambers have two LINK sensors and only a single DCOPS reference sensor and are detailed in Table A.5.

Chamber	**Inner DCOPS**			**Outer DCOPS**		
	X (mm)	**Z (mm)**	**Rotation about Y (°)**	**X (mm)**	**Z (mm)**	**Rotation about Y (°)**
ME 2/2, 3/2, 4/2	19.922	-1317.833	180 + 5	280.199	1657.151	180 + 5
ME 1/3 Type 1	223.292	840.437	5	373.344	874.776	5
ME 1/3 Type 2	354.790	840.437	5	504.842	874.776	5
ME 2/1	272.081	-992.094	10	13.107	884.330	180 + 10
ME 3/1	272.081	-892.145	180 +10	22.158	776.567	180 + 10
ME 4/1	272.081	-792.603	10	12.931	677.112	180 + 10

Aside from placement of DCOPS sensors on the left or right side of the CSC chambers, ME 2/1, 3/1, and 4/1 DCOPS placement differs slightly as these chambers are different lengths (symmetry about the geometrical center line is still maintained). The high degree of symmetry in the construction of the CSC chambers means that the entire CMS Endcap system can be modeled from four generic CSC chambers (Table A.2). Since each CSC chamber can only be "Left Handed" or "Right Handed", there are eight unique CSC chambers in the ME ±1/3, ±2, ±3, ±4 system.

A.2.3 ME ±2, ±3, ±4 Straight Line Monitoring (SLM) Line Layout

Placement of DCOPS sensors on the CSC chambers has been done in a way which permits a line to be drawn parallel to a line drawn down the center of the DCOPS sensor active areas across the CMS detector. To avoid the beam pipe, the closest approach of this line to the CMS detector Z axis is made at CMS R = 300 mm. These lines are designated as Straight Line Monitor (SLM) Reference lines and denote the optimal placement of DCOPS sensors in CMS. Furthermore, the CSC chambers and DCOPS are orientated in a manner such that the CCD planes of the DCOPS sensors are exactly perpendicular to these lines.

The construction of a simulated SLM lines in COCOA is done from four CSC chambers (two left handed, two right handed), two crosshair lasers, and two reference sensors (mounted on transfer plates) placed in a local SLM coordinate system. The crosshair lasers are initially placed at opposing ends of the local SLM X axis and orientated such that the center of the crosshair beam coincides exactly with the SLM X axis. The reference sensors (on the transfer plate) are placed facing the crosshair lasers and offset so that the center of the DCOPS active area is on the SLM X= 0 axis with the DCOPS Y axis parallel to the SLM Y axis. The arrangement of CSC chambers in ME2, ME-3, and ME-4 requires the SLM lines to be constructed with left handed chambers along the +X SLM axis and right handed chambers along the -X SLM axis. ME-2, ME3, and ME4 SLM layouts have right handed chambers along the +X SLM axis and left handed chambers along the -X SLM axis.

There are only two types of SLM lines in the CMS detector. Both SLM lines have two left-handed and two right handed chambers and differ only in which side of the +X SLM axis these chambers are placed. In practice, there are also slight differences in the transfer plate assemblies due to integration issues and space constraints. However, these differences will not be important for the simulation or reconstruction of the system in COCOA though they have been incorporated into the simulation.

Table A.3: Location and Orientation of CSC Chamber Centers Along all SLM Lines in the CMS Detector. Dimensions are given with respect to the local SLM coordinate system origin. Locations and orientations of chambers in the +η and -η Endcap exhibit mirror symmetry about the CMS XY plane. Coordinates have been extracted from CMS layout drawings.

Chamber	**Chamber Active Center**		
	X (mm)	**Z (mm)**	**Rotation about Y (°)**
ME 2/2,	±5225.848	157.202	±85
ME 3/2, 4/2	±5225.848	-157.202	±95
ME 2/1	±2371.279	118.164	±80
ME 3/1	±2469.704	-135.5275	±100
ME 4/1	±2567.735	-152.813	±100
ME -2/2,	±5225.848	-157.202	± 95
ME -3/2, -4/2	±5225.848	157.202	±85
ME -2/1	±2371.279	-118.164	±100
ME -3/1	±2469.704	135.528	±80
ME -4/1	±2567.735	-152.813	±80

The six Muon Endcap Station ±2, ±3, and ±4 (ME ±2, ±3, ±4) layouts are composed of three identical SLM lines. The endpoints of the SLM lines are designated as SLM reference points and numbered 1-6 starting with the point closest to the +X CMS axis and moving clockwise as viewed from the CMS Z = 0 interaction point (Figure A.6).

The placement of SLM lines and SLM Reference Points is the same for all ME ±2, ±3, and ±4 layers, though the orientation of chambers requires SLM lines in layers ME 2, -3, and -4 to be flipped 180 degrees from the otherwise similar ME -2, 3, and 4 SLM lines (see Table A.4). When the SLM lines on these ME layers are constructed in this manner,

the final position and orientation of all CSC chambers, SLM lines, and SLM Reference Points will overlap in the global CMS XY Plane. Coverage of incident particles across RΦ in the Endcaps is not compromised in this arrangement since the overlapping of CSC chambers is accomplished within individual ME layers.

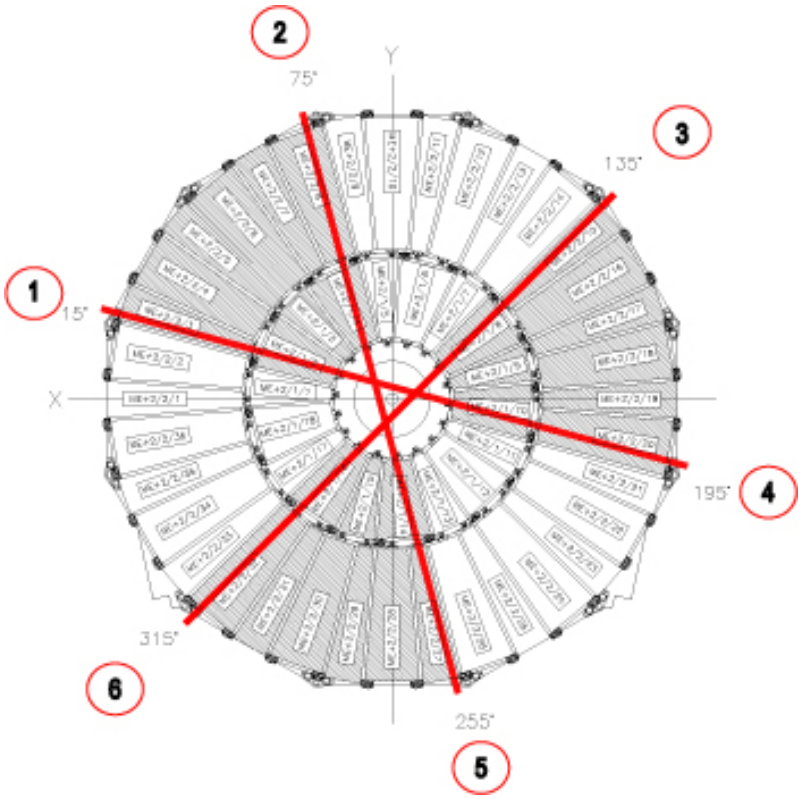

Figure A.6: Detail of SLM Lines and SLM Reference Points 1-6 for ME 2 [A.1]

Table A.4: COCOA Position and Rotation of SLM Lines For All ME Stations.

ME Layer	SLM Line	COCOA Rotation About X (CMS) Axis	COCOA Rotation About Z (CMS) Axis	Position	
				X (CMS)	Y (CMS)
ME 2	1	+90	15	-77.6457	289.7777
ME -3	2	+90	255	289.7777	-77.6457
ME -4	3	+90	135	-212.132	-212.132
ME -2	1	-90	15	-77.6457	289.7777
ME 3	2	-90	255	289.7777	-77.6457
ME 4	3	-90	135	-212.132	-212.132

A.2.4 Muon Endcap Station ±1 (ME ±1) Layout

The chambers in the ME ±1 layer are arranged into three rings rather than two rings as in the ME ±2, ±3, ±4 Endcaps. Each ring of chambers is separated along the CMS Z axis. The inner ME ±1/1 ring of chambers is not within the scope of the EMU alignment proposal, however, the EMU alignment system must reference ME ±1/2 and ±1/3 chambers to the tracker coordinate system.

In the ME ±1 Endcaps, the SLM line arrangement in ME ±2, ±3, and ±4 Endcaps cannot be duplicated due to the separation of the rings along the CMS Z axis. The large amount of Iron behind the ME ±1/1 chambers precludes SLM laser lines from traversing the ME ±1 disc. In this case, the outer reference points for the SLM laser lines are defined by transfer plates (as in the other ME layers) while inner reference points are provided by the LINK Alignment Group.

As previously discussed, the Link Alignment System is charged with transferring the tracker coordinate system to the Endcap and Barrel Alignment Systems. The transfer is accomplished by a series of laser lines that reference the tracker coordinate system to the six rigid MAB structures. The primary Link laser lines that are used in this process are split with a rhomboid prism to create a secondary Link laser line that runs parallel to the primary laser line. This Secondary Link laser line is then used to provide alignment to the ME ±1/2 ring of chambers and establish an inner reference for the ME ±1 SLM lines. Figure A.7 shows the arrangement of the ME ±1/2 and ±1/3 chambers as well as the location of the ME ±1 SLM and Secondary Link laser lines.

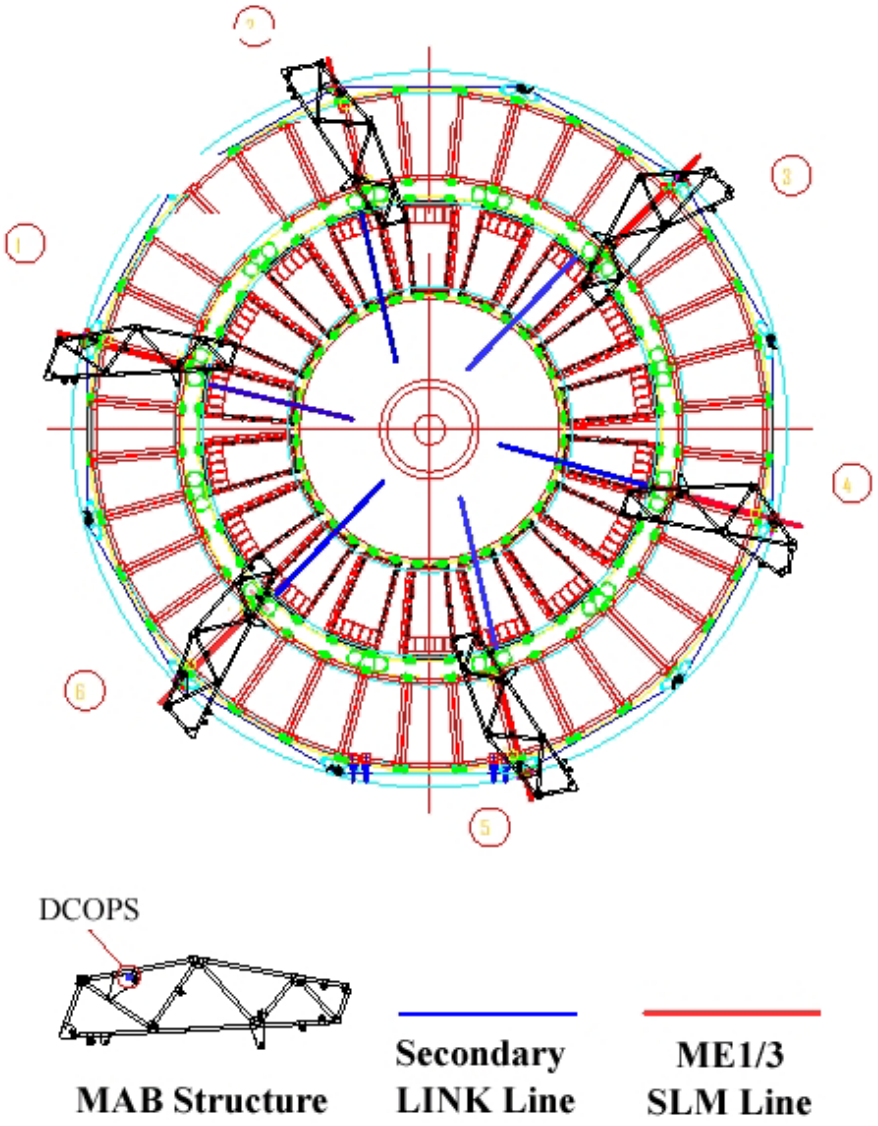

Figure A.7: ME ±1 Chamber Arrangement and Placement of SLM and Secondary Link Laser Lines. Overlap of MAB Structures is shown, though they do not touch ME±1. ME 1/1 chambers are not shown. Note SLM lines do not cross the disc, but terminate at the edge of the ME±1/2 rings. [A.1]

Since the secondary Link laser line is a beam and not a crosshair laser, DCOPS sensors cannot be used to reference this laser line to the ME ±1/2 chambers. The sensors employed to reference the secondary Link line to the ME ±1/2 chambers are two dimensional transparent sensors developed by the Link group that employ photosensitive

strips etched onto a highly transparent glass substrate. Once these sensors determine the location of the ME ±1/2 chambers, a DCOPS sensor attached to the outer end of the chamber can then be used as the endpoint of the SLM crosshair laser line. Figure A.6 illustrates the arrangement of the Secondary Link laser line and the inner SLM DCOPS reference sensor. Table A.5 and Table A.6 detail the precise definition of these lines in the COCOA simulation. Table A.7 details the placement of DCOPS sensors on the ME ±1 chambers.

Table A.5: COCOA Position and Rotation of SLM Lines For ME ±1 Stations. ME ±1 SLM lines do not traverse the entire ME disc, rather they terminate at the reference DCOPS sensor placed on the ME ±1/2 frame. The SLM lines project along lines parallel to the Secondary Link Lines from (0,0, ± 6782), but offset ±66mm.

SLM Line	COCOA Rotation About X (CMS) Axis	COCOA Rotation About Z (CMS) Axis	Position	
			X (CMS)	Y (CMS)
1	-90	15	-17.0821	63.7511
2	-90	75	63.7511	-17.0821
3	-90	135	46.6690	46.6690

Table A.6: COCOA Position and Rotation of Secondary Link Lines In ME ±1. All Primary Link Lines project from (0, 0, ±6690). Secondary Link Lines run parallel to Primary Lines and are offset by ±66.000 mm in the CMS XY Plane.

Secondary Link Line	COCOA Rotation About Z (CMS) Axis	Position	
		X (CMS)	Y (CMS)
1	15	12.941	-48.296
2	75	48.296	-12.941
3	135	35.355	35.355
4	195	-12.941	48.296
5	255	-48.296	12.941
6	315	-35.355	-35.355

Table A.7: DCOPS Primary Dowel References and Sensor Orientations for ME ±1/2 CSCs. Sensors on the ME ±1/2 chambers have rotations of -185 or 5 degrees and two possible locations for the placement of the reference DCOPS (designated as type 1 or 2), both are dictated by the projection of ideal laser lines along the ME±1 SLM lines. Dimensions are given with respect to the CSC Reference Center in local chamber coordinates. Coordinates have been extracted from CMS CSC production drawings (FNAL). ME ±1/2 chambers have two LINK sensors and only a single DCOPS reference sensor.

	Inner Sensor			**Outer Sensor**		
	X (mm)	**Z (mm)**	**Rotation about Y (°)**	**X (mm)**	**Z (mm)**	**Rotation about Y (°)**
Link Sensors	194.571	880.221	-185 or 5	348.589	880.221	-185 or 5
DCOPS Ref Type 1	N/A	N/A	N/A	498.330	1014.108	-185 or 5
DCOPS Ref Type 2	N/A	N/A	N/A	498.330	1002.539	-185 or 5

A.2.5 Transfer Lines

The Transfer Lines in the COCOA simulation are not modeled as distinct objects in the simulation since the placement of transfer plates at each SLM Reference Point on the individual ME layers form the bulk of the transfer system. The only additional component required to complete the system are the placement of crosshair lasers and additional Mechanical Alignment Bar (MAB) reference sensors.

The positioning of the MABs in CMS is dictated by the placement of the Barrel Muon Stations and the mounting brackets which affix the Barrel Muon Chambers to the RF iron. Since the arrangement of the Barrel Muon chambers is not symmetric in CMS Φ, the placement of the MABs and Transfer Lines cannot be symmetric in CMS.

The MAB structures are approximated as compound objects consisting of a DCOPS sensor and a proximity sensor (to provide CMS Z monitoring). In the final reconstruction of the EMU alignment system, these simulated MAB structures will have to be replaced by DCOPS sensors affixed to MABs that are interfaced to the LINK alignment group. The placement of the MAB sensors in the simulation is dictated by the predefined orientation and location of the transfer lasers (Table A.8).

Table A.8: COCOA/CMS Position of Transfer Lines and MAB Reference Sensors

Transfer Line #	**Transfer Line Positions In CMS**		**MAB Sensor Positions In CMS**		
	Φ (°)	**R (mm)**	**X (mm)**	**Y (mm)**	**Z (mm)**
1	14.052	7250	7033.049	1760.317	± 6650.000
2	74.099	7250	1986.326	6972.590	± 6650.000
3	135.901	7250	-5206.504	5045.277	± 6650.000
4	195.948	7250	-6970.958	-1992.045	± 6650.000
5	254.052	7250	-1992.045	-6970.958	± 6650.000
6	314.099	7250	5045.277	-5206.504	± 6650.000

As previously discussed, the Transfer Plates are to provide a physical coupling between the SLM and Transfer Lines. This is accomplished by constructing a mechanical assembly consisting of two DCOPS sensors (Figure A.8). These assemblies are designed to be placed along the SLM Lines such that one DCOPS sensor is centered along the SLM Line and the second DCOPS sensor is centered along the Transfer Line. The local coordinate system of the Transfer Plate is taken to be the same as the local coordinate system of the reference SLM DCOPS sensor. This means that the location of the Reference SLM DCOPS sensor will be (0,0,0) on all transfer plates with all local coordinate axes overlapping. Due the varying location of the Transfer Lines in CMS, 21 unique Transfer Plates are required to completely couple all Transfer Lines to the SLM Lines.

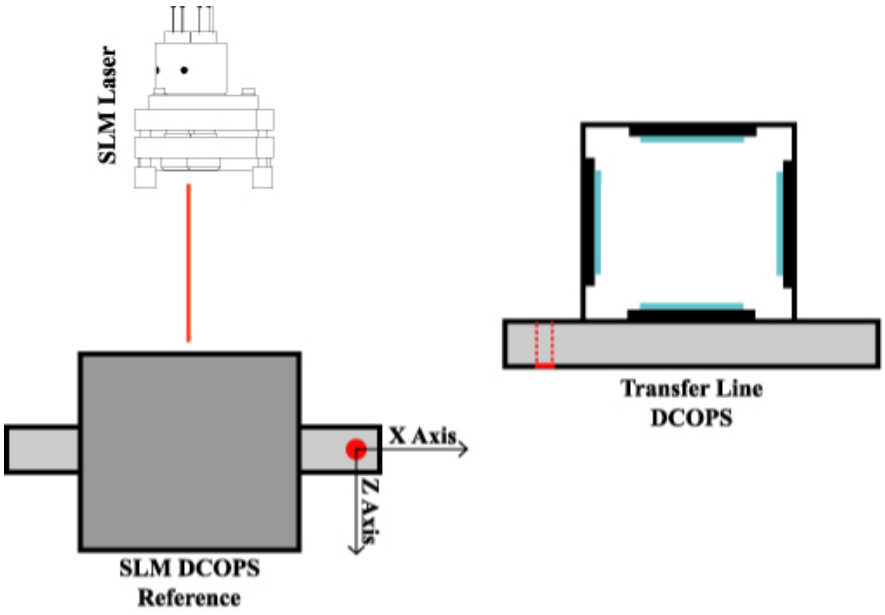

Figure A.8: Sample Layout of Transfer Plate. The figure shows the relative orientation of the two DCOPS sensors on a ME2 Point 2 transfer plate as well as the location of the SLM crosshair laser. The dashed red line on the Transfer DCOPS sensor denotes the slot assembly for the calibration pin.

Table A.9: Transfer Plate Definition. ME4 Transfer Plates are identical to those in the ME3 layer. ME-3 and ME-4 Transfer Plates are mirror symmetric to ME2 Transfer Plates with the exception of ME-3 Plate 5. ME-2 Plates are mirror symmetric to ME3 plates.

Transfer Plate #	**Transfer Sensor Placement (Relative to TP Reference Point)**			**Transfer Sensor Rotation (Rotation about TP Axes)**		
	X (mm)	Y (mm)	Z (mm)	X	Y	Z
ME1 Plate 1	-230.950	19.150	-9.350	-90	180	0
ME1 Plate 2	-225.000	19.150	-9.350	-90	180	0
ME1 Plate 3	135.000	19.150	-9.350	-90	180	0
ME1 Plate 4	141.000	19.150	-9.350	-90	180	0
ME1 Plate 5	-230.950	19.150	-9.350	-90	180	0
ME1 Plate 6	-225.000	19.150	-9.350	-90	180	0
ME2 Plate 1	-464.951	84.250	-9.350	-90	180	0
ME2 Plate 2	141.000	84.250	-9.350	-90	180	0
ME2 Plate 3	-231.000	84.250	-9.350	-90	180	0
ME2 Plate 4	374.951	84.250	-9.350	-90	180	0
ME2 Plate 5	-464.951	84.250	-9.350	-90	180	0
ME2 Plate 6	141.000	84.250	-9.350	-90	180	0
ME3 Plate 1	374.951	84.250	-9.350	-90	180	0
ME3 Plate 2	-231.000	84.250	-9.350	-90	180	0
ME3 Plate 3	141.000	84.250	-9.350	-90	180	0
ME3 Plate 4	-419.951	84.250	-9.350	90	0	0
ME3 Plate 5	419.951	-302.250	-203.350	90	0	0
ME3 Plate 6	-231.000	84.250	-9.350	-90	180	0
ME-2 Plate 5	375.000	84.250	-9.350	-90	180	0
ME-3 Plate 5	-419.951	-302.250	-203.350	90	0	0

Table A.10: COCOA/CMS Position of Transfer Plate. ME4 Transfer Plates locations along the SLM lines are identical to those in the ME3 layer. ME-3 and ME-4 Transfer Plate locations are mirror symmetric to ME2 Transfer Plate locations and orientations with the exception of ME-3 Plate 5. ME-2 Plates are mirror symmetric to ME3 Plates with the exception of ME-2 Plate 5.

Transfer Plate #	**Transfer Plate Placement (Relative to SLM Center Point)**			**Transfer Plate Orientation (Rotations About SLM Axes)**		
	X (mm)	**Y (mm)**	**Z (mm)**	**X**	**Y**	**Z**
ME1 Plate 1	7282.907	-43.25	22.5	0	-90	0
ME1 Plate 2	7283.007	-43.25	154.5	0	-90	0
ME1 Plate 3	7283.004	-43.25	22.5	0	-90	0
ME1 Plate 4	-7282.907	-43.25	-22.5	0	90	0
ME1 Plate 5	-7282.907	-43.25	-22.5	0	90	0
ME1 Plate 6	-7283.004	-43.25	-22.5	0	90	0
ME2 Plate 1	7282.907	-43.25	22.5	0	-90	0
ME2 Plate 2	-7282.907	-43.25	-22.5	0	90	0
ME2 Plate 3	7282.907	-43.25	22.5	0	-90	0
ME2 Plate 4	-7282.907	-43.25	-22.5	0	90	0
ME2 Plate 5	7282.907	-43.25	22.5	0	-90	0
ME2 Plate 6	-7282.907	-43.25	-22.5	0	90	0
ME3 Plate 1	7282.907	-43.25	22.5	0	-90	0
ME3 Plate 2	-7283.003	-43.25	-22.5	0	90	0
ME3 Plate 3	7283.007	-43.25	22.5	0	-90	0
ME3 Plate 4	-7282.907	-43.25	-22.5	0	90	0
ME3 Plate 5	7088.908	-43.25	22.5	0	-90	0
ME3 Plate 6	-7283.004	-43.25	-22.5	0	90	0
ME-2 Plate 5	7282.907	-43.25	22.5	0	-90	0
ME-3 Plate 5	7088.908	-43.25	22.5	0	-90	0

A.2.6 Script Labeling Conventions

Based on the COCOA scripting syntax and the parent-child relationships between components, the labeling conventions in Table A.11 have been adopted for EMU elements in COCOA Simulation Scripts.

Table A.11: Labeling of EMU Objects in COCOA Scripts.

CMS Designation	**COCOA Script Designation**
ME 2 SLM 1-4	slm21
ME -2 SLM 1-4	slm-21
ME 2 Laser 1	las21
ME 2/2/3	me22_3
ME 2/1/10	me21_10
ME 2/1/10 Outer DCOPS	cops_outer21_10
ME 2/1/10 Inner DCOPS	cops_inner21_10
Transfer Line 1	Not Needed in Script
MAB Sensor at Transfer Point 1, Z = +6500 mm	mab1
MAB Sensor at Transfer Point 1, Z = -6500 mm	mab-1
Transfer Laser 1 (located in + Endcap)	transfer1
Transfer Laser -1 (located in - Endcap)	transfer-1
ME 2 Transfer Plate 1	transfer_plate21
ME 2 Transfer Plate 1 SLM Reference DCOPS	me2_reference1
ME 2 Transfer Plate 1 Transfer Line DCOPS	me2_transfer1

A.2.7 Final Scripts Compared to Theoretical Placement

The complete model of the CMS EMU Alignment System constructed with the components previously detailed show layout and placement errors in the COCOA EMU simulation components of <5 μm along the Transfer Line (average deviation of .05 μm) and 10 μm along the SLM Line (average deviation of .81 μm). The discrepancies on SLM on the order of 10 μm occur only on the placement the inner ME21/ ME-21 DCOPS sensors relative to the ME21/ME-21 CSC chamber centers. It has been decided that this error lies in the corresponding ME21/ME-21 production drawings. The decision has been made to match components in the COCOA simulation to the final production drawings rather than a perfect CMS geometry. It is expected that the tolerance on the construction of the components comprising the system will greatly exceed any of these small discrepancies in the production drawings.

VITA

VITA

Robert Lee [redacted] began undergraduate studies at Purdue University while enrolled in Air Force ROTC and started working with the CMS EMU Alignment Group at Fermilab during the summer. He completed his Physics B.S. in 1998 and subsequently received a commission as an officer in the US Air Force. Work began on his Ph.D. research in late 1998, when he resumed work with the CMS collaboration at Fermilab. He completed his thesis in April 2002 and earned his doctorate in physics from Purdue University in May 2002.